Mesoscopic scale analysis of inertial transition in granular materials

Adriane Clerc

Aix-Marseille Université

Ecole doctorale 353 – Sciences pour l'ingénieur : mécanique, physique, micro et nanoélectronique

Thèse présentée pour obtenir le grade universitaire de docteur de l'université d'Aix Marseille

par

Adriane CLERC

Discipline : Mécanique des Solides
Laboratoire d'accueil : INRAE Aix-en-Provence, UMR RECOVER

Analyse mésoscopique de la transition inertielle dans les milieux granulaires.

Mesoscopic scale analysis of inertial transition in granular materials.

Soutenue le 10/02/2022 devant le jury :

Jérôme CRASSOUS	Université de Rennes	Rapporteur
Claudio DI PRISCO	Politecnico di Milano	Rapporteur
Vanessa MAGNANIMO	University of Twente	Examinatrice
Farhang RADJAI	LMGC Université Montpellier	Examinateur
Antoine WAUTIER	INRAE Aix en Provence	Co-Encadrant de thèse
François NICOT	Université Savoie Mont Blanc	Co-Directeur de thèse
Stéphane BONELLI	INRAE Aix en Provence	Directeur de thèse

Remerciements

Je voudrais exprimer ma profonde gratitude en premier lieu pour mes directeurs de thèse. Officiellement il n'y en a qu'un, Stéphane Bonelli mais officieusement François Nicot et Antoine Wautier ont été plus que des co-directeurs ou encadrants. Je les remercie de m'avoir soutenue tout au long de ma thèse malgré ma formation plus géophysicienne que physicienne. Merci à Antoine sans qui mon sujet n'aura pas existé et qui a toujours été présent pour appuyer mes réflexions et même corriger mes erreurs de code. Merci à Stéphane pour son soutien, ses cours particuliers et ses appels en plein confinement pour vérifier ma santé mentale. Enfin, merci à François pour toutes les discussions enrichissantes que nous avons eu à Grenoble, puis en ligne. Grace à Antoine et François et leurs réunions scientifiques hebdomadaires durant le confinement pour leurs doctorants, j'ai pu mieux comprendre les travaux des autres doctorants de notre groupe, et rester stimulée et motivée scientifiquement.

Je tiens également à remercier les membres de mon jury de thèse qui ont accepté de participer à cet effort de thèse. Je suis reconnaissante que Claudio Di Prisco et Jérôme Crassous aient été mes rapporteurs. Leurs rapports et leurs questions lors de ma soutenance m'ont permis d'avoir une nouvelle vision sur certains points de mes travaux. Parallèlement, je remercie Vanessa Magnanimo et Farhang Radjai pour leur présence en tant qu'examinateurs. Merci pour leurs remarques qui enrichissent mes travaux et qui viendront m'aider à les valoriser.

Je n'oublie pas Francesco Froiio, Claire Silvani et Yannick Thiery pour avoir fait parties de mon comité de thèse et avoir ainsi porté un bel intérêt à mon travail. Je les remercie d'avoir pris du temps chaque année de mon doctorat pour partager leur point de vue et leurs conseils.

J'ai passé mes trois années de doctorat sur le site du Tholonet de l'IRSTEA qui est devenu l'INRAE entre temps. Merci à tous mes collègues doctorants ou non. Malgré la pandémie, j'ai énormément apprécié le peu de moments conviviaux que nous avons eu (je garde un très bon souvenir de mon premier week-end d'escalade à Orpierre). Parmi les (anciens) doctorants, j'ai une dette immense envers Marie Miot qui m'a supportée quelques soirs par semaine et prêtée son canapé lit pendant deux ans, à l'époque où je pensais encore que vivre sur Avignon et travailler sur Aix en Provence était une bonne idée. Merci à tous les autres doctorant.e.s, docteur.e.s, ingénieur.e.s et les moments de détente que nous avons eu. Merci à Antoine pour m'avoir invitée à courir et à grimper sur la Sainte Victoire.

Évidemment, je souligne l'appui de mes parents, qui ont tenus à être présents à ma soutenance. Ils ne m'ont jamais bridée dans mes aspirations

professionnelles et personnelles, et je crois que cela a plutôt réussi. Je remercie mes ami.e.s pour leur soutien, j'ai une pensée pour Benoit qui est mon socle amical et scientifique, Mathilde et Célie, Sébastien, et Pauline. Enfin, the least but not the last, Diavel, ma compagne à poils et à quatre pattes, sans qui, certains jours auraient été bien plus difficiles. Merci pour son soutien à mon travail de thèse, sur mes genoux ou sur le bureau, appuyée sur un ou deux de mes bras, ou même étalée sur mon clavier.

Résumé

Un milieu granulaire est un milieu composé de grains en contacts dans une phase fluide (du gaz et/ou de l'eau). Composants d'un pierrier, d'une dune de sable, d'un manteau neigeux, d'une digue maritime ou fluviale, les milieux granulaires sont omniprésents dans nos vies. Leur grande complexité et originalité résident dans le fait que ces milieux peuvent se comporter comme un solide, un liquide et même un gaz. Une avalanche, un mouvement de terrain, sont les conséquences de la transition solide - fluide d'un matériau granulaire. Les régions montagneuses concernées représentent environ un quart du territoire français métropolitain. De plus, la France présente un nombre conséquent de barrages (plusieurs dizaines de milliers de petits barrages, environ mille grands barrages) et des dizaines de milliers de kilomètres de digues fluviales et maritimes. De part les nombreuses applications associées à la gestion du risque, il est nécessaire de mieux comprendre les mécanismes de la transition inertielle, plus particulièrement identifier les causes de son initiation et les éventuels signaux précurseurs.

Dans ce travail, la transition inertielle est vue comme une instabilité mécanique, et les bouffées d'énergie cinétique associées à sa survenue, sont considérées comme des signatures d'instabilités mécaniques pré-existantes. Ainsi, afin de mieux comprendre les mécanismes amenant à la transition inertielle, l'apparition et la propagation des bouffées d'énergie cinétique sont étudiés grâce à des expériences numériques quasi 2D, utilisant la méthode aux éléments discrets (DEM). Les milieux granulaires sont considérés comme un milieu continu à l'échelle de la pente ou de l'ouvrage. Cependant leur microstructure, c'est à dire la distribution spatiale des grains et de leur contacts, conditionne leur comportement mécanique. La DEM permet de faire la jonction entre ces deux visions, notamment en introduisant une échelle mésoscopique entre les grains et le volume élémentaire représentatif. Dans cette thèse, les cycles de grains, définis comme la partition du milieu basée sur le réseau de contacts entre les grains, sont les méso-domaines à partir desquels les bouffées d'énergie sont étudiées. Des indicateurs mésoscopiques comme un tenseur de déformation et un tenseur de contrainte mésoscopiques (compatibles avec les tenseurs macroscopiques) sont définis en vue de tester l'application du critère du travail du second ordre à l'échelle mésoscopique. Le travail du second ordre correspond au produit doublement contracté entre un tenseur de contrainte incrémentale et un tenseur de déformation incrémentale. D'une manière générale, les quantitées mésoscopiques peuvent être définies selon deux visions : une vision de partition qui permet de retrouver la quantité macroscopique par homogénéisation spatiale, et une vision structurale, indispensable à la formulation d'un critère du second ordre mésoscopique, et dont le lien avec la quantité macroscopique se fait par homogénéisation statistique.

Dans un premier temps, des échantillons de densité différentes sont soumis à un essai biaxial, et des bouffées d'énergie cinétique sont étudiées lorsque le régime stationnaire est atteint, l'état critique. Après avoir isolé une zone de propagation autour de chaque bouffée du reste de l'échantillon, il est montré que les bouffées d'énergies cinétiques apparaissent dans une région où les contacts sont proches du seuil de glissement et qui est plus lâche, avec des cycles de grains de plus grande porosité, que dans le reste de l'échantillon. L'annulation du travail du second ordre mésoscopique à l'intérieur de la zone de la bouffée est un précurseur à son initiation. Durant la propagation de la bouffée d'énergie cinétique, la micro-structure dans la zone de la bouffée est réarrangée. Les cycles de grains d'ordre élévé et les particules libres sont des acteurs majeurs de la réorganisation. Une bouffée d'énergie cinétique est considérée comme une réorganisation à court terme d'une partie de la micro-structure. Dans ce contexte d'essai biaxial à l'état critique, les bouffées d'énergie cinétique restent localisées (ne se propagent pas à tous l'échantillon) car les réorganisations sont efficaces pour retrouver une stabilité mécanique et permettent d'enrayer sa propagation à tout l'échantillon, résultat qui est retrouvé avec l'évolution du travail du second-ordre mésoscopique structural.

Dans un deuxième temps, la démarche mise en place pour un cisaillement dans un essai biaxial est appliquée à un cisaillement gravitaire afin de se rapprocher de l'exemple concret d'un glissement de terrain. L'échantillon est incliné de manière progressive en présence de gravité. Deux types de simulations sont effectuées et comparées. L'une des simulations conserve des conditions aux frontières avec des murs rigides, alors que des conditions limites périodiques sont choisies pour l'autre simulation. De manière générale, les deux conditions limites aboutissent à une transition inertielle pour le même angle de pente mais l'état de contrainte est modifiée par la présence de murs rigides. Comme pour l'essai biaxial, l'étude des bouffées d'énergies cinétiques suggère une évolution progressive vers la transition inertielle : les bouffées d'énergie cinétique deviennent de moins en moins localisées au fur et à mesure que la pente se fait forte, jusqu'à la fin de la transition inertielle qui est suivi d'un déplacement des grains en continu.

Mots clés : Matériaux granulaires, Instabilités mécaniques, Transition inertielle, Echelle mésoscopique, Cycles de grains, Méthode aux élément discrets, Critère du travail du second-ordre.

Abstract

A granular material is a media composed of grains in contact with each other immersed a fluid phase (gaz and/or water). Components of a scree, of a sand dune, of a snowpack, of sea and river dikes, granular materials are widely present in our life. Their great complexity and originality come from the fact that granular media can behave like a solid, a fluid and even a gaz. An avalanche, a landslide may result from the solid-fluid transition in a granular material. Mountain regions, that are widely concerned, represent a quarter of the continental french territory. Moreover, France owns a large number of dams (several tens of thousand of small dams, about a thousand of big dams) and tens of thousands of kilometers of sea and river dikes. Because of the numerous applications associated to risk management, it is necessary to understand the mechanisms of the inertial transition. More particulary, it is necessary to identify the causes of the inertial transition and if any precursors exist.

In this work, inertial transition is a mechanical instability, and bursts of kinetic energy are considered as early precursors of pre-existing mechanical instabilities. Thus, occurence and propagation of bursts of kinetic energy are studied, in order to better understand the mechanisms leading to the inertial transition. This is done thanks to quasi 2D numerical experiments with the use of the discrete element method (DEM). Granular materials can be considered as a continuous media as the macroscopic scale. However their micro-structure, the spatial distribution of grains and their contacts, drive their mechanical behaviour. DEM enables to bridge the gap between these two points of view, in particular with the introduction of an intermediate scale, the mesoscopic scale, between the grain and the representative elementary volume. Grain loops, which are defined from the partition of the contact network of the media, are the meso-domains from which bursts of kinetic energy are analysed. Mesoscopic indicators are defined such as strain and stress mesoscopic tensors (consistents with related macroscopic quantities) in order to defined a second-order work criterion at the mesoscopic scale. The second-order work correponds to the double dot contraction product between an incremental stress tensor and an incremental strain tensor. Generally, there are two approaches to define a meso-physical quantity. On one hand, a partition approach from which the macroscopic quantity can be found by spatial homogeneization. On the other hand, a structural approach, necessary for the second-order mesoscopic work criterion formulation and from which the macroscopic quantity can be found back by means of statistical homogenization.

In a first time, granular samples of different density are submitted to a

biaxial test and bursts of kinetic energy are analysed during the critical state regime. A propagation zone is defined around the burst of kinetic energy to show that bursts of kinetic energy occur in regions where the proportion of contacts closed to sliding is higher than in the rest of the sample. Moreover the burst region is also looser, with grain loops of higher porosity. The vanishing of the second-order work at the mesoscopic scale, inside the burst region, is a precursor to the initiation of the burst. During the propagation of the burst, the micro-structures of the burst area are rearranged. High order loops and rattlers (grains with no or one contact) play a key role in the reorganization. Bursts of kinetic energy can be viewed as short time reorganizations of a portion of the system. During a biaxial test, at the critical state, bursts of kinetic energy remain localized (do not affect the whole sample). The micro-structure reorganizations are able to stabilize the region, mitigating the propagation of bursts to the whole sample. The vanishing and then positive values of the structural second-order mesoscopic work underline this point.

In a second time, the approach put in place for biaxial tests is applied to granular packings on a slope, in order to get closer to the pratical exemple of a landslide. Samples are titled progressively under gravity. Two simulations with different boundary conditions are compared. One simulation has rigid boundary conditions. The other simulation has periodic boundary conditions. Both type of simulations exhibit an inertial transition at the same slope angle. However in the rigid boundary conditions simulation, the stress state and the failure is non homogeneous because of the presence of the rigid walls. The analysis of bursts of kinetic energy analysis suggests a gradual evolution towards inertial transition. The steeper the slope gets, the less localized and the more numerous bursts of kinetic energy are, until the inertial transition, followed by a persisting movement of grains.

Mots clés : Granular material, Mechanical instabilities, Inertial transition, Mesoscopique scale, Grains loops, Discrete element method, second-order work criterion.

Contents

List of Figures

List of Tables

Chapter 1

Introduction

Many granular materials surround us, from the beach to the kitchen ingredients and through seismic gauge, mountains slopes and earthen dams among many others. Their size variety is also wide, from ten of microns for powders up to ten of meters for rocks in mountain screes. Conceptually, a granular material is a set of solid particles in interaction and immersed in a fluid (liquid or/and gas) filling the pore space. It can be *dry* if the fluid is gas, *partially saturated* if liquid and gas coexist (mainly water and air) or *saturated* if the liquid phase fill all the pore space.

Behind an apparent simplicity at the grain scale, granular media exhibit a great diversity of behaviours under different solicitations at the scale of an assembly of grains. Who has never play with sand and see his/her castle crumble after the sea came by or because of a consolidation default ? From a quasi-static solid regime, and under certain mechanical loadings or hydraulic conditions, the granular assembly can flow like a liquid and even behave like a gas (Figure 1.1).

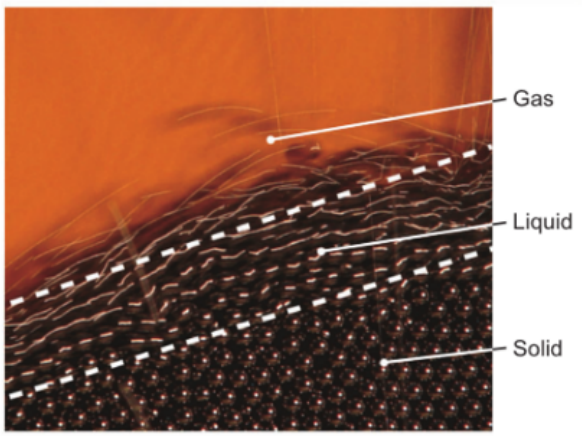

Figure 1.1 – The flow regimes of granular material : solid, liquid, gas obtained by pouring steel beads on a pile (Forterre and Pouliquen, 2008)

Illustrations of the consequences of the solid-fluid like transition are given in Figure 1.2. In France, montains area represent about 22% of the total area. They attract a lot of people either for tourism or for living. Slope stability consequences can have a substantial impact on the population and human

activities. Moreover, France also exhibits signifiants numbers of hydraulic structures. The total linear length of dikes represent more than 9,000 km as protection against flooding, 10,000km of dikes for navigation canals, 1,000km of hydroelectrics canals and 1,000km of maritime dikes (Bonelli, 2012). In addition, ten of thousands small embankement dams (smaller than 15m) and about 600 large dams are enumerated. Many of these hydraulic structures are made of compacted layers of soil which may be subjected to the solid-fluid like transition resulting in dike or dam failure. Those numbers and the related risks underline the importance of being able to anticipate failure with dramatic consequences.

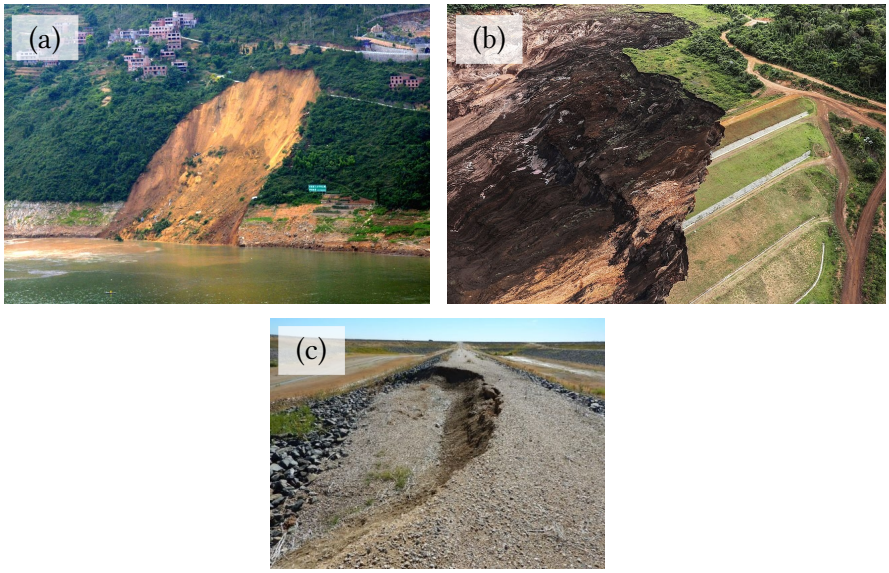

Figure 1.2 – (a)Rotationnal landslide at the Daning River, Wushan County in Yangqing Miunicipality, China (24.06.2015), (b) Liquefaction of the dam at Vale's Corrego do Feijao mine in southeastern Brazil (25.01.2019), (c)Slope failure at north cell of Woman Creek Dam (2013) *source : the Colorado State Engineer's Office*

The transition between solid and fluid like behaviours is called the inertial transition. To summarize, inertial transition is known to play an important role in the triggering of natural hazards such as debris flow, landslides and avalanches. It plays also a role in the destabilization of dikes or dams subjected to internal erosion (Wautier et al., 2018a). Understanding and modelling the inertial transition is still an active subject (Cambou et al., 2013; Forterre and Pouliquen, 2008; Di Prisco and Pisanò, 2011; Vescovi et al., 2018).

At the material point scale, existence of bursts of kinetic energy are considered as a signature of effective failure (di Prisco and Imposimato, 1997; Wan et al., 2017). They stand for early warnings of inertial transition (Darve et al., 2004; Wautier, 2018), and by consequence, studying bursts of kinetic energy makes a lot of sense to anticipate regime changes (Welker and McNamara, 2011; Walker et al., 2014; Gaume et al., 2018). Although these failure have consequences at the macro-scale, they come from micro-changes (contact grain loss and grain displacement), at the scale of a grain. Micro-scale investigations are thus needed to identify inertial transition mechanisms. In the desire to brigde the gap between the contact scale properties and the scale of the entire material, multiscale approaches are used to study granular materials (Staron et al., 2005; Zhu et al., 2016c; Liu et al., 2018). Those upscaling approaches have proven that introducing an intermediate scale -the meso-scale- is relevant. Indeed, macroscopic behaviour relies widely on the geometrical arrangements of grains. Force chains (Radjai et al., 1996; Tordesillas, 2007) and grain loops (Zhu et al., 2017; Liu et al., 2020) have proven to be revelant to give information on how forces and geometrical reorganizations take place.

Since its introduction by Hill in 1958 (Hill, 1958), the second-order work criterion has proved to be a useful and versatile tool to identify unstable states (Wan et al., 2016). Unstable materials, in the sense of second-order work criterion, will exhibit unbounded brutal increase in kinetic energy if a suitable incremental loading is applied. The vanishing of the second-order work is a necessary condition and a precursor of inertial transition. The second-order work criterion is defined at the macro-scale (Nicot and Darve, 2007; Nicot et al., 2009, 2012b) and at the micro-scale (Nicot et al., 2007; Hadda et al., 2013), but no works proposed yet a meso-scale definition.

The aim of this PhD thesis is to go back to the discrete nature of a granular material in order to analyse and understand the elementary micro- and meso-mechanics leading to the sudden appearance of kinetic energy, signature of a static/inertial transition. The consequences of outbursts at the micro-scale and the meso-scale are analysed for different sample density. Precursors of the bursts of kinetic energy are looked at the grain scale and at the meso-scale. Chapter 2 introduces the necessary concepts and background to understand the work done here. The issue of instability in granular material is reviewed, especially in the framework of inertial transition. The importance of defining a meso-scale is underlined, and the grain loop concept is reviewed. The numerical simulation choice is underpined, and the principles of Discrete Element Method is reviewed. All the concepts and tools needed and used in this work to perform micro-mechanical analyses are given in Chapter 3. In particular, we introduce two complementary perspectives to

define meso-structures and attached meso-scale quantities: the structural and the partition points of view. Meso-stresses and potential definitions of a second-order mesoscopic work are introduced and discussed in relation to the associated macroscopic quantities. In Chapter 4, the results obtained in the context of a biaxial test are presented. Chapter 4 represents an extension of the published paper (Clerc et al., 2021). It presents the meso-scale reorganisations during a burst of kinetic energy, precursors and elements responsible for the localisation of the outburst. Second-order mesoscopic work definitions introduced in Chapter 3 are then tested. The methodology developed in Chapter 4 for studying representative elementary volumes of granular materials are eventually applied to the analysis of a gravitational instability issue in Chapter 5. Two approaches to simulate gravitational instabilities are compared: with rigid boundary conditions or with periodic boundary conditions.

Chapter 2

State of the art: instabilities in granular materials and numerical methods for modelling the inertial transition

The aim of this chapter is to provide the state of the art, concepts and methods necessary for the understanding of this PhD thesis. Let specify first the material studied. Granular materials are, by definition, sets of solid particles in contact, in a fluid phase. In this work, the fluid is not considered. Also the grains studied here are large enough (radius > 100 μm) so that their interactions are only frictional and elastic. They are not dominated by short range interaction forces (electrostatic, molecular etc.). The overall behaviours of granular materials depends also on the grain shape and distribution of grain saizes. In this work, grains are simplified as spheres. The inertial transition plays a key role in the triggering of natural hazards, and in the failure of civil engineering structures. The first section of this chapter is devoted to the instability modes in granular materials. This section aims to explain how kinetic energy relates to mechanical destabilization and how the second-order work criterion, first established from a continuum point of view by (Hill, 1958), could be used as a necessary condition to observe inertial transition in granular media. Gravitational instability is also reviewed in this section. Inertial transition can be studied experimentaly and or numerically (Cambou et al., 2013; Forterre and Pouliquen, 2008; Vescovi et al., 2018). In this PhD thesis, the numerical simulations relies on a Discrete Element Method (DEM), whose principles are detailed in the second section. The mesoscopic scale appears to be important to brigde the gap between the grain scale and the scale of the material. Meso-structures, especially grain loops, are introduced in the third section. Meso and micro-quantities, able to quantify rearrangements in the micro-structure, are presented in the same section.

2.1 Instabilities in granular materials

2.1.1 Instability criteria

The first attempt of definition of the stability in a mechanical system is attributed to Lyapunov (Lyapunov, 1907) for celestial bodies. This orignal definition is based on the principle that if small perturbations are imposed on the position and/or the velocity, then the difference between the trajectories and the velocities with or without perturbations are limited. The principle can be extended to continuous materials by introducing adequate variables to describe the strain/stress state of the system (Darve et al., 1995). For a given continuous material, with a given loading history, let δl be an incremental loading applied to the system, and δr the response of the material. The system is stable if and only if $\forall\ \mu > 0, \exists\ \eta > 0,\ \|\delta l\| < \eta\ \Rightarrow\ \|\delta r\| < \mu$. In

other terms, a material is stable if any limited sollicitation creates a limited response.

However, there is a need for a more practical criterion. According to Hill's sufficient condition of stability (Hill, 1958), the strain/stress state is unstable if there exists at least one loading direction for which associated strain rate can exist without external energy. This criterion can be written as an energy balance in the general framework of continuum mechanics (Nicot and Darve, 2007; Nicot et al., 2009, 2012b). In this case, Hill's criterion applied to a material point states that, for a given stress/strain equilibrium ($\boldsymbol{\sigma}$,$\boldsymbol{\varepsilon}$) reached after a given loading history, the material point is unstable if there is a least one couple ($\Delta\boldsymbol{\sigma}$,$\Delta\boldsymbol{\varepsilon}$) linked by the material's constitutive law such as $\Delta\boldsymbol{\sigma} : \Delta\boldsymbol{\varepsilon} < 0$.

Let Ω be a mechanical system. An equilibrium state is characterized by a zero kinetic energy and by the fact that any variation of kinetic energy from the current state is a second-order function of the applied perturbation. The variation of the kinetic energy is given by :

$$\Delta t^2 \ddot{E}_c = \Delta t^2 \int_\Omega I dV + \int_{\delta\Omega} W_2^{ext} dS - \int_\Omega W_2^{int} dV \tag{2.1}$$

with

$$\Delta t^2 \ddot{E}_c = 2\left(E_c(t+\Delta t) - E_c(t)\right) - 2\dot{E}_c \Delta t \tag{2.2}$$

$$W_2^{ext} = \Delta \boldsymbol{f} \cdot \Delta \boldsymbol{u} \tag{2.3}$$

$$W_2^{int} = \Delta\boldsymbol{\sigma} : \Delta\boldsymbol{\varepsilon} \tag{2.4}$$

E_c is the kinetic energy of the system, W_2^{ext} is called the external second-order work, W_2^{int} is called the internal second-order work, I encapsulates inertial terms, $\boldsymbol{f} = \boldsymbol{\sigma} \cdot \boldsymbol{n}$ and $\boldsymbol{u}$ are the stress and displacement vectors on $\delta\Omega$, $\boldsymbol{\sigma}$ and $\boldsymbol{\varepsilon}$ denote the stress and strain tensors in Ω, and Δ represents the increment between times t and $t + \Delta t$.

This equation states that the external work is always larger than the integral of the internal second-order work of the system. If there is no external work change, a negative internal second-order work associated to a equilibrium position will result in an increase in kinetic energy ($\Delta t^2 \ddot{E}_c > 0$). The second-order work criterion only describes the potential ability of a system Ω to develop kinetic energy with no external disturbance from an equilibrium

state. With this criterion, the link between kinetic energy and instabilities is clearly underlined. Bursts of kinetic energy are indeed considered as signatures of mechanical instability (Nicot et al., 2012b).

An efficient use of the second-order work criterion to anticipate a burst of kinetic energy, requires that :

1. The system control parameters are kept constant or $\Delta \boldsymbol{f} \cdot \Delta \boldsymbol{u} = 0$ on $\delta\Omega$. This will help put forward situations where the deformation of the system can be carried on without any input of energy on the system boundaries.
2. The system must be balanced initially, that is to say $E_c = 0$ and $\dot{E}_c = 0$.

According to the first requirement, $W_2^{ext} = 0$. Then the second requirement gives that the system evolves from a static situation ($E_c = 0$) to an inertial regime (which corresponds to $E_c(t + \Delta t) > 0$) only if $W_2^{int} < 0$. Recent papers have shown the ability of the internal second-order work to anticipate the occurence of a burst of kinetic energy, at the macro-scale (Nicot et al., 2009; Daouadji et al., 2011; Nicot et al., 2012b; Wan et al., 2013; Nicot et al., 2017; Wautier et al., 2018b). More specifically, it has been proven that the vanishing of the internal second-order work is the most general stability criterion. It is a precursor to all other instability mechanisms (Nicot et al., 2009; Challamel et al., 2010; Daouadji et al., 2011; Wan et al., 2013) and other instability criteria are particular cases linked to specific failure mechanisms (such as localized failure with (Rudnicki and Rice, 1975)).

2.1.2 Strain localization and failure

Failure can be diffuse (the whole system reach the stress limit state at the same time), or localized. A shear band is a typical signature of a localized failure (Vardoulakis et al., 1978). It is also considered as a bifurcation problem since from a homogenous deformation field, the system changes to a discontinuous deformation field (Sadrekarimi and Olson, 2010). Hill (1962); Mandel (1964); Rudnicki and Rice (1975) successfully analysed the emergence and inclination of shear bands. The localization of the deformation occurs in a dense sample, just before the stress peak (Figure 2.1). At the macro-scale, shear band formation is associated to non affine deformation (Tordesillas et al., 2008). At the micro-scale, contact rolling and sliding have been proved to play a great role in shear band formation (Oda and Kazama, 1998; Liu et al., 2018, 2019). An explicit relation between microscopic behaviours and macroscopic responses is missing.

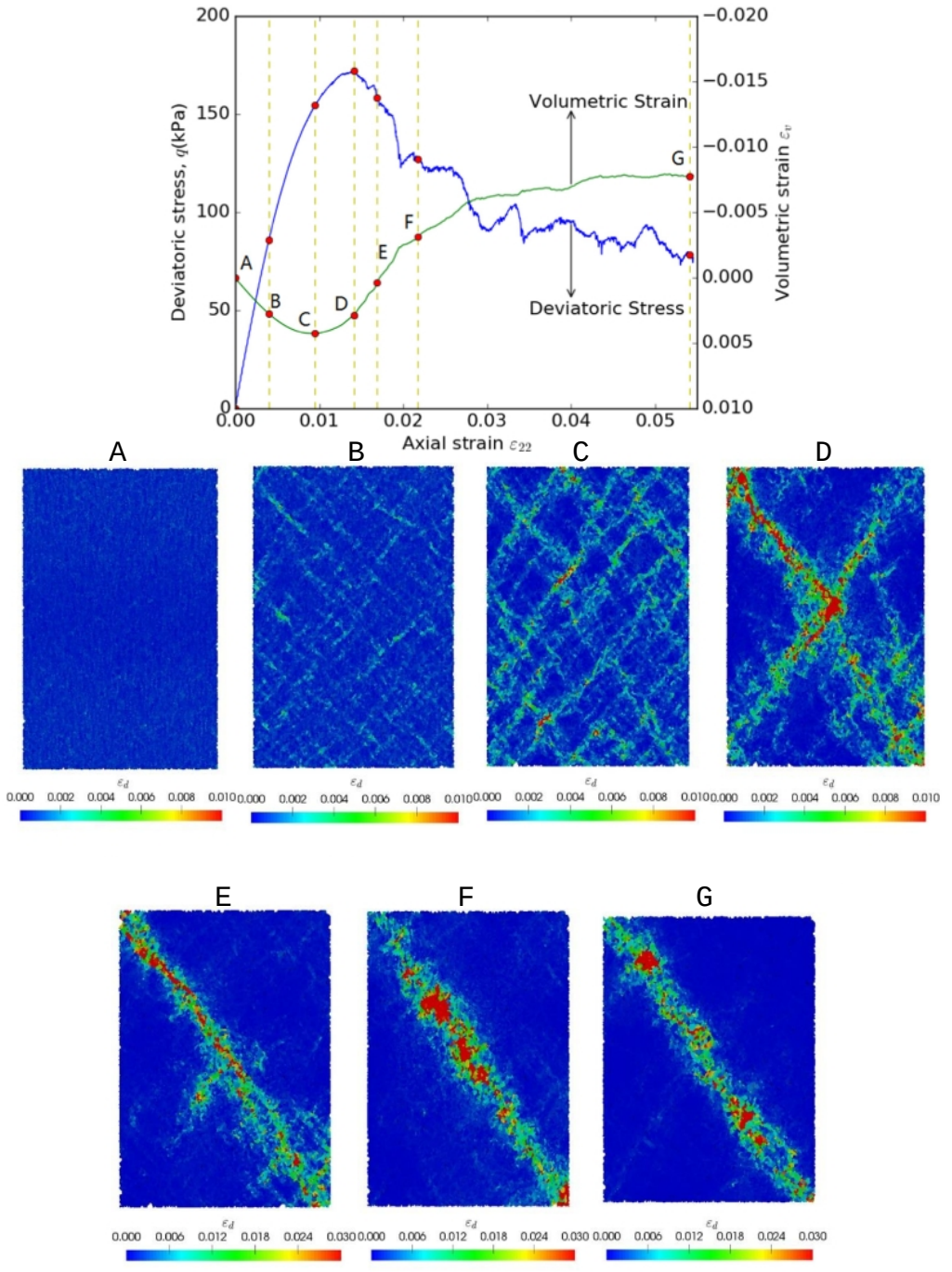

Figure 2.1 – Deviatoric stress and volumetric strain curves against the axial strain for a biaxial test (Liu et al., 2018). Seven moments are pointed out on those curves, and their deviatoric strain is displayed, illustrating the formation of a shear band. The shear band is completely formed after the peak of the deviatoric stress.

2.1.3 The inertial transition

General definition

The inertial transition can be seen as being the transition from a solid behaviour to a liquid behaviour. No internal stress scale exists for rigid grains, on the contrary to other complex systems (e.g. Bingham fluids). Thus, the onset of the inertial transition in a granular media is governed, as zero order description, by contact between grains. The inititiation of the transition is sensitive to the system preparation and to its history. Many soils mechanics researches consist in modelling the solid-fluid transition and investigating, among others, the impact of initial deformation, coupling between stress and strain and the volume fraction (Roux and Radjai, 1998). Researches have proposed elasto-plastic constitutive relations, trying to link the microstructure to the macroscopic behavior (Roux and Combe, 2002; Da Cruz, 2004; Vescovi et al., 2018, 2020; Marveggio et al., 2021). Concerning the dense flow regime, for frictionless and mono-disperse granular materials, Da Cruz et al. (2005) and Lois et al. (2005) observe that a the system is controlled by a dimensionless parameter which quantifies dynamic effects: the inertial number I. It is the ratio between inertial forces and imposed forces. For large systems, and in the case of granular material with rigid particles, it reads :

$$I = \frac{\dot{\gamma} d}{\sqrt{P/\rho}} \tag{2.5}$$

where $\dot{\gamma}$ is the shear rate, d the mean diameter of the particles, P the macroscopic pressure and ρ the density of the packing. The inertial number could also be seen as a ratio between two time scales (MiDi, 2004):

1. $d/\sqrt{P/\rho}$ is a microscopic time scale, it represents the time a particle takes to fall in a hole of size d under the pressure P. In other words, it is the characteric time of rearrangements.
2. $\frac{1}{\dot{\gamma}}$ is a macroscopic time scale linked to the mean deformation.

Small values of I (typically $I < 10^{-3}$ (Da Cruz, 2004)) corresponds to quasitatic regimes as macroscopic deformation is slow compared to microscopic rearrangements. Large values of I ($10^{-3} < I < 10^{-1}$ for the inertial regime, $10^{-1} < I$ for the collisonal regime) correspond to rapid flows, where either the shear strain is significant or the pressure is low. We can note that it is the only dimensionless number for monodisperse granular material without cohesion and adhesion forces (Da Cruz, 2004).

Inertial transition as a bifurcation

The inertial transition can be seen as a bifurcation: an abrupt and discontinuous change in the state of the system and its response under the gradually and continous evolution of state variables. The bifurcation domain is then the set of states from which the system regime can evolve from quasi-static to inertial state, while loading parameters evolve continuously (Nicot et al., 2012a). In that case, the second-order work criterion is also considered as a bifurcation criterion.

Gravitational slope instabilities

Flows of granular materials have attracted research attention at the frontier between physics and mechanics. Slope stability has indeed a wide and important range of applications, from geophysics (triggering of avalanches, landslide, fault sliding) to industrial processes (storage and handling of powders, food, granulates). The main goal of this analysis is to relate the slope failure to its physical origins at the scale of the grains and their contacts. There are different ways to simulate flows (see Figure 2.2) (Daerr and Douady, 1999). The application for natural hazards such as landslide is our motivation for simulating granular flows. Thus, we are interested in simulating a granular packing on an inclined plane (Figure 2.2(d)).

The main challenge, in simulating a grain packing on a inclined plane submitted to gravity is to minimize the effect of the walls containing the sample. In the case of 2D simulations, there are two solutions to adress this issue :

- Be careful on the dimensions of the packing so that the vertical dimension is smaller than the horizontal direction. According to the literature (Aguirre et al., 2001; Staron et al., 2006; Oger et al., 2021), the horizontal dimension should be at least 2.5 times bigger than the vertical dimension. This threshold is really a minimum to avoid significant wall effect in granular packings.
- Opting for periodic boundary conditions, which enable to suppress walls in the horizontal direction. It will create a continuous path in the horizontal dimension (Staron, 2008).

Lateral walls (in the third dimension) have been proved to influence the behavior of the media (Jop et al., 2005, 2007). In order to simplify the simulation, 2D simulations are a reasonable option to study the initiation of gravitational instabilities. Different studies (Daerr and Douady, 1999; Staron et al., 2006; Staron, 2008) have shown that a pre-avalanche interval exists. Before the theoritical angle of failure θ_c predicted by Mohr-Coulomb crite-

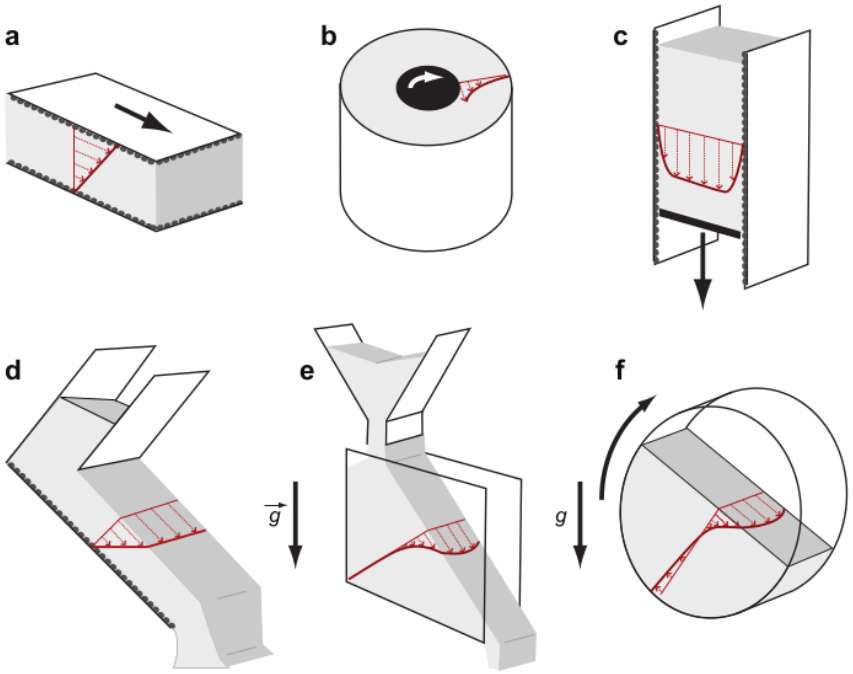

Figure 2.2 – Different configurations to create granular flows (either in a numerical or experimental simulations) from (Forterre and Pouliquen, 2008). (a) Plane shear, (b) Couette cell, (c) Silo (Staron and Hinch, 2005; Lube et al., 2005), (d) flows on a inclined plane, (e) flows on a pile (Daerr and Douady, 1999), (f) flows in a rotating drum (Jain et al., 2002). The (a) and (b) options are not necessary conducted under gravity.

rion, the sample exhibits important rearrangements and signs of instabilities. This pre-destabilization phase occurs after a certain angle θ_d which varies in function of the sample. θ_c is the static friction angle and θ_d the dynamic friction angle. The interval $[\theta_d, \theta_c]$ is an interesting period where precursors can emmerge (stick slip, area of weak contacts, etc.). Contact law, shape and size of particles have a great influence on the stability of the slope and can change the range of pre-avalanche angle.

Finally, simple rheological descriptions have been formulated to describe the behaviour of inertial flow of granular material. They are functions of a friction coefficient and the inertial number I (Da Cruz, 2004; Pouliquen et al., 2005; Jop et al., 2007; Marveggio et al., 2021).

2.2 Discrete Element Method

Granular material can be considered as a continuous medium at the macro scale. However, at the micro-scale, granular materials are discrete materials, composed of grains interacting with each other through contact laws. In terms of numerical simulation, either discrete methods or continuum methods can be used to model granular media depending on the scale of interest. In the scope of this PhD thesis, micro-mechanisms of inertial instability are our main goal and continuum mechanics is not suitable framework. Discrete element modelling is the method chosen in order to capture micro-structure modifications due and/or linked to inertial transitions. Historically, Discrete Element Method (DEM) started with (Cundall and Strack, 1979). It allows working at the Representative Elementary Volume (REV) scale (Hill, 1958), at which discrete and continuum descriptions merge. Through the use of a REV, DEM simulations can be compared with experimental tests (Nicot et al., 2013a; Haddad et al., 2015). Thanks to the increase in the computing power, DEM is now an effective and efficient method to account for the complex behaviour of granular materials (Luding, 2004; Šmilauer et al., 2015; Walker and Tordesillas, 2010; Zhu et al., 2016a). In DEM, the geometry of the grains and the interaction forces between them are the two main information needed to account for the evolution of the mechanical and numerical systems. Among the two approaches developed in discrete methods, the smooth contact dynamics approach is chosen in this work (often simply called DEM). Grain interpenetration is allowed so that the contact between two grains corresponds to a unique variation in the contact forces, and calculation can be done contact per contact. This method relies on an explicit integration scheme, as opposed to implicit integration scheme used in non smooth contact dynamics approaches, where grain overlapping is strictly

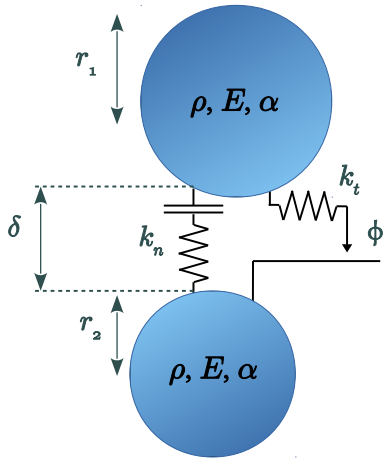

Figure 2.3 – Scheme of the elasto-frictionnal law used in the numerical simulations (no viscosity).

prohibited. In this PhD thesis, all simulations were realised with the open code source YADE (Yet Another Dynamic Engine) developed in the research laboratory 3SR in Grenoble, France (Šmilauer et al., 2015). The computation loop consists in four steps:

1. from the position of the particles, the contact points are identified. In the case of spherical particles, the condition for contact between the particles i and j can be basically summed up to $\|\boldsymbol{x}_i - \boldsymbol{x}_j\| \leqslant r_i + r_j$ where $\boldsymbol{x}_i$ and r_i (resp. $\boldsymbol{x}_j$ and r_j) is the position vector of the particle i and its radius (resp j).
2. from the incremental kinematics of the particles i and j at contact, the tangential and normal forces at the contact are computed based on the contact law.
3. from the contact forces, the resulting acceleration for each particle can be estimated, based on the second law of Newton.
4. the translational and rotational displacements of the particles are calculated and the particle positions are updated.

2.2.1 Contact law

The interaction between the particles is defined by the contact law. In this work, we use the elasto-frictionnal contact law that was initially introduced

by (Cundall and Strack, 1979). It assumes that a contact is created by two particles overlapping. The contact law is defined by two linear springs and a slider (Figure 2.3).

At time t, the normal force $\boldsymbol{F}_n(t)$ is a function of the outward normal unit vector of the contact $\boldsymbol{n}(t)$, the normal stiffness k_n and the overlapping distance between the two spherical particles (1 and 2) $\delta(t)$:

$$\boldsymbol{F}_n(t) = -k_n \delta(t) \boldsymbol{n}(t) \tag{2.6}$$

The normal stiffness depends on the harmonic average of the two spheres's radii r_1 and r_2 in contact and a material Modulus E :

$$k_n = E \frac{2r_1 r_2}{r_1 + r_2} \tag{2.7}$$

The overlapping distance at the time t is

$$\delta(t) = r_1 + r_2 - \|\boldsymbol{x}_2(t) - \boldsymbol{x}_1(t)\| \tag{2.8}$$

where $x_i(t)$ is the mass center position of the particle i at time t.

The tangential force $\boldsymbol{F}_\tau(t)$ is defined by the tangential stiffness and the tangential displacement of the contact $\boldsymbol{u}_\tau(t)$:

$$\boldsymbol{F}_\tau(t) = -k_t \boldsymbol{u}_\tau(t) \tag{2.9}$$

The tangential stiffness k_t is linked to its normal couterpart k_n by the stiffness ratio α.

$$k_t = \alpha k_n \tag{2.10}$$

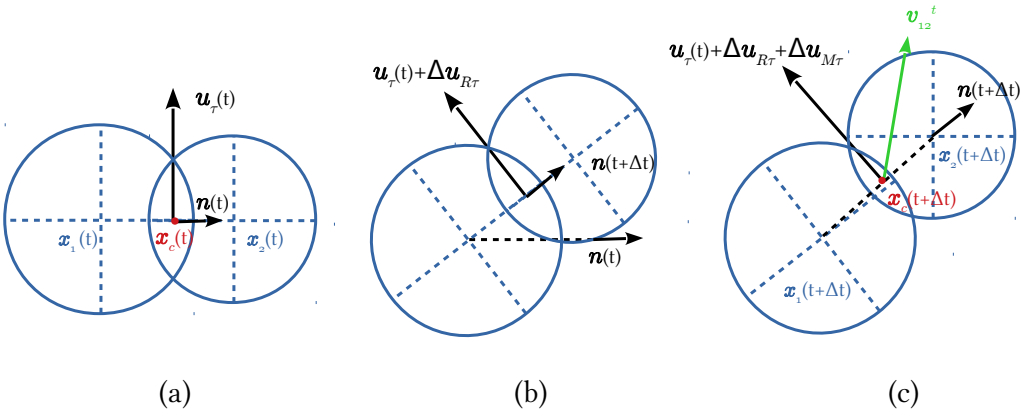

Figure 2.4 – Three steps during the incremental update of the accumulated shear displacement $\boldsymbol{u}_\tau$ for the computation of the tangential force. (a) Initial situation with a contact of between two spherical particles, (b) First correction linked to the rotation of the two particles, (c) Second correction linked to relative velocity between the two particles.

Despite the apparent simple definition of the tangential force $\boldsymbol{F}_\tau(t)$, it depends on the loading history and the accumulated tangential displacement $\boldsymbol{u}_\tau(t)$. The next paragraph gives the expression of the incremental update of the tangential displacement $\boldsymbol{u}_\tau(t)$ as it is implemented in YADE. Figure 2.4 illustrates the following equations.

At time t, two spherical particles labeled 1 and 2 are in contact. The outward normal vector $\boldsymbol{n}(t)$ of the particle 1 (so from particle 1 to particle 2) is

$$\boldsymbol{n}(t) = \frac{\boldsymbol{x}_2(t) - \boldsymbol{x}_1(t)}{\|\boldsymbol{x}_2(t) - \boldsymbol{x}_1(t)\|} \tag{2.11}$$

The contact point $\boldsymbol{x}_c(t)$ is located at the middle of the overlapping zone :

$$\boldsymbol{x}_c(t) = \boldsymbol{x}_1(t) + \left(R_1 - \frac{\delta(t)}{2}\right)\boldsymbol{n}(t) \tag{2.12}$$

with $\delta(t) = R_1 + R_2 - \|\boldsymbol{x}(t)_2 - \boldsymbol{x}(t)_1\|$

At time $t + \Delta t$, the two spheres move to new positions, $\boldsymbol{x}_1(t + \Delta t)$ and $\boldsymbol{x}_2(t + \Delta t)$ respectively. If they are still in contact, the updated normal vector is noted $\boldsymbol{n}(t + \Delta t)$ and the new contact position is $\boldsymbol{x}_c(t + \Delta t)$. The tangential displacement is updated by introducing a correction term linked to the rotation of the normal vector at contact $\Delta\boldsymbol{u}_{R\tau}$ and another correction term due to the relative motion between them $\Delta\boldsymbol{u}_{M\tau}$.

Let $\boldsymbol{w}_1(t)$ and $\boldsymbol{w}_2(t)$ be the respective rotation rate of particles 1 and 2. The correction term linked to the rotation of the normal vector at contact takes into account the rotation of the normal vector with a rotation rate of $\frac{\boldsymbol{w}_1(t)+\boldsymbol{w}_2(t)}{2}$ and the mutual movement correction is coming from the relative motion of spheres $\boldsymbol{v}_{1/2}(t)$ at the contact point:

$$\boldsymbol{v}_{1/2}(t) = \left(\frac{d\boldsymbol{x}_2}{dt}\right)_t - \left(\frac{d\boldsymbol{x}_1}{dt}\right)_t + \boldsymbol{w}_2(t)(\boldsymbol{x}_c(t) - \boldsymbol{x}_2(t)) - \boldsymbol{w}_1(t)(\boldsymbol{x}_c(t) - \boldsymbol{x}_1(t)) \tag{2.13}$$

Then, the incremental tangential displacement $\Delta\boldsymbol{u}_{M\tau}$ is computed :

$$\Delta\boldsymbol{u}_{M\tau} = \Delta t\left[\boldsymbol{v}_{1/2}(t) - \big(\boldsymbol{v}_{1/2}(t)\cdot\boldsymbol{n}(t+\Delta t)\big)\,\boldsymbol{n}(t+\Delta t)\right] \tag{2.14}$$

Finally, at time $t + \Delta t$, the tangential displacement is updated as follow :

$$\boldsymbol{u}(t + \Delta t)_\tau = \boldsymbol{u}(t)_\tau + \Delta\boldsymbol{u}_{R\tau} + \Delta\boldsymbol{u}_{M\tau} \tag{2.15}$$

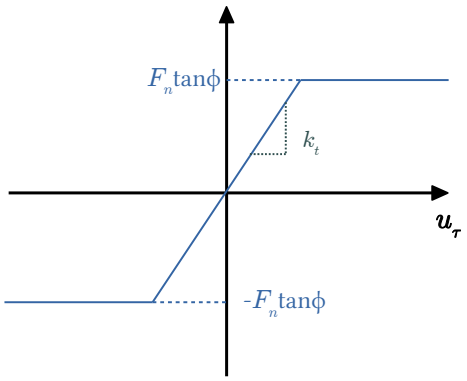

Figure 2.5 – Coulomb criterion with afriction angle ϕ

The expression 2.9 of the tangential force is only valid as long as the contact is not sliding. A Coulomb criteria with the contact friction angle ϕ provides the formulation of the tangential force in function of ϕ and the normal force (Figure 2.5). Thus, the final expression of the tangential force $\boldsymbol{F}_\tau(t)$ is given as :

$$\boldsymbol{F}_\tau(t) = \begin{cases} -k(t)\boldsymbol{u}(t)_\tau & \text{if } F_\tau(t) < \tan\phi F^n(t) \\ -\tan\phi \; F_n(t) \; \frac{\boldsymbol{u}(t)_\tau}{||\boldsymbol{u}(t)_\tau||} & \text{otherwise} \end{cases} \tag{2.16}$$

2.2.2 Newton's second law of motion

After computing the accumulated forces for each particle from its contacts, the integration of the second Newton's law of motion for rigid solid bodies leads to update the position and the orientation of each particles. The current acceleration $\ddot{\boldsymbol{x}}(t)$ is used to update the position from its value at time t, $\boldsymbol{x}(t)$, to its value at the next step $t + \Delta t$, $\boldsymbol{x}(t + \Delta t)$. The position and orientation of the particles are known at step points (i.e. $t + i\Delta t$ with $i \in \mathbb{Z}$) while velocities are know at mid-step points (i.e. $t + \frac{i}{2}\Delta t$ with $i \in \mathbb{Z}$). For a single particle of mass density ρ and volume V, the force balance equation is

$$\rho V \ddot{\boldsymbol{x}}(t) = \sum_c \boldsymbol{F}_c(t) \tag{2.17}$$

where $\boldsymbol{x}(t)$ is the position of its mass center and $\boldsymbol{F}_c(t)$ the contact forces applied at the particles at the contact c. For rigid particles in a dry granular packing, the only forces applied on the particle are contact forces (on internal forces or other type of external forces). Thus, at the time t the acceleration of the particle is known. By using the second-order finite difference, the position at the time $t + \Delta t$ relates to the acceleration $\ddot{\boldsymbol{x}}(t)$:

$$\ddot{\boldsymbol{x}}(t) = \frac{\boldsymbol{x}(t - \Delta t) - 2\boldsymbol{x}(t) + \boldsymbol{x}(t + \Delta t)}{\Delta t^2} \tag{2.18}$$

$$\boldsymbol{x}(t + \Delta t) = 2\boldsymbol{x}(t) - \boldsymbol{x}(t - \Delta t) + \ddot{\boldsymbol{x}}(t)\Delta t^2 \tag{2.19}$$

However, at time t only the position the position $\boldsymbol{x}(t)$ and the velocity $\dot{\boldsymbol{x}}\left(t - \frac{\Delta t}{2}\right)$ are known. The position $\boldsymbol{x}(t - \Delta t)$ is not known anymore, but it can be expressed using the mean velocity at the previous step :

$$\dot{\boldsymbol{x}}(t - \frac{\Delta t}{2}) = \frac{\boldsymbol{x}(t) - \boldsymbol{x}(t - \Delta t)}{\Delta t} \tag{2.20}$$

Finally, using Equation 2.20 in Equation 2.19, the next position of the particle is given by :

$$\boldsymbol{x}(t + \Delta t) = \boldsymbol{x}(t) + \Delta t \left[\dot{\boldsymbol{x}}(t - \frac{\Delta t}{2}) + \ddot{\boldsymbol{x}}(t)\Delta t\right] \tag{2.21}$$

The mid-step velocity $\dot{\boldsymbol{x}}\left(t + \frac{\Delta t}{2}\right)$ is computed in order to be used in the computation of the next on-step position $\boldsymbol{x}(t + \Delta t)$.

$$\dot{\boldsymbol{x}}\left(t + \frac{\Delta t}{2}\right) = \dot{\boldsymbol{x}}\left(t - \frac{\Delta t}{2}\right) + \ddot{\boldsymbol{x}}(t)\Delta t \tag{2.22}$$

$$\boldsymbol{x}(t + \Delta t) = \boldsymbol{x}(t) + \dot{\boldsymbol{x}}\left(t + \frac{\Delta t}{2}\right)\Delta t \tag{2.23}$$

The Newton's second law is used (Equation 2.24) and the same approximation as for the position are done for the rotation rate $\boldsymbol{w}$ (Equation 2.25).

The particle orientation is then deduced from these equations and the use of quaternion algebra (Šmilauer et al., 2010).

$$J\dot{\boldsymbol{w}}(t) = \sum_c r\boldsymbol{n}_c\boldsymbol{F}_c(t) \tag{2.24}$$

$$\boldsymbol{w}\left(t + \frac{\Delta t}{2}\right) = \boldsymbol{w}\left(t - \frac{\Delta t}{2}\right) + \dot{\boldsymbol{w}}(t)\Delta t \tag{2.25}$$

with $J = \frac{2}{5}\rho V r^2$ the inertial moment of a sphere, r being the radius of the particle and $\boldsymbol{n}_c$ the outer normal vector of the contact c.

2.2.3 Computational constraints

The use of smooth contact dynamics with elasto-frictionnal contact law imposes two constraints : a condition on the time step and the introduction of a numerical damping. The first constraint is a Courant-Friedrichs-Lewy (CFL) condition. It imposes a time step Δt smaller than a critical time step Δt_{cr}. In YADE, the critical time step is fixed as a function of the highest eigenfrequency within the system w_{max}.

$$\Delta t_{cr} = \frac{2}{w_{max}} \tag{2.26}$$

For a single mass spring system, the characteristic angular frequency is function of the stiffness and the mass of the system. Since there is one single mass, the highest eigenfrequency is the angular frequency $w_{max} = \sqrt{\frac{k}{m}}$. Thus, for this simplified system, the critical timestep is $\Delta t_{cr} = 2\sqrt{\frac{k}{m}}$. For a set of spheres linked by springs, the highest frequency is given for two connected masses in opposite motion $w_{max} = \max_i \sqrt{\frac{2k_i}{m_i}}$. The critical timestep for whole set of particles is thus given by :

$$\Delta t_{cr} = \frac{2}{w_{max}} = \min^i \sqrt{\frac{2m_i}{k_i}} \tag{2.27}$$

The time step is defined from the critical P-wave time step. The stiffness is the normal stiffness approximated by $k_n \simeq Er$, where r is the harmonic

average of the two spheres's radii in contact (Equation 2.7). As an approximation, the critical time step is

$$\Delta t_{cr} \simeq \min_i \sqrt{\frac{4/3\pi r^3 \rho}{2Er}} \simeq r_{min}\sqrt{\frac{\rho}{E}} \tag{2.28}$$

The second constraint is the absence of damping in the elasto-frictionnal contact law for non sliding contacts. It is be necessary to dissipate kinetic energy to prevent the system from permanently oscillating. An artificial numerical damping is introduced in the form of dimensionless parameter, the damping coeficient λ_d. The principle is to decrease (resp. increase) the resultant contact forces $\sum \boldsymbol{F}_c$ on the particle to increase (resp. decrease) its velocity by the increment $\Delta \boldsymbol{F}_d$, as a function of the acceleration. For the component i of the summary force acting on a grain, the definition of the damping adds a correction term ΔF_d^i :

$$\frac{\Delta F_d^i}{\sum_c F_c^i} = -\lambda_d \text{ sign}\left[\left(\sum_c F_c^i\right) \cdot \left(\dot{x}^i(t - \frac{\Delta t}{2}) + \ddot{x}^i(t)\frac{\Delta t}{2}\right)\right] \tag{2.29}$$

This definition acts on forces and accelerations and thus does not constrain uniform motion. Moreover, it allows an equal damping for all particles (Šmilauer et al., 2015).

2.2.4 Unbalanced forces

The unbalanced forces F_{unb} is the ratio of mean resultant force on the particles and mean contact force magnitude on the contacts. It is used as a condition in the numerical simulation to assess the convergence towards the equilibrium of the sample. At perfect static equilibrium, it will be zero, even though zero won't be reached because of computation precision.

$$F_{unb} = \frac{\frac{1}{N_p}\sum_{p=1}^{N_p} \|\sum_c \boldsymbol{F}_c^p\|}{\frac{1}{N_c}\sum_{c=1}^{N_c} \|\boldsymbol{F}_c\|} \tag{2.30}$$

where N_p and N_c are respectively the number of particles and the number of contacts in the system. A typical value of 10^{-5} is used throughout this work.

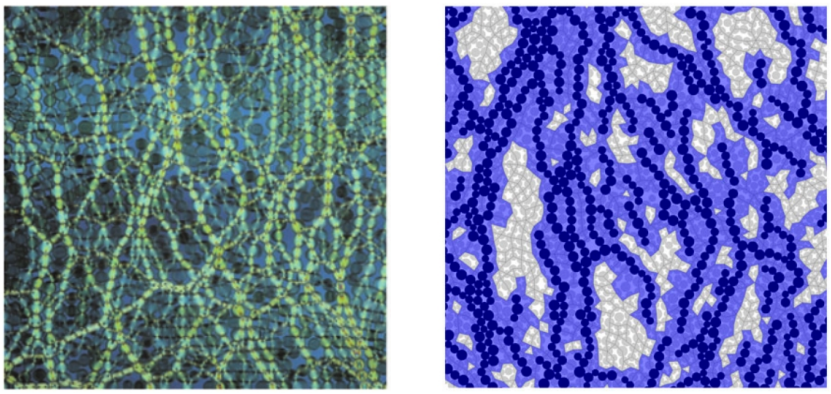

(a) (b)

Figure 2.6 – (a) Force chains visualisation in a granular assembly of photo-elastic disks (Majmudar and Behringer, 2005). (b) Interplay between loops and force chains in a 2D numerical sample (Zhu, 2015).

2.3 Mesoscopic point of view to describe granular materials behaviour

Granular systems complexity stems from their discrete nature, their microstructure. Contact scale properties and geometrical effects dictate the overall mechanical behaviour of the granular materials. In this section, the contact and force network is seen through meso-structure. Physical quantities relative to contacts and meso-structures are given to analyse reorganizations.

2.3.1 Meso-strucures

Numerical studies using DEM and experimental studies using (among others), photo-elastic grains have shown that forces inside a granular material is not homogeneously distributed and relies on limited structures, called force chains (Drescher and De Jong, 1972; Jaeger et al., 1996; Oda et al., 2004; Radjai et al., 1998; Tordesillas and Muthuswamy, 2009). Force chains exhibit a strong anisotropy linked to the external loading applied to the material (Figure 2.6(a)).

A force based approach consists in separating the force contact network in a strong network (force chains) and a weak network composed of less loaded

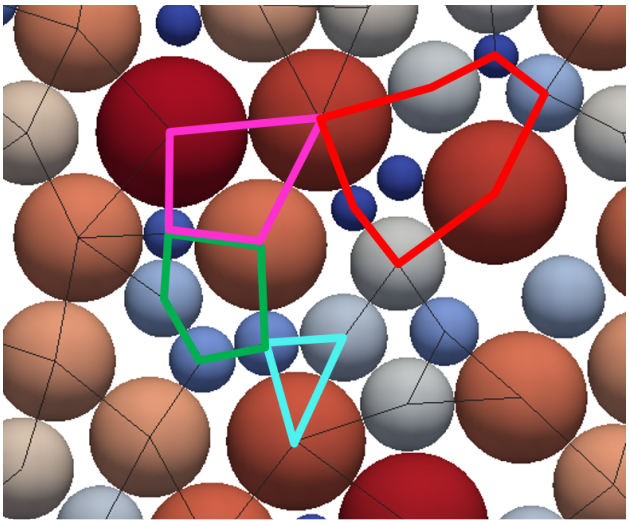

Figure 2.7 – Different loops order illustration in a granular material. Thin black lines account for the contact network between grains. L3 : blue loop ; L4 : pink loop ; L5 : green loop, L6+ :red loop.

grains surrounding the force chains, called grain loops. The advantage of the grain loops is that, in a 2D sample, they result from the tesselation of the sample area based on contact between grains, and thus provides a mesoscopic scale between micro and macro scales. Compared to force chains that account for the load bearing capacity, the grain loops account for the deformability of the sample. Moreover the grain loops surrounding the force chains are proven to ensure their mechanical stability (Zhu et al., 2016c,b) (see Figure 2.6(b)).

Grain loops are domains delineated by the contact network inside the granular material. It exists only a unique partition of grain loops of the granular material. Grain loops are computed through an algorithm which starts from an arbitary grain and looks for its closer contact neighbour with a minimization of the angle made between the two branch contacts (Figure 2.8(a)). The sample is then decomposed in an unique pavement of four categories of grain loops based on the number of grains they are composed of : L3, L4, L5, L6+ (Figure 2.7). The higher the order, the more deformable the loops is. Recent works (Zhu et al., 2017; Liu et al., 2018) have proven that the L3 and L6+ are the most active order loops in granular materials. In this work, the walls of the DEM simulation are included in the loop detection (Figure 2.8(b)).

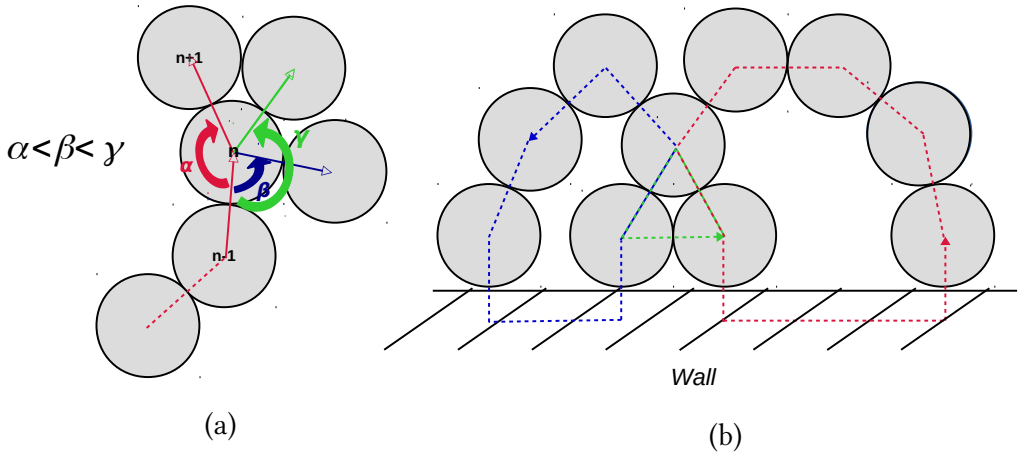

Figure 2.8 – Sketch for the definition of loops without wall (a), and with a wall (b). (a) n and $n-1$ are the grains already detected by the algorithm. The next grain $n+1$ of the loop is detected by looking for the grain in contact with n which minimize the angle between $(n-1,\, n)$ and $(n,\, n+1)$. (b) Walls are considered like grains and can be part of loops in order to avoid fixing an arbitrary maximal order loop.

2.3.2 Reorganizations at the micro- and meso-scale

Mesoscopic methods have been developed to investigate changes among meso-structures. The aim is to quantify the transformations at different scales, to better understand how a granular sample is affected by an inertial evolution.

Sliding index

The sliding index is an indicator showing how close is a contact from sliding. In the case of an elasto-frictional contact law and a Coulomb criteron, a contact slides if the magnitude of the shear contact force exceeds a threshold imposed by the norm of the normal contact force and the friction angle. The sliding index for each contact is then defined as :

$$I_p = \frac{\|\boldsymbol{F}_\tau\|}{\tan\phi F_n(t)} \tag{2.31}$$

The sliding index varies between the [0,1[interval. 1 is considerer as not reached because when the contact slides, the loss of the contact is often forthcoming, but not systematically . The closer to 1 the index is, the higher probability to slide. The value above which the contact is considered sufficiently close to sliding is chosen as $I_p \geqslant 0.9$. Previous work (Wautier et al., 2018b) has demonstrated that contacts with $I_p \geqslant 0.9$ are likely to slide if a small perturbation of the stress state is imposed (a perturbation whose magnitude is 1% of the mean stress value).

Relative evolution of a given set of meso-structures

The relative evolution is a way to quantify the changes in micro-structures of a granular material. It compares the set of meso-structures at a time t to the set of meso-structures at a time $t + \Delta t$ (Figure 2.9). The loss of meso-structures reads :

$$L_m^{t+\Delta t} = \frac{\left|S_m^t - S_m^t \cap S_m^{t+\Delta t}\right|}{\left|S_m^{t_{ref}}\right|} \tag{2.32}$$

where m is the type of micro- or meso-structure analysed (rattlers, grain loops of different orders, etc.), S_m^t (resp. $S_m^{t+\Delta t}$) is the set of meso-structures

Figure 2.9 – The black circle represent the set of meso-structures m at the time t and the blue circle the set of meso-structures m at the time $t+\Delta t$. They have a hatched joint portion, but outside this joint set, what remains from the black circle is the loss meso-structures and, respectively, what remains of the blue circle is the gained meso-structures.

m at the time t (resp. $t+\Delta t$) and $\left|S_m^{t_{ref}}\right|$ the total number of meso-structures m at a given time of reference. Similary, the gain of meso-structures reads :

$$G_m^{t+\Delta t} = \frac{\left|S_m^{t+\Delta t} - S_m^t \cap S_m^{t+\Delta t}\right|}{\left|S_m^{t_{ref}}\right|} \tag{2.33}$$

Life expectancy of meso-structures

In order quantify the renewal of the meso-structures, lifespan and life expectancy are useful concepts, inspired from biology. The lifespan of a meso-structure corresponds to the time it has continuously existed since its formation, starting from a reference conformation. On the contrary the life expectancy of a meso-structure is its remaining time of existance before disappearing. These concepts measure how fast a granular system is losing the memory of its past state (Zhu et al., 2016a; Wautier et al., 2018a; Deng et al., 2021b).

Instead of measuring time of existence, the surviving rate $R_m(t)$ of a set of meso-structures S_m computes the percentage of the set of meso-structures still existing at a time t ($S_m(t)$) with respect to the set of meso-structures

which existed at time $t_{ref} < t$ ($S_m(t_{ref})$).

$$R_m(t) = \frac{|S_m(t_{ref}) - S_m(t_{ref}) \cap S_m(t)|}{|S_m(t_{ref})|} \tag{2.34}$$

The time in these three concepts may denote physical time or any other forcing parameters measuring the application of external loading. For biaxial test, the time is the axial strain, for a titling slope submitted to gravity, it is the slope angle.

2.4 Conclusion

In this Chapter, the theoretical background of inertial transition has been defined. The links between inertial transition, mechanical instabilities and bursts of kinetic energy have been highlighted. Studying bursts of kinetic energy is a relevant approach to understand the mechanisms of the inertial transition. The second-order work criterion has been presented as a powerful tool to detect instabilities, and a definition at the mesoscopic scale is formulated in the next Chapter. In order to simulate the behaviour of granular materials, Discrete Element Method with an elasto-frictional contact law is introduced. The discrete methods are based on a simple four steps computational loop, and all the equations related to the computation of forces and displacements are explained. Lastly, grain loops are defined, as well four methods to study the rearrangements in the micro-structure: sliding index of a contact, relative evolution, lifespan and life expectancy of a set of meso-structures. Physical quantities at the mesoscopic scale are defined in the next Chapter, for the purpose of supporting analyses and defining a second-order work at this intermediate scale.

Chapter 3

Quantities at the mesoscopic scale

This chapter introduces new mechanical quantities to analyse the inertial transition at an intermediate scale. There are two approaches to define quantities at the mesoscopic scale. On one side, meso-structures are considered independently from one another, this is the structural approach. The macro quantities derived from these meso-definitions are optained by statistical homogenization. On the other side, meso-structures are defined such as that they form a partition of the sample domain, surrounded by neighbouring meso-structures. This is the partition approach, and the macro quantities are directly derived from a spatial homogenization. In the first section the question of quasi 2D simulation is addressed. The choice of the 2D simulation and important parameters resulting from the 2D simulation choice are introduced. In the second section the mesoscopic porosity and mesoscopic energies, relative to grain loops, are introduced. Finally, in the third section, the definition of mesoscopic strains and stresses are presented, in order to define an internal second-order mesoscopic work.

3.1 Quasi 2D simulation choices

The choice was made to use 2D simulations. YADE is a DEM software made for 3D simulations, with 3D bodies. A way of computing 2D simulations with YADE is to use 3D bodies (here spherical particles) constrained to move within a plane, which is called a quasi 2D simulation.

3.1.1 Choice of 2D over 3D simulations

The 3D description are a more meanningful choice to simulate and capture all the behaviours of a real sample. However, the 3D system can be complex for an initial analysis and opting for a 2D system is a way to simplify the system and its graphical representation, while preserving most of the physical process of micro-structure reorganisation. The aim is to come back to the elementary mechanisms of inertial transition and develop tools which help to understand it. These 2D numerical simulations can be viewed as a first step to tackle the issue. Moreover, a challenge in granular materials studies is to bridge the gap between the the particle scale and the sample scale. The starting point of an analysis at an intermediate scale is the grain loops which is well defined in 2D conditions. 3D equivalent of grain loops is still a matter of discussion out of the scope of the present work (Nguyen et al., 2020) and only very recent work enabled to extend the grain loop concept to 3D (Chueire et al., 2021). Note that despite the fact that grain loops can be defined in 3D, the bijective link between the loop structure and an enclosed

volume is lost. This is another reason to choose a 2D description.

3.1.2 The third dimension in a quasi 2D simulation

In quasi 2D, spheres are used instead of disks, and they are constrained to move only centered within a plane (here the x-y plane). In such a set up, the out of the plane dimension has no particular meaning. No forces and kinematics can develop along the axis orthogonal to the plane under consideration (contrary to 2D finite element descriptions which have a real physical meaning). The lenght separating the walls in the z-direction is used to compute stresses (here σ_{xx} and σ_{yy}) from contact forces. Defining stresses instead of forces per unit lenght (N/m) is interesting to ease the comparison with 3D studies and experiments. There are two main possibilities to set the out of plane dimension as illustrated in Figure 3.1 :

- the two walls in the z-direction are fixed at one lenght unity of each other. The values in N/m and Pa are then equivalent. The drawback is that grain overlap is not similar in 2D or 3D simulations performed under the same stress.
- the two walls in the z-direction are fixed at one maximum diameter of each other. In that case, 2D and 3D simulations which are conducted under the same stress result in similar grain interpenetration (the contact forces are of the same magnitude).

Both methods were used in Chapter 4.

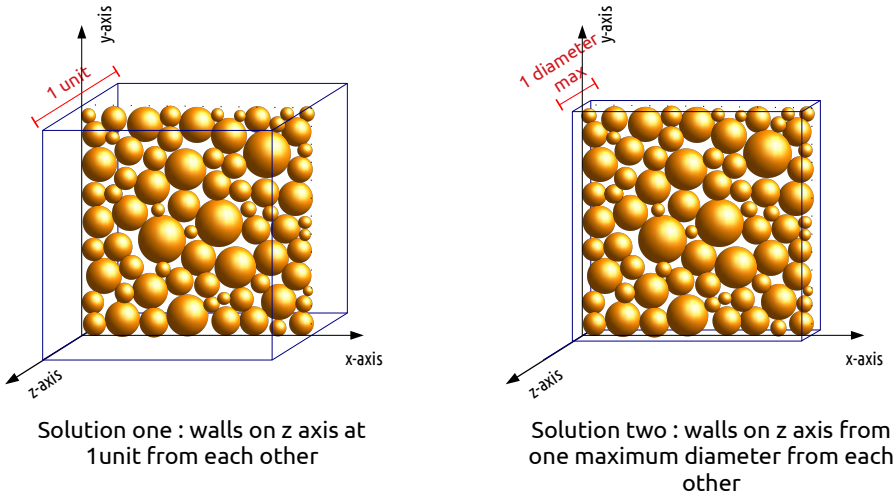

Figure 3.1 – Scheme of the two possibilities to set the walls in the third dimension.

3.1.3 Macro stress and strain in a quasi 2D representative elementary volume

The macroscopic stress and strain characterize a triaxial test, as they are computed from the forces and displacements of the boundary walls. For a representative elementary volume of granular material enclosed between walls, the macroscopic stress tensor $\boldsymbol{\sigma}$ is computed from the resulting forces on the walls. With use of frictionless walls, the stress tensor is diagonal. Concerning the strain tensor, the diagonal terms correspond to the relative variations of the box dimensions. Keeping the boundary walls forming a rectangular box, the strain tensor is also diagonal (no distorsion). From this context, the 2D deviatoric stress q, the 2D mean pressure p, the 2D deviatoric strain ε_d and the 2D volumetric strain ε_v can be deduced directly as:

$$q = |\sigma_{yy} - \sigma_{xx}| \tag{3.1}$$

$$\varepsilon_v = \mathrm{Tr}(\boldsymbol{\varepsilon}) = \varepsilon_{xx} + \varepsilon_{yy} \tag{3.2}$$

$$p = \frac{1}{2}(\sigma_{xx} + \sigma_{yy}) \tag{3.3}$$

$$\varepsilon_d = \frac{|\varepsilon_{yy} - \varepsilon_{xx}|}{2} \tag{3.4}$$

These definitions are compatible with the expression of the internal power $\boldsymbol{P}$ as sum of product between conjugated variables :

$$\boldsymbol{P} = \boldsymbol{\sigma} : \dot{\boldsymbol{\varepsilon}} = p\dot{\varepsilon}_v + q\dot{\varepsilon}_d \tag{3.5}$$

3.2 Mesoscopic quantities

3.2.1 Structural and partition approaches at the meso-scale

Macro- (strain, stress, porosity) or micro- (energy) quantities are adapted to be expressed at the scale of a grain loop l at a time t. There are two ways to create meso-quantities relative to the meso-domains. On one hand, the meso-quantities can be considered as a partition of the macro-quantity. There are defined so that their spatial average equals the meso-quantity, it is the partition approach. On the other hand, the meso-quantity of a meso-domain can be defined without considering the neighbouring meso-domains. In that case, the statistical averaging of the meso-quantities equals the macro-quantity, it is the structural approach. As an illustration, the polygon in Figure 3.2(a) will be the partition grain loop domain, while the surface incorporating the loop area and the total area of the loop's spheres (Figure 3.2(b)) corresponds to the structural grain loop domain.

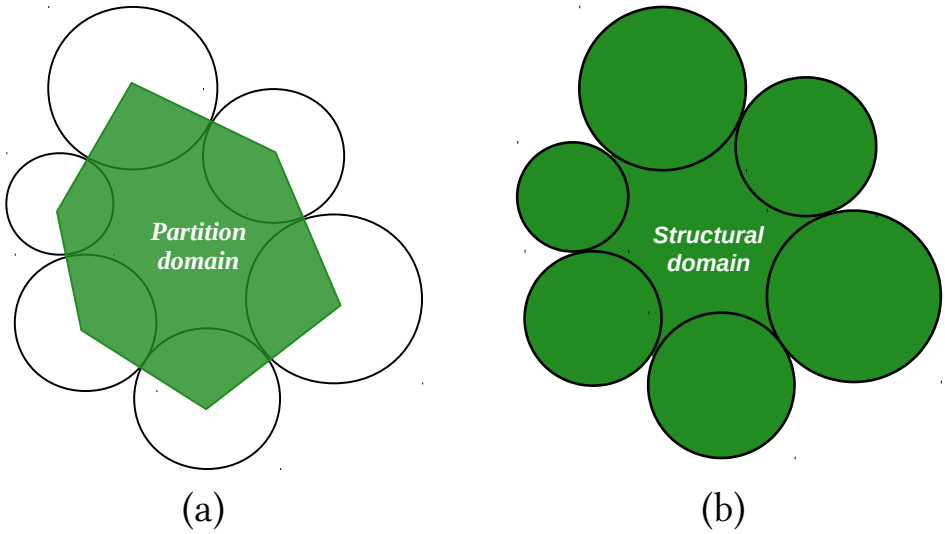

Figure 3.2 – (a) Grain loop partition domain, based on the contact branches, (b) Grain loop structural domain, some part of the spheres will be contained in several domains.)

3.2.2 Mesoscopic porosity

Grain loops enclose polygons with edges correponding to the branch vectors joining the grains center involved in the loop (Figure 3.3). Considering the polygon formed by the loop, the porosity of grain loops can be studied to capture the meso-volumetric behaviour of granular material (especially for the highest order loops order). Stokes theorem is used in order to compute the surface from the outer normal vectors and the position of the centers of the grain loop edges.

$$A_l^{part} = \frac{1}{2} \sum_{k}^{N_e} \boldsymbol{x}_{mid}^k \cdot \boldsymbol{n}^k \tag{3.6}$$

where N_e is the number of edges, $\boldsymbol{x}_{mid}^k$ is the vector position of the center of the edge l^k (see Figure 3.3), and $\boldsymbol{n}^k$ the outer normal vector of the edge l^k and whose norm is equal to the length of the l^k edge.

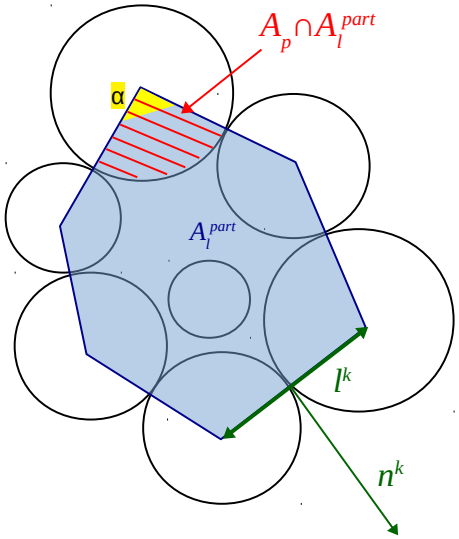

Figure 3.3 – The blue polygon is the grain loop l area. The hatched red area is the area of a grain inside the grain loop area, which is part of the solid area in the computation of the porosity. The k^{th} edge l^k and its outer normal $\boldsymbol{n}^k$ displayed for illustration of the computation of the loop area A^{part}.

The area of a loop containing a wall can be calculated by considering the particle/wall contact points. The real loop porosity p_l^{real} is calculated simply by accounting for the area of the particles inside the grain loop area as solid parts (Figure 3.3) :

$$p_l^{real} = \frac{A_l^{part} - \sum_g A_g \cap A_l^{part}}{A_l^{part}} \tag{3.7}$$

If the grain loop analysed is of a high order (6 grains or more), it may contain rattlers inside its void area. In that case, the effective porosity of the loop l p_l^{eff} is defined as :

$$p_l^{eff} = \frac{A_l - \left(\sum_g A_g \cap A_l + \sum_{r=1}^{N_r} A_r\right)}{A_l} \tag{3.8}$$

where $A_r = \pi R_r^2$ is the area of the N_r rattlers inside the grain loops, of radius R_r. For small order loops (L3 or L4), the effective and the real porosities are equal.

3.2.3 Mesoscopic energies

Mesoscopic kinetic energy

For a spherical particle, the kinetic energy is calculated from the translational kinetic velocity of the particle v_p and the rotational velocity of the particle w_p :

$$E_c^p = \frac{1}{2} m_p \left\| \boldsymbol{v}_p \right\|^2 + \frac{1}{2} J \left\| \boldsymbol{w}_p \right\|^2 \tag{3.9}$$

where J is the moment of inertia a sphere (Equation 2.24). The kinetic energy of a grain loop l is the sum of the micro-kinetic energy of the particles considered. For the effective kinetic energy, the N_p particles defining the meso-structure l and the N_r rattlers contain inside the loop l are all considered. For the real kinetic energy, only the N_p particles defining the meso-structure l are accounted for.

$$\left[E_c^l\right]_{eff}^{struct} = \sum_{p=1}^{N_p} E_c^p + \sum_{r=1}^{N_r} E_c^r \tag{3.10}$$

$$\left[E_c^l\right]_{real}^{struct} = \sum_{p=1}^{N_p} E_c^p \tag{3.11}$$

These structural definitions may be revelant in the case where the grain loop l is studied, independently of neighbouring loops. It may be useful for instance in the framework of the internal second-order work computation. However, if all the meso-structures are studied, this definition is not extensive. To recover the sample kinetic energy by summing the mesoscopic kinetic energies, the partition definiton of the kinetic meso-energy consists in taking into account only the kinetic energy of the portion of the particles inside the loop area (Figure 3.4).

$$\left[E_c^l\right]_{real}^{part} = \sum_{p=1}^{N_p} \frac{|V_p \cap \Omega_l|}{|\Omega_l|} E_c^p \tag{3.12}$$

If there are N_r rattlers inside the grain loops, the partition and effective kinetic meso-energy is

$$\left[E_c^l\right]_{eff}^{part} = \sum_{p=1}^{N_p} \frac{|V_p \cap \Omega_l|}{|\Omega_l|} E_c^p + \sum_{r=1}^{N_r} E_c^r \tag{3.13}$$

Mesoscopic elastic energy

The elastic energy is computed at the contact scale. In the case of elasto-frictional contacts, the elastic energy E_e^c stored in a contact c is

$$E_e^c = \frac{1}{2}k_n \left(u_n^c\right)^2 + \frac{1}{2}k_t \left\|\boldsymbol{u}_\tau^c\right\|^2 = \frac{1}{2}k_n^{-1} \left(F_n^c\right)^2 + \frac{1}{2}k_t^{-1} \left\|\boldsymbol{F}_\tau^c\right\|^2 \tag{3.14}$$

with k_n and k_t the stiffnesses of the normal and tangential, as given in Section 2.2 ; $\boldsymbol{u}_n^c$ and $\boldsymbol{u}_\tau^c$ the normal and tangential displacements of the contact ; $\boldsymbol{F}_n$ and $\boldsymbol{F}_\tau$ the normal and tangential forces.

The structural point of view elastic mesoscopic energy is deduced from the sum of the micro-elastic energy of the N_c contacts inside the grainloop l (including the contacts between a particle and a wall) :

$$\left[E_e^l\right]_{real}^{struct} = \sum_{c=1}^{N_c} E_e^c \tag{3.15}$$

For the partition perspective, neighbouring grain loops of the loop l are considered. Since each contact belong to two loops, the elastic energy of the contacts have to be divided by two :

$$\left[E_e^l\right]^{part} = \sum_{c=1}^{N_c} \frac{1}{2}E_e^c \tag{3.16}$$

In case rattlers collide with its surrounding grains, elastic energy be stored in this transient contact. in that case, we can add the contribution of this contact to the elastic meso-energy (effective elastic meso-energy).

The case of plastic dissipation

Plastic dissipation corresponds to the cumulative energy dissipated when a contact slides (when $\left\|\boldsymbol{F}_\tau^c\right\| = \phi F_n^c$) giving rise to a dissipative tangential displacement velocity $\dot{\boldsymbol{u}}_\tau^c$. The incremental dissipation at a sliding contact c during a time increment dt reads :

$$dD_p^c = \dot{\boldsymbol{u}}_\tau^c \cdot \boldsymbol{F}_\tau^c dt \tag{3.17}$$

In DEM simulation, an accurate estimation of the plastic dissipation requires an updating procedure every time steptime step. The tesselation of a grain assembly into grain loops is computationnaly expensive, which prevent to compute in practice the meso-scale plastic dissipation.

3.3 Stress, strain and internal second-order work definitions at the mesoscopic scale

3.3.1 Internal second-order work at the mesoscopic scale

Studying the occurrence of bursts of kinetic energy is related to investigating the ability of the specimen to develop kinetic energy with a zero external second order work. The second-order work criterion is revelant for this stability analysis, under the condition that the continuum mechanics framework holds (see Equation 2.1). At the meso-scale, the continuum framework is questionable. There is a priori no reason for the meso-domains to fulfill the two requirements given in Section 2.1.1 and thus, no reason to use this criterion to anticipate bursts of kinetic energy.

Despite these restrictions, meso-stresses and meso-strains in a mesoscopic domain can be defined to build a so-called internal second-order mesoscopic work. This approach assumes that the Macro-Homogeneity condition (second-order Hill-Mandel lemma) is respected in the meso-domain Ω_l :

$$\langle \Delta\boldsymbol{\sigma} : \Delta\boldsymbol{\varepsilon} \rangle_{\Omega_l} = \langle \Delta\boldsymbol{\sigma} \rangle_{\Omega_l} : \langle \Delta\boldsymbol{\varepsilon} \rangle_{\Omega_l} \tag{3.18}$$

where

$$\langle \bullet \rangle_{\Omega_l} = \frac{1}{|\Omega_l|} \int_{\Omega_l} \bullet dV \tag{3.19}$$

The necessary conditions to ensure the validity of the lemma is discussed in (Nicot et al., 2017) at the scale of a representative elementary volume. Thus, this lemma was not discussed for meso-domains.

$$\left(W_2^{int}\right)_{\Omega_l} = \langle \Delta\boldsymbol{\sigma} \rangle_{\Omega_l} : \langle \Delta\boldsymbol{\varepsilon} \rangle_{\Omega_l} \tag{3.20}$$

Keeping in mind those restrictions and approximations, definitions of strain and stress at the meso-scale are detailed in the next sub-sections. While the definition of an incremental meso-strain does not cause significant problems, the definition of an incremental meso-stress in not straightforward. Three potential formulations are proposed, all consistent with the macroscopic stress definition. The criterion that will enable to select the best formulations can be based on the minimization of the residue in the balance equation of second-order work. The residue is composed of the terms difficult

to estimate at the meso-scale, among which the inertial terms. Starting from Equations 2.1 and 2.2, we obtain :

$$2\left(E_c(t+\Delta t)-E_c(t)\right)-2\Delta t\dot{E}_c=\Delta t^2\int_\Omega I dV+\int_{\delta\Omega}W_2^{ext}dS-\int_\Omega W_2^{int}dV \tag{3.21}$$

so

$$\Delta t^2\int_\Omega I dV+2\Delta t\dot{E}_c=2\Delta E_c-\left(\int_{\delta\Omega}W_2^{ext}dS-\int_\Omega W_2^{int}dV\right) \tag{3.22}$$

$$Residue=\Delta E_c-\frac{1}{2}\left(\int_{\delta\Omega}W_2^{ext}dS-\int_\Omega W_2^{int}dV\right) \tag{3.23}$$

The residue is zero only if the system is at quasi-static regime. It is not zero in the context of the analysis of a burst of kinetic energy. However, the smaller the residue is in absolute, the smaller the inertial terms are. By comparing the residue optained from the different definitions of W_2^{int} according to the meso-stress chosen, the best formulation of the meso-stress in the framework of the balance equation of second-order work should be found. It will be verified later in the numerical simulations (Chapter 4).

For the following equations, $\otimes_s$ is the symmetric tensor product : $\boldsymbol{a}\otimes_s\boldsymbol{b}=\frac{1}{2}\left(\boldsymbol{a}\otimes\boldsymbol{b}+\boldsymbol{b}\otimes\boldsymbol{a}\right)$ with $\boldsymbol{a}$ and $\boldsymbol{b}$ two vectors.

3.3.2 Strain and incremental strain at the mesoscopic scale

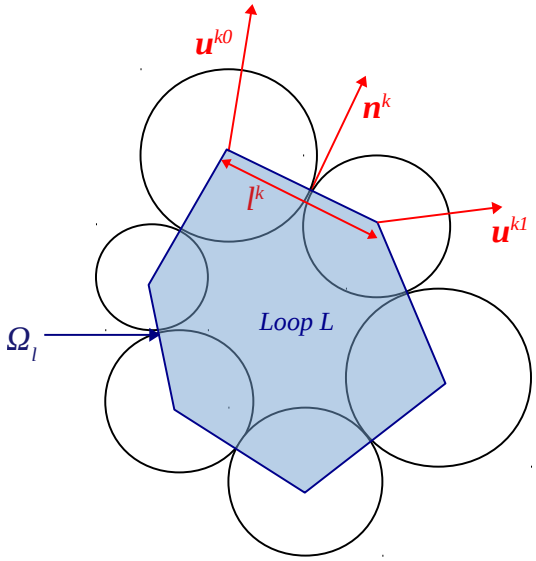

Figure 3.4 – Sketch of the calculation of the strain. The edge l^k and its associated displacements $\boldsymbol{u}^{ki}$ and outer normal $\boldsymbol{n}^k$ are displayed. Note that $\Omega_l = V^{part}$

At the loop scale, the meso-strain is the average strain $\langle \boldsymbol{\varepsilon} \rangle_{\Omega_l}$ within the domain of the grain loop Ω_l (Figure 3.4). It can be completely defined from a boundary formulation, as follows :

$$\langle \boldsymbol{\varepsilon} \rangle_{\Omega_l} = \frac{1}{|\Omega_l|} \int_{\partial \Omega_l} \boldsymbol{u} \otimes_s \boldsymbol{n} dA \tag{3.24}$$

where $\boldsymbol{u}$ is the displacement vector, $\boldsymbol{n}$ the outward normal to the domain Ω_l. By computing strain at time t and $t + \Delta t$, an incremental strain can be deduced. Note that the time steps Δt should be small enough so that the grain loop undergoes small perturbation between $\Omega_l(t)$ and $\Omega_l(t + \Delta t)$. The incremental meso-strain between t and $t + \Delta t$ can be expressed as a function of the incremental displacement vector $\Delta \boldsymbol{u} = \boldsymbol{u}(t + \Delta t) - \boldsymbol{u}(t)$:

$$\langle \Delta \boldsymbol{\varepsilon} \rangle_{\Omega_l} = \frac{1}{|\Omega_l|} \int_{\partial \Omega_l} \Delta \boldsymbol{u} \otimes_s \boldsymbol{n} dA \tag{3.25}$$

where $\boldsymbol{n}$ and Ω_l are considered at time t. Note also that the grain loop can disappear in the interval Δt with this definition of the incremental meso-strain, since the definition relies only on grain incremental displacements

that are always well defined. In practice, the calculation of the meso-strain is based on the polygon shaped by the branch vectors of the grain loop (Figure 3.4). Thus, the meso-strain tensor for a grain loop l is expressed as a function of a linear interpolation of the incremental displacements of the particles (Kruyt and Rothenburg, 1996; Bonelli et al., 2012; Liu et al., 2020):

$$\langle \Delta\boldsymbol{\varepsilon} \rangle_{\Omega_l} = \frac{1}{|\Omega_l|} \sum_{k \in \partial\Omega_l} \frac{1}{2} \left(\Delta\boldsymbol{u}_k^0 + \Delta\boldsymbol{u}_k^1 \right) \otimes_s \boldsymbol{n}^k l^k \tag{3.26}$$

where $\boldsymbol{u}_k^0$ and $\boldsymbol{u}_k^1$ are the displacement vectors of the vertices of the k^{th} edge, l_k its length and $\boldsymbol{n}^k$ its outside normal vector (see Figure 3.4).

3.3.3 Stress and incremental stress at the mesoscopic scale

Using Love-Weber or more general Bagi definitions (Bagi, 1996; Nicot et al., 2013b), the meso-stress can be expressed at time t based on contact forces. However a direct use of this definition makes an incremental formulation between time t and $t + \Delta t$ more tricky to define as it relies on contact forces and thus requires that the grain loop is not reorganized (persisting contacts). In order to address this issue, two formulations are presented, according to the two approaches to define meso-quantities. The first formulation uses the Love-Weber stress in the grains belonging to the meso-domain while the second is based on a mesoscopic stress definition (Bagi and Weber).

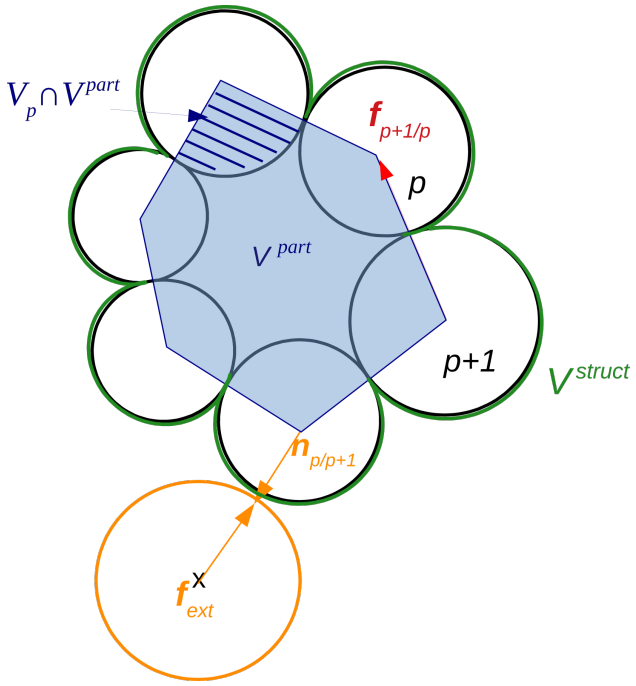

Figure 3.5 – Sketch to illustrate the computation of the different meso-strains. The portion of the grain inside the loop domain is displayed. V^{struct} incorporates all the grains and the void inside the loop. External and internal forces are mapped. Note that $\Omega_l = V^{part}$

Grain averaged mesostress formulation

In this formulation the meso-stress is espressed as the spatial average on the domain Ω_l (partition volume) of the micro stresses :

$$\langle \boldsymbol{\sigma} \rangle_{\Omega_l} = \frac{1}{|\Omega_l|} \int_{\Omega_l} \boldsymbol{\sigma} dV \tag{3.27}$$

As the local stress tensor $\boldsymbol{\sigma}$ is equal to zero where there is no particles, the integral can be transformed into a sum over the portions of the particles included in the domain Ω_l, noted $V_p \cap \Omega_l$ (Figure 3.5):

$$\langle \boldsymbol{\sigma} \rangle_{\Omega_l} = \frac{1}{|\Omega_l|} \sum_{p \in \Omega_l} \int_{V_p \cap \Omega_l} \boldsymbol{\sigma} dV \tag{3.28}$$

The integral over the portion $V_g \cap \Omega_l$ of the local stress tensor $\boldsymbol{\sigma}$ is the average stress in this portion of the particle p weighted by the volume of this portion, noted $\langle \boldsymbol{\sigma} \rangle_{V_p \cap \Omega_l}$:

$$\langle \boldsymbol{\sigma} \rangle_{\Omega_l} = \frac{1}{|\Omega_l|} \sum_{p \in \Omega_l} |V_p \cap \Omega_l| \langle \boldsymbol{\sigma} \rangle_{V_p \cap \Omega_l} \tag{3.29}$$

We assume that the average stress in the portion inside the domain of the grain loop is equal to the average stress of the particle. With this hypothesis, we optain :

$$\langle \boldsymbol{\sigma} \rangle_{\Omega_l} = \frac{1}{|\Omega_l|} \sum_{p \in \Omega_l} |V_p \cap \Omega_l| \langle \boldsymbol{\sigma} \rangle_{V_p} \tag{3.30}$$

The calculation of the average stress of the particle p has to be detailed. Particles are subjected to a symmetrical second-order tensor local stress which verifies the equation of motion $\rho \ddot{\boldsymbol{x}} = div(\boldsymbol{\sigma})$ and $\boldsymbol{\sigma} = \boldsymbol{\sigma}^{\boldsymbol{T}}$. In the scope of dynamic evolution, the average stress $\langle \boldsymbol{\sigma} \rangle_{V_p}$ is written :

$$\langle \boldsymbol{\sigma} \rangle_{V_p} = \frac{1}{|V_p|} \int_{\partial V_p} \boldsymbol{\sigma} \cdot \boldsymbol{n} \otimes_s (\boldsymbol{x} - \boldsymbol{c}_p) dA + \frac{1}{|V_p|} \int_{V_p} \rho \ddot{\boldsymbol{x}} \otimes_s (\boldsymbol{x} - \boldsymbol{c}_p) dV \tag{3.31}$$

where $\boldsymbol{x}$ is the vector position of a point in V_p and $\boldsymbol{c}_p$ the vector position of the center of the particle. Let's develop and simplify the two integrals in the

right side of Equation 3.31. Particles are only subjected to contact forces $\boldsymbol{f}_c$ on their surface ∂V_g. Thus the first integral becomes :

$$\frac{1}{|V_p|}\int_{\partial V_p} \boldsymbol{\sigma}\cdot\boldsymbol{n}\otimes_s(\boldsymbol{x}-\boldsymbol{c}_p)dA = \frac{D_p}{2\,|V_p|}\sum_{c\in\partial V_g}^{N_c}\boldsymbol{f}_c\otimes_s\boldsymbol{n}_c \tag{3.32}$$

where N_c the number of contacts of the particle, D_p its grain diameter and $\boldsymbol{n}_c$ the outward normal to V_g at contact c.

The second integral concerns kinematics. For a spherical rigid particle, its is expressed by :

$$\dot{\boldsymbol{x}} = \dot{\boldsymbol{c}}_p + \boldsymbol{Q}_p\cdot(\boldsymbol{x}-\boldsymbol{c}_p) \tag{3.33}$$

$$\ddot{\boldsymbol{x}} = \ddot{\boldsymbol{c}}_p + (\dot{\boldsymbol{Q}}_p + \boldsymbol{Q}_p^2)\cdot(\boldsymbol{x}-\boldsymbol{c}_p) \tag{3.34}$$

with $\boldsymbol{Q}_p$ the second-order skew symmetric tensor corresponding to the particle rotation rate. Thus, the second integral on the right side of Equation 3.31 is

$$\frac{1}{|V_p|}\int_{V_p}\rho\ddot{\boldsymbol{x}}\otimes_s(\boldsymbol{x}-\boldsymbol{c}_p)dV = \frac{\rho D_p^2}{10}(\dot{\boldsymbol{Q}}_p+\boldsymbol{Q}_p^2) \tag{3.35}$$

As the ratio between Equation 3.35 and Equation 3.32 scales with D_p^4, the contribution of the particle rotation is assumed to be negligible compared to contact forces's. This point is contestable since contact forces may become weak during a burst of kinetic energy.

Finally, the expression of the meso-stress, based on the particles stresses, is

$$\langle\boldsymbol{\sigma}\rangle_{\Omega_l} = \frac{1}{|\Omega_l|}\sum_{p\in\partial\Omega_l}\frac{D_p\,|V_p\cap\Omega_l|}{2\,|V_p|}\sum_{c\in\partial V_g}^{N_c}\boldsymbol{f}_c\otimes_s\boldsymbol{n}_c \tag{3.36}$$

It is different from the Love-Weber formula for the set of particles concerned, because the domain Ω_l (partition volume) is defined by the centers of the particles (partition view) and does not contain their entire volume (structural view) (Figure 3.5). Moreover, this definition is not restricited to a quasi-static regime and it can be use for dynamical cases when the contributions of rotation (equation 3.35) are non neglegible. A meso-stress is

an artificial concept. It is not linked to a constitutive behaviour law. The sum of the mean meso-stress resulting in the macro-stress is a way to make this meso-stress definition consistent. This grain averaged meso-stress formulation is extensive and is consistent with the macro-stress definition at the REV scale (sample domain S) (see Section 4.3.1).

$$\langle \boldsymbol{\sigma} \rangle_S = \frac{1}{|S|} \int_S \boldsymbol{\sigma} dV = \frac{1}{|S|} \sum_{p \in S} |V_p| \langle \boldsymbol{\sigma} \rangle_{V_p} \tag{3.37}$$

so

$$\langle \boldsymbol{\sigma} \rangle_S = \frac{1}{|S|} \sum_l \sum_{p \in \Omega_l} |V_p \cap \Omega_l| \langle \boldsymbol{\sigma} \rangle_{V_p} = \frac{1}{|S|} \sum_l |\Omega_l| \langle \boldsymbol{\sigma} \rangle_{\Omega_l} \tag{3.38}$$

Following the hypothesis that geometric transformations between the times t and $t + \Delta t$ are small, we assume that :

$$\langle \Delta \boldsymbol{\sigma} \rangle_{\Omega_l} = \Delta \langle \boldsymbol{\sigma} \rangle_{\Omega_l} = \langle \boldsymbol{\sigma}(t + \Delta t) \rangle_{\Omega_l} - \langle \boldsymbol{\sigma}(t) \rangle_{\Omega_l} \tag{3.39}$$

where Ω_l is considered at time t. As the domain Ω_l is updated at each increment, it is an updated Lagrangian description.

Meso-formulation of Bagi stress

Another way to define a mesoscopic stress is to apply the Bagi formulation (Bagi, 1996) to the meso-domain V^{struct}, which takes into account all the volume of particles (Figure 3.2(a), 3.5). It is composed of two terms :

1. A *Weber* internal stress, based on internal contact forces between the particles of the meso-domain ($\boldsymbol{f}_{g+1/g}$ in Figure 3.5).
2. A *Bagi correction term* taking into account external forces applied on the meso-domain V^{struct} ($\boldsymbol{f}_{ext}$ in Figure 3.5).

The mesoscopic Bagi stress is thus written :

$$\left\langle \boldsymbol{\sigma}^{Bagi} \right\rangle_{V^{struct}} = \frac{1}{|V^{struct}|} \int_{V_{ext}} \boldsymbol{f}_c \otimes R \boldsymbol{n}_c dV + \frac{1}{|V^{struct}|} \int_{\partial V^{struct}} \boldsymbol{f}_{ext} \otimes r \boldsymbol{n}_{ext} dA \tag{3.40}$$

where $\boldsymbol{f}_c$ is the intern contact force between two consecutives particles, R is the sum of the two particles in contact, $\boldsymbol{n}_c$ is the normal contact vector between them, $\boldsymbol{f}_{ext}$ is an external force applied on the surface of V^{struct}, r the radius of the particle inside V^{struct} where the force is applied and $\boldsymbol{n}_{ext}$ the normal vector to the external contact point.

As all the forces are ponctual, the mesoscopic Bagi stress can be expressed as:

$$\begin{aligned}\left\langle \boldsymbol{\sigma}^{Bagi} \right\rangle_{V^{struct}} =& \frac{1}{|V^{struct}|} \sum_{p \in V^{struct}} \boldsymbol{f}_{p+1/p} \otimes (R_p + R_{p+1}) \boldsymbol{n}_{p/p+1} \\ &+ \frac{1}{|V^{struct}|} \sum_{p \in \partial V^{struct}} \boldsymbol{f}_{p_{ext}/p} \otimes R_p \boldsymbol{n}_{p/p_{ext}}\end{aligned} \tag{3.41}$$

with $\boldsymbol{f}_{a/b}$ is a force applied by the particle a to the particle b and $\boldsymbol{n}_{a/b}$ is the normal vector form the center of the particle a to the particle b, p is a article belonging to the extended meso-domain V^{struct} and p_{ext} is a particle outside the domain but in contact with it (Figure 3.5).

The first term of Equation 3.41 corresponds to the well known Love-Weber formula applied at the meso-scale. The Weber stress $\boldsymbol{\sigma}^{Weber}$ gives Equation 3.42 here. For large numbers of grains, the Bagi stress is approximated by the Weber stress, as the contribution of internal part is greater than the external part (as volume grows faster than surface).

$$\left\langle \boldsymbol{\sigma}^{Weber} \right\rangle_{V^{struct}} = \frac{1}{|V^{struct}|} \sum_{p \in V^{struct}} \boldsymbol{f}_{p+1/p} \otimes (R_p + R_{p+1}) \boldsymbol{n}_{p/p+1} \tag{3.42}$$

Since Equation 3.41 and Equation 3.42 converge towards the macroscopic definition of the stress when the number of grains gets large enough, the Bagi and the Weber definitions are candidates for the definition of a mesoscopic stress. Contrary to the previous grain averaged mesostress definition, the Bagi and Weber expression are not extensives (contacts are counted several times in the summation), and the macro stress is deduced from the statistical homogenization of the meso-stresses.

The hypothesis of small geometric incremental transformations is still required here and the incremental mesoscopic Bagi stress can be written as in Equation 3.39. The domain V^{struct} is also updated at each increment of time, so it is an updated Lagrangian description.

3.4 Conclusion

This Chapter introduces new mechanical quantities to analyse the inertial transition at an intermediate scale. The starting point for an analysis at an intermediate scale is the grain loops. Although 2D numerical simulations do

not make physical sense with DEM modelling (unlike FEM modelling), all numerical simulations are 2D which has proven in previous research studies to be still relevant to capture most of the granular physics. Meso-quantities have been defined and can be divided in two categories : either structural (Energies : Equation 3.12, Equation 3.13, Equation 3.15 ; Stress : Equation 3.36) or partition (Energies : Equation 3.11, Equation 3.10, Equation 3.16 ; Stress : Equation 3.41). Both approaches are useful. The partition view gives a clear meaning to the quantities created, which can be a bit artificial like the meso-stress. The structural view is necessary for the application of the second-order mesoscopic criterion and the estimation of the residue.

Chapter 4

Outbursts of kinetic energy in numerical 2D granular media under biaxial test

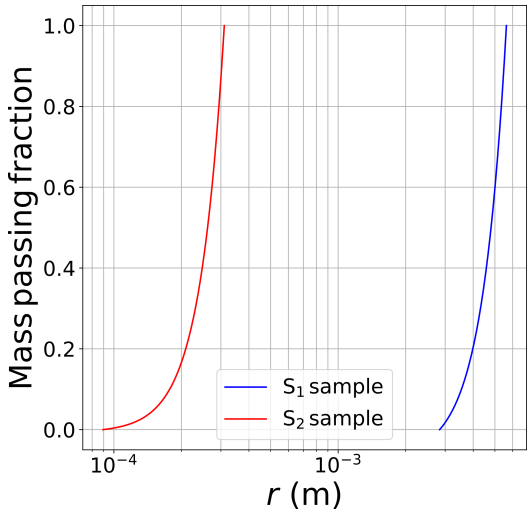

Figure 4.1 – Grain size distribution of the sample S_1 (blue curve) and sample S_2 (red curve).

Inertial transitions result from the sudden release of energy in the form of kinetic energy. In granular systems, these bursts of kinetic energy appear at specific locations and propagate to the neighbourhood. In order to understand how these bursts form and modify the microstructure, we propose to analyze this issue in a well known environnement, i.e. homogeneous material domain. Critical state is interesting for the study of bursts. Indeed, when approaching the failure surface, we can observe bursts which are not propagating to the whole specimen. Thus, biaxial tests, common and well documented tests, are chosen to observe the behaviour of a specimen subjected to a deviatoric loading. Different numerical samples are created and subjected to a biaxial test, using YADE. In this Chapter, the numerical set up of biaxial tests is presented first. In a second part, the analysis of selected bursts during critical state is detailed. Precursors of bursts initiation are looked for. Second-order work criterion is investigated at the meso-scale as presented in Section 3.3 and conclusions about the different definitions are drawn in the last part.

4.1 Numerical experiment at REV scale

4.1.1 Sample preparation

Numerical experiments are carried out with quasi 2D numerical samples, as described in Section 3.1.

Two types of samples are created, type S_1 (Liu et al., 2020) and type S_2 (Deng et al., 2021b) inspired from the two cited works. Characteristics of the two samples are summarized in Table 4.1. The PSD of both samples are illustrated in Figure 4.1 and general views of the two samples at the beginning of the test are shown in Figure 4.2. For the sample S_1, it has been chosen to fix the out of plane walls at 1 m from each other, while it has been fixed at 0.04 m for the sample S_2. The two samples configuration corresponds to the two options for the out of plane wall exposed in Section 3.1.2, to express stresses in Pa in 2D numerical set ups. Also, the grain density is multiplied by 8 between the sample S_1 and the sample S_2. Refering to Equation 2.28, it is an artificial way to speed up the simulation. Thus, this change influences the speed of the simulation and the amplitude of the energy values, but it has been checked that it does not influence the essential physics of bursts of kinetic energy (see Section 4.1.5).

Samples S_1 and S_2 are created with the same protocol. The spheres are first placed randomly in a square domain, with a smaller radius than targeted. They grow homothetically until the desired confining pressure is reached and the unbalance forces remain below a certain threshold (Equation 2.30). This threshold ensure that the forces applied on the spheres are very low compared to the contact forces (see Section 2.2.4). Secondly, the inter particles friction angle Φ can be reduced from its initial value to obtained samples with the same particle size distribution but different densities. To obtain a dense sample, Φ for each contact is decreased from 35° to 0° while maintaining a confining pressure of 100 kPa. A loose sample is obtained by keeping the friction angle to 35°. Again, the quasi-static regime of the sample is verified through unbalance forces. With this protocol a loose and a dense specimen are created for material of type S_2 (Table 4.2).

The biaxial test consists in two parts. An isotropic compression of $\sigma_0 =$ 100kPa is first applied until unbalanced forces decrease below a fixed threshold. Then, the confining pressure σ_0 is maintained on the lateral walls while a strain rate $\dot{\varepsilon}$ is imposed in the vertical direction (Figure 4.2). The numerical damping for the sample creation step and the biaxial test is set to a low value (0.05), in order not to inhibit the creation and propagation of kinetic outbursts.

Table 4.1 – Characteristics of the two type of samples and parameters of the biaxial test.

Parameters	Sample S_1	Sample S_2
Number of spheres	$25,000$	$20,000$
Grain density	$3,000$ kg.m^{-3}	$3,000 \times 8$ kg.m^{-3}
R_{mean}	3×10^{-4} m	4×10^{-3} m
D_{max}/D_{min}	3.5	2
Sample Aspect Ratio (Height/Length)	1	1.5
Interparticle friction angle Φ	35°	35°
k_n/D	356 MPa	356 MPa
k_t/k_n	0.42	0.42
Numerical damping coefficient	0.05	0.05
Confining stress σ_0	100 kPa	100 kPa
Loading rate $\dot{\varepsilon}$	0.01.s^{-1}	0.01.s^{-1}

Table 4.2 – 2D Porosity of the samples

Sample S_1 dense	Sample S_2 dense	Sample S_2 loose
0.1670	0.1603	0.2082

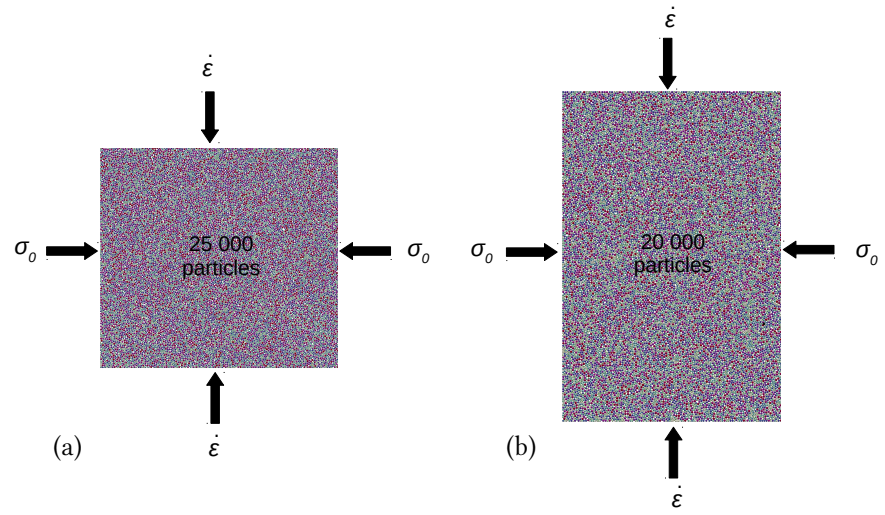

Figure 4.2 – Scheme of the biaxial test for the sample S_1 (a) and the sample S_2 (b). The ratio of size between the two samples is not respected. However one can notice the different aspect ratios of the two types of sample. During the second part of the biaxial test, the confining pressure σ_0 is maintained lateraly, while a strain rate $\dot{\varepsilon}$ is applied along the horizontal direction.

4.1.2 Drained biaxial test

In order to check whether our simulations are consistent with experimental observations, the deviatoric stress and the volumetric strain curves are plotted for each sample in Figure 4.3. The 2D expressions of the deviatoric stress and the volumetric strain are given in Equation 3.1 and 3.2 in Section 3.1.3. The vertical lines A and B represent respectively the characteristic point of volumetric strain ε_{yy} and the maximum deviatoric stress q.

The curves in Figure 4.3(a) and 4.3(c) are typical responses for dense sample S_1: they exhibit hardening with contractancy phase followed by a softening with dilatancy phase. In other terms, the q curve shows a strong increase leading to a peak followed by a decrease and a plateau. The q peak is around at 1% of axial strain for both specimens (line B in Figures 4.3 (a) and (c)). For the dense sample S_1, no localization of the deformation is observed, contrary to the dense sample S_2 .

The curves in Figure 4.3(b) are typical response for a loose sample: the sample experiences hardening with contractancy. The deviatoric stress increases until reaching a plateau at around 6% of axial strain (Figure 4.3 (b)).

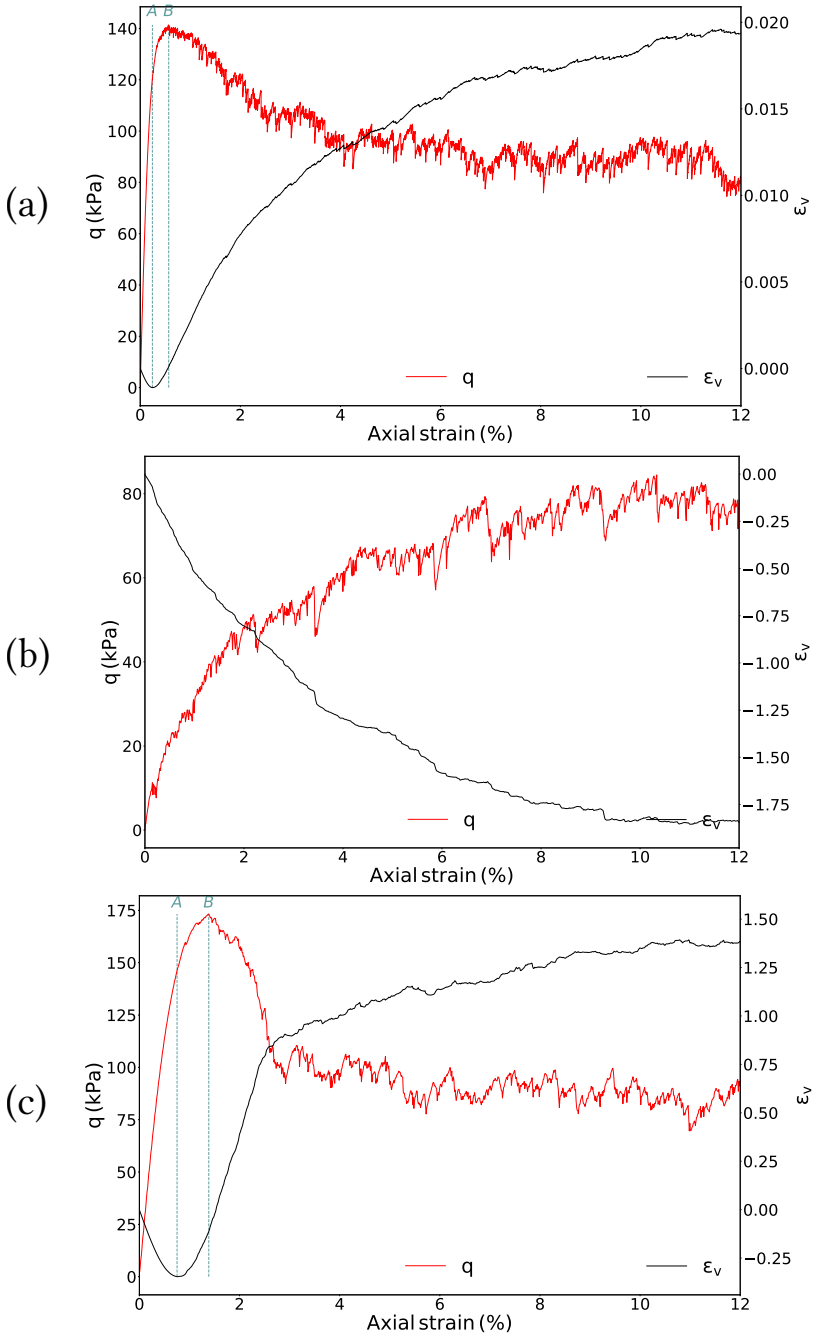

Figure 4.3 – Deviatoric stress and volumetric strain for (a) dense sample S_1, (b) loose sample S_2, (c) dense sample S_2 as a function of the axial strain during the biaxial test. The A and B vertical lines on dense samples graphs represent respectively the maximum contractancy and the maximum deviatoric stress.

4.1.3 Meso-structures evolution benchmark

In Section 2.3, the definition of meso-structures as grain loops was introduced. This unique partition is defined for each sample and the evolution of each grain loop order is presented in Figure 4.4. Figure 4.4 illustrates that the ratio of each grain loop order depends on the nature of the sample and the loading history. Each sample presents a different evolution along the biaxial test.

For the loose sample S_2 (Figure 4.4(b)), the low variations (not more than 2%) in the composition of meso-structures as a function of the axial strain show that the sample is close to the ultimate composition at critical state. L6+ loops are in larger amounts than the smallest orders (L3 and L4) and the L5 order.

The dense sample S_1 (Figure 4.4(a)) exhibits the same ranking in the composition of grains loops. Before the maximum contractancy (line A in Figure 4.3(a)) the L6+ order is in minority while the small orders are in majority (10% against 70% for the L3 and L4 orders together). However after the maximum deviatoric stress (line B Figure 4.3(a)), highest order loops outnumber the smallest ones, and the composition ressembles the one in the loose sample S_2. The dense sample S_2 (Figure 4.3(c)) at the beginning of the biaxial test has a similar composition as the dense sample S_1. However, after the maximum deviatoric stress state, the smallest order loops are still in majority (about 60% of the composition) and followed by the L6+ order and the L5 order.

In the dense sample S_1, no strain localization is observed contrary to the dense sample S_2 because of the different aspect ratios of the two samples (see Figure 4.2). The $1:1$ aspect ratio of dense sample S_1 prevents the formation of a shear band which is not the case for the dense sample S_2 of aspect ratio $1:1.5$. Thus, the final loops composition of the dense sample S_1 is similar to the one in Liu et al. (2018) when restricting the analysis to the shear band domain.

4.1.4 Energy analysis

At the scale of the sample, the evolution of the different energies are similar in the different samples. Figure 4.5 shows the variations in kinetic energy, plastic dissipation and elastic strain energy as a function of axial strain. The analytical expressions of these energies are reviewed in Chapter 3.2.3. The variation of these energies corresponds to the difference between the energy at a given axial strain and the same energy just before the deviatoric loading is applied. Elastic strain energy increases earlier (until the peak of deviatoric

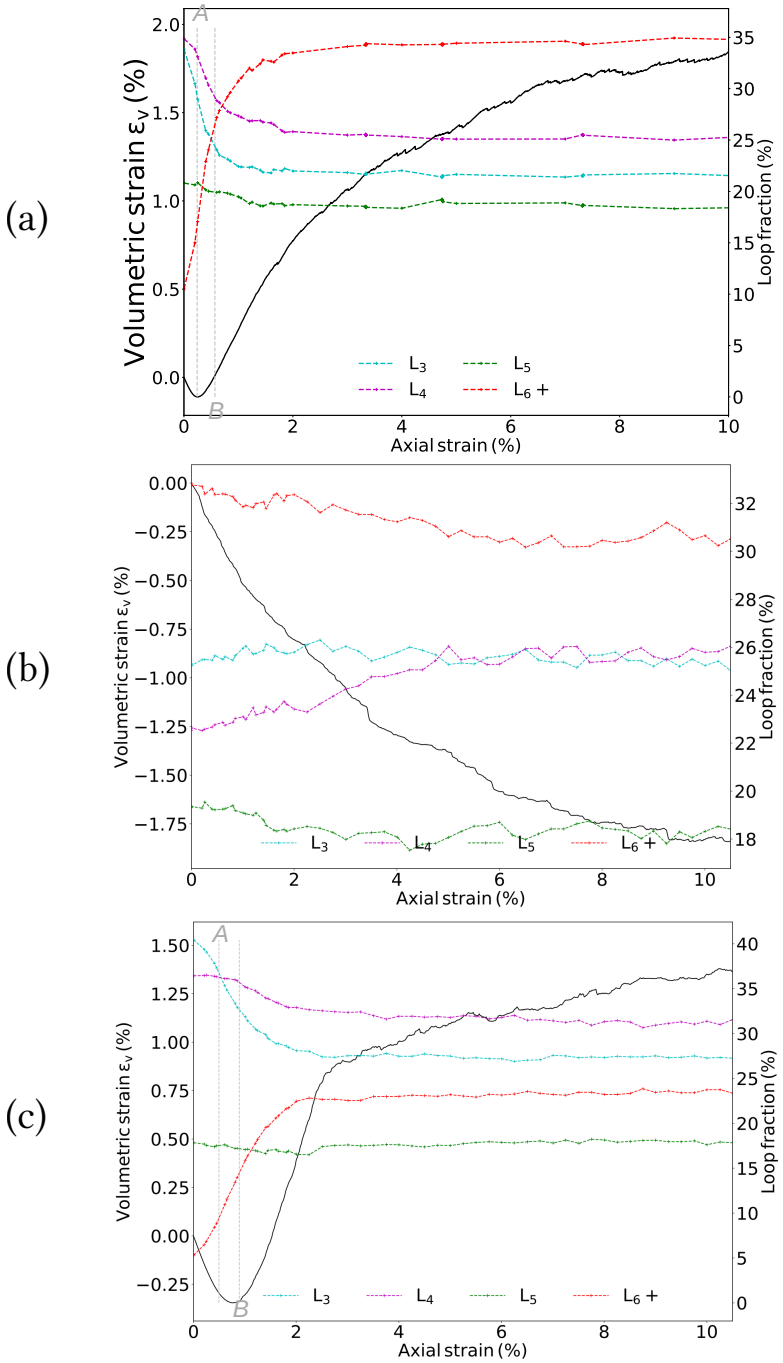

Figure 4.4 – Loops evolution for (a) dense sample S_1, (b) loose sample S_2, (c) dense sample S_2 as a function of the axial strain during the biaxial test. The A and B vertical lines on dense samples graphs represent respectively the maximum contractancy and the maximum deviatoric stress as in Figure 4.4.

Table 4.3 – Mean kinetic energies for the three samples at critical state

Parameters	sample S_1	sample S_2 loose	sample S_2 dense
Mean E_c total	1.7×10^{-8} J	1.6×10^{-2} J	2.2×10^{-2} J
Mean E_c per grain	6.4×10^{-13} J	7.8×10^{-7} J	1.1×10^{-6} J

stress represented by the line B in Figures 4.5(a) and (c)), then decreases and reaches a plateau. Plastic dissipation increases at a constant rate except at the very beginning corresponding to the pseudo elastic regime.

The mean and max values of the kinetic energy for the samples S_2 are higher than for the sample S_1, considering the higher grain density. Kinetic energy fluctuates a lot around the mean values as shown in Figures 4.5. However, note that the kinetic energy is three order of magnitude smaller than the elastic strain energy and the plastic dissipation. It shows that macroscopically, the material remains in a quasi-static regime, where most of the dissipation is done through friction. Local outbursts of kinetic energy are detected through the following criterion : a grain is assumed to be part of a burst of kinetic energy if its energy is several times above the mean grain kinetic energy at critical state. In practice, five times the mean grain kinetic energy is the threshold taken. Each sample exhibits different mean macroscopic kinetic energy and mean kinetic energy per grain. The values are given in the Table 4.3.

We shall have a close look on the deviatoric stress q curve around the appearance of bursts of kinetic energy, given in Figure 4.6. The onset of a burst corresponds indeed to a drop in q. Thus, a localized outburst of kinetic energy has macroscopic consequences in the form of a small transient instability with drops of deviatoric stress q.

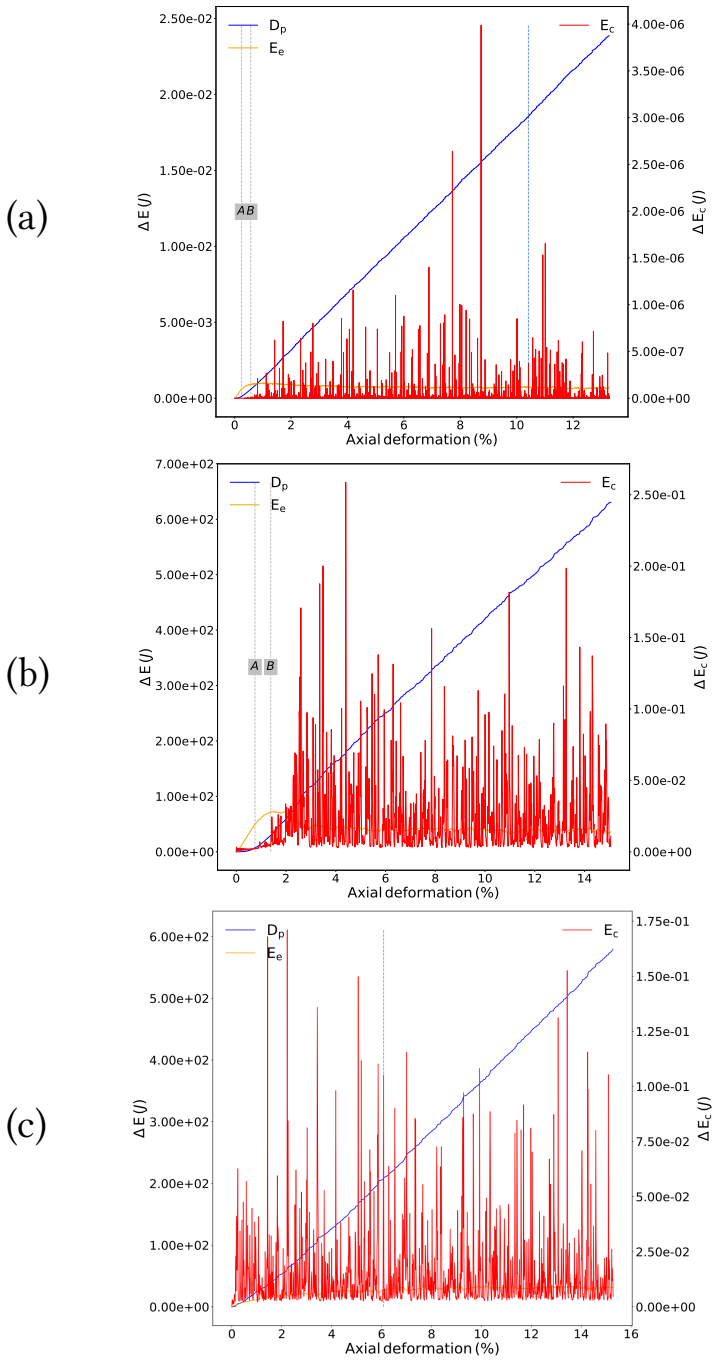

Figure 4.5 – Evolution of elastic strain energy E_e, plastic dissipation E_p (left $y-axis$) and kinetic energy E_c (right $y-axis$) for (a) the dense sample S_1, (b) loose sample S_2, (c) dense sample S_2 as a function of the axial strain during the biaxial test. The reference state corresponds to the isotropic compression state reached before the deviatoric loading is applied. The A and B vertical lines on dense samples graphs represent respectively the maximum contractancy and the maximum deviatoric stress, as in Figure 4.4 and Figure 4.3.

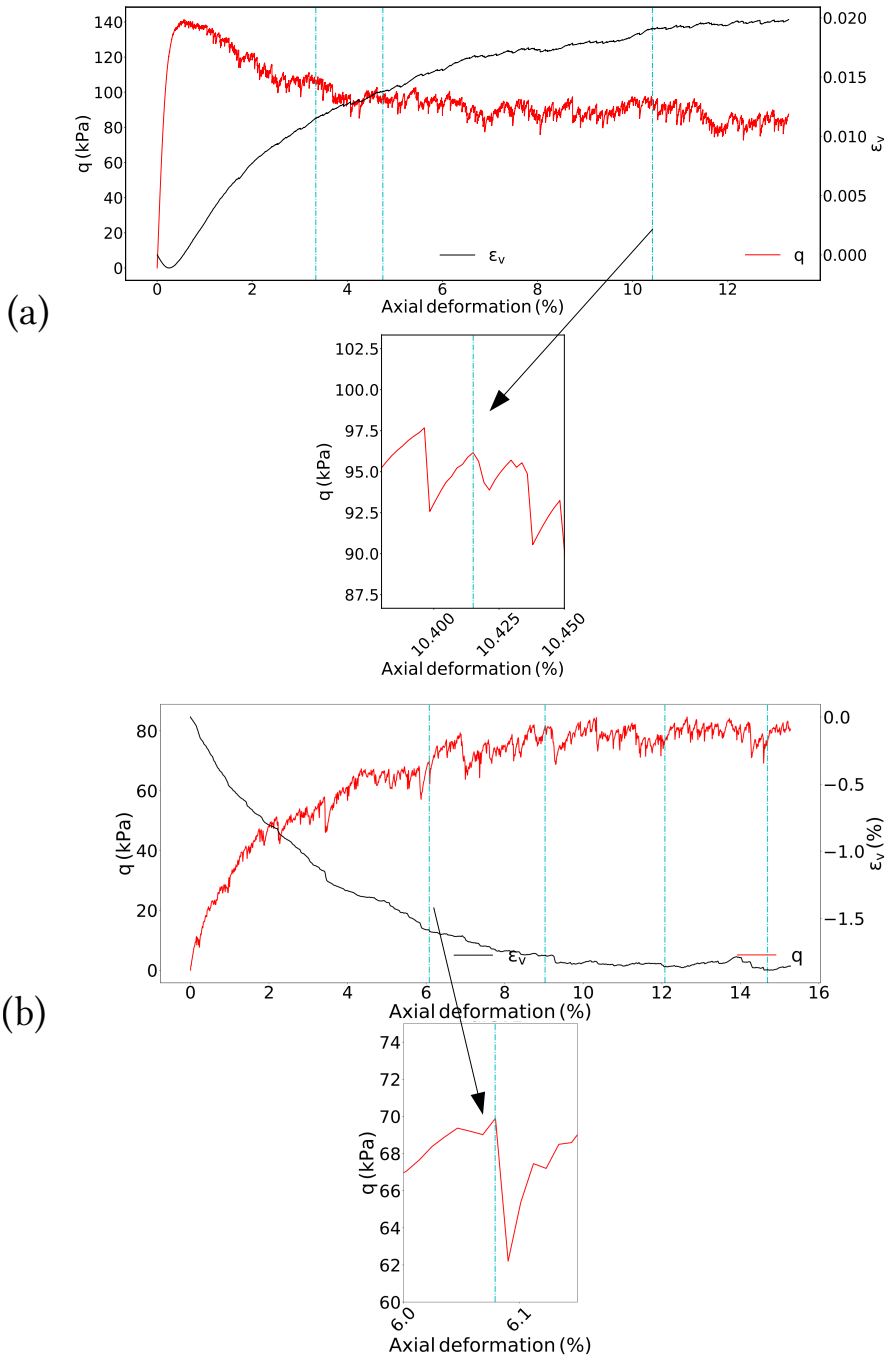

Figure 4.6 – Correlation between drops in deviatoric stress and bursts of kinetic energy in the (a) dense sample S_1 and (b) loose sample S_2. A zoom is made for one burst to show the decrease of q at the onset of a burst.

Among all the bursts of kinetic energy observed at critical state, four or three bursts are selected arbitrarily for the three different samples as shown by horizontal blue hashed lines in Figure 4.6. Those selected bursts are analysed in details in the next sections. They are chosen along the q plateau where a quasi-stationnary regime is reached, so they are all supposed equivalent.

4.1.5 Influence of the grain density

In order to check that increasing the particle density in the simulation has not physically irrevelant consequences for studying outbursts of kinetic energy, another dense sample S_2 is created with a grain density of $2,400$ kg.m^{-3}. All the characteristics of this new sample S_2 are the same as for the dense sample S_2 given in Table 4.1. This sample is subjected to the same drained biaxial test as described in Section 4.1.2. The deviatoric stress q and the volumetric strain ε_v of the this new sample are compared to the dense sample S_2 with a grain density of $3,000 \times 8$ kg.m^{-3} in Figure 4.7. The variation for both quantities are the same for both samples. The denser sample is a bit more contractant at the beginning of the hardening phase (Figure 4.7(b)), but the characteristic point and the q peak occur at the same axial strains. In other words, both samples have the same mechanical response along the drained test.

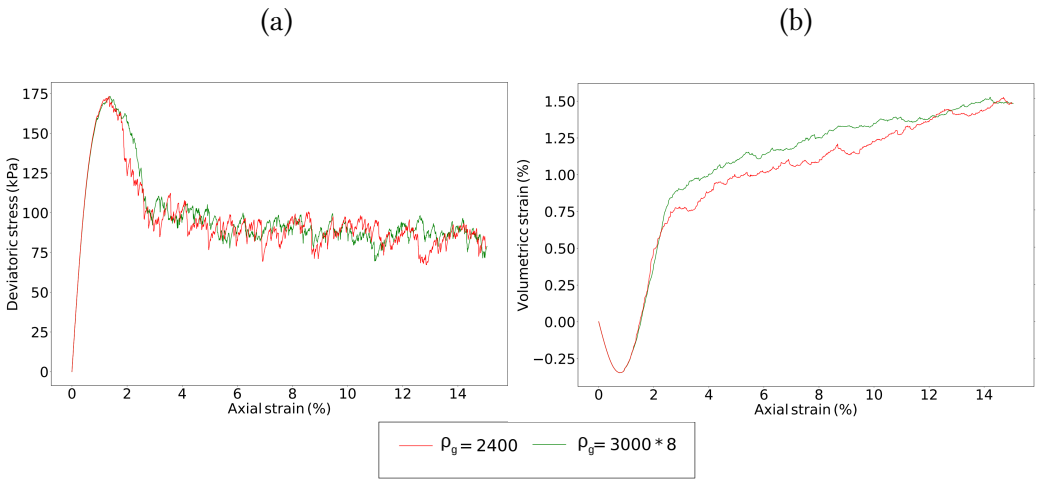

Figure 4.7 – Deviatoric stress (a) and volumetric strain (b) for sample S_1 with a density of $2,400$ kg.m^{-3} (red curves) and for sample S_1 with a density of $3,000 \times 8$ kg.m^{-3} (green curves).

As for energy variations, both samples exhibit the same order of values for plastic dissipation (Figure 4.8(a)), elastic strain energy (Figure 4.8(b)) and kinetic energy (Figure 4.8(c)). However the level of kinetic energy for the sample with a grain density of $2,400$ kg.m^{-3} is a bit lower (see Table 4.4). By counting the number of times the kinetic energy of the sample is exceeding a fixed threshold, the number of potential inertial events is established (Table 4.4). The threshold is fixed at five times the mean kinetic energy of the sample during critical state. The number of potential events is smaller for the sample with the highest grain density. It is due to the fact that more energy is needed to move a heavy grain, so burst may occur a bit less frequently. The values of kinetic energy variations of both samples being the same, the potential events have the same amplitude and are as important in both samples.

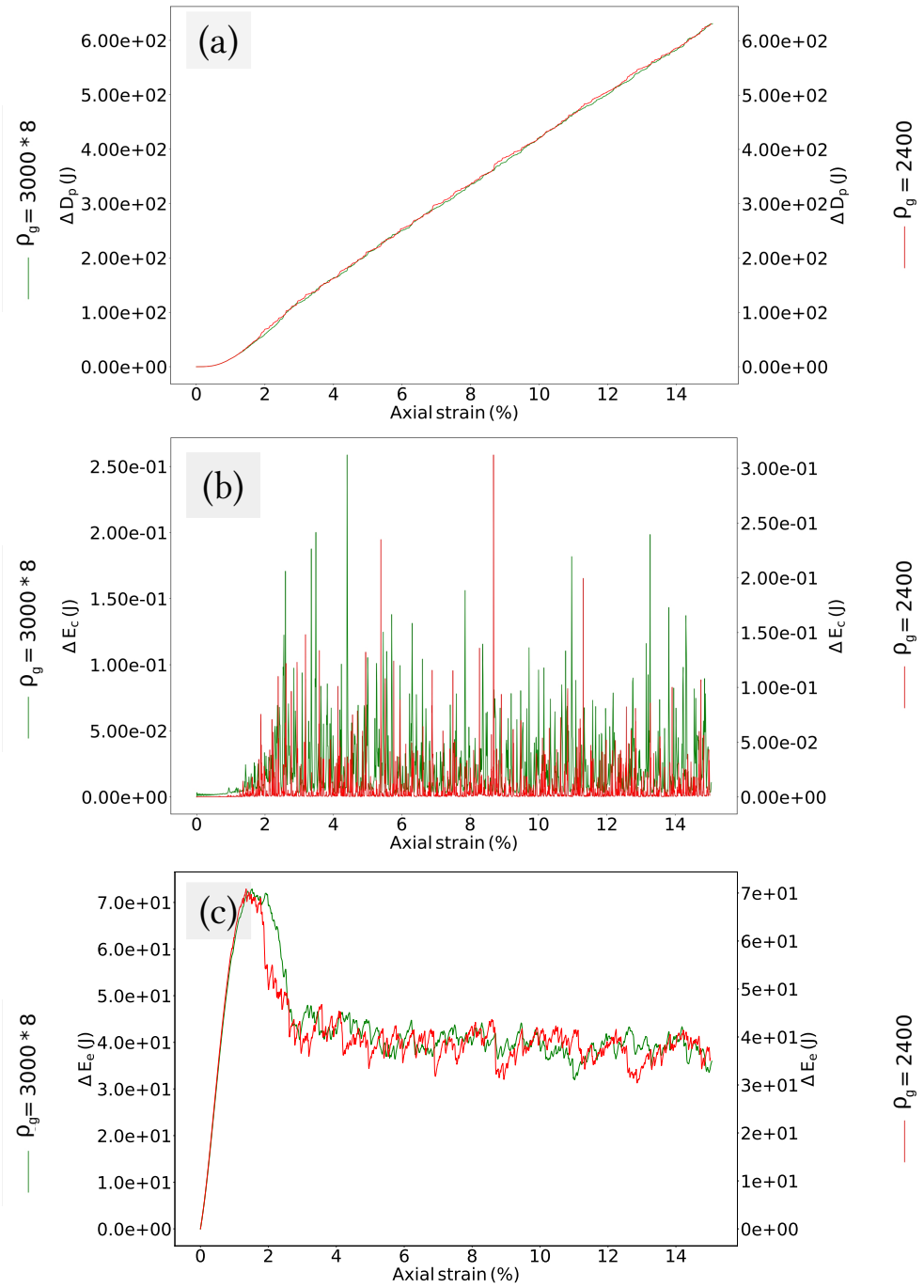

Figure 4.8 – Variation of plastic dissipation (a), kinetic energy (b) and elastic strain energy (c) for sample S_2 with a density of $2,400$ kg.m^{-3} (red curves, values on the left vertical axis) and for sample S_1 with a density of $3,000 \times 8$ kg.m^{-3} (green curves, values on the right vertical axis).

Table 4.4 – Mean kinetic energies and number of potential outburst events for the dense grain comparison.

Parameters	Sample $3,000 \times 8$ kg.m^{-3}	Sample $2,400$ kg.m^{-3}
Mean E_c total	2.1×10^{-2} J	7.4×10^{-3} J
Number of outburst events	154	100

To conclude, in absence of gravity, increasing the grain density of sample S_1 to decrease the time of execution of the simulation has no impact on the mechanical response and no significant impact on the energy variations.

4.2 Analysis of bursts of kinetic energy

4.2.1 Burst definition

With the study of numerous bursts per sample, a lot of data is available. Thus, for the sake of clarity, in this chapter, the results of a single burst of the dense sample S_1 are presented. If not specified otherwise, all the following results are qualitatively similar for other bursts in the same sample and in the other samples S_2. In order to illustrate the similarities (and the limited differences), the results obtained for a burst in the loose sample S_2 are given in the Appendix C.1.

Figure 4.9 shows a reduced time lapse of the burst studied. It shows a typical evolution in time and space of an outburst. Before the burst, the kinetic energy of the spheres is very low. Then the initiation affects few grains whose kinetic energy increases drastically. The burst spreads to about a half of the sample before disappearing. During its initiation, propagation and attenuation, the center of the burst moves sightly on the right of the x-axis but it remains localized in space and time, and does not propagate to the entire sample. Other bursts may propagate less or more than the presented burst, but in all cases, they do not affect the whole sample (which explains limited drops in macro deviatoric stress q). Our aim is to better understand the triggering and propagating mechanisms of a burst. Thus we need to distinguish the area concerned by the burst from the other part of the sample. In Figure 4.9(c), the immediate neighbourhood of the burst is displayed as a red square. This zone is defined manually once for all and it takes into account the location of the initiation and the direction of propagation. For simultaneous bursts with different centers, several boxes are considered in Appendix C.1.

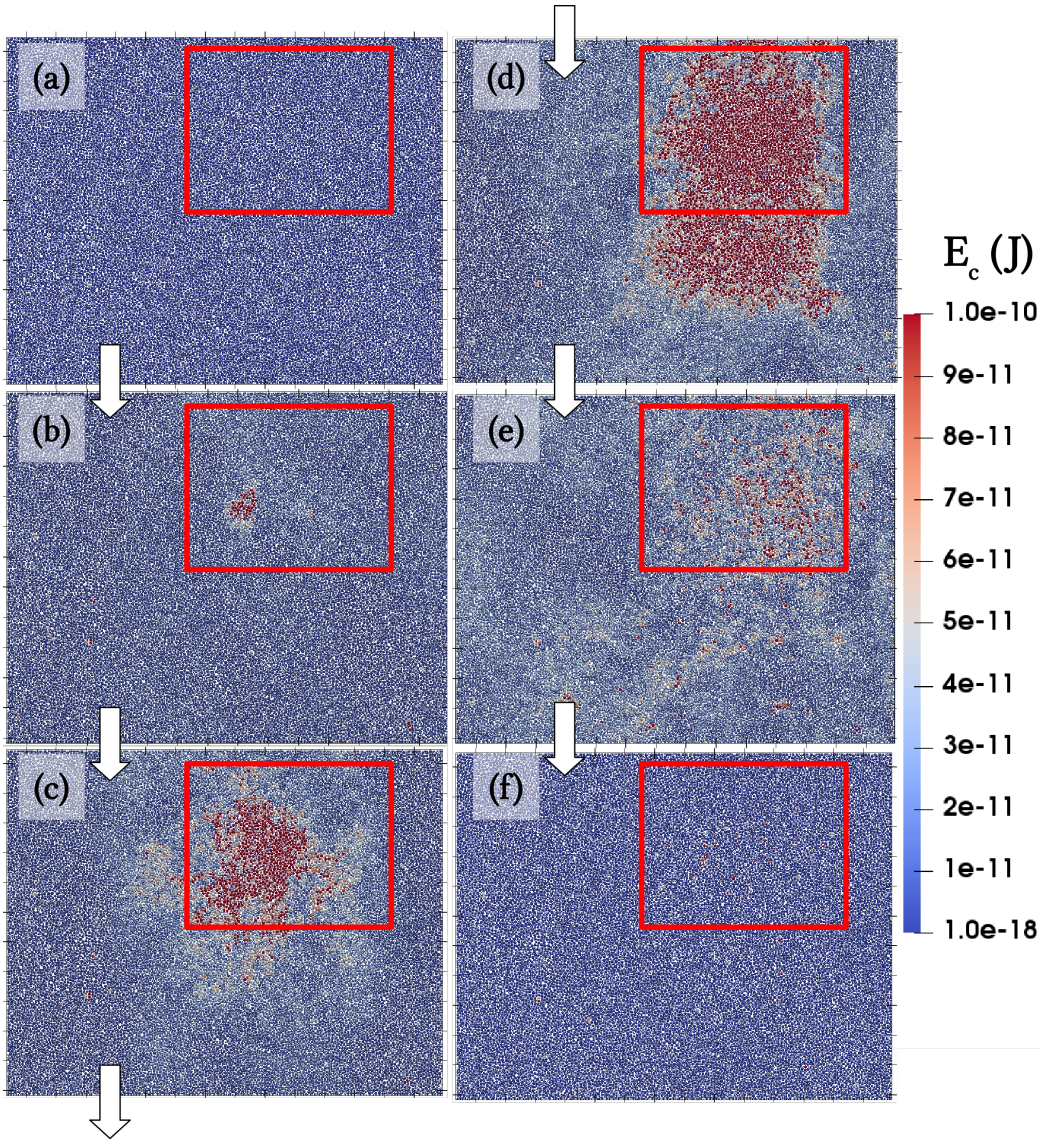

Figure 4.9 – Reduced time lapse of the burst. Particles are coloured according to their kinetic energy expressed in Joule. The bounding box used to provide an approximate definition of the burst domain is displayed in red.

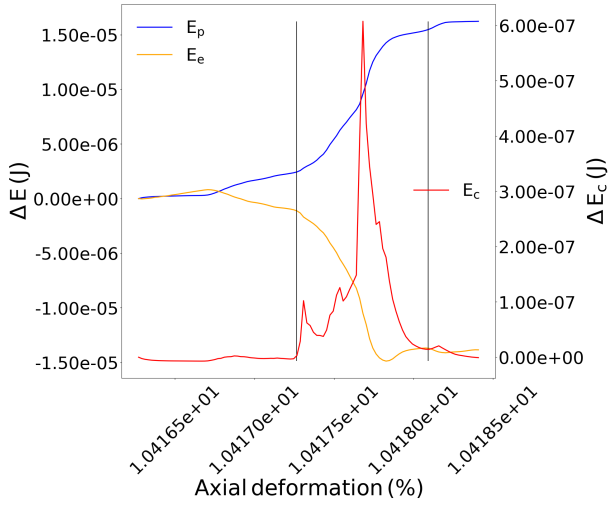

Figure 4.10 – Evolution of the elastic strain energy E_e, the plastic dissipation E_p (on the left y-axis), and the kinetic energy E_c (on the right left y-axis) during the burst of kinetic energy.

The same energy analysis at the scale of the whole sample in Figure 4.5 is done at the burst scale in Figure 4.10. This analysis shows that the kinetic energy variations is only a fraction of the energy variations and exchanges during a burst, at critical state in a drained biaxial test. During the outburst (between vertical lines), the kinetic energy passes through a peak while the elastic strain energy decreases and the plastic dissipation increases (Figure 4.10). The minimum of elastic strain energy is reached at the same moment that kinetic energy is at its maximum, while the end of the plastic dissipation occurs a bit later. From these basic observations, we can deduce that there is an excess in elastic energy stored in the contacts which is then transformed into kinetic energy (translation or rotation of the grains) and also dissipated by friction (slip between the grains at the concidered contacts). As shown by the double axis of Figure 4.10, the variations of plastic dissipation are larger than the variation of kinetic energy. Frictional dissipation remains the main mechanism during an outburst. This is related to the imposed confining pressure and the lack of contractancy (the burst occurs at critical state), where the micro-structure rearranges with no volume change which makes it difficult to have a lot of free grains.

4.2.2 Co-localization of the strain and the bursts of kinetic energy

As seen in Chapter 2, shear band in frictional granular materials is a great subject of interest in many fields and still need research to understand how it develops. Shear band concentrates the deformation, contact rolling and sliding. In the context of localized failure, it is interesting to investigate the potential localization of bursts of kinetic energy.

Mean deviatoric meso-strain is computed from the beginning of the critical state (corresponding to the formation of the shear band, see Section 2.1.2), noted t_i, until the end of the biaxial test t_f. The strain of a loop can be calculated even if the loop (as a meso-domain of spheres in contact) does not exist anymore and the meso-strain definition is given in Equation 3.26. The mean deviatoric meso-strain of a loop l reads :

$$\langle \varepsilon_d \rangle^l_{\Delta t_c} = \frac{\left(\varepsilon^l_I\right)_{\Delta t_c} - \left(\varepsilon^l_{II}\right)_{\Delta t_c}}{\left(\varepsilon_{yy}(t_f) - \varepsilon_{yy}(t_i)\right)_{\Delta t_c}} \tag{4.1}$$

where $\left(\varepsilon^l_I\right)_{\Delta t_c} > \left(\varepsilon^l_{II}\right)_{\Delta t_c}$ are eigen values of the meso-strain tensor $\boldsymbol{\varepsilon}_l$ computed during $t_f - t_i$, ε_{yy} the axial strain sample scale.

As expected from the aspect ratio of samples S_1 and S_2 and according to Liu (2018), no shear band in the dense sample S_1 is observed (Figure 4.11). The dense sample S_2 exhibits strain localization (Figure 4.12(a)). The loose sample S_2 which does not present a shear band, stands as a comparison (Figure 4.12(b)). In the dense sample S_2, a second and smaller shear band is obeserved, reflecting in the left corner.

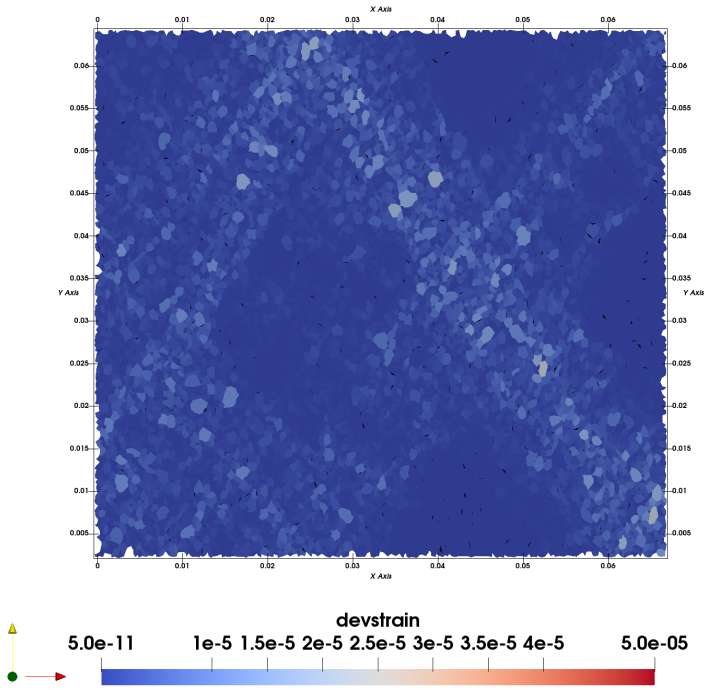

Figure 4.11 – Mean deviatoric strain field for the dense sample S_1. The meso-mean deviatoric strain map of the sample ressembles the one given for a sample of the same aspect ratio in (Liu, 2018).

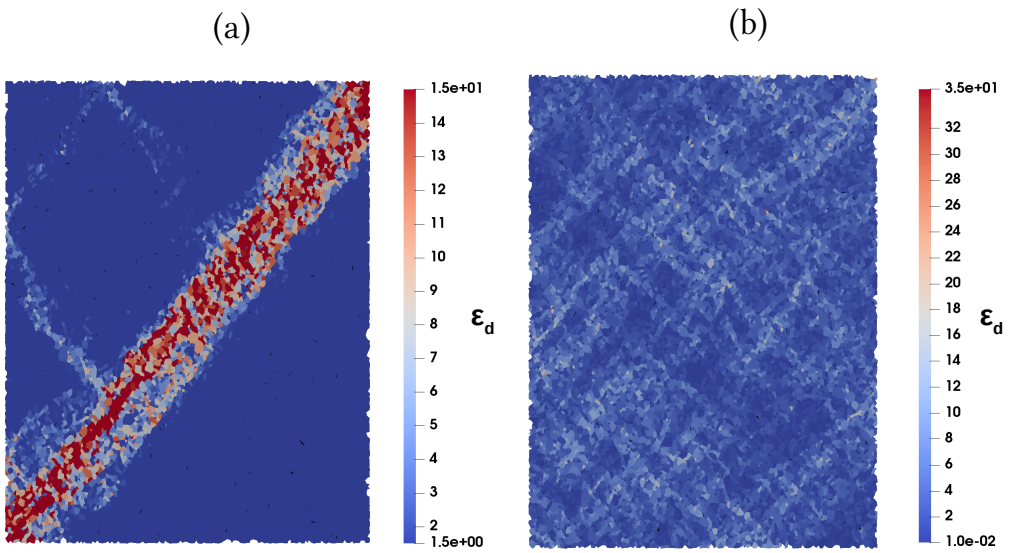

Figure 4.12 – Mean deviatoric strain for the dense sample S_2 (a) and the loose sample S_2 (b). A main diagonal shear band is observed in the dense sample S_2, with even a second small shear band reflecting in the left corner.

Similary to the mean meso-strain, the mean kinetic meso-energy is computed as the mean kinetic energy of the spheres over the critical state, inside a loop which exists at the beginning of the critical state. Thus, the same partition of the mean quantities (kinetic energy and strain) are obtained. The mean kinetic meso-energy of a loop l during Δt_c relies on the partition definition of the kinetic meso-energy (Equation 3.12), and it reads :

$$\langle E_c \rangle^l_{\Delta t_c} = \sum_{p=1}^{N_p} \frac{\left| (V_p)_{t_i} \cap (\Omega_l)_{t_i} \right|}{\left| (\Omega_l)_{t_i} \right|} \langle E_c^p \rangle_{\Delta t_c} \tag{4.2}$$

where N_p is the number of spheres in the loop at the time t_i, $(\Omega_l)_{t_i}$ the domain of the loop at the time t_i, $(V_p)_{t_i} \cap (\Omega_l)_{t_i}$ the portion of the sphere p inside the domain $(\Omega_l)_{t_i}$ and $\langle E_c^p \rangle$ is the mean kinetic energy of the sphere p. Rattlers are not considered.

The mean meso-strain maps for the dense and loose samples S_2 are given in Figure 4.13. The localization of the mean kinetic meso-energy in the same area as the mean deviatoric meso-strain is clear (Figure 4.13(a) and Figure 4.12(a)). A small reflecting secondary band is also visible : in the reflexion with the upper wall and in the join with the main shear band on the bottom left. On the contrary, no localization of the kinetic energy is visible for the loose sample S_2 (Figure 4.13(b)).

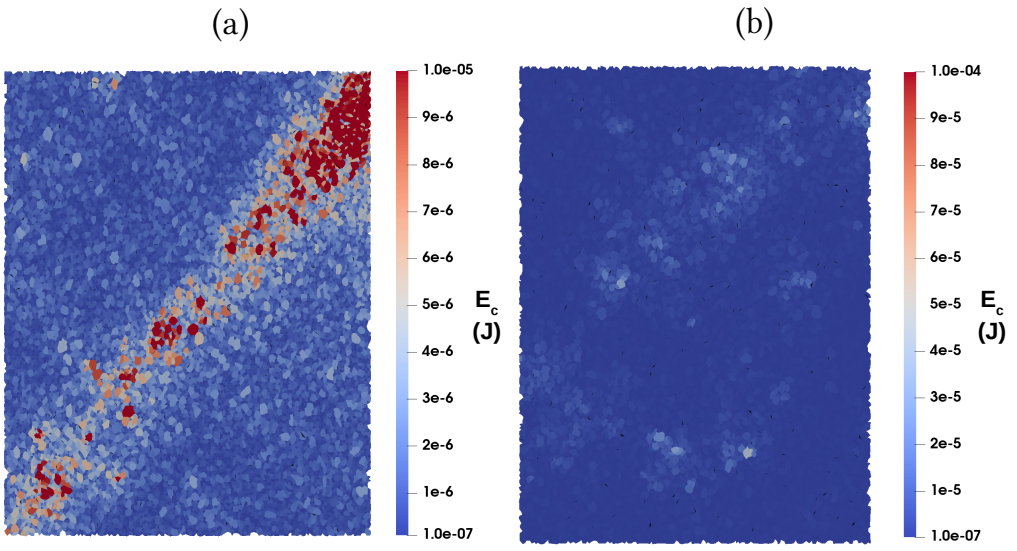

Figure 4.13 – Mean kinetic meso-energy for the dense sample S_2 (a) and the loose sample S_2 (b).

Thus, kinetic energy is co-localized in the same area as strain, and bursts of kinetic energy only initiate and propagate in the shear band. If Figure 4.12(a) and Figure 4.13(a) are compared, one can see the width of the shear band as defined with loops of incremental deviatoric strain larger than the mean value coincides with the with band defined from the grains with larger kinetic energy with respect to the mean value. In Figure 4.14 and in Figure 4.15, the shear band is kept as a background by displaying the loops with large incremental deviatoric strains (light blue to red color scale). The spheres with kinetic energy larger than 10 times the mean kinetic energy per grain during the critical state (Table 4.3) are superimposed in black. Figure 4.14 illustrates that bursts only occur inside the shear band and their expanfing outside the shear band is scarce. Futhermore, very large bursts that escape from the shear band domain, propagate in one side of the shear band and do not cross it. Figure 4.15 gives a time lapse of a burst occuring in the top right corner and propagating only *below* the shear band.

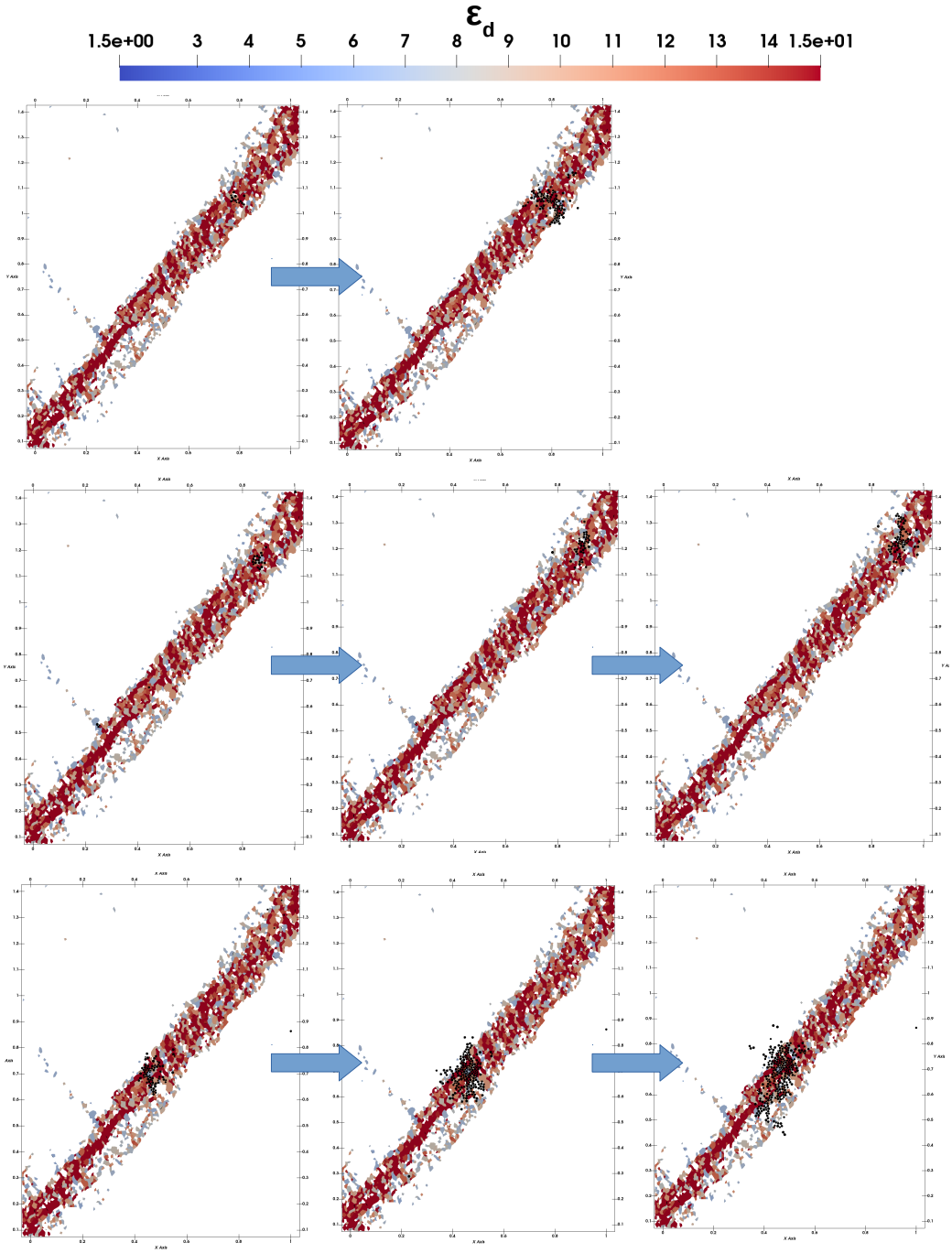

Figure 4.14 – Three examples of burst of kinetic energy originating only from inside the shear band. Only spheres the kinetic energy of which is above the burst criterion are displayed in black. For more visual clarity, only loop belonging to the shear band are displayed.

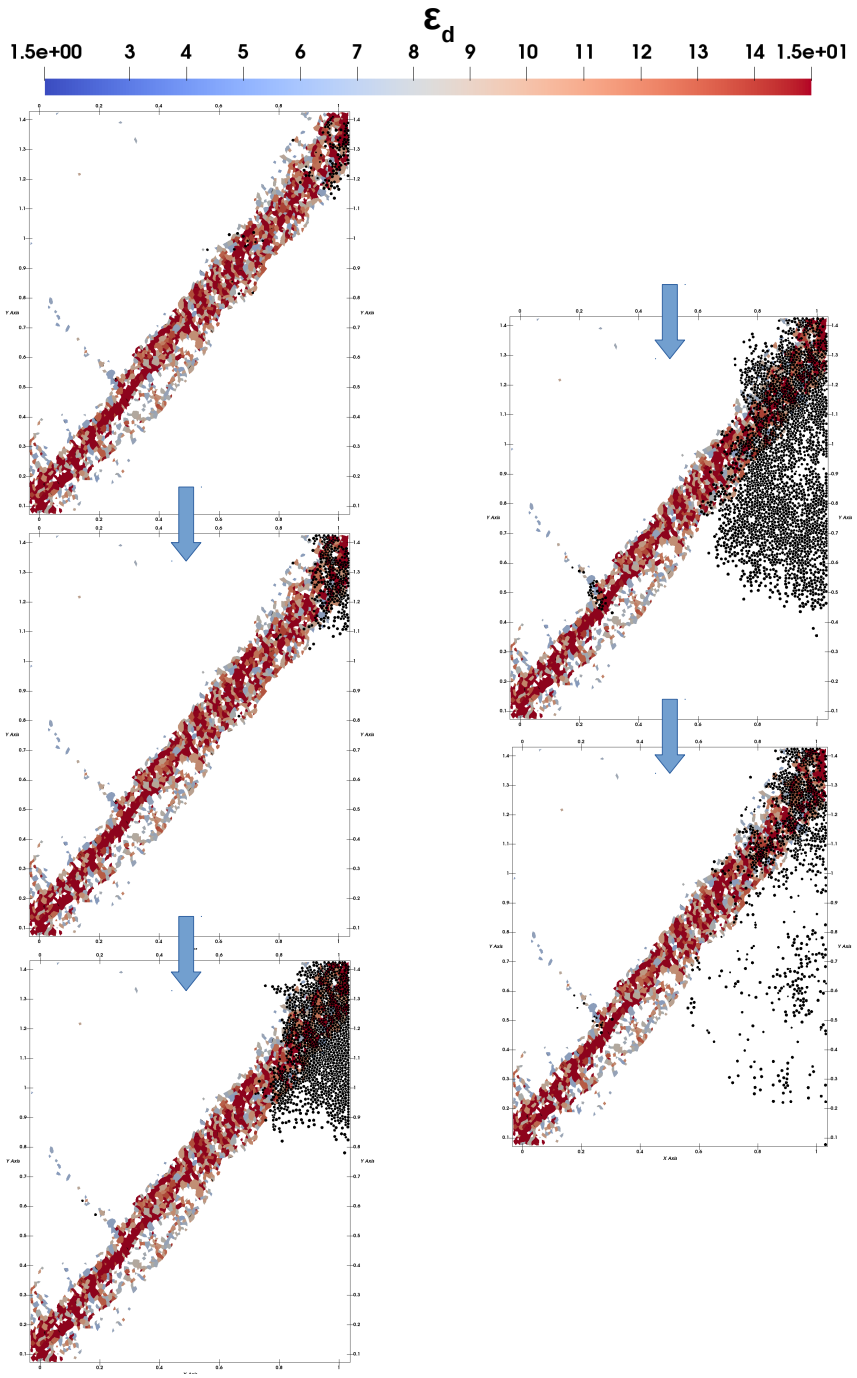

Figure 4.15 – Time lapse of a large burst occuring in the top right corner and propagating only in the part of the sample at the right of the shear band. Only spheres the kinetic energy of which is above the burst criterion are displayed in black.

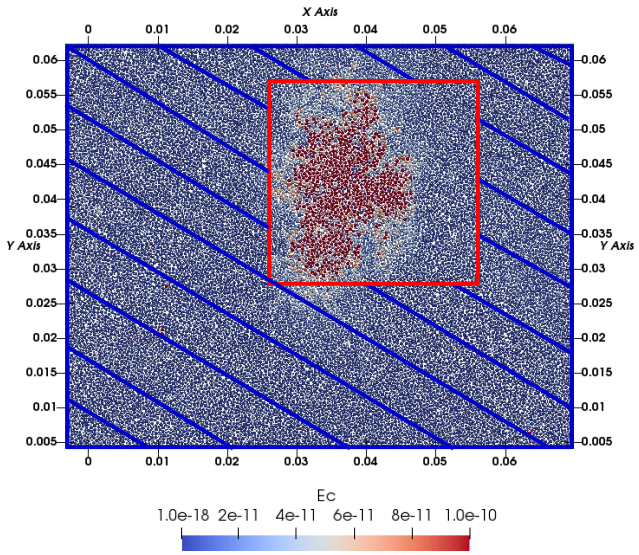

Figure 4.16 – Different zones for the analysis. The burst area is displayed in red (iner domain), as in Figure 4.9. The rest of the sample (outter domain) is displayed with blue hatching.

As a conclusion, in a sample with a localized deviatoric strain, bursts originate only from inside the shear band. If the burst of kinetic energy is large enough, it will escape only on one side of the shear band. The analysis could be pushed further.

4.2.3 Micro-structure precursors

Energy analyses are only a first step in order to identify the origins of outbursts. there is a need to identify precursors in order to understand the localisation of the burst in a specific area. In order to do this, we compare the micro-structure in the burst domain to the region where the burst does not propagate. The *inner* and *outter* domains are displayed in Figure 4.16.

Sliding index

The sliding index I_p for each contact, as defined in Section 2.3.2, is a suitable precursor candidate at the contact scale. The probability densities of I_p computed from contacts in the inner and outter domains of the burst (see Figure 4.16) are given in Figure 4.17. Before the burst (Figure 4.17(a)), there are more contacts close to sliding (I_p close to 1) inside the burst area than outside. Moreover the outter domain contains much more stable contacts (I_p

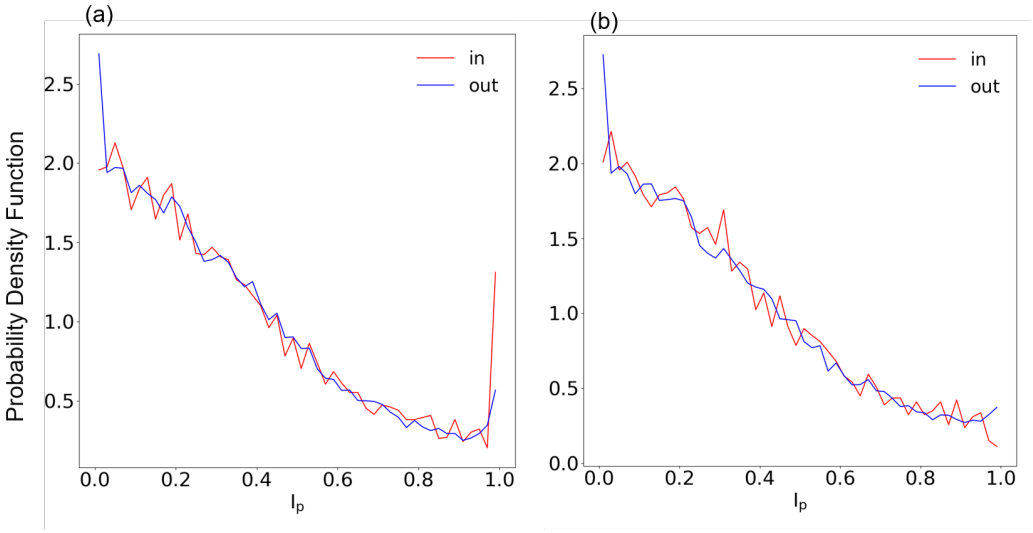

Figure 4.17 – Sliding Index's propability density before (a) and after (b) the burst of kinetic energy in the inner domain (red) and the outter domain (blue) the burst area.

close to 0). After the occurrence of the burst, the tail of the I_p probability function has dropped for the contacts inside (Figure 4.17(b)). The burst area has even a lower probability to contain unstable contacts than the outter domain. Thus, I_p close to 1 is a necessary condition to observe outbursts in a specific area, which supports the idea already underlined in Wautier et al. (2018b). This result also contributes to a rational delimitation of the burst domain. There is a strong contrast between the behaviour of grains in the inner and the outter domains. The outburst is rooted in a zone with a high level of elastic energy storage and contacts close to their sliding limit.

Porosity at mesoscopic scale

In addition to sliding index related to the grain scale, meso-structures can be a mean to bring structural and micro-changes out. In the next sections, meso-structures as grain loops are studied to better understand how the micro-structure rearranges during the outburst.

The porosity for the inner and outter domains is given in Figure 4.18. The porosity is computed from the effective porosity of the loops (Equation 3.8) weighted by their surface area. Thus, it gives more weight to the high order loops which are responsible for the porosity. The effective weighted

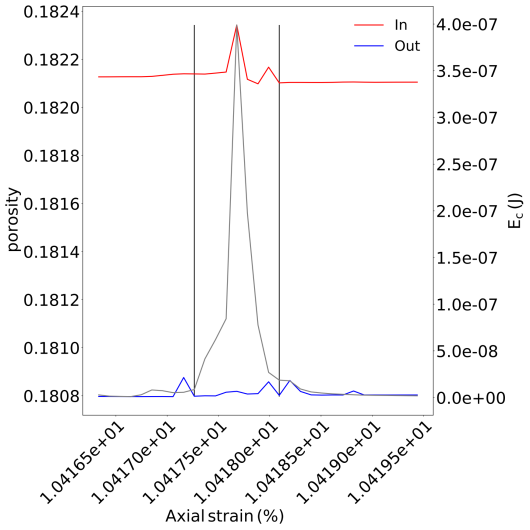

Figure 4.18 – Porosity in the inner (red) and the outter (blue) domains. The kinetic energy is displayed (in grey) to compare the evolution of the porosity according to the evolution of the burst.

porosity reads:

$$\varphi = \frac{1}{|\Omega|} \sum_{l \in \Omega} p_l^{eff} |\Omega_l| \tag{4.3}$$

where Ω is the zone of interest (i.e. burst area), p_l^{eff} the effective porosity of the loop l as noted in Equation 3.8 and $|\Omega_l|$ the area of the loop domain l ($|\Omega_l| = \sum_{l \in \Omega} |\Omega_p|$) .

As seen in Figure 4.18, the inner domain of the burst of kinetic energy presents a looser micro-structure than the outter domain. During the burst of kinetic energy occurrence, the porosity of the inner domain has a slight increase, whereas it is nearly constant in the outter domain, underlining the localized meso-structure changes inside the burst area. During the burst of kinetic energy in the sample S_2, the porosity decreases inside the inner domain, while in the outter domain no significant changes are observed (Figure 4.18). The evolution of the inner domain curve is not the same in the sample S_1 than S_2. This difference will be explained later. However, both porosity changes are localized in the inner domain and during the burst life time. Thus the burst develops inside a domain which is slightly looser on average in comparison to the outter the domain.

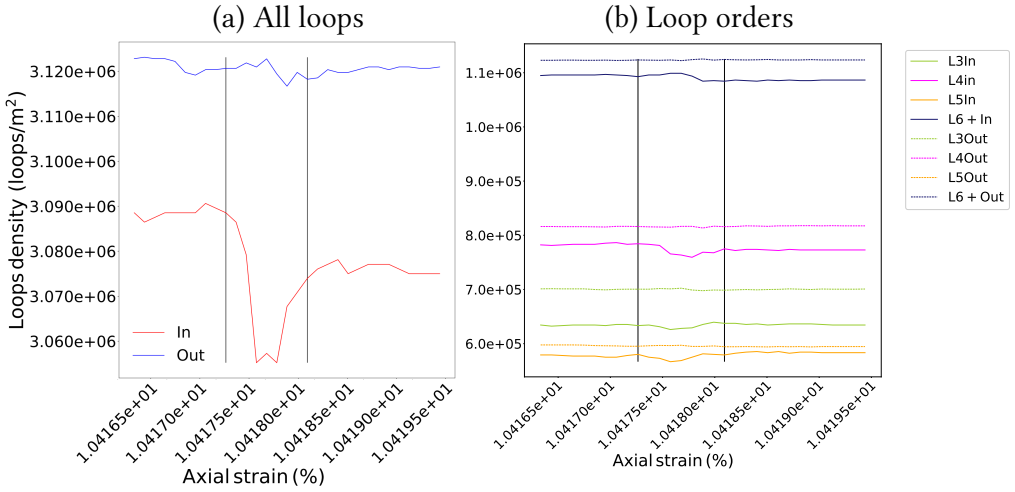

Figure 4.19 – Loops densities comparison between the inner and outter domains. (a) Loop densities computed with all loop orders (b) loop densities per loop order. For both graphs, the kinetic energy is displayed to relate the evolution of the porosity to the propagation of the burst.

To complete the analysis, the density of loops (number of loop of the same order per unit area) for the inner and outter domains is computed (Figure 4.19). The loop density is smaller in the inner burst domain than in the outter domain, and decreases during the increase in kinetic energy. The same results are obtained for the sample S_2 (Figure C.6). In Figure 4.19(b), the loop density for each loop order is compared between the inner and outter burst domains. The inside loop density is smaller for each order. However, the gap between the inside and outside loop densities is small and their evolutions are marginal. The burst area keeps a meso-structure similar to the outter domain, and the composition of the meso-structure is consistent with the one given in Figure 4.4. Inside the burst domain, the combination of larger porosity and smaller loop densities for all grain loop categories suggests that loops are larger inside the burst domain. In other words, it means the high order loops are larger (mainly L6+) since low order loops configurations (L3, L4) can not vary much. To summarize, the burst inner domain is more porous, with bigger high order loops.

While focusing on high order loops, the mean real and the mean effective porosities are compared for the inner and outter domains (Figure 4.20). As suggested by our previous analysis on the weighted effective porosity, the

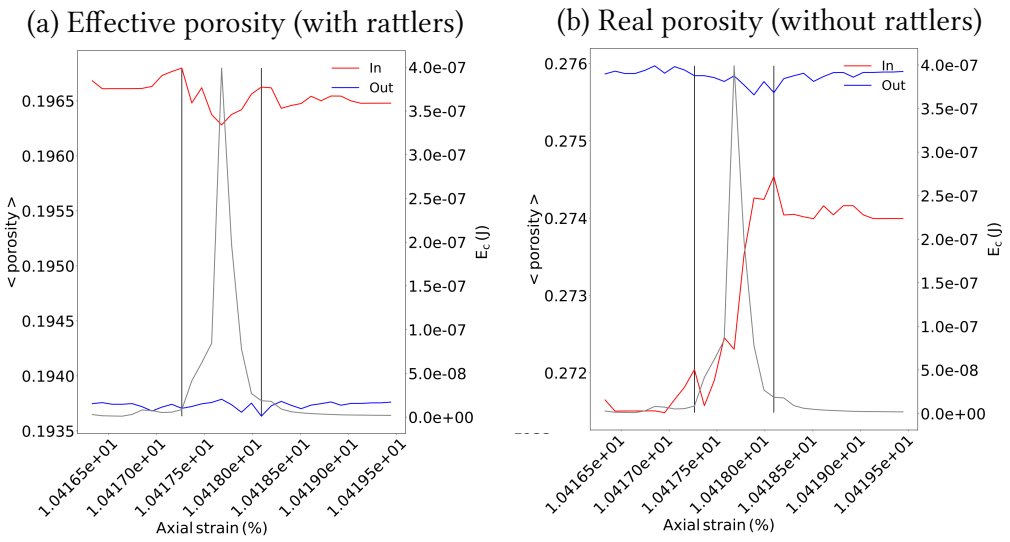

Figure 4.20 – (a) Mean effective porosity and (b) mean real porosity for high order of loops iin the inner and outter burst domain. The kinetic energy is displayed to relate the evolution of the porosity to the propagation of the burst.

mean effective porosity inside the domain of the burst is higher than outside (Figure 4.20(a)). However, considering the real porosity, the outside domain is looser (Figure 4.20(b)). These two results suggest that the high order loops in the inner domain contain less rattlers than in the outter domain, which result in a larger loop deformability. Knowing that rattlers play an important role in mechanical stability (Wautier et al., 2019; Wang et al., 2021), this result highlights that the meso-structures in the inner domain are more prone to mechanical instability. The small drop in the mean effective porosity and the small increase in the mean real porosity inside show that the high order loops get enriched of rattlers during the outburst. This first observation on high order loops containing less rattlers inside the burst domain is not found back in the sample S_2 (Figure C.11). On the contrary, the evolution of the mean real and mean effective porosities for high order loops indicates that the inner domain contains more rattlers. However, they do get enriched in rattlers during the outburst. To conclude, the proportion of rattlers contained in high order loops can not be a criterion for the occurence of the burst. The difference between the two samples can be explained by their grain size distribution and their density. It is a point which needs further investigation.

Statistical noise makes the inner / outter domain comparison analysis questionnable. It could be suggested that comparing areas of the same size is more significant. However, this comparison is far from being easy. Eventually, the choice of the outter domain may not be revelant, but it gives an overall state of the sample and really highlights the localization of a burst in a specific domain and not everywhere else.

To conclude, a common criterion for the occurence of a burst of kinetic energy is that the related domain is looser and contains larger meso-loops (i.e. high order loops). The difference in the porosity and size of high order loops is reduced if the analysis is carried out for few percents of axial strain latter in the same area, provided that there is not other bursts occurring or about to occur in this area.

4.2.4 Meso-structure reorganizations

In this part, the qualitative evolution of meso-structures is studied during the burst of kinetic energy, inside and outside the burst area.

Evolution of meso-structures during the burst of kinetic energy and surviving rates

First, the relative evolution of each loop order categories is studied. The expression of the relative evolution is given in Section 2.3.2. Figure 4.21(a) shows the changes inside the burst area for the four main order loops. There is about the same loss and gain amounts for each order of loops and this amount is not zero during the burst (between the vertical lines in Figure 4.21(a). This observation complements the flat evolution of the loop density in the inner domain given in Figure 4.19(b). Thus, the meso-structures population remains statically stable despite changes due to reorganisations in the contacts during the burst occurrence. The 6+ order loops are created and lost with the same proportions at the same time and they are the most affected meso-structures. However we can notice that the 3, 4 and 5 order grain loops present a dissymmetry in the "gain" and "loss" curves : loops are broken first (peak of lost loops before the maximum of kinetic energy) and then created (peak of gain loops after the maximum of kinetic energy). In conclusion, the lowest order loops are transformed into the highest order loops before the peak of kinetic energy and then created back while the highest order loops are constantly being created and destroyed during the outburst of kinetic energy.

Figure 4.21(b) shows the relative evolution of rattlers during the burst appearance in the inner domain. The maximum and minimum relative evo-

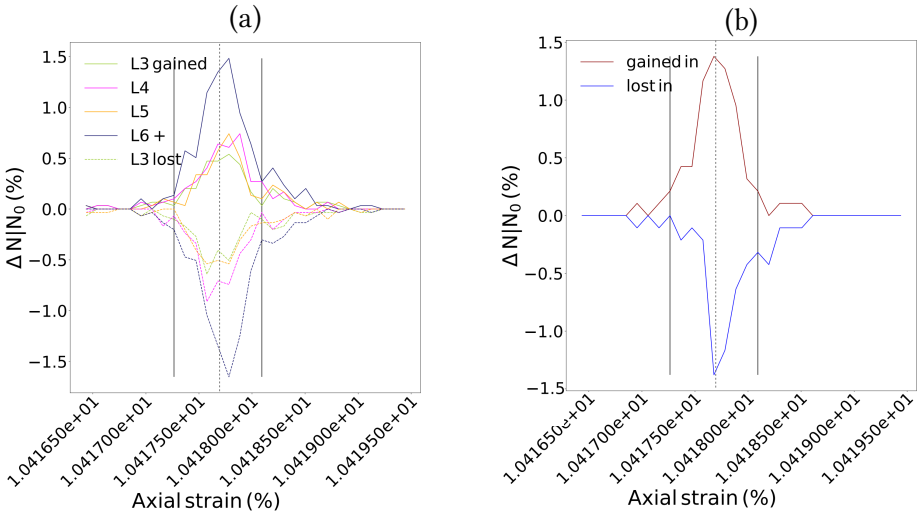

Figure 4.21 – Relative variation of the number of grain loops (a) and rattlers (b) in the inner domain compared with the corresponding numbers N_0 before the occurence of the burst. The vertical dotted lines stand for the maximum of kinetic energy during the burst, as in Figures of the previous section 4.2.3

lutions are not reached simultaneously, which means that the rattlers are first generated and then lost. This observation matches with the ones for the grain loops. Before the peak of kinetic energy, a significant amount of low order loops are broken, thus creating rattlers. L6+ loops in the burst area contain rattlers and their breakage may also free some rattlers, even though they may be used for building new loops (Wautier et al., 2019). When kinetic energy decreases, rattlers are used to create low order loops. In the outter domain, no significant trends can be highlighted, neither in rattlers (Figure 4.22(b)) nor in grain loops evolutions (Figure 4.22(a)). Figure 4.21 and Figure 4.22 show that meso-structure populations evolve only inside the burst domain. We assume that once the meso-structure population stabilizes, the kinetic energy starts dissipating. In other terms, the percentage of changes in the meso-structure is correlated with the level of kinetic energy.

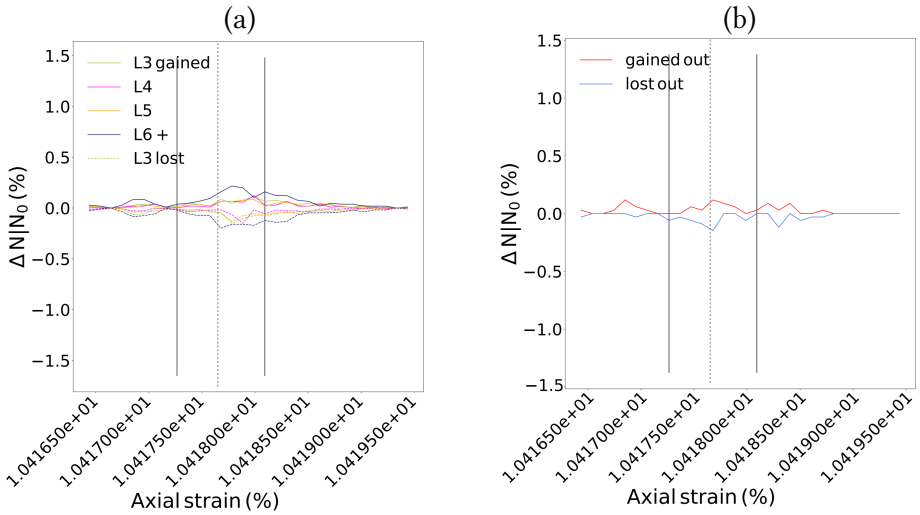

Figure 4.22 – Relative variation of the numbers of grain loops (a) and rattlers (b) in the outter domain compared with the corresponding numbers N_0 before the occurence of the burst. The vertical dotted lines stand for the maximum of kinetic energy during the burst.

Meso-structure surviving rates

Secondly, the surviving rate is studied for the four main order loops during the burst of kinetic energy, inside and outside the burst area. As explained in Chapter 2.3.2, the surviving rate measures qualitatively how many structures have persisted from a reference state. The nature of the meso-structure at a given axial strain is compared to the one at the beginning of the window of observation (before the onset of the burst of kinetic energy). In the inner domain, there is an important drop in the surviving rate of all the grain loops (Figure 4.23(a)). After the burst, 22% of L6+ loops existing before the burst have disappeared, which is the highest percentage. Lower order loop exhibit a slightly higher percentage of survival rates. This ranking underlines once more the fact that L6+ loops are more involved in the micro-structure changes during the kinetic energy outburst. At the end of the outburst, the area is stabilized as the surviving rates do not decrease after the burst and exhibit a plateau. The new micro-structure is stable enough not to change immediately after the burst, at least inside this area. Outside the burst area, there is not a huge drop, and thus, not such a percentage of changes among the meso-structures (only 2%) (Figure 4.23(b)). This is consistent with the flat relative evolution of the meso-structures in the outter

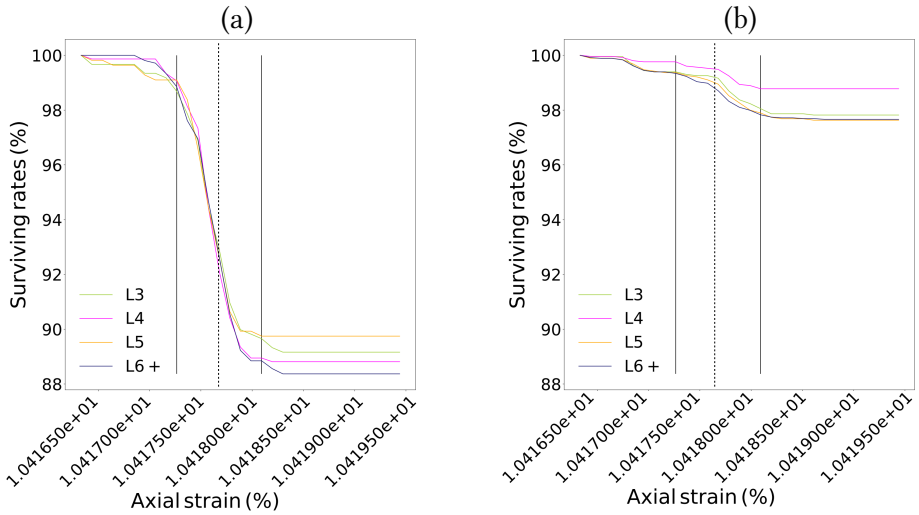

Figure 4.23 – Surviving rates for the four main grain loop orders (a) in the inner and (b) the outter domains. The vertical dotted lines stand for the maximum of kinetic energy during the burst.

domain (section 4.2.4). The changes in the micro- and meso-structures are concentrated in the inner burst domain. However bursts of kinetic energy influence meso-structure reorganization even far from its neighbourhood (in the outter domain). Indeed, in the mid of the outburst, which corresponds to the peak of kinetic energy, the curves in Figure 4.23(b) display a change in their steepness. The outter domain is influenced by the propagation of the outburst and gives rise to some micro-structural reorganization. The micro-structure is rearranging to cope with the inertial instability and thus, surviving rates decreases (surviving rates slope increases) for all loop order categories.

Identifying changes at the microscopic scale can be done from the study of different evolution patterns of the meso-domains. By studying meso-structures, it is possible to highlight changes in the burst area and understand the mechanisms of reorganisation of the micro-structure undergone during a burst of kinetic energy.

4.3 Second-order meso-work insights during bursts of kinetic energy

As recalled in section 2.1, the second-order work criterion is used for judging, under certain conditions, whether a system can develop kinetic energy under external disturbance. In this section and thanks to the tools developed in Chapter 3.3 at the meso-scale, the variations of the different formulations of the internal second-order mesoscopic work are computed (Equation 3.20). For the next sections, meso-stress and meso-strain are calculated during macroscopic increments of axial strain of $1E-6$. From now on, to avoid excessive heaviness in the labelling, the internal second-order mesocopic work is named second-order mesoscopic work or second-order meso-work.

4.3.1 Grain averaged second-order mesoscopic work evolution

Spatial homogenization of the grain averaged meso-stress

In Chapter 3, the partition view of the meso-stress was defined (the grain averaged meso-stress). In Figure 4.24, each component of the macroscopic stress is compared to the corresponding component of the weighted average of grain averaged meso-stress, in order to check the consistency between the macro-scale stress definition and the spatial homogenization of the proposed meso-stress definition. In the weighted average computation, a loop contributes for its fraction area of the total sample domain. The comparison is made for the whole sample domain and over all the biaxial test. The dotted lines represent the components of the sum of the weighted average meso-stress, while solid lines represent the components of the macro-stress. The components of the weighted average meso-stress agree very well with the evolution of each corresponding macro-component. The proposed grain averaged meso-stress definition is compatible with the macro-stress through a spatial averaging.

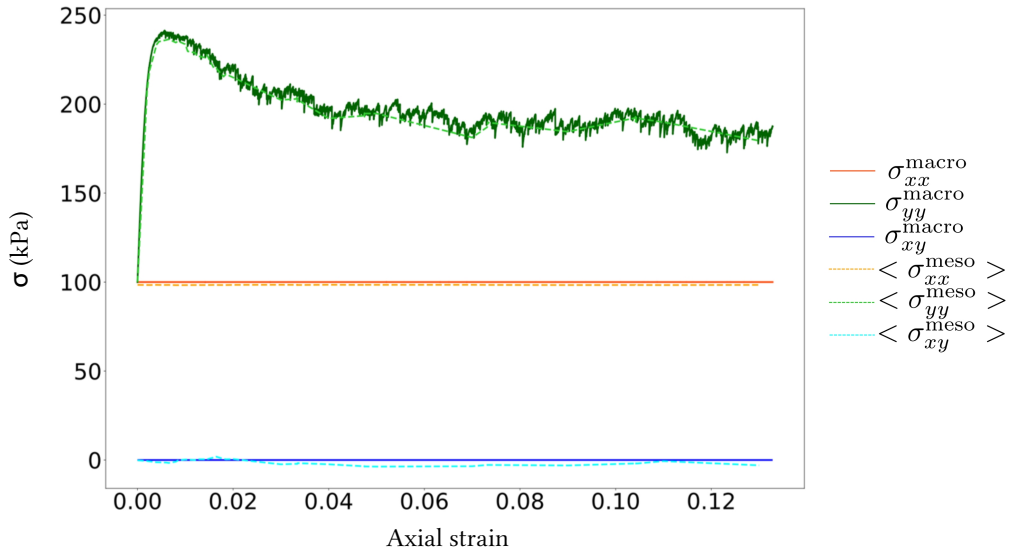

Figure 4.24 – Comparison between the macroscopic stress σ^{macro} and the weighted average of the grain averaged mesoscopic stress $\langle \sigma^m \rangle$

Evolution during a burst of kinetic energy

In this section, the second-order mesoscopic work is computed from the meso-strain (Equation 3.26) and the grain averaged meso-stress definition (Equation 3.36). It will be noted W_2^m.

In Figure 4.25, the spatial distribution of grain averaged second-order mesoscopic work during the propagation of the burst is displayed. Each panel in Figure 4.25 corresponds to the same labelled panel in Figure 4.9, with the exception of the panel $(*)$ that corresponds to an additional step prior to the detection of the burst of kinetic energy. The variations of the grain averaged meso-stress (negative or positive) are in line with the variations of the kinetic energy, with wider borders and distinct limits. The loops corresponding to the center of the burst, that is to say the kinetic energy of which is the highest (Figure 4.9), exhibits negative values at the onset of the burst (panel (b) of Figure 4.25). The extra panel $(*)$ suggests that the instability results from a perturbation initiated in the right lower corner. This is still visible in the panel (b). Thus, the variations of the grain averaged second-order meso-work can provide additional information on the origins of the burst. In conclusion, large absolute values of second-order meso-work correlate with the variations of kinetic energy and can reveal additional details prior to the detection of the burst of kinetic energy (if there is any). It enables to see the nucleation of the burst in advance and stands therefore as a precursor.

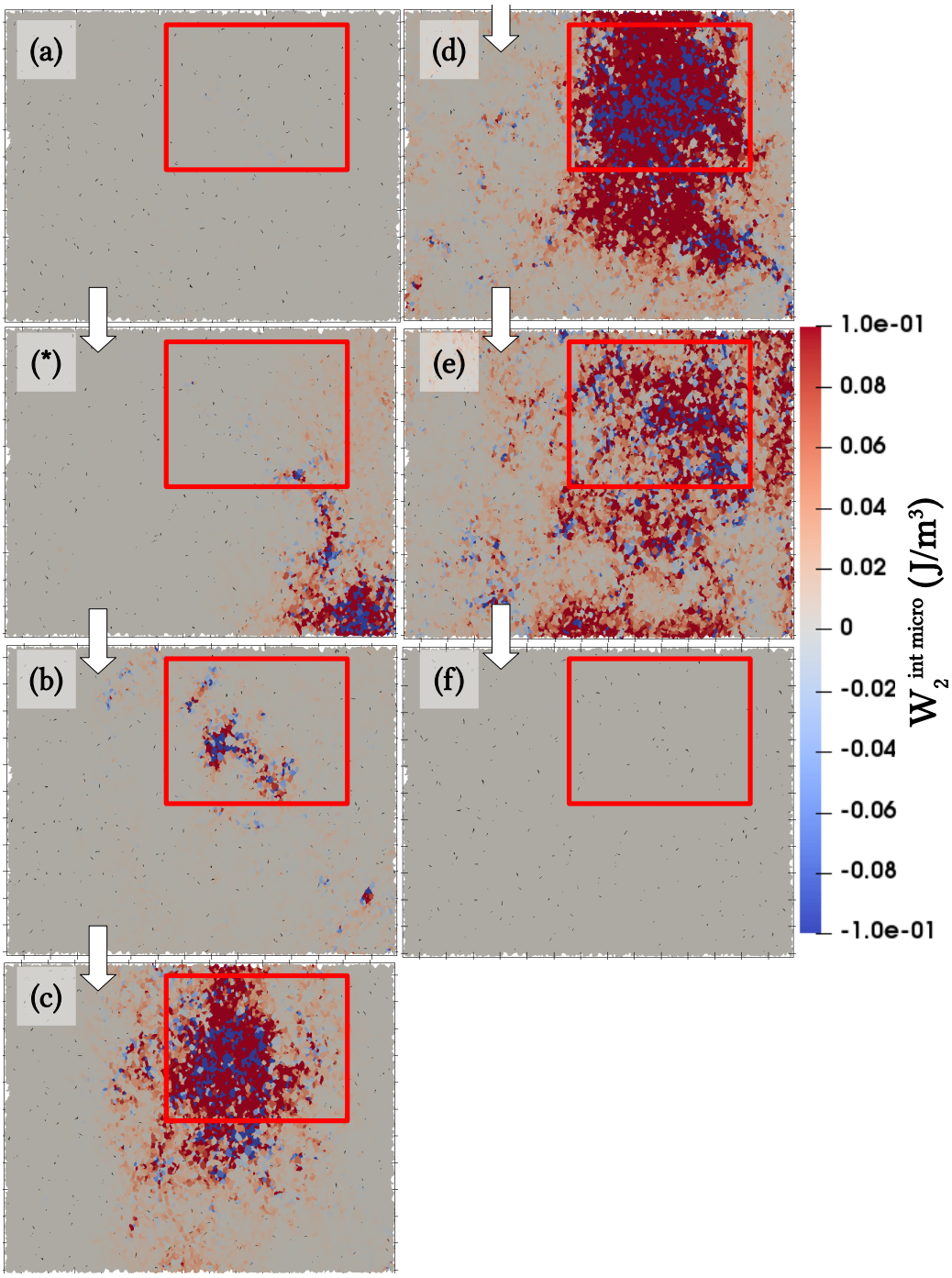

Figure 4.25 – Reduced time sequence of second-order mesoscopic work W_2^m. (a) (b) (c) (d) (e) (f) correspond to the same steps in Figure 4.9 while (*) corresponds to an additional step between (a) and (b).

One can notice that the whole burst area does not exhibit negative second-order meso-work works. Negative and positive second-order meso-work works are observed next to each other. In order to assess the predominance of negative or positive second-order meso-work work in the burst area, the volume weighted average second-order work $\langle W_2^{int} \rangle_\Omega$ is computed over the burst domain Ω :

$$\left\langle W_2^{int} \right\rangle_\Omega = \frac{1}{\sum_{l \in \Omega} |\Omega_l|} \sum_{l \in \Omega} |\Omega_l| \, {W_2^m}_l \tag{4.4}$$

with l reffering to loops inside the area of interest Ω.

Its evolution inside and outside the outburst area is given in Figure 3.5. $\langle W_2 \rangle_\Omega$ is negative only at the nucleation of the burst. It increases with positive values during the burst and then returns to its almost null pre-burst value. On the contrary, The outside domain shows no negative values. The vanishing of $\langle W_2 \rangle_\Omega$ just before the release of kinetic energy can be seen as a signature of underlying mechanical instability in the burst domain. The following increase shows the active and rapid reorganisations of the microstructure, underlined in the previous sections (section 4.2.4). Thus, these reorganizations allow a quick restabilization of the burst domain and prevent the burst from propagating to the entire sample. As a result, the burst subsides and remains localized.

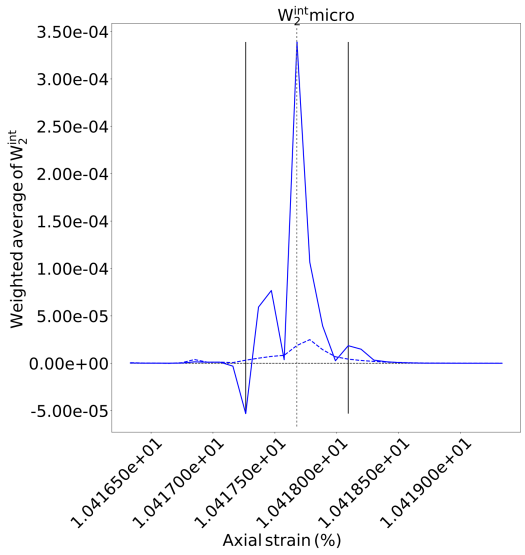

Figure 4.26 – Volume weighted average of the second-order meso-work W_2^m during the burst of kinetic energy, in the neighbour of the initiation of the burst. The peak of kinetic energy is marked with the grey dash-dot vertical line. The dashed blue line is the evolution of the weighted average of the second-order meso-work W_2^m outside the burst domain, as a reference. The two vertical solid lines correspond to the initiation and the end of the burst of kinetic energy.

4.3.2 Definition based on Bagi and Weber formulation of the stress

The formulations of the meso-stress chosen in this section to compute the second-order meso-work are the Bagi meso-stress definition (Equation 3.41) and the Weber meso-stress definition (Equation 3.42). Note that these alternative meso-stress definitions remain consistent with the macroscopic stress definition through spatial averaging as the well known Love-Weber equation is recovered at the sample scale (the Bagi correction term corresponding to boundary forces became negligeable as soon as the number of grains become large).The resulting second order meso-works are noted respectively W_2^{Bagi} and W_2^{Weber}.

Figures 4.27 and 4.28 represent the reduced time sequence for respectively W_2^{Bagi} and W_2^{Weber}. The variations of both meso-stresses are in line with the kinetic energy evolution, negative and positive values are exhibited along each other. The variations of W_2^{Weber} are of the same order of W_2^m, but concern less meso-domains (smaller spatial expansion). The variations of W_2^{Bagi} are one order of magnitude greater which is consistent with the fact that the meso-Bagi stress is greater than the meso-Weber stress (due to additional boundary terms in the definition). Similary, but not exactly as for the variations of the grain averaged second-order mesoscopic work W_2^m, the panels (*) of Figures 4.27 and 4.28 give some details on the origins of the burst.

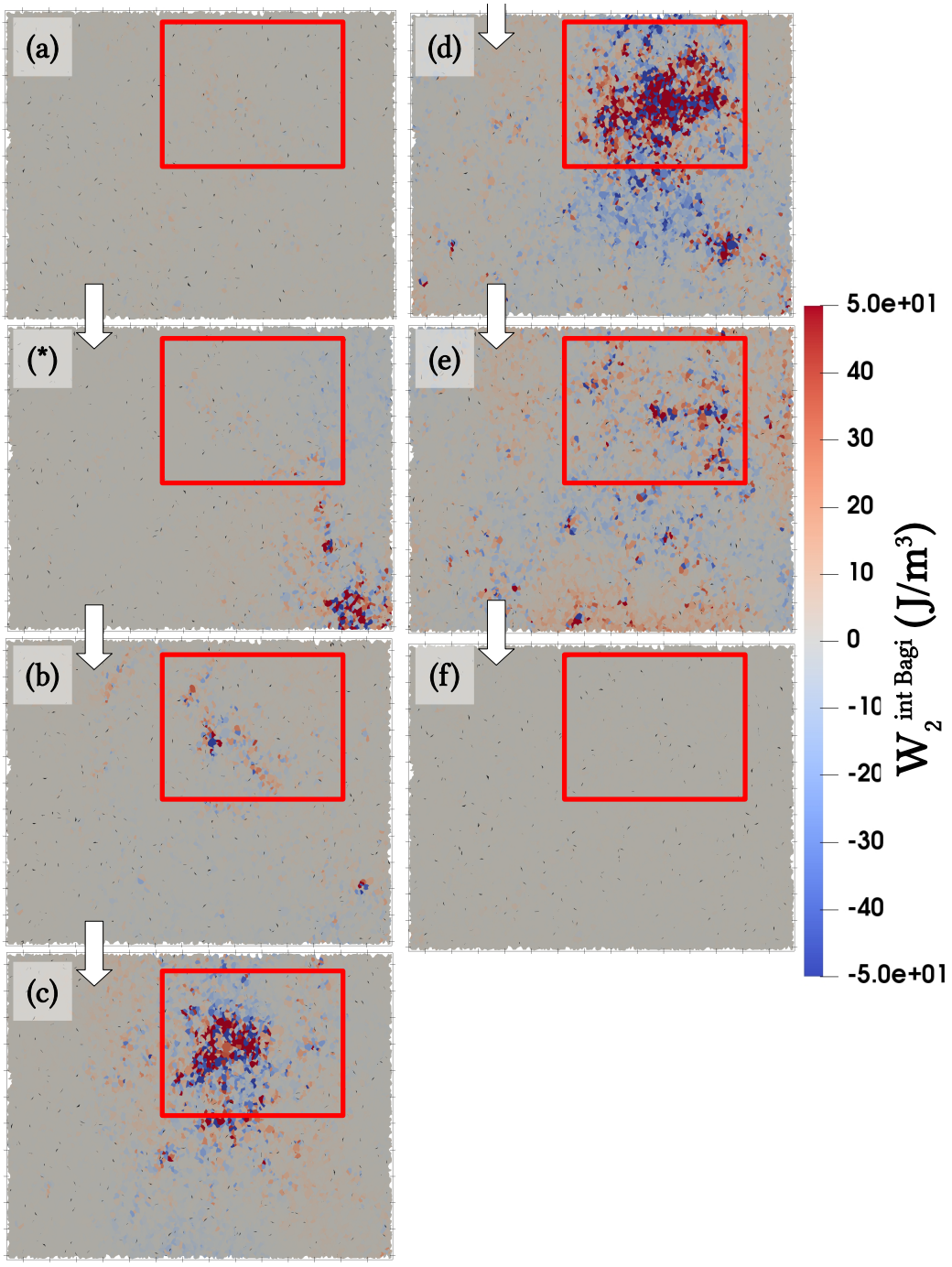

Figure 4.27 – Reduced time sequence of second-order mesoscopic work W_2^{Bagi}. (a) (b) (c) (d) (e) (f) correspond to the same step of Figure 4.9 while (*) corresponds to an additional step between (a) and (b).

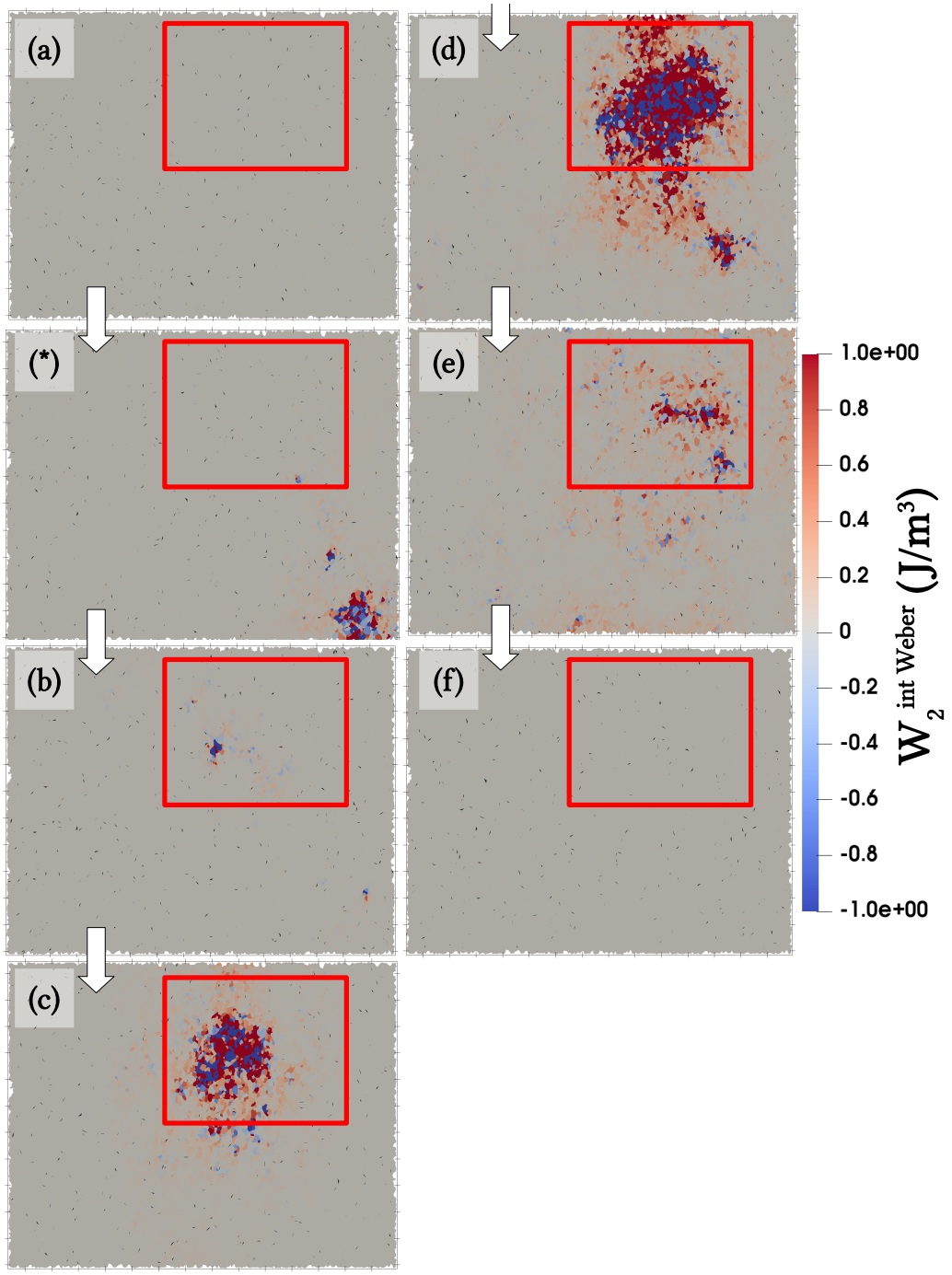

Figure 4.28 – Reduced time sequence of second-order mesoscopic work W_2^{Weber}. (a) (b) (c) (d) (e) (f) correspond to the same step of Figure 4.9 while (*) corresponds to an additional step between (a) and (b). The order of magnitude of the Weber second-order mesoscopic work variations are of the same order as the ones of W_2^m in Figure 4.25.

In order to conclude on the precursor nature of those definitions of second order mesoscopic work, their weighted averages inside the burst area and outside are computed as in Equation 4.4 and given in Figure 4.29. Note that Bagi and Weber second-order mesoscopic works are defined on the loop domain including the entire grain domain (structural and not partition view point as shown in Figure 3.2) so the weights in the averaging are different from the previous ones given in Equation 4.4. The weighted average of W_2^{Bagi} exhibits positive values at the onset of the outburst and peaks at maximum kinetic energy (Figure 4.29(a)). The weighted average of W_2^{Weber} vanishes at the onset of the burst and it is after the peak of kinetic energy that it increases with positive values (Figure 4.29(b)). The vanishing of the Weber second-order meso-work can be seen as a signature of the instability in the burst domain (no negative values are exhibited in the outside domain). Soon after the weighted average of W_2^{Weber} becomes positive again, the kinetic energy decreases. The time scale necessary for the micro-structure reorganizations and the increase in positive values of W_2^{Weber} may be link to the microscopic rearrangements time scale $d/\sqrt{P/\rho}$ evoked in the definition of the inertial number (Section 2.1.3). The scenario in which the efficient reorganizations of the micro-structure restrict the limitation of the outburst in space and time is definitively supported by the varitions of weighted average of Weber second-order mesoscopic work.

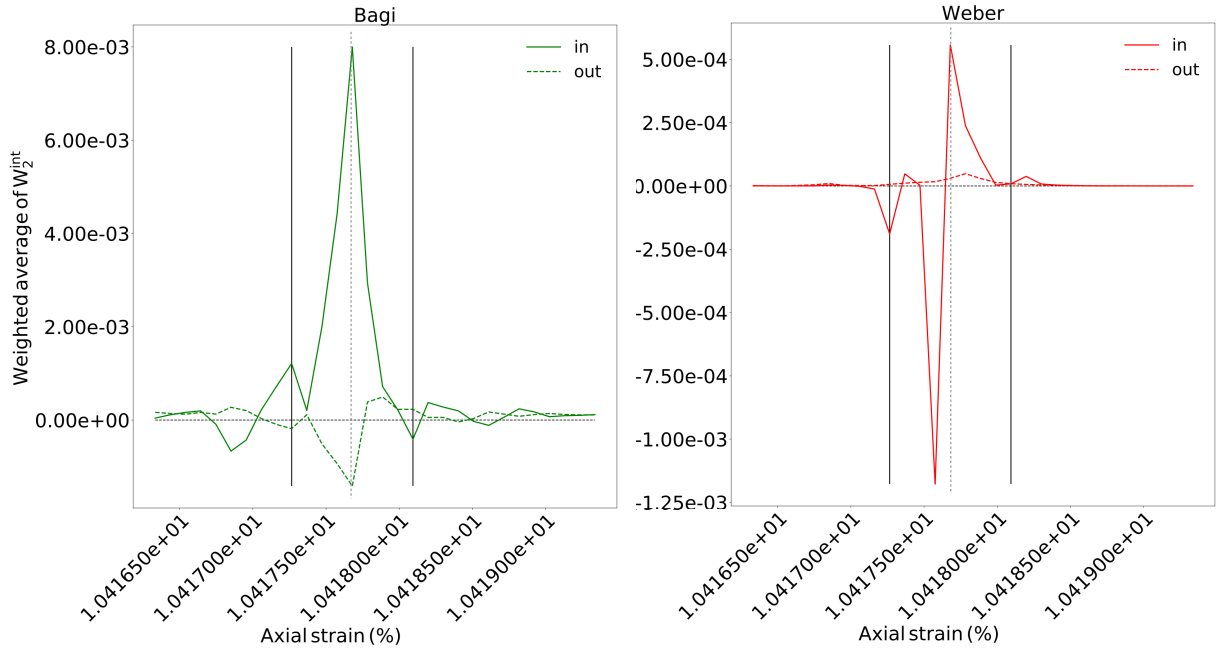

Figure 4.29 – Volume weighted average of the Bagi and Weber second-order meso-work during the burst of kinetic energy, in the neighbour of the initiation of the burst. The peak of kinetic energy is marked with the grey dash-dot vertical lines. The two vertical solid lines correspond to the initiation and the end of the burst of kinetic energy.

4.3.3 Energy balance validation of the second-order meso-work definitions

Three different definitions of the second-order mesoscopic work for the second-order meso-work criterion have been considered. Without taking into account the nature of precursor presented by the grain averaged and Weber definition, the best definition may be chosen on a mesoscopic residue minimization criterion (Equation 3.23). This minimization criterion should enable to derive a link between the mesoscopic and macroscopic definition of the second-order work. The double contraction product prevents the derivation of the macroscopic second-order work from spatial averaging. This requires the validity of Hill's lemma which is not straightforward to demonstrate in the present case. The mesoscopic residue in the case of the grain averaged second-order meso-work is not computable as the second-order work is defined on the partition volume of the meso-domain Ω_l (or V^{part}), whereas the external second-order work is defined from the structural volume V^{struct}. Consequently, only the residue of the Bagi and Weber second-order meso-works are computed. The absolute mean residues during the burst of kinetic energy are given in Figure 4.30. For both definitions, the absolute mean residue peaks at the maximum of kinetic energy. The values of the Weber residue are more than three times smaller than the Bagi residue, which makes the Weber definition a better candidate as second-order mesoscopic work.

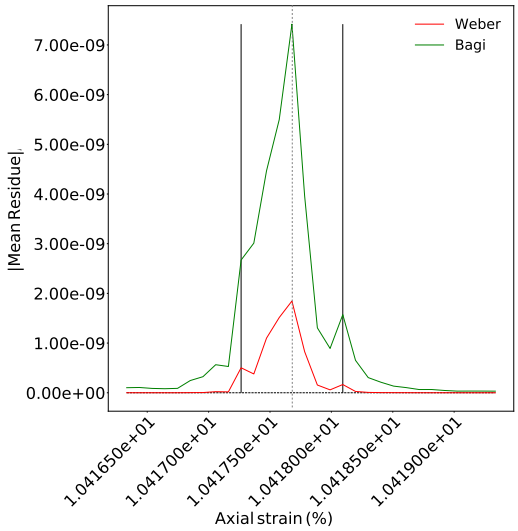

Figure 4.30 – Mean residue for Bagi and Weber second-order mesoscopic work. The peak of kinetic energy is represented as the grey dotted vertical line.

To conclude, the Weber second-order mesoscopic work minimizes the residue derived from the balance equation of the second-order meso-workcriterion. Thus, it is the Weber second-order meso-work which should be considered for local analyses. Furthemore, the Weber second-order meso-work vanishes on the onset of a burst of kinetic energy, and it measures the time needed by the micro-structure to stabilize. It is a meso-precursor for mechanical instability in a given domain.

4.4 Conclusion

In this chapter, analyses of outbursts of kinetic energy during drained biaxial tests on various samples highlight the existence of precursors and propensity elements for outbursts. We have seen that if there is a localization of the deformation, bursts of kinetic energy are also localized in the shear band. It has been established that an outburst occurs in an area which is looser and in which contacts are closer to slide than in the rest of the sample where the burst does not propagate. Mesoscopic stresses and mesoscopic second-order works were defined. The grain averaged W_2^m and the Weber W_2^{Weber} second-order mesoscopic works vanish inside the burst area on the onset of the burst and thus are considered as precursors of mechanical insta-

bility. During the outburst, the microstructure is reorganized. High order loops and rattlers play a great role during this transition. The evolution of meso-structures and the variation of the weighted average of second-order mesoscopic works (W_2^m and W_2^{Weber}) have shown that this is the quick microstructure reorganization that enables the outburst to propagate to the rest of the sample.

Chapter 5

Triggering of gravitational instabilities

In Chapter 4, post processing techniques and mesoscopic quantities definitions wereintroduced in order to better understand the initiation of inertial transition. The study took place at the material point scale in samples considered as representative elementary volumes. The fertile background on which a burst can appear and develop were defined, even though a global inertial transition has not been observed at the scale of the whole sample. Indeed, rearrangements in the micro-structure during a burst limits its propagation. Our observations and conclusions are limited to the onset of inertial transition. Nevertheless the approach developed is versatile and can be applied to a more concrete case : a mechanical destabilization in a granular slope subjected to gravity.

The aim here is to study the beginning of the destabilization, i.e the solid/fluid-like transition only, not to study the fluid regime. Two sets of simulation were set up : one simulation with rigid boundaries, as for the samples in Chapter 4, and one simulation with periodic boundary conditions. In the first section, the generation of the samples and the different steps of the simulation are presented. In the second section, the evolution of different parameters is studied in order to delineate the quasi-static regime and understand the different stages undergone by the sample. In the third section, the influence of the porosity and the boundary conditions is analysed. In the last section, occurence of bursts of kinetic energy without periodic conditions are studied to discuss the link between burst of kinetic energy and landslides.

5.1 Gravity test principles

In the present section, the generation and the progress of gravity instability tests are introduced. The simulation with rigid boundaries is noted *rbc* and the simulation with periodic boundary conditions is noted *pbc*. These two simulations with different boundary conditions are two different ways to simulate a granular gravitational collapse. In the case of rigid boundaries, the samples are defined sufficiently elongated to minimize the perturbation induced by the walls on the micro-structure (Section 2.1.3).

5.1.1 Creation of the sample

A sample *rbc* is created according to the same protocol presented in Section 4.1.1). With respect to the walls effect described in Section 2.1.3, the aspect ratio of the box is 0.14 (horizontal length = $7.05m$; vertical length = $0.94m$), as illustrated in Figure 5.1. The number of grains in this type of analysis is smaller than in drained biaxial test, the total number of spheres

is here $8,000$.

The aim is to obtain samples with the same characteristics as the samples S_2 created in the Chapter 4. Thus, the third dimension is settled at one maximum diameter. Moreover, the granular size distribution, normalized by the mean radius is the same. From this original specimen, two samples of different porosities are created. The interparticle friction angle is decreased until the porosity of the sample ressembles the porosity of the targeted sample S_2 (dense or loose). All the characteristics are given in Table 5.1.

Table 5.1 – Characteristics of the samples with rigid boundaries *rbc*.

Parameters	Samples Dense (D) & Loose (L)
Number of spheres	$8,000$
Grain density	$3,000$ kg.m^{-3}
R_{mean}	1.5×10^{-2} m
D_{max}/D_{min}	1.98
Porosity	$D : 0.163; L : 0.198$
Sample Aspect Ratio (Height/Length)	0.14
Interparticle Friction angle Φ	$35°$
Particle/Wall Friction angle	$0°$
k_n/D	356 MPa
k_t/k_n	0.42
Numerical damping coefficient	0.05
Angle velocity for gravity	$0.18°.s^{-1}$

5.1.2 Gravity driven instabilities test

In order to create a slope, there are two options: either the box or the vector gravity is tilted. Technically, the second option is easier to implement. After the preparation step, gravity is turned on. The spheres in contact with the bottom wall are fixed to it in order to avoid sliding along the bottom wall (Figure 5.2(b)). The top wall, that was used to compact the sample, is lifted in order to create a free surface (Figure 5.2(c)). This is done sufficiently slow so that the unbalanced forces remains smaller than 10^{-5} (this prevents spheres from being ejected because of sudden release in consolidation stress). The top wall is placed far enough to observe an inertial transition before the spheres enter in contact with it, at five times the mean radius from its position after consolidation (Figure 5.2(c)). When the three initial steps are achieved, then gravity is tilted with a constant velocity given in Table 5.1. It is a velocity chosen as a compromise beetween a time consuming lower

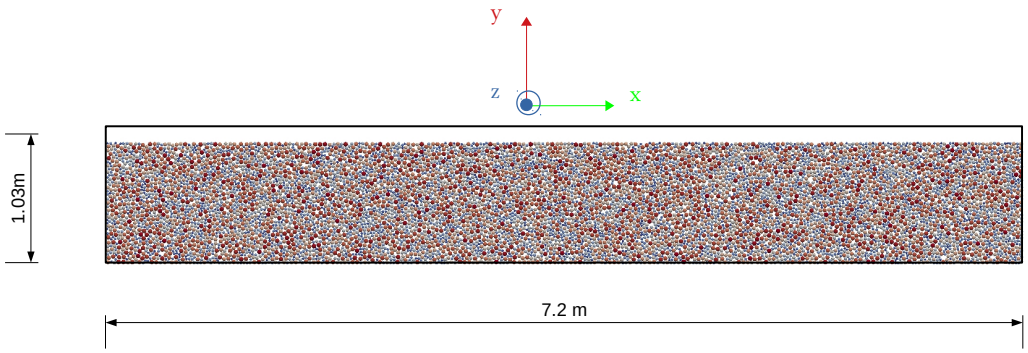

Figure 5.1 – Dense sample with rigid boundaries after the preparation step. The grains are coloured as a function of their radius.

value and keeping the simulation rate independant as long as possible. The simulation is stopped, when the angle of gravity reached 50°.

5.1.3 Influence of the type of boundary counditions : periodic conditions

Another type of sample is created with periodic boundary conditions (Wenrui, 2021). Periodic boundary conditions are used in the x-axis direction, and rigid walls are placed in the other directions. The characterics of the created samples are listed in Table 5.2. The preparation is slightly different from the preparation of the sample *rbc*. Once a cloud of $5,000$ particles with the characterics given in Table 5.2 is generated in a box of dimension X : 1.25 m $\times$ Y : 1.20 m, gravity activates. After gravity deposition, the interparticle friction is decreased to generate three samples with different porosities (Table 5.2). Eventually, the grains in contact with the bottom wall are fixed to it in order to avoid grain sliding on the bottom wall. Gravity vector is titled with a higher angle velocity ()$0.5°.s^{-1}$) than for the samples *rbc* . The simulation stops when the slope angle reaches 40°.

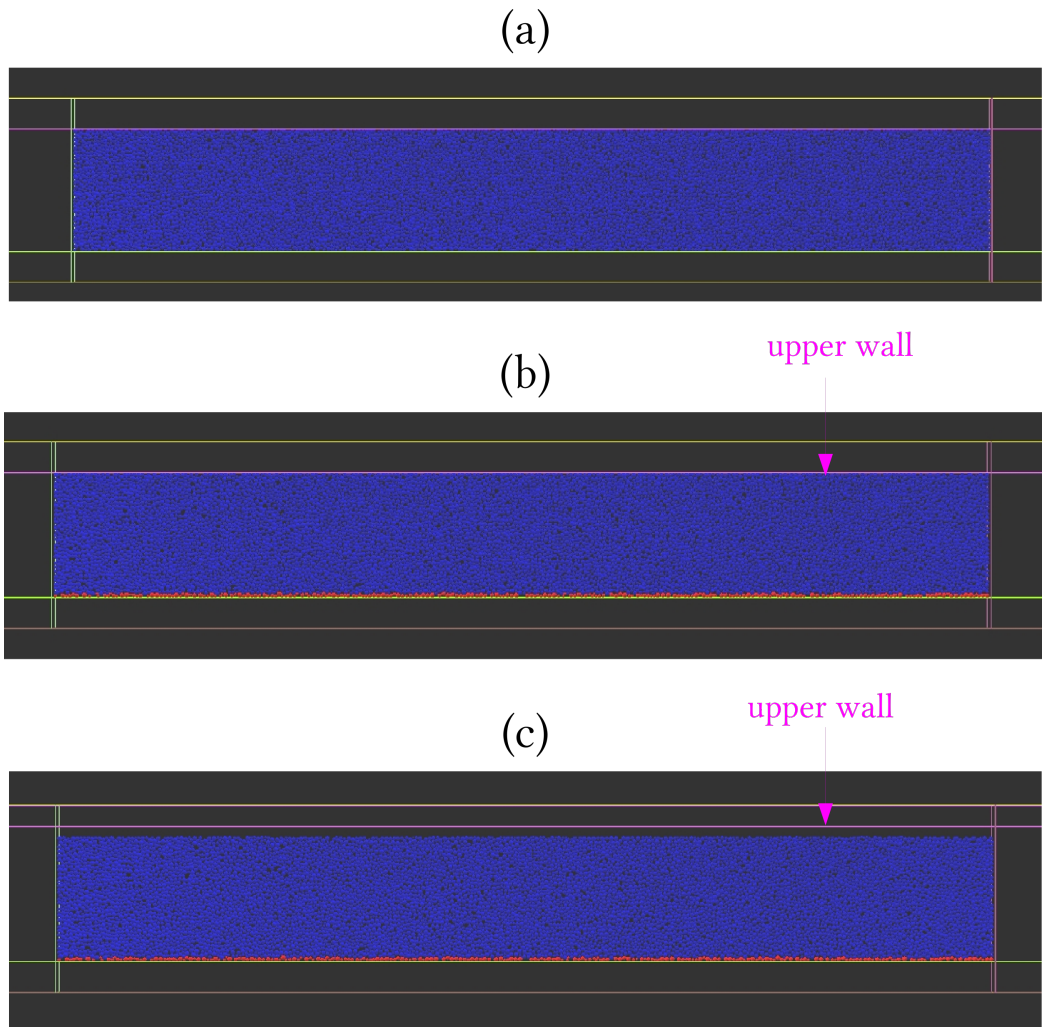

Figure 5.2 – Sketch of the steps before the beginning of the simulation : (a) the sample is isotropically compacted, (b) gravity is activated and spheres in contact with the lower wall are fixed (colored in red), (c) the upper wall is lifted up at a distance of five times the mean radius of the sample.

Table 5.2 – Characteristics of the samples with periodic boundary conditions *pbc*.

Parameters	Samples Dense (D) & Loose (L) & Intermediate (I)
Number of spheres	$5,000$
Grain density	$3,000$ kg.m^{-3}
R_{mean}	5.4×10^{-3} m
D_{max}/D_{min}	1.98
Porosity	D : 0.162 ; L: 0.212 ; I :$0,192$
Interparticle Friction angle Φ	35°
Particle/Wall Friction angle	35°
k_n/D	356 MPa
k_t/k_n	0.42
Numerical damping coefficient	0.05
Angle velocity for gravity	0.5°.s^{-1}

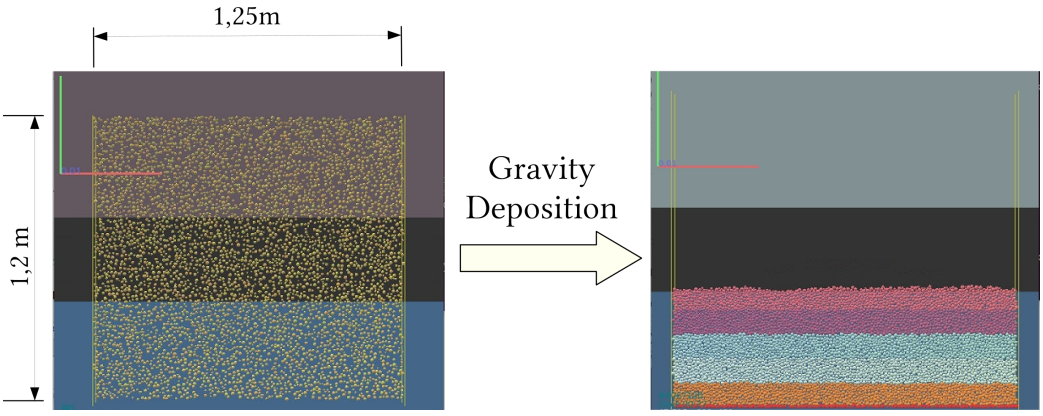

Figure 5.3 – Sketch of the sample creation with periodic boundary conditions. On the left : the cloud of particles in the box of dimension 1.25 m $\times$ 1.20 m. On the right : the sample after gravity deposition. Particles in red at the bottom of the sample are fixed.

5.2 Evolution of quasi-static macro-scale quantities

In this section, a quasi-static analysis is conducted in order to understand how the sample evolves during the titling of gravity. To verify the extent to which the problem of interest may be considered as quasi-static, the inertial number of the sample is computed first. The sample *rbc* with an initial porosity of 0.198 and the sample *pbc* with an initial porosity of 0.192 are compared, as they have similar initial porosities. For this section, and for the sake of brevity, the two samples will be referred as *rbc* and *pbc* without specifying the initial porosity. The influence of the porosity and the boundary conditions will be discussed in the next section.

5.2.1 Enforcability of quasi-static analysis

The inertial number I formulation is given in Equation 2.5. As recalled in Section 2.1.3, a grain packing is considered out of the quasi-static regime if $I > 10^{-3}$. The mean diameter d and the particle density ρ are known material properties. For the pressure P, which is not homogeneous in the sample, an order of magnitude is obtained in the middle of the sample considering the vertical stress applied by a column of granular material of height $H/2$:

$$P = (1 - \Phi)\rho g \frac{H}{2} \tag{5.1}$$

where g is the magnitude of the gravitational acceleration, Φ the porosity of the sample and H the height of the grain packing.

In both simulations, it is observed that the velocity of the particles is not homogeneous. On the free surface, the velocity is maximal, while velocity is minimal at the bottom (Figure 5.4(a)). This velocity profile on slope granular flow can be found in the litterature (Pouliquen et al., 2005; Jop et al., 2007). Thus, the order of magnitude of the tangential velocity $\dot{\gamma}$ is approximated as the difference between a mean free surface velocity v_{max} and mean bottom velocity v_{min} :

$$\dot{\gamma} = \frac{v_{max} - v_{min}}{H} \tag{5.2}$$

Figure 5.5 shows the evolution of the inertial number during the simulation for both samples. The inertial number for the sample *pbc* increases slowly and even linearly after 20°. For this sample, $\theta_i^{pbc} = 31°$ is the limit of the quasi-static regime. The sample *rbc* exhibits the same quasi-static

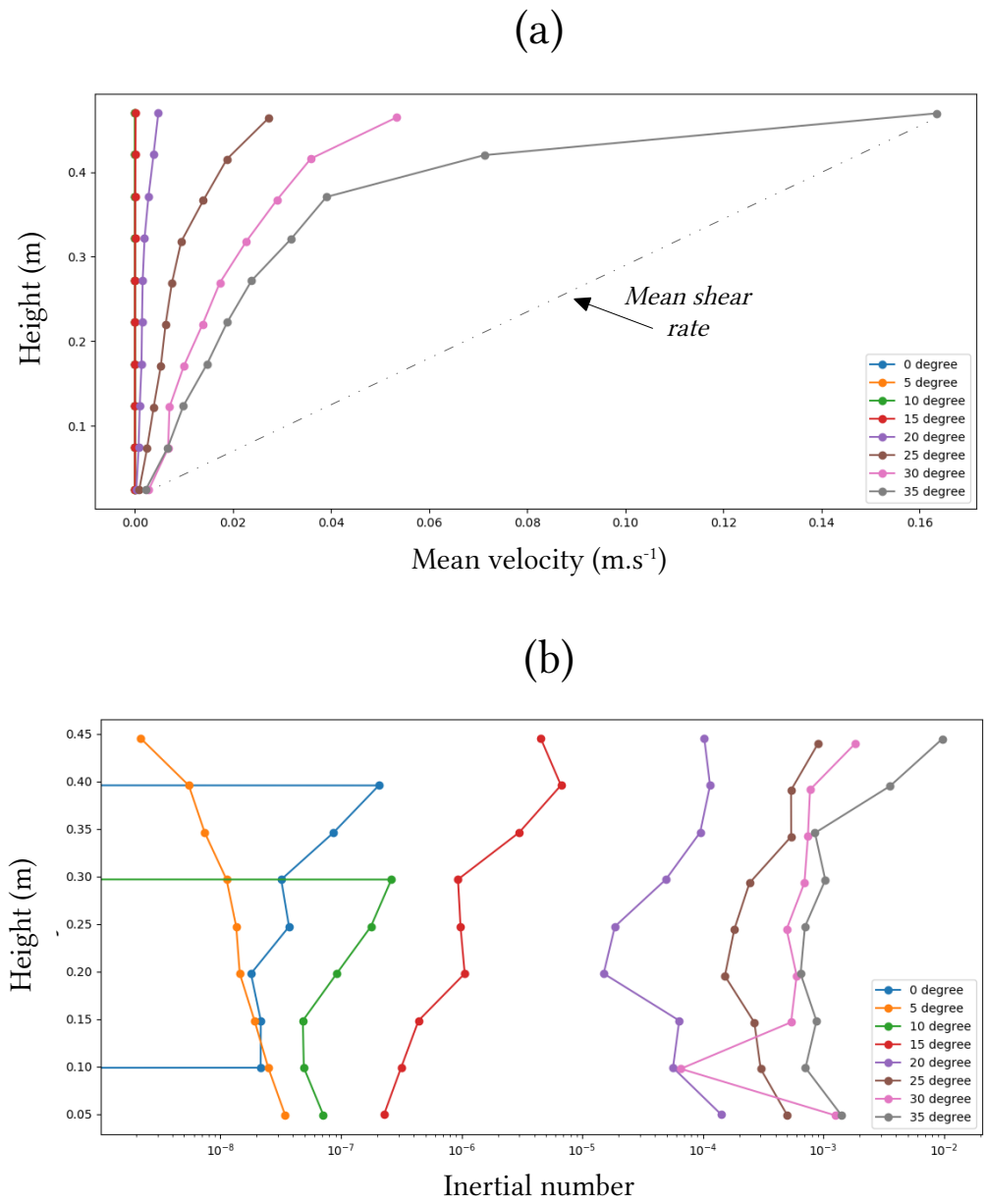

Figure 5.4 – (a) Mean velocity in function of sample's depth and (b) inertial number as a function of sample's depth in the sample *pbc*. Same types of curves are found for the sample *rbc*.

limit $\theta_i^{rbc} = 31°$, even though the increase is linear from the early beginning. Even though, particle velocity field is not homogeneous, inertial numbers for different layers are still of the same order of magnitude (Figure5.4(b)). To summarize, both samples are out of the quasi-static regime after 31°.

One can notice that there is a drop of the inertial number around $\theta_s = 35°$ for the sample *rbc* (Figure 5.5(a)). This is due to the fact that the grains touch the top wall and clog the flow. At the beginning of the simulation, there is a free surface on the top of the sample, and there is no contact with the upper wall (Figure 5.6(a)). When the sample starts flowing, the space between the initial free surface and the upper wall is quickly filled up, stopping the flow (Figure 5.6(b)). From an angle of 35°, just after the beginning of the dense regime, the sample is stuck in the left part of the box and the flow dynamics vanishes. Note that the sample is considered as stuck when meso-structures are formed in the corner (Figure 5.6(b)). Thus, the data collected for the sample *rbc* after the angle θ_s is reached are not revelant for the triggering of instability. Similary, the data collected after the θ_i^{rbc} is reached are out of the scope of our static model. Thus, in the next figures, the data after θ_i for both samples are shaded.

5.2.2 Depth averaged stress behaviour

In the context of the slope simulation, the stress is not homogeneous in the sample. Nevertheless, the hypothesis is made that in thin layers at a given depth, the stress state can be considered homogeneous. Thus, both samples are divided in five different layers and the stress in each layer is computed as spatial average of the Love & Weber stress inside the layer :

$$\langle \sigma_{layer} \rangle = \frac{1}{|\Omega_{layer}|} \sum_{p \in \Omega_{layer}} \sigma_p V_p \tag{5.3}$$

where Ω_{layer} is the domain of the considered layer, σ_p the Love & Weber stress for the particle p and V_p its volume. The particles in contact with the bottom wall and thus fixed to it are not considered in the computation.

The deviatoric stress and the mean stress are deduced from the principal stresses in a 2D context. The expression of the mean stress is the same as in Equation 3.3 and of the stress is given in Equation 3.1.

$q - p$ curves for each layer for both samples are presented in Figure 5.7. The curves for the sample *pbc* are almost vertical and reach the failure line at the point corresponding to the inclination angle of 18.5° (Figure 5.7(c)). So the inner friction angle of the sample *pbc* equals the slope angle for which the stress path reaches a failure limit. The curves for the sample *rbc* do not

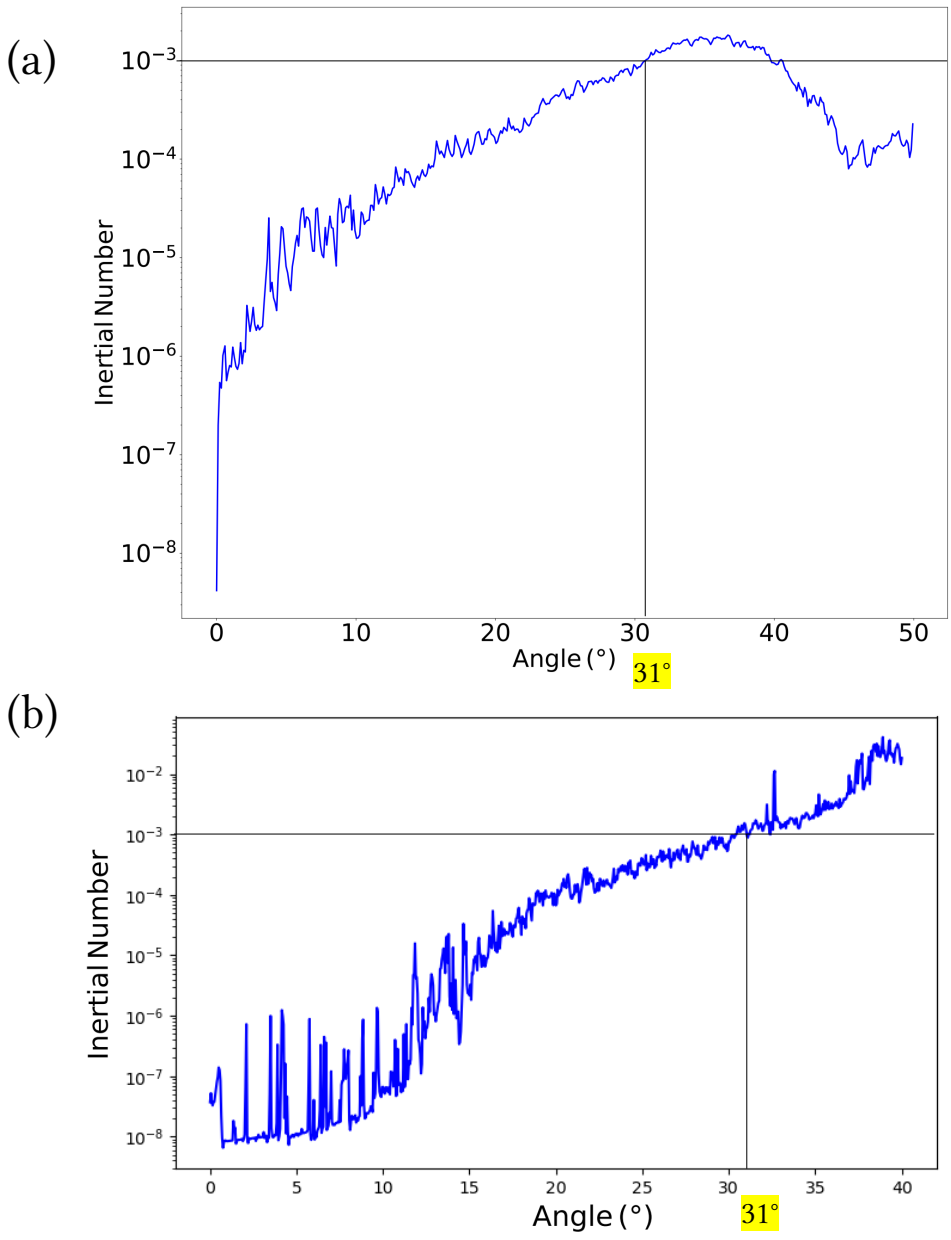

Figure 5.5 – Evolution of the inertial number I as a function of the slope angle for the sample *rbc* (a) and the sample *pbc* (b). The angle for which each sample enters in the inertial regime is pointed out (vertical solid line).

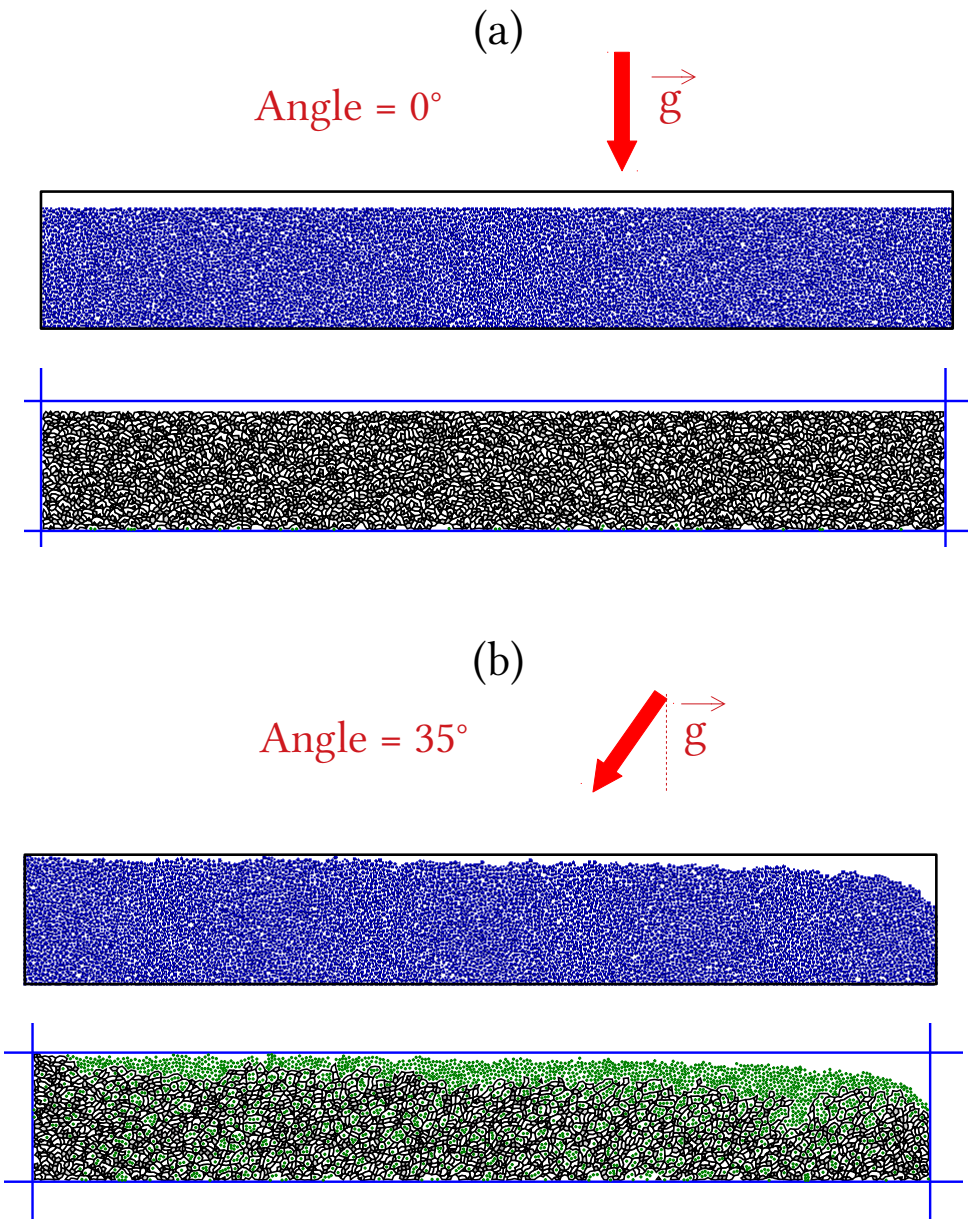

Figure 5.6 – Illustration of the titling of the sample *rbc* and the up wall cloging. (a) The sample when the slope angle is at 0° : the spheres are displayed in blue, the grain loops are displayed in black. (b) The sample when the slope angle is at 35° : the spheres are displayed in blue, the grain loops in black and the rattlers in green are displayed.

exhibit initial zero or quasi zero q values as for the sample *pbc*. The pre-simulation stress imposed on the walls is responsible for these values. In this sample, all the layers do not reach the failure line for an inclination angle of 16°. Only the top layers do (Figure 5.7(b)). This is an other consequence of the confining walls. The difference of magnitude in the p and q values stems from the difference in the mean radii between the two types of samples, for the same out of the plane dimension (see Section 3.1.2), and from the effects of the confining walls.

The sample *rbc* is not homogeneous in the sense that five layers have different initial stress ratio q/p. This is related to the lateral walls kept the memory of the horizontal pre-stress imposed during the preparation step (isotropic compression) while the vertical pre-stress has been released with the lift of the top wall. For both samples, the interparticle friction angle (set to 35°) is different from the internal friction angle (measured in Figure 5.7 16° or 18.5°). The plastic limit surface in the $q - p$ plane is reached for a slope of 18.5° (or 16°), which is consistent with the standard Mohr-Coulomb model. For both samples, we can make the hypothesis of a pre-avalanche interval as introduced in the litterature (Daerr and Douady, 1999; Staron et al., 2006; Staron, 2008). The lower limit of the pre-avalanche interval (pre- destabilization angle noted θ_d in Section 2.1.3) is the internal friction angle (*rbc* : 16°, *pbc* :18.5°) and its upper limit is the angle from which the sample is no longer in a quasi static regime (*rbc* : 31° , *pbc* : 31°).

5.2.3 Macroscopic and mesoscopic evolutions

After specifying the limits of our quasi-static analysis, the behaviour of both samples is analysed with more details thanks to the grain loops and the porosity evolutions. The differences so far between the two samples are attributed to their boundary conditions.

Meso-structure evolution

In Chapter 4, it has been shown that the macroscopic behaviour of the sample can be illustrated by the evolution of its meso-loops. Figure 5.8 gives the evolution of the numer of loops (for each loop order) divided by the total number of spheres for both samples. For the sample *rbc* (Figure 5.8(a)), the number of loops does not evolve much for low order loops, it decreases slightly. However, the number of the highest order loops increases until the clogged configuration of the sample. For the sample *pbc* (Figure 5.8(b)), a decrease in the number of small order loops is also observed, as well as an increase in the number of the highest order loops until 18.5°, which corresponds to

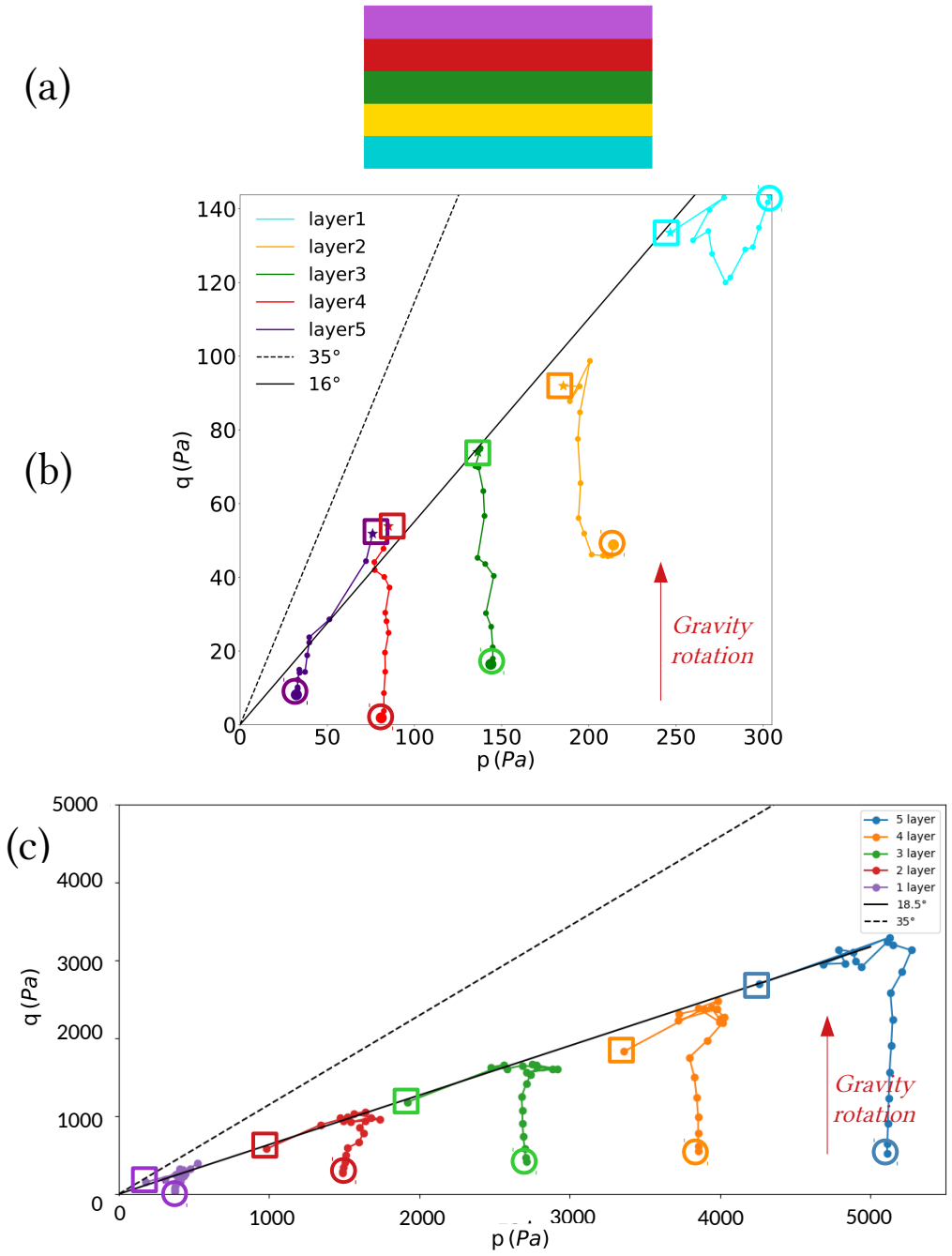

Figure 5.7 – $p-q$ path of 5 layers (a) for (b) the sample *rbc* and (c) the sample *pbc*. For both samples, the first point of the curves (horizontal slope) is surrounded by a circle and the last point (inertial transition) by a square (see the red arrow for the direction of the $p-q$ path). Every point corresponds to a 2° increment of the slope angle.

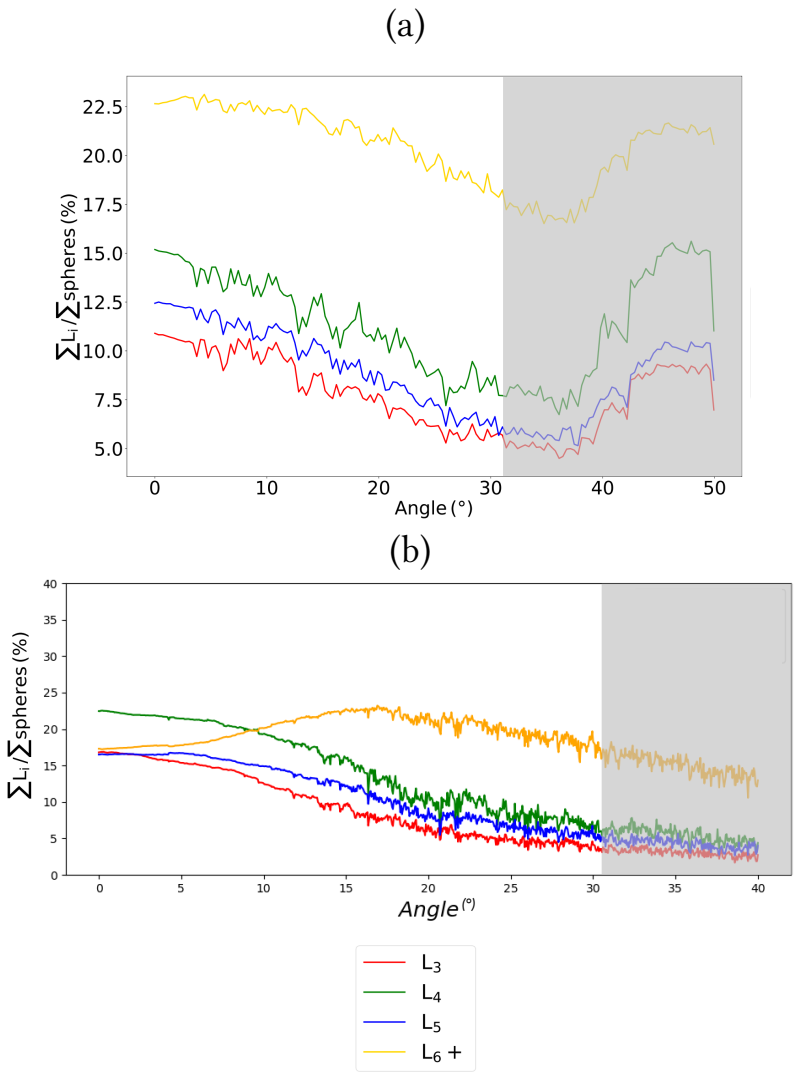

Figure 5.8 – Evolution of the number of loops per category, normalized by the number of grains for (a) the sample *rbc* and (b) the sample *pbc*. Grey parts correspond to the data after the sample enters in the inertial regime.

the failure line (Figure 5.7(c)). We can observe that both samples do not have the same loop composition at the beginning of the test, despite their similar initial porosity. With a majority of L6+ loops from the beginning, the sample *rbc* has indeed a looser micro-structure than the sample *pbc*.

Lifespan and life expectancy of all meso-structures are also analysed in order to evaluate the importance of grain loops changes. Lifespan and life expectancy are computed for a reference slope angle (here 7.5°), in Figure

5.9. The lifespan is given on the left, in blue, and the life expectancy is given on the right, in red. For both samples, there are a majority of loops that exist from the beginning of the simulation (high blue column at angle 0°). These long-living loops completely disapear when the sample enters in the inertial regime, which correponds to the complete renewal of meso-structures. Few or none of the meso-structures present at 7.5° are present at the initiation of inertial transition. Moreover, most of them will even disappear before the slope angle reaches 20° in both samples (Figure 5.9(b) and Figure 5.9(d)) corresponding to the internal friction (the material reaches the Mohr-Coulomb failure line).

For the sample *pbc*, there are peaks of life expectancy around 15°, which corresponds to massive reorganisations occuring before failure line (Figure 5.9(a)). On the contrary, for the sample *rbc*, the lifespan - life expectancy histogramm is bell shaped, showing important reorganisations from early stage of the simulation (Figure 5.9(c)). This might be due to the fact that the sample *rbc* is looser than the sample *pbc* (higher order loops for the same porosity).

Porosity evolution and role of rattlers

For free surface samples, the macro porosity is defined from the weighted average of the grain loop porosity. The weight corresponds to the loop area and the grain loop is either computed with rattlers (effective porosity, Equation 3.8) or without (real porosity, Equation 3.8) (see Equation 4.3). For the sample *pbc*, in which the free surface stays horizontal thanks to the periodic boundary conditions, a reference height may be alternatively chosen to define a rectangular domain where the porosity is estimated. A reference height of 80% of the height sample is chosen (Figure 5.10(a)). By definition, φ_{80}^{eff} is an effective porosity (all grains takien into account). The porosity φ_{80}^{eff} is also computed for the sample *rbc*, as a comparison. Indeed, before the inertial transition, the inclinaison of the free surface allows to compute φ_{80}^{eff} (no big depresion on the right of the sample yet). The φ_{80}^{eff} porosity reads :

$$\varphi_{80}^{eff} = 1 - \frac{\sum_{i \in \Omega_{80}} A_i}{|\Omega_{80}|} \tag{5.4}$$

where Ω_{80} is the area of the sample below the reference height of 80%, and A_i the area of the particle i inside the domain Ω_{80} .

The φ_{80} porosity evolutions are given for samples *pbc* and *rbc* in Figure 5.10. The sample *pbc* is only dilatant after the first failure line angle, corresponding to the predominance of L6+ loops (Figure 5.10(b)). The sample *rbc*

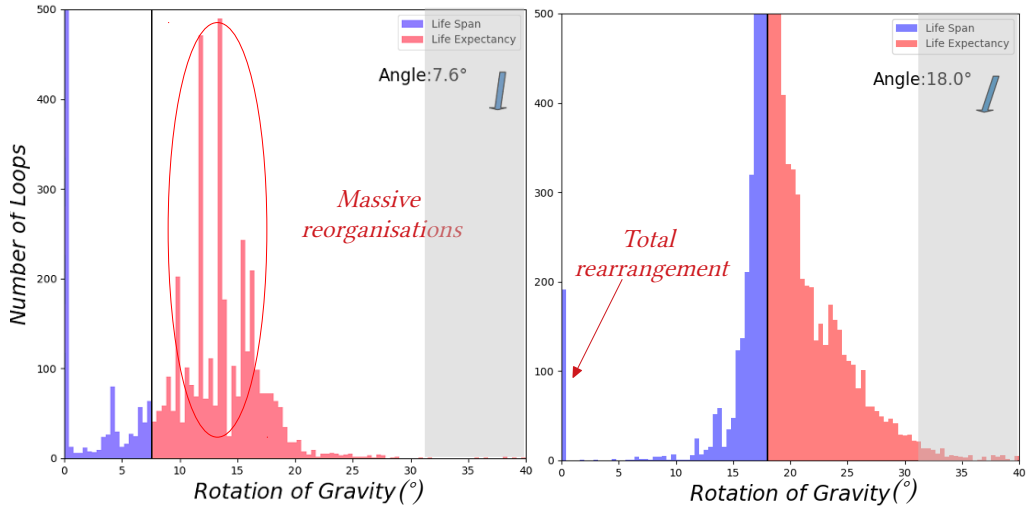

(a) *pbc* 7.6° (b) *pbc* 18°

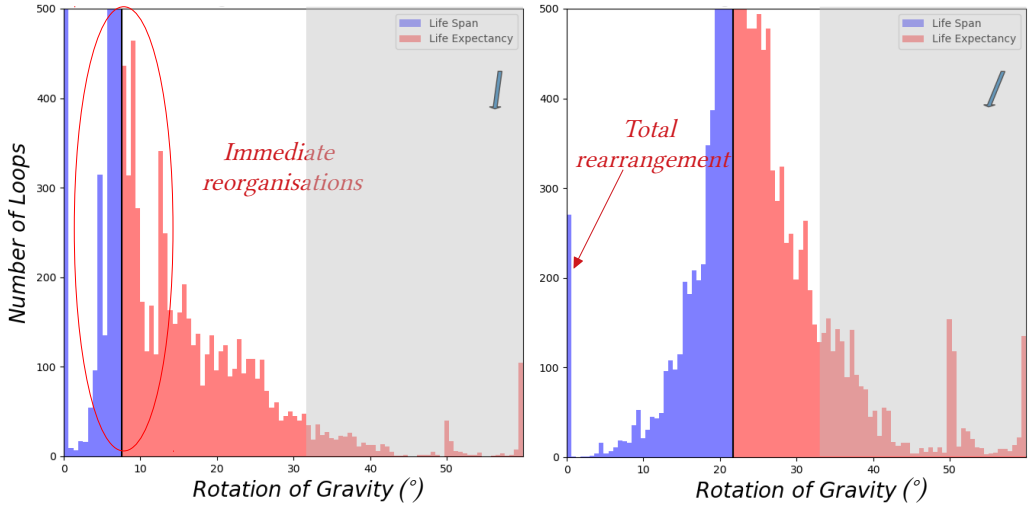

(c) *rbc* 7.6° (d) *rbc* 18°

Figure 5.9 – Lifespan (blue) and life expenctancy (red) for the sample *pbc* (respectively sample *rbc*) at 7.5° (a) (resp. (c)) and 18° (b) (resp. (d)). The grey parts correspond to the data after the sample enters the inertial regime.

exibits a slight contractancy before the inertial transition (Figure 5.10(c)). The contractant behavior is typical of a loose sample.

The weighted real porosity (without taking into account rattlers, Equation 3.7) and the weighted effective porosity (taking into account rattlers, Equation 3.8) for the sample *rbc* are compared in Figure 5.11. Without rattlers, the behaviour is fully dilatant, with a porosity increasing until the sample reaches the upper wall. By considering the rattlers, the weigthed average porosity increases slightly. With this formulation of the porosity, the total area is not fixed (which explains dilatancy) and the free surface (made only of rattlers) is not accounted for.

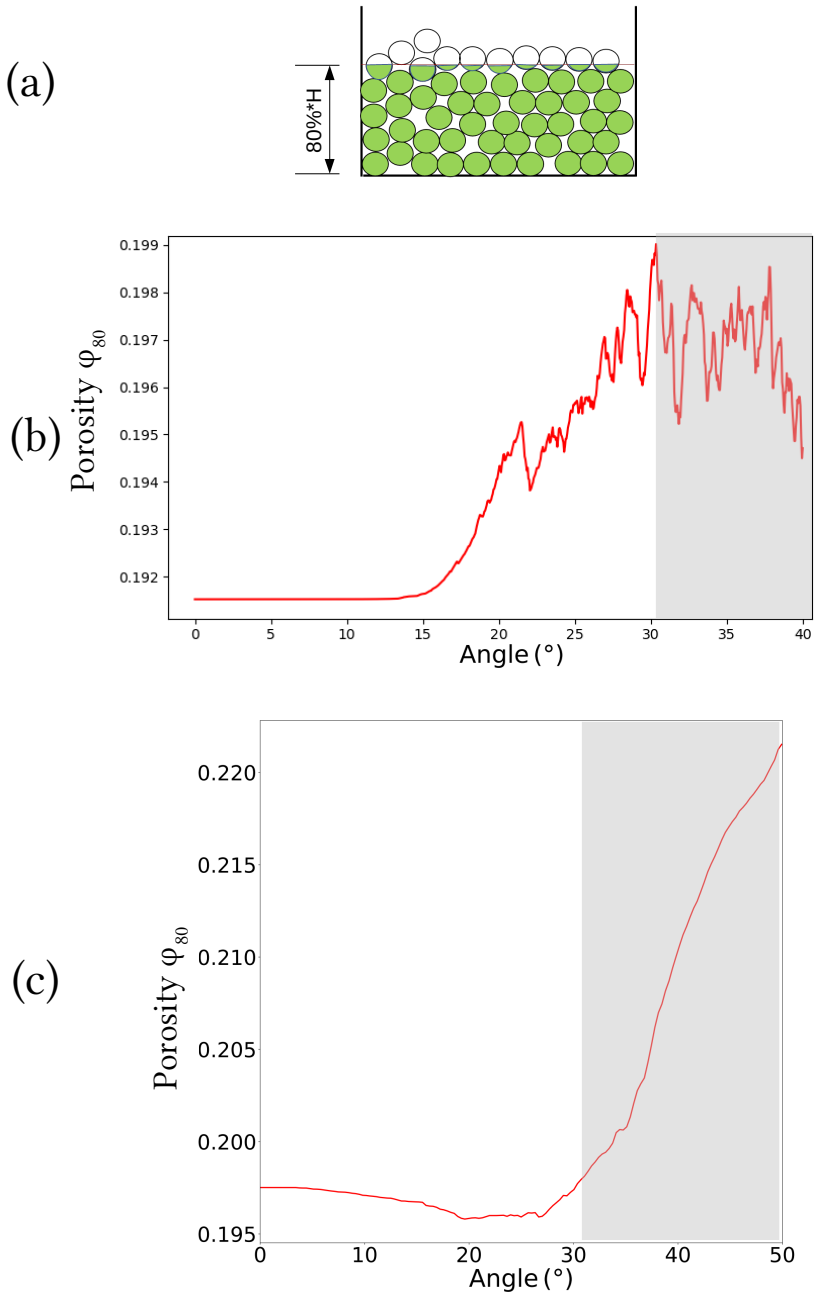

Figure 5.10 – (a) Sketch of the computation of the φ_{80} porosity, evolution of the φ_{80} porosity for (b) the sample *pbc* and (c) the sample *rbc*. Grey part corresponds to the data after the sample enters in the inertial regime.

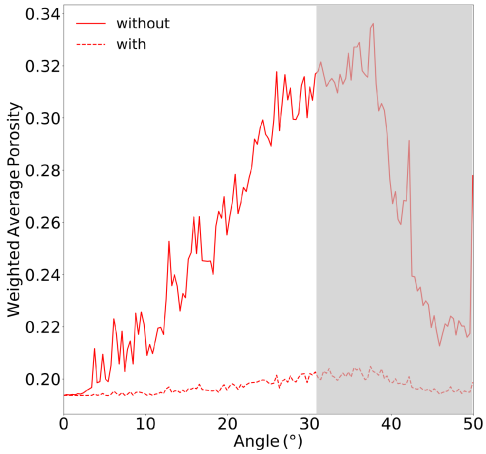

Figure 5.11 – Effective (with rattlers) and real (without rattlers) weighted average porosities of the sample *rbc*. Grey part corresponds to the data after the sample enters in the inertial regime.

Figure 5.12 shows grain loops and rattlers of both samples at different slope angles. For both samples, the grain loops are larger and contain more rattlers when the slope angle increases. The upper layer close to the free surface contains only rattlers for high slope angles (Figure 5.12(c)).

By combining Figures 5.10, 5.11 and 5.12, few conclusions can be drawn. Grain loops are becoming larger with the inclination angle which is underlined by the increasing weighted average real porosity for the sample *rbc* and the φ_{80}^{eff} porosity for the sample *pbc*. The difference between φ_{80}^{eff} and the weighted average effective porosity for the sample *rbc* is due to the top layer, which contains only rattlers near the inertial transition. The fact that rattlers are created inside those larger grain loops, filling up the space created, is highlighted by the weighted average effective porosity for the sample *rbc* which does not evolve much (contrary to the real porosity as shown in Figure 5.11).

Note that rattlers are not present at the beginning of the simulation (Figure 5.12(a)). Indeed, in a simulation without gravity, rattlers are defined as grains with one or no contact with another grain, and thus they are not part of grain loops. However, with the introduction of gravity, those free particles fall at the bottom of the loop, and form L3 grain loops which do not contribute to the main micro-structure of the sample (Figure 5.13). Another definition of rattlers is formulated in (Wenrui, 2021) to identify the settled rattlers in loops as illustrated in Figure 5.13, but it is not investigated here.

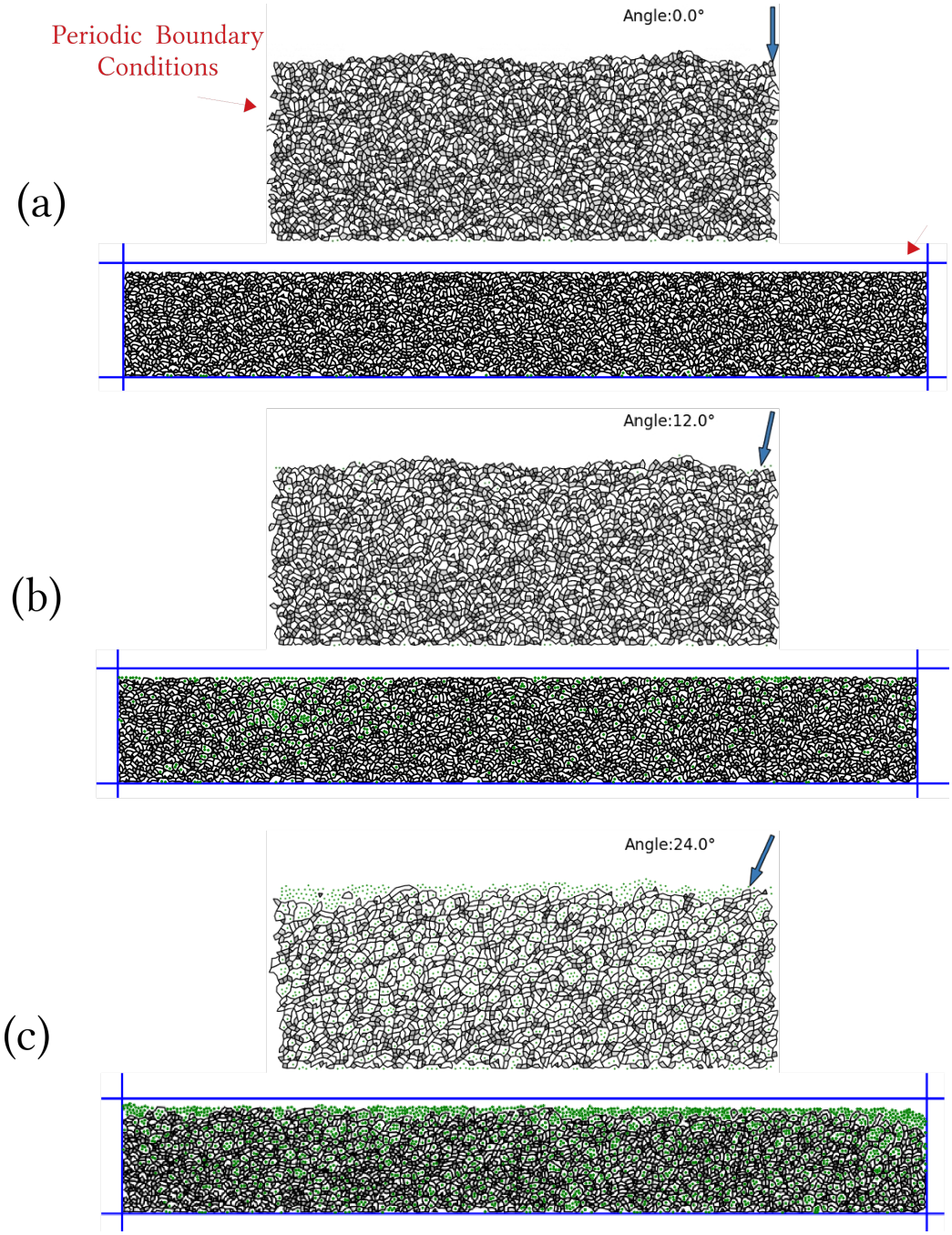

Figure 5.12 – Loops and rattlers for the *pbc* and sample *rbc* at 0° (a), 12° (b), 24° (c) of inclination.

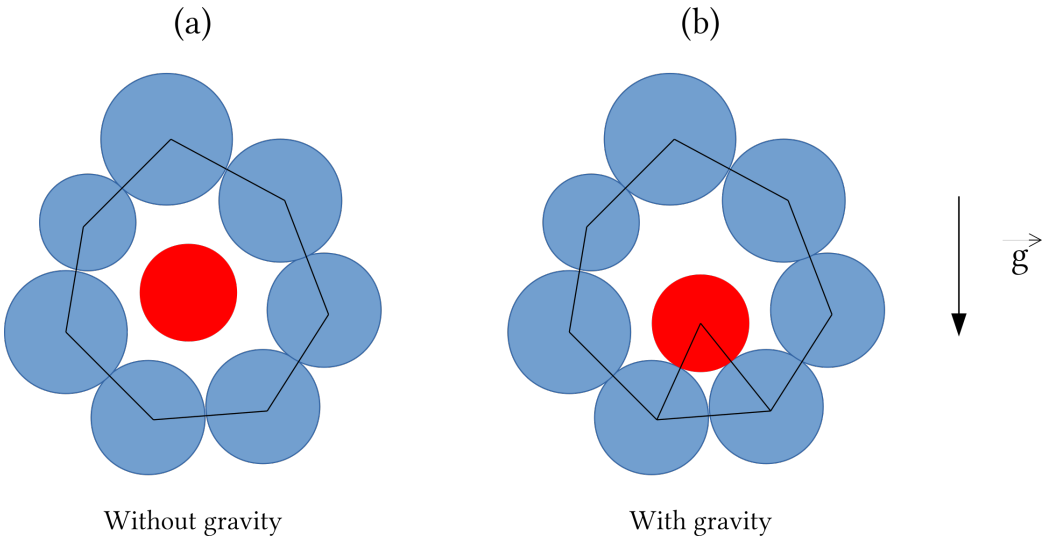

Figure 5.13 – Sketch of a position of a rattlers without gravity (a) and with gravity (b). In (b) the rattler forms a small loop that does not participate to stress transmission.

As a conclusion, for both samples the inclination of gravity creates larger meso-structures, elongated in the slope direction (Figures 5.12), and rattlers appear increasingly inside the grain loops and also at the free surface. The slight difference in the dilatancy between both samples shows they are not of the same density (despite their initial comparable porosities). The sample *pbc* is denser and the sample *rbc* tends to be looser for similar porosities. This conclusion is also supported by the meso-structure evolution in Section 5.2.3.

5.3 Influence of porosity and boundary conditions

In the previous section, two samples of similar porosities but with different boundary conditions have been compared in parallel. Despite their similar initial porosities, they exhibit for some points, different behaviours. In order to highlight the influence of the porosity and of the boundary conditions, the three samples with periodic boundary conditions (Table 5.3) are compared to the two samples with rigid boundary conditions (Table 5.4). The data from the loose samples are displayed in blue, the dense samples in red and the intermediate sample in green in the following figures. The data after the inertial transition is shaded on the figures. Light grey parts correspond to

Table 5.3 – Porosities of the sample *pbc*

Samples	Dense (D)	Loose (L)	Intermediate (I)
Porosity	0.162	0.212	0.192

Table 5.4 – Porosities of the sample *rbc*

Samples	Dense (D)	Loose (L)
Porosity	0.163	0.198

the loose and intermediate samples inertial transition and dark grey parts coorespond to the dense ones.

5.3.1 Inertial transition and kinetic energy

The inertial number is compared between the different samples in Figure 5.14. For the *pbc* simulation, one can see the dense sample enters in the inertial regime later (Figure 5.14(a)). This is the same for the samples *rbc* (Figure 5.14(b)), but with a larger gap.

Figure 5.15 compares the kinetic energy of all the samples. In *pbc* simulations, the looser the sample, the greater the kinetic energy (Figure 5.15(a)). Indeed, a dense sample has a more compact micro-structure able to adapt to evolving loading conditions for small slope inclinations. The kinetic energy of the loose and intermediate samples are converging when they reach 17°. This angle corresponds to the plastic limit for loose and intermediate samples (see Figure 5.7) where no softening occurs. The kinetic energy in the dense sample increases later and converges after 30°. The convergence of the kinetic energy could be explained by the convergence of micro-structure as during the critical state in a biaxial test. However, we need to be cautious because it happens after the inertial transition while the concept of critical state is defined in quasi-static regime. (Da Cruz et al., 2005) already underlined the non influence of the sample preparation on the steady flow characterics, but with no gravity. Thus, the hypothesis can be made that the convergence of all the samples toward the same level of kinetic energy is due to the steady flow regime.

Similar observations are drawn from the curves obtained with the sample *rbc* (Figure 5.15(b)). The kinetic energy is greater at the beginning in the loose sample than in the dense sample. Nevertheless, there is two differences due to the boundary conditions. Firstly, the kinetic energy of the two samples is of the same order of magnitude for small angles (before 5°). Secondly, no

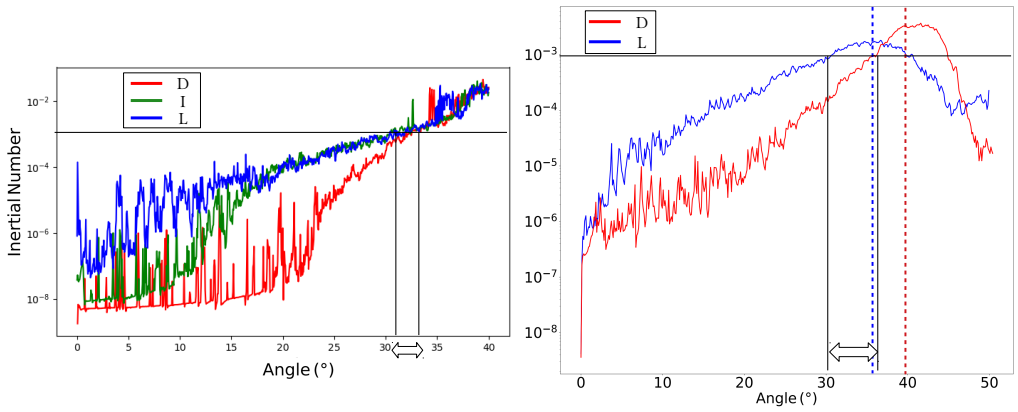

(a) (b)

Figure 5.14 – Inertial number of the three samples *pbc* (a) and the two samples *rbc* (b). Black lines spot the inertial transition angle. For samples *rbc*,vertical lines show when the granular packing get into contact with the upper wall.

convergence of the kinetic energy is observed because the two samples *pbc* reach the upper wall and clogg for different slope angles (around 35° for the loose sample, just after 40° for the dense sample).

The boundary conditions have no significant influence on the kinetic energy evolution nor the inertial number evolution except through the presence of an upper wall.

5.3.2 Depth averaged stress behaviour

Stresses for all the samples are computed as in Section 5.2.2. The intermediate and the loose samples *pbc* exhibit a similar behaviour as observed previously in Figure 5.7 (Figure 5.16(a) and 5.16(b)). In contrast, the stress response of the dense sample reaches a failure line at 25° and then comes back on the 18° failure line. It is comparable to the softening observed for a dense sample in a biaxial test (see section 4.1.5 for example). Note that the deviatoric stress at the beginning of the simulation is almost zero for the dense sample (Figure 5.16(c)). This can be explained by the fact that during the preparation of the sample, the interparticle friction angle was lowered to 0°, resulting in negligeable tangential forces at contact, and with an isotropic micro-structure.

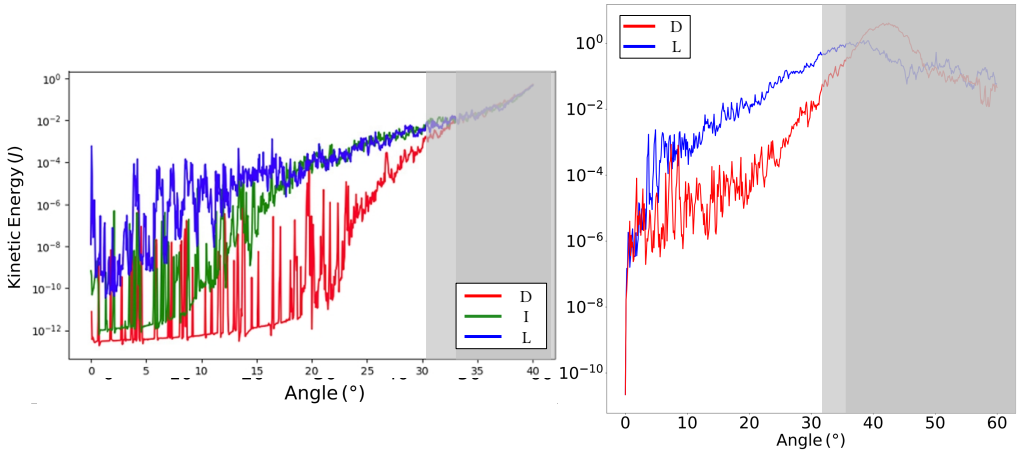

(a) (b)

Figure 5.15 – Kinetic energy of the three samples *pbc* (a) and the two samples *rbc* (b). Grey parts show the inertial regime : the light grey part corresponds to the loose samples inertial transition, the dark grey part cooresponds to the dense ones.

For samples *rbc*, the free surface layers of the dense sample reach a failure line at 24°, but no return to a lower failure line is observed (Figure 5.17(a)). Contrary to *pbc* samples, the initial stress state has a non zero deviatoric stress. It is a consequence of the rigid boundary conditions which maintain a lateral confining stress even after the vertical stress is released in the preparation steps. The non vertical stress responses, for the bottom loose layer (Figure 5.17(b)) and for the dense sample also underline the confining effect of the lateral walls. The confining effect of the wall prevents some of the layers from reaching the failure line, thus leading to a non homogeneous stress field. Reaching of the top wall, and the lateral concentration of the stress when titling the gravity may also inhibit the softening of the dense sample *rbc*.

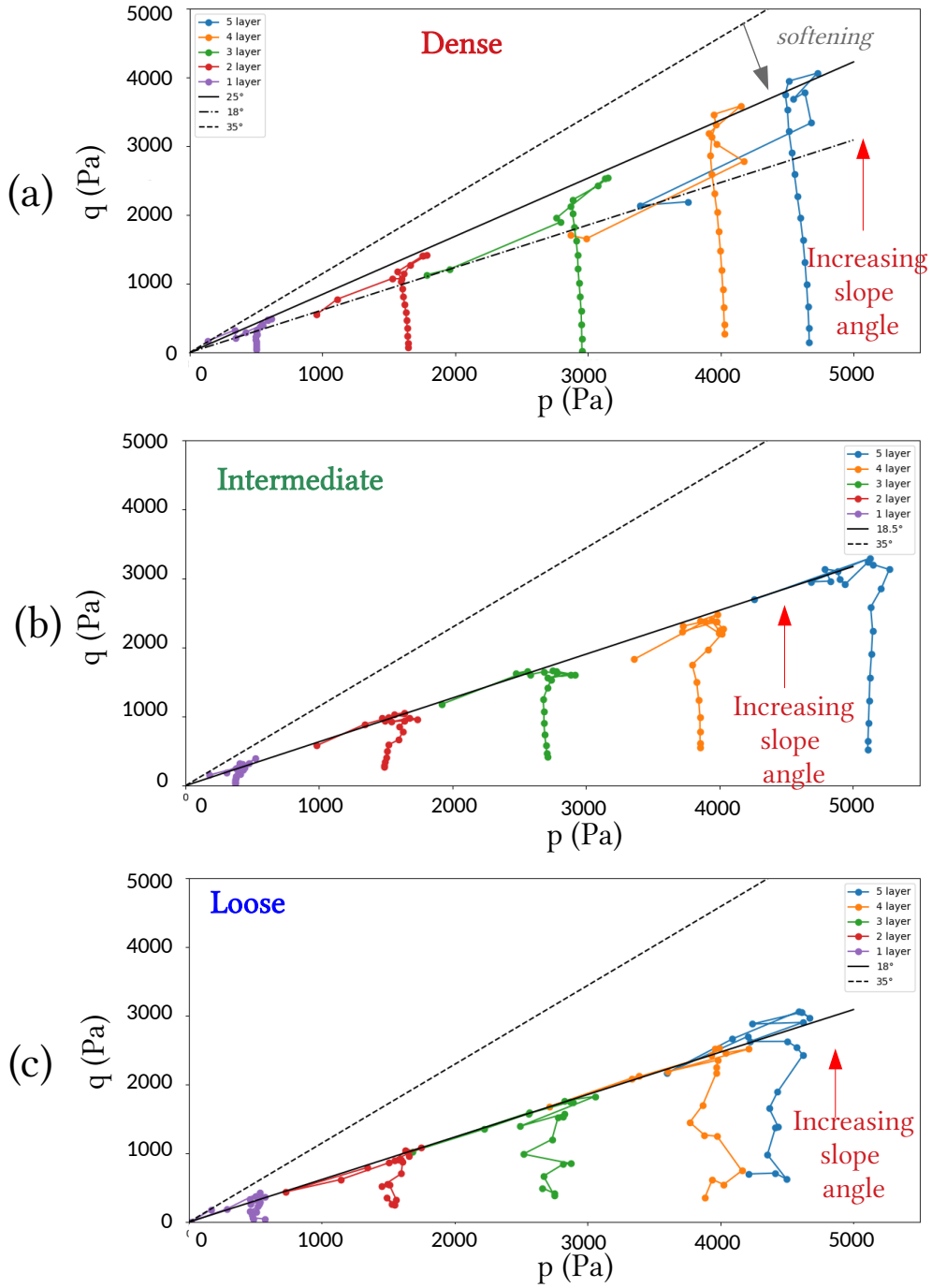

Figure 5.16 – $q - p$ curves for the dense sample *pbc* (a), the intermediate sample (b), the loose sample *pbc* (c). The five layers are the same as defined in Figure 5.7(a).

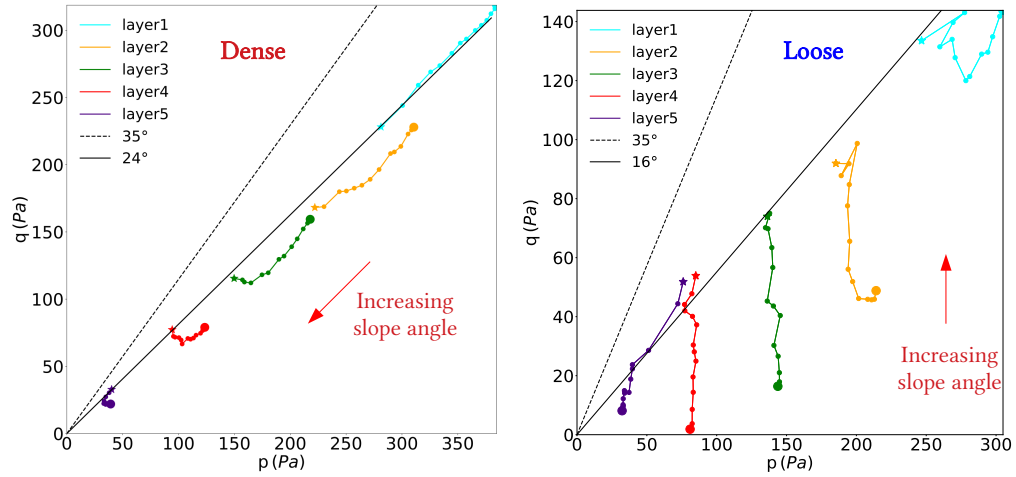

(a) (b)

Figure 5.17 – $q - p$ curves for the dense sample *rbc* (a) and the loose sample *rbc* (b). The five layers are the same as defined in Figure 5.7(a)

5.3.3 Volumetric behaviour and meso-structure evolution

Porosity

Figure 5.18 presents the φ_{80} porosity of all samples (Equation 5.4). In samples *pbc*, the dense sample is dilatant, the loose sample is contractant and the intermediate sample is slightly dilatant (Figure 5.18(a)). The porosities converge towards a unique porosity after the transition in the inertial regime. For samples *rbc*, the loose sample is slighly contractant before it reaches the wall as seen in Figure 5.10 (Figure 5.18(b)). For the dense sample, the behaviour is dilatant as the dense sample *pbc*. Porosities do not converge because of the influence of the upper wall.

Grain loops ratios

In terms of meso-structures, the ratios of the number of each loop order against the total number of grains are compared in Figure 5.19. For samples *pbc*, the behaviour of each sample is aligned with their porosity: intermediate and dense samples show decreasing ratio for low order loops while their ratio for high order loops are increasing, before decreasing at angles around their failure line (18° or 24°). The loose sample evolves less through decreasing

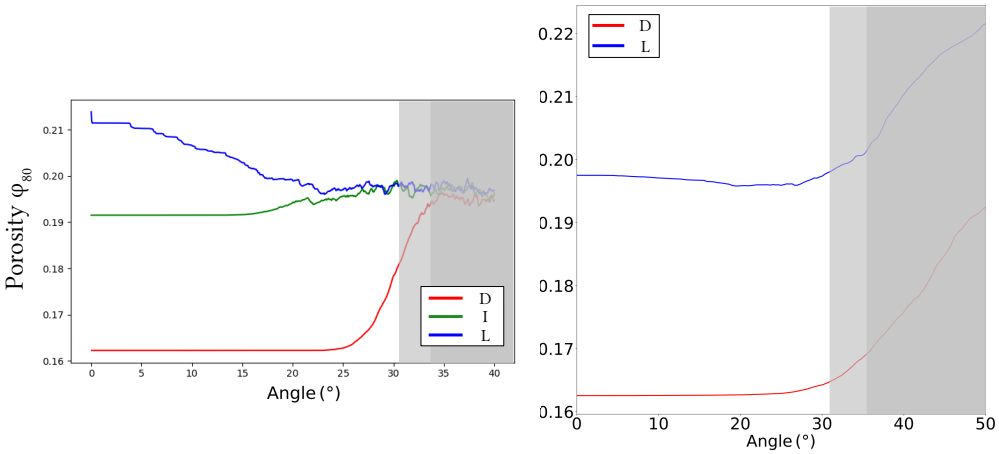

(a) (b)

Figure 5.18 – φ_{80}^{eff} porosity of samples *pbc* (a) and weighted effective porosities for the samples *rbc*. Grey parts show the inertial regime : the light grey part corresponds to the loose samples inertial transition, the dark grey part cooresponds to the dense ones.

number of loops per categories. All meso-structures ratios align after the inertial transition. Loose sample has more high order loops at the beginning while the intermediate and dense samples have more low order loops. For samples *rbc*, the varitions of the ratios are the same as for the dense and loose samples *pbc*. Low order loop ratios are decreasing for both but the dense sample has higher ratios. For high order loops, their ratios are both decreasing, but the loose sample has a greater ratio before 15°. The decrease of high order loop ratio for the dense sample begins after the failure line is reached. Ratios of grain loops are not converging because of the influence of the upper wall.

Grain loops lifespan and life expectancy

A last remark on the reorganisation of the grain loops is made in Figures 5.20 and 5.21. The birth and death histogramm shows that dense and intermediate samples *pbc* (Figures 5.20(a) and 5.20(b)) experience reorganisations later, between slope angles coresponding to the internal friction angle and to the inertial transition. However for the loose samples, the reorganisations are more instantaneous with bell shape histogramms. Grain loops have short life expectancy (Figures 5.20(c) and 5.21(b)). The dense sample *rbc* has a

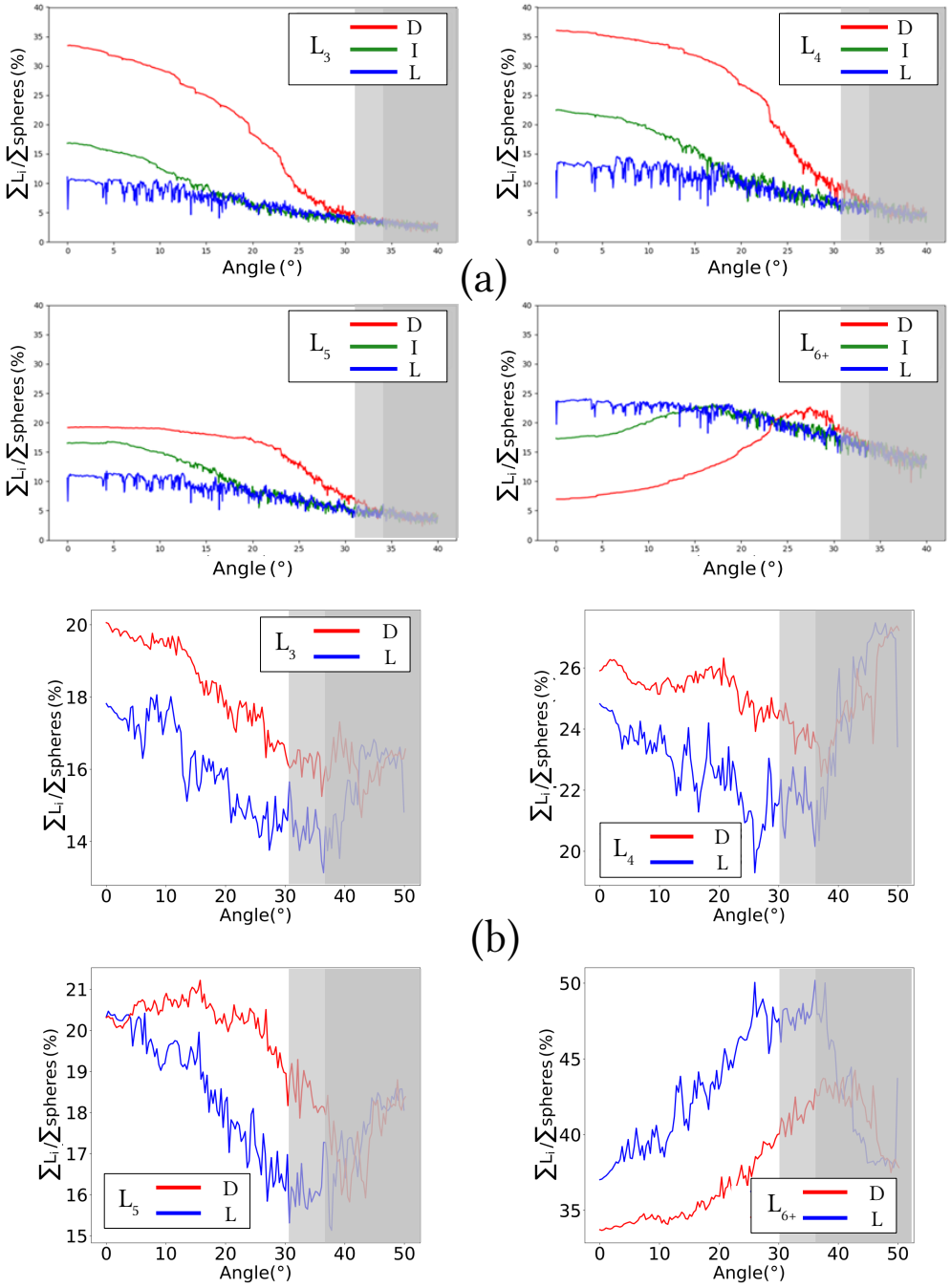

Figure 5.19 – Evolution of L3, L4, L5 and L6+ for samples *pbc* (a) and for samples *pbc* (b). Grey parts show the inertial regime : the light grey part begins for the loose sample inertial transition, the dark grey part begins for the dense's.

small bell shape histogramm, and some reorganizations occur later, around the failure line (Figures 5.21(a)). It seems that the dense sample is a bit more prone to early reorganizations than it is expected to be.

5.3.4 Conclusion on the influence of boundary conditions

In the last sections, differences in the behaviour of the sample of similar porosity but with different boundary conditions are raised. As underlined in the previous Section 5.2, the intermediate sample *pbc* and loose sample *rbc* do not have similar behaviour despite their similar initial porosities. The intermediate sample *pbc* shows some characterics corresponding to a dense sample (porosity and grain loops evolution), and other ones corresponding of a loose sample (stress path). The loose sample *rbc* has a loose behaviour, even though its contractant behavior is limited. Thus, the difference in porosity and grain loops evolution between the intermediate sample *pbc* and loose sample *rbc* is not the consequence of their different boundary conditions.

The samples with periodic boundary conditions reach a steady flow and converge to the same sample characteristics (Da Cruz et al., 2005). On the contrary, the samples with rigid boundary conditions exhibit a limited steady flow because of the clogging in the left up corner just after the inertial transition. They do not converge toward the same characteristics. Nevertheless, all the samples exhibit patterns of mechanical instability prior to the inertial transition, especially underlined by the life span and life expectancy diagramms for intermediate and dense samples *pbc* (Figure 5.20). For all samples, these marks of instability are even prior to the failure line reached before the inertial transition (Section 5.3.2). Those information are consistent with a pre-avalanche interval in (Daerr and Douady, 1999; Staron et al., 2006; Staron, 2008), in which the micro-structure undergoes numerous modifications. However, the pre-destabilization angle θ_d supposed in Section 5.2.2 should be reajusted considering the rearrangements spotted in the samples (Figure 5.20). The pre-destabilization angle is lower than the slope angle associated with the failure line. The closer the slope angle is from the inertial transition angle, the more important the micro-structure rearrangments are.

In brief, concerning the type of boundary conditions, two important consequences should be put forward:

- The confining pressure of the rigid walls creates non homogeneous samples in terms of stress state and with an initial non zero deviatoric stress.
- The upper wall prevents the samples to flow and avoids to observe the

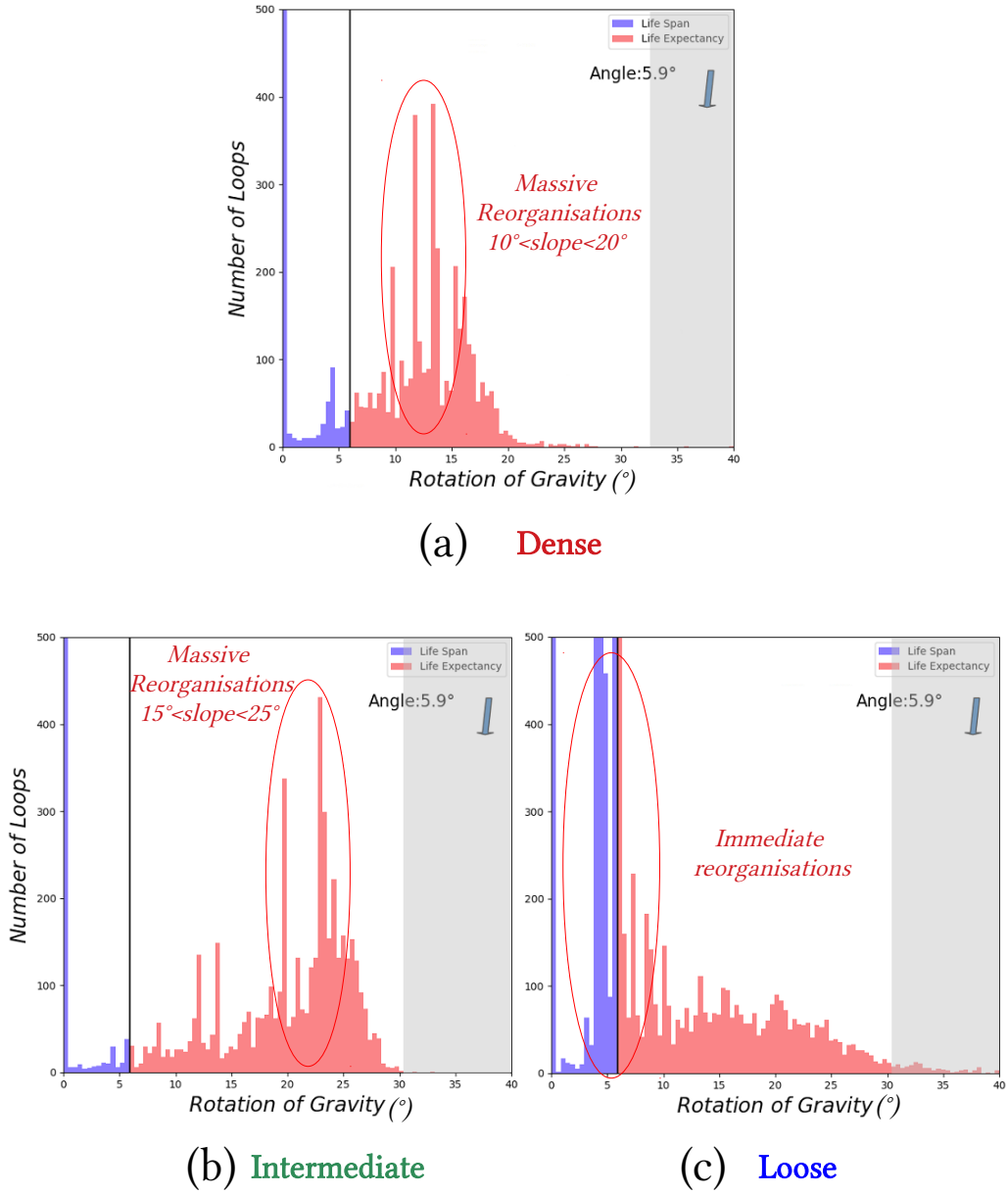

Figure 5.20 – Birth death histogramms for the dense sample *pbc* (a), the intermediate sample *pbc* (b), the loose sample *pbc* (c). Grey parts show the inertial regime.

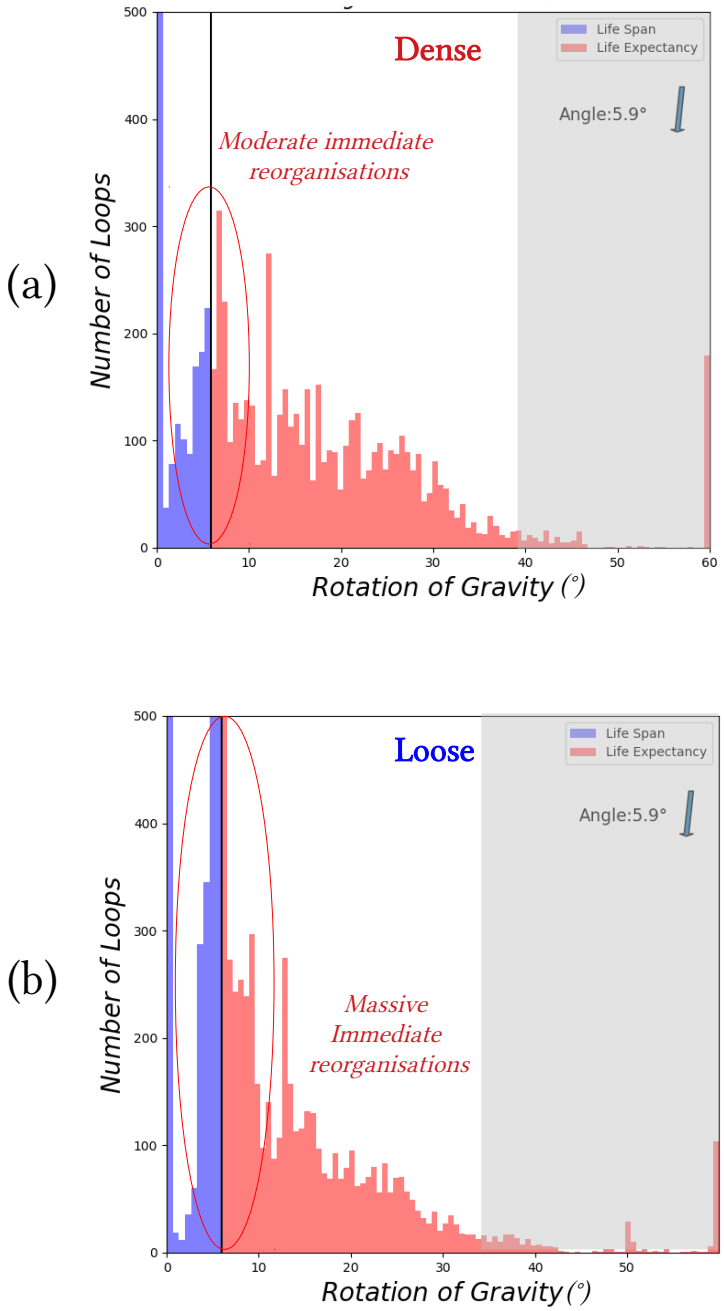

Figure 5.21 – Birth death histogramms for the dense sample *rbc* (a), the loose sample *rbc* (b). Grey parts show the inertial regime.

microstructure convergence.

A parallel between samples with rigid boundary conditions and retaining barrier on steep slopes can be drawn. In both cases, the stress state is lower than without rigid walls / barriers. The presence of barriers modify the stress state and enables important reorganizations during pre-rupture stage.

5.4 Analysis of bursts of kinetic energy

General behaviour of a granular packing during the two simulations with different boundary conditions has been studied along with the limitations of rigid boundaries. Analysis in this section is mainly focused on the loose sample *rbc*. The general onset of the failure is detailed in the first section. In a second part, two bursts of kinetic energy are studied with in the same framework as in Section 4.2.

5.4.1 Diffuse failure

The potential failure of the slope can be assessed with the sliding Index I_p (Equation 2.31) at the scale of the sample. Maps of I_p are given for the loose samples *pbc* and *rbc* (Figure 5.22). Contacts are represented by their branch segments (segment linking the center of both spheres in contact) and the color of the line depends on the value of the contact sliding index. The closer the contact is to sliding, the darker the color is. For both samples, the density of critical contacts ($I_p > 0.9$) increases with the slope angle. Moreover, the density of critical contacts is homogeneous in the sample *pbc* (Figure 5.22), meaning the failure is likely to be diffuse. This is consistent with the fact that the different parts of the sample reach the failure state at the same inclination angle (see Figure 5.7(c)). For the sample *rbc*, the proportion of contacts close to sliding is higher than in the sample *pbc*. However, the density of critical contacts is also homogeneous in the loose sample *rbc*. Similar I_p maps are obtained for the other samples (dense and intermediate). Thus, dense, loose or intermediate samples have a diffuse slope failure. Bursts of kinetic energy can appear everywhere in the sample.

For all samples, after the inertial transition, the kinetic energy increases strongly (but shortly for the samples *rbc*). The reorganisations in the microstructure are not sufficient to dissipate the external work, kinetic energy is thus increasing, and movement of grains becomes continuous. A grain velocity gradient exists, distributed along the cross direction. As a consequence, there is also a kinetic energy gradient inside the sample during the flow regime (Figure 5.23).

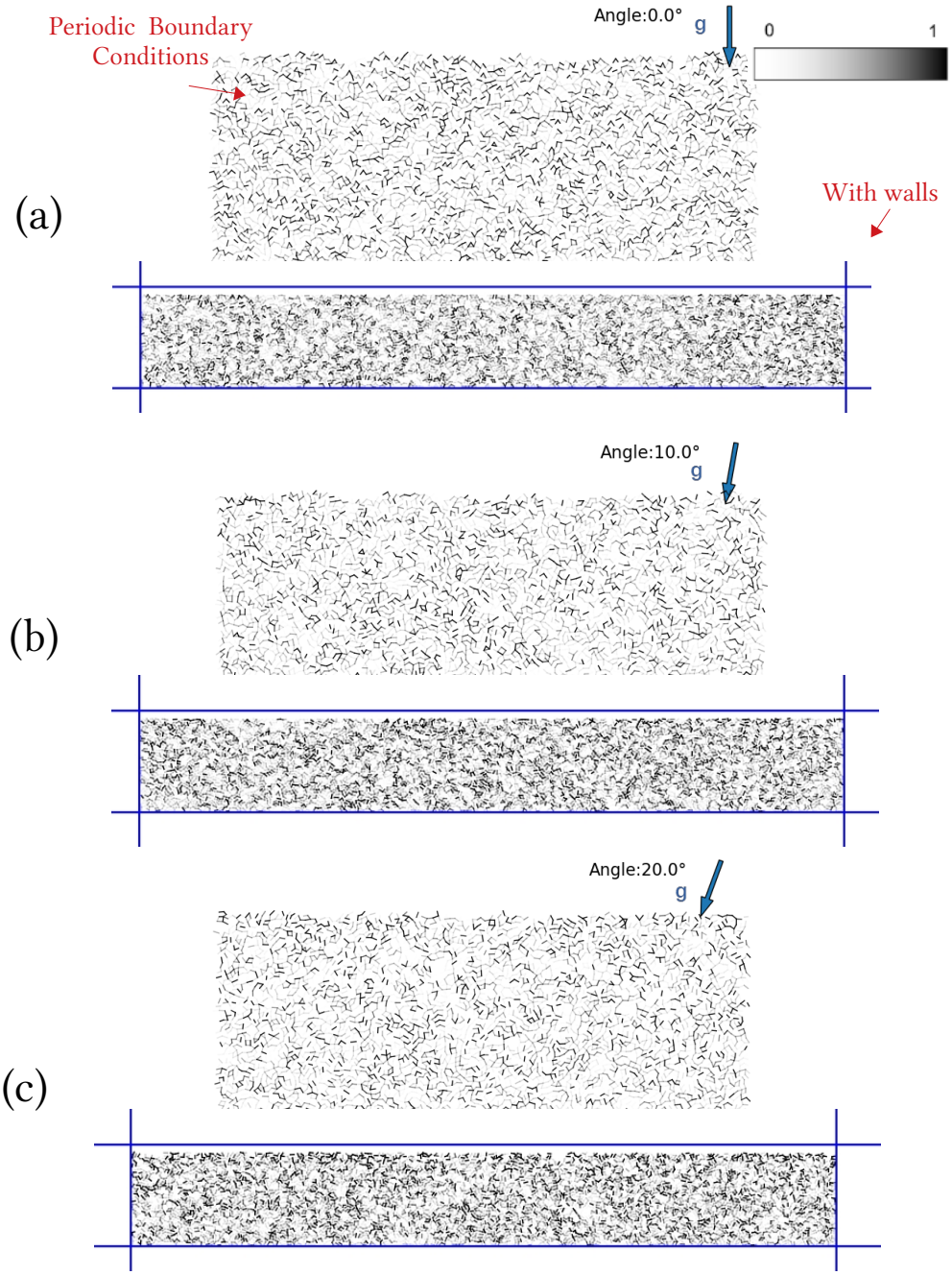

Figure 5.22 – Sliding index I_p representation for the loose sample *pbc* and loose sample *rbc* for 0° (a), 10° (b), 20° (c) showing the homogenous increase of the number of contacts close to sliding.

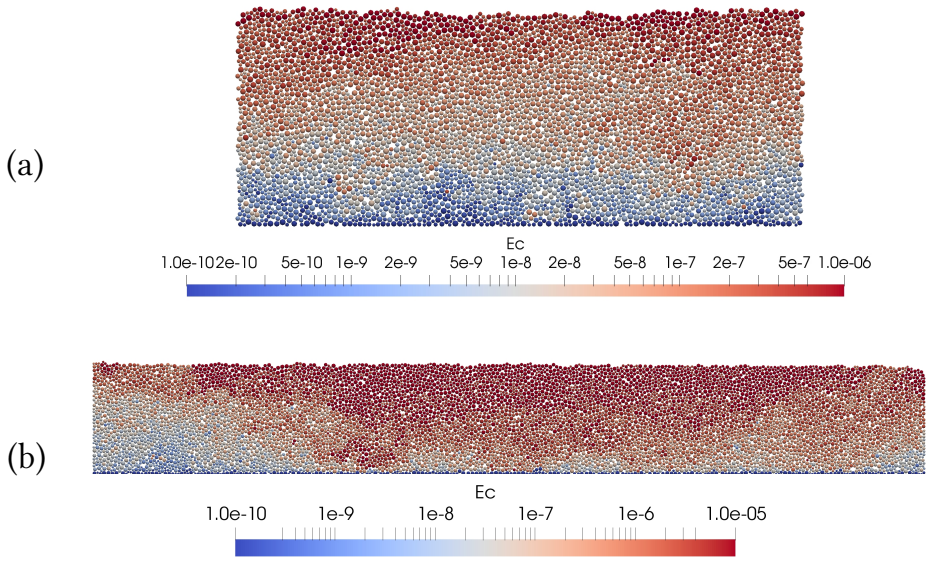

Figure 5.23 – Kinetic energy of particles in the loose sample *pbc*(a) and loose sample *rbc* (b).

To confirm the macroscopic diffuse failure, the weigthed average mesosecond-order work W_2^m is computed for the loose sample *rbc* (Figure 5.24). The grain averaged definition is selected in order to compute the weighted average since the macro second-order work results from the spatial homogeneization of the partition definition of the second-order work (see Section 3.2). Early vanishings of weighted average of W_2^m are exhibited by the sample (around 15°), before the failure line is reached. This observation is consistent with the existence of a bifurcation domain for granular materials. The larger the angle of inclination, the more frequent larger vanishing for the second-order work. Thus the entire sample experiences destabilization before its global inertial transition.

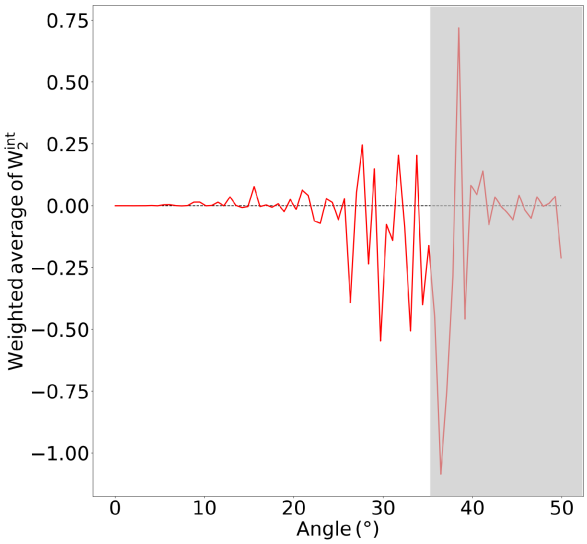

Figure 5.24 – Weighted average second-order mesoscopic work W_2^m along the entire gravitational stability test for the loose sample *rbc*. Grey area corresponds to the data after the sample reaches the top wall.

5.4.2 Bursts of kinetic energy in the loose sample *rbc*

Bursts of kinetic energy can appear everywhere in the sample, even though there are more bursts close to the free surface. In Chapter 4, bursts are detected by comparing the grain kinetic energy to the mean grain kinetic energy at critical state, which is (on average) a stationnary regime. No such stationnary regime exists in the present simulations. Therefore, the definition of a burst should be adjusted. The criterion becomes the following: a grain is assumed to be part of a burst if its kinetic energy is above the mean grain kinetic energy in the sample at the time of interest. Two bursts are arbitrary selected in the loose sample *rbc* (Figure 5.25), between 11.8° and 12.5°. They occur within the same angle range, but one after the other, one at the bottom of the sample, the other near the free surface.

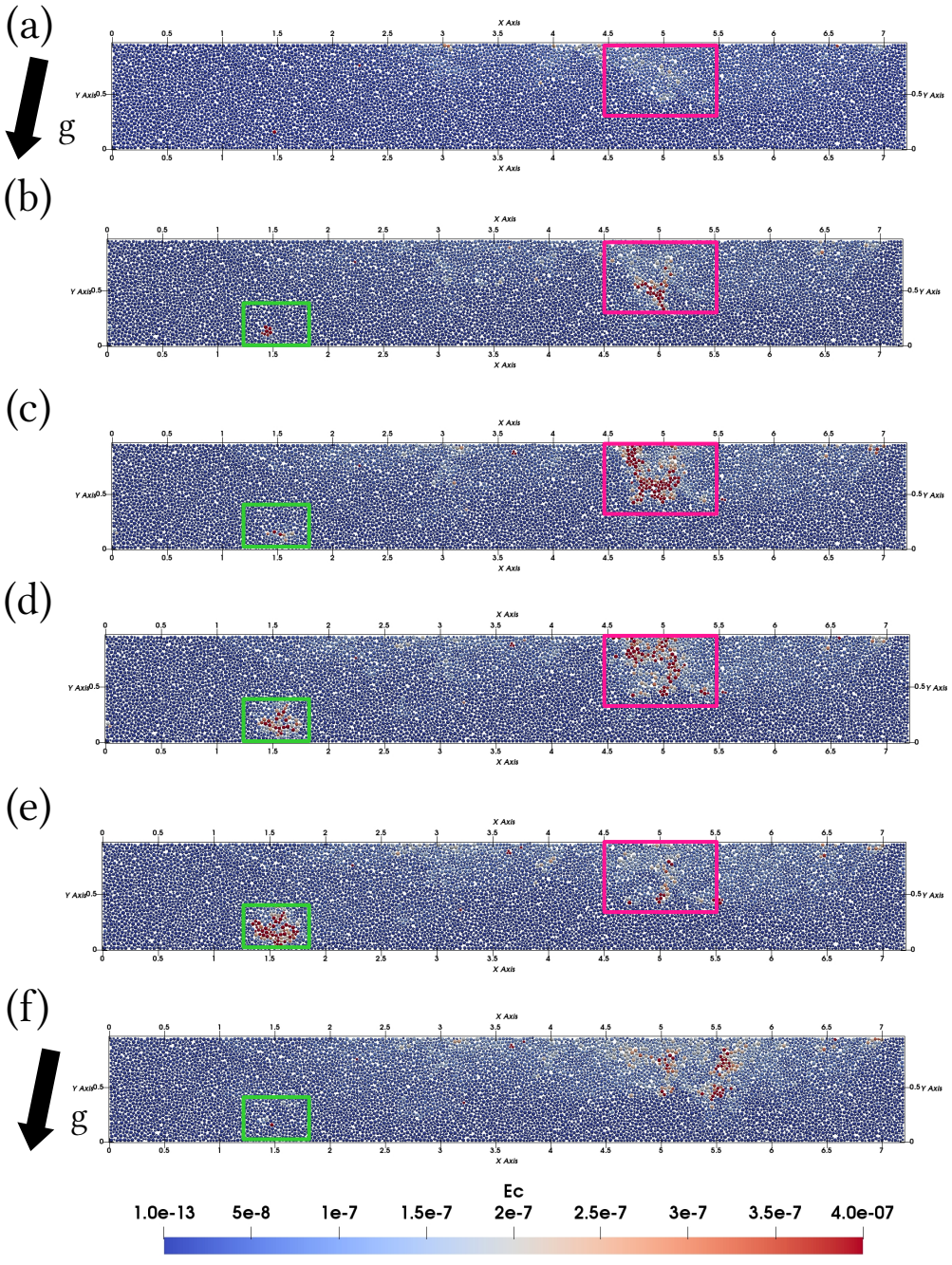

Figure 5.25 – Time lapse of the two bursts and their associated area (in pink for the shallow burst, in green for the deep burst).

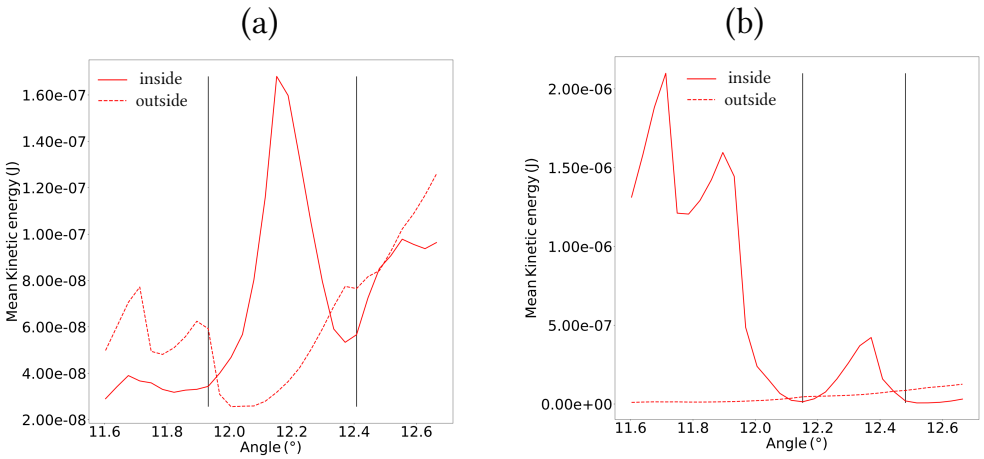

Figure 5.26 – Mean kinetic energy per particle inside and outside the shallow burst (a) and the deep burst (b).

The mean kinetic energy per grain in the inner burst domains confirms the two events selected are bursts. The kinetic energy inside the burst area is four time larger than outside (Figure 5.26). The two areas are *active*, that is to say other bursts have occured or will occur in the same area (for example, before the deep burst in Figure 5.26(b)).

Deep burst of kinetic energy

The probability density function of the sliding index I_p in the inner (green box in Figure 5.25) and outter domains before and after the burst is given in Figure 5.27. The difference between the two states is not well marked as for the burst in the biaxial test (section 4.2.3), but the proportion of contacts close to sliding ($I_p > 0.8$) decreases after the burst. The pdf of the sliding index outside is suggesting that the rest of the sample is quite unstable too (increase in the pdf close to $I_p = 1$).

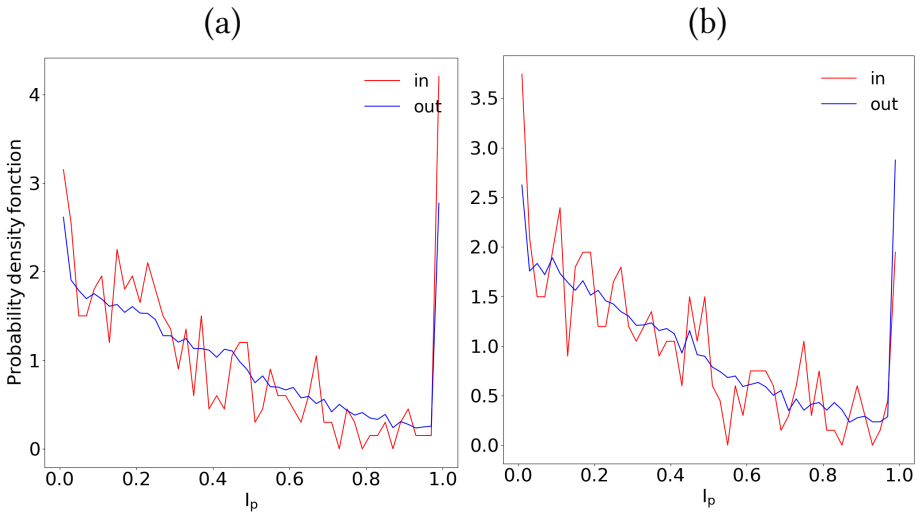

Figure 5.27 – Probability density function of the sliding index I_p for the contacts inside the inner and outter domains for the deep burst area, before the burst (a), and after (b).

The same tendency can be found for the relative evolution of the meso-structures (Figure 5.28) and the surviving rates (Figure 5.29) in the inner and outter burst areas. For the relative evolution, the active changes outside the burst area blur the changes inside the burst area (Figure 5.28(b)). Moreover, this inner area is concerned by two successive bursts (5.26(b)) and the concentration in time and space for the relative evolution of meso-structures is no longer striking. The succession of two bursts is also apparent for the life expectancy of the meso-structures inside the burst area (Figure 5.29(a)). The slope of the grain loops surviving rate is already steep before the occurence of the burst studied. However the stabilization is clear after the burst (plateau). in the outter burst area, the slope of the curve has a smaller coefficient, indicating less reorganizations take place in the rest of the sample (occuring at a smaller rate). These observations are consistent with those reported in Section 4.2.4 for biaxial tests.

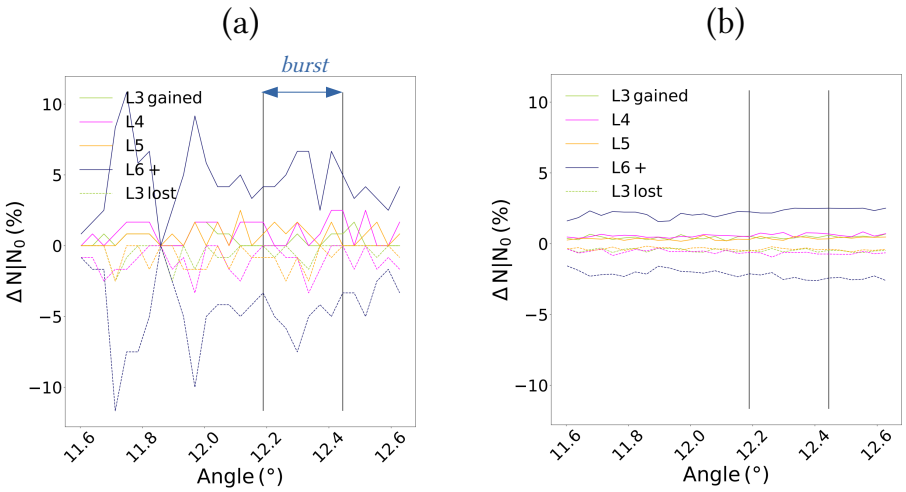

Figure 5.28 – Relative evolution of the four different orders of loops inside (a) and outside (b) the deep burst area.

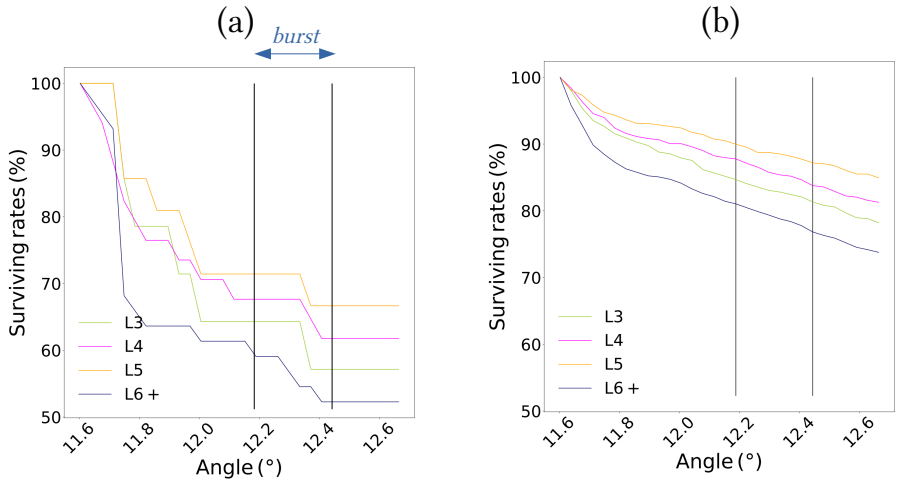

Figure 5.29 – Surviving rates of the four different orders of loops inside (a) and outside (b) the deep burst area.

The weighted average of the second-order work W_2^{Weber} inside the deep burst area shows that there is a vanishing of the second-order mesoscopic work, just before the burst (Figure 5.30). This results confirms the ability

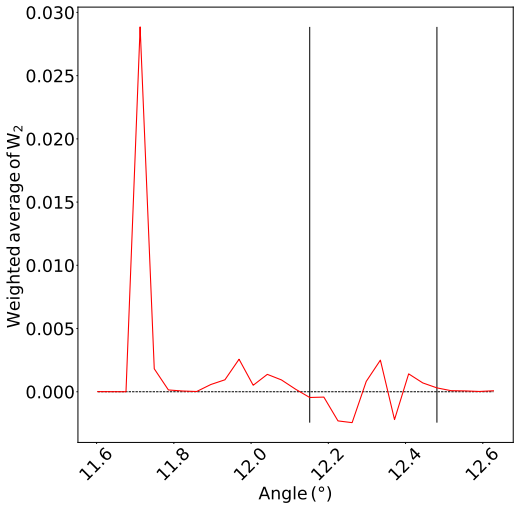

Figure 5.30 – Weighted average of *Weber* second-order mesoscopic work inside the deep burst area.

of the Weber second-order meso-work as a precursor for bursts of kinetic energy occurence, according to the results given in Chapter 4. Thus, local vanishing of the second-order meso-work can occur prior to the failure state, underlining local mechanical instabilities. Similar results can be found in the litterature for granular media resting in a slope configuration. Even though second-order mesoscopic work is not computed in (Darve and Laouafa, 2000), local vanishing of the second-order work in a granular medium on a slope is exhibited prior to the failure.

Shallow burst of kinetic energy

The observations for the shallow burst are the same as for the burst occuring deeper in the sample. The shallow burst area (pink box in Figure 5.25) undergoes successive bursts of kinetic energy. As a consequence, the relative evolution of the meso-structure in the inner burst domain is not occuring only during the burst event (Figure 5.32(a)). The global instability of the sample creates a steady percentage of reorganizations, which is still less than inside the burst area (Figure 5.32(b)). The surviving rates curve in the inner domain has a steeper slope than in the outter, but with no plateau at the end of the burst (Figure 5.32(c)). It is linked to the fact that the free surface starts moving continuously before the bottom of the sample does. However

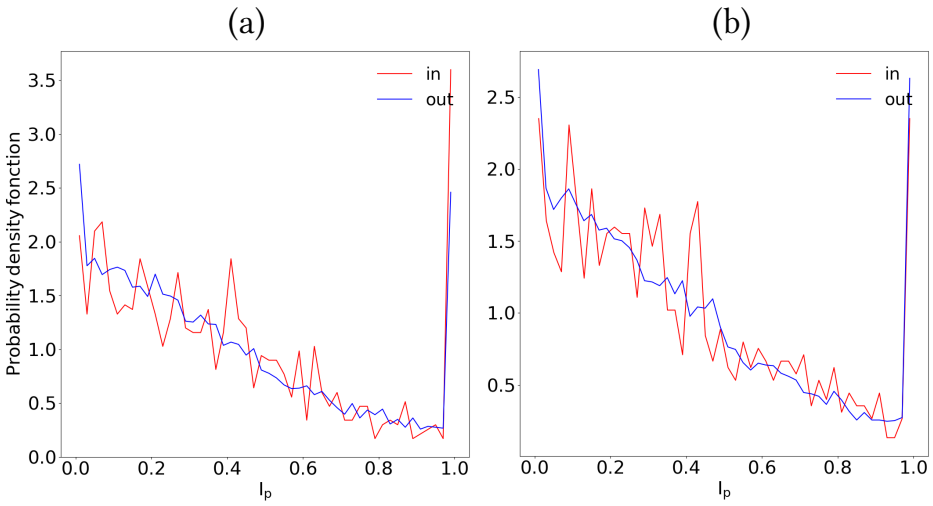

Figure 5.31 – Probability density function of the sliding index I_p for the contacts inside and outside the shallow burst area, before the burst (a), and after (b).

there is still a decrease in the proportion of unstable contacts inside the area after the burst (Figure 5.31(b)). This decrease underlines a stabilization effect of the reorganizations inside the burst area, but according to Figure 5.32, this effect is limited. Again, the weighted average of the second-order mesoscopic work W_2^{Weber} vanishes before the burst (Figure 5.33), and proves again to be a good indicator of instability.

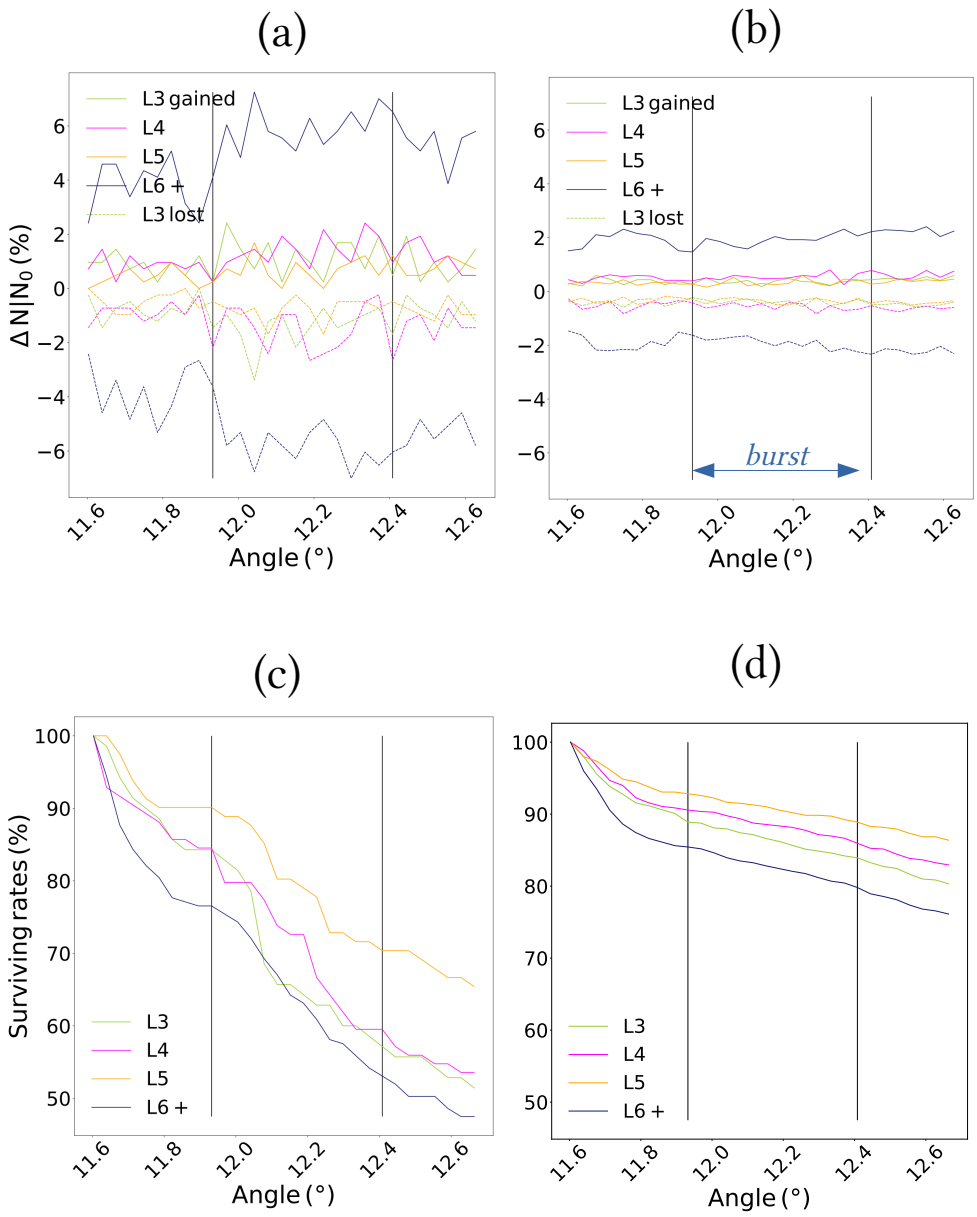

Figure 5.32 – Relative evolution (resp. surviving rates) of the four different orders of loops inside (a) (resp. (c)) and outside (b) (resp (d)) the shallow burst area.

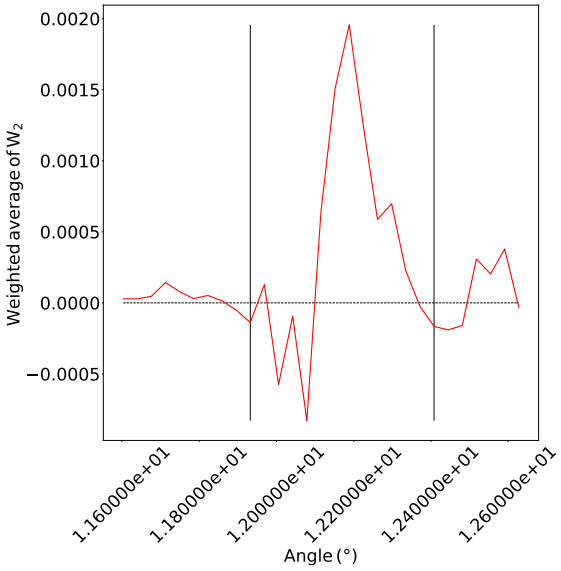

Figure 5.33 – Weighted average *Weber* second-order mesoscopic work inside the shallow burst area.

5.4.3 Conclusion on specific patterns for bursts of kinetic energy

In this section, the diffuse and progresive failure of the loose sample *rbc* is further proved by studying bursts of kinetic energy occuring close to the free surface or deeper in the sample. The same results are found in the sample *pbc* (Wenrui, 2021). The bursts studied in the loose sample *rbc* are occuring when the sample is already well destabilized, but the features observed during the biaxial test are globally recovered, especially for the second-order mesoscopic work variations.

Even though analysis of bursts in the very early stage of the simulation lacks to reach a conclusion, a hypothesis on the links between bursts of kinetic energy and slope instability can be formulated. The failure can be seen as the succession of bursts of kinetic energy. Bursts of kinetic energy are short time events corresponding to localized reorganizations as seen in Chapter 4. The study of the bursts in the loose sample *rbc* shows that the succession of bursts creates a greater rate of rearrangements (Figure 5.29, 5.28 and 5.32). The inertial transition results in the constant movement of the sample, especially at the free surface (Figure 5.23). Consequently, the accumulation of short term reorganization and localized bursts of kinetic energy leads to a long term reorganization and global inertial transition (Deng et al., 2021b,a).

5.5 Conclusion

Gravitational slope instability simulations have been carried out with two different methods. Periodic boundary conditions allow to study the full destabilization. The rigid boundary conditions enable to study the inertial transition and the beginning of the flow regime, because of sample clogging in a corner with the upper wall. In other words, both boundary conditions can be used for the inertial transition and bursts of kinetic analysis. Although the stress state is modified by the presence of rigid boundaries, similar slope angles are observed for the inertial transition and the failure line for both boundary conditions. A pre-avalanche slope angle range is noticed for both boundary conditions. The pre-destabilization angle θ_d is inferior to the slope angle for which the failure line is reached (around 15°), and the upper limit is the slope angle for which the inertial regime i sestablished (around 30°). Diffuse failure is highlighted for both boundary conditions, irrespective of the initial porosity. Analysis of bursts during the simulations proves the revelance of the framework introduced in Chapter 4. With the results obtained from the detailed analysis of outbursts, an assumption can be made on the link between bursts of kinetic energy and inertial transition. If bursts of kinetic energy are regarded as short term reorganization, then the inertial transition can be considered as an accumulation of outbursts leading to a long term reorganization.

Chapter 6

General conclusion and perspectives

6.1 Synthesis of the main outcomes

The present work introduced an approach at the mesoscopic scale to define and analyse bursts of kinetic energy, using 2D DEM simulations. This investigation was based on the definition of meso-structures as grain loops and related meso-quantities, especially meso-stresses, meso-strain and second-order mesoscopic works. The objective was to identify precursors for localized bursts of kinetic energy. In the meantime, the mechanisms of the propagation of bursts were also identified and allowed to understand why bursts stay localized or propagate. The meso-quantities are applied to gravitational instability, reinforcing the link between bursts of kinetic energy and inertial transition.

6.1.1 Meso-structures analysis to identify precursors of bursts of kinetic energy

The new quantities defined in Chapter 3 at the mesoscopic scale were applied in Chapter 4 and Chapter 5 to the analysis of bursts of kinetic energy. There are two approaches for defining the meso-quantities. One vision is structural, focusing on only one meso-structure independently from any neighboring meso-structures. In this approach, macro-scale quantities can be found from statistic homogenization. The other vision is based on the partition of the specimen, macro-scale quantities are then recovered from the spatial homogenization of the meso-quantities. The structural approach is necessary for the application of the second-order mesoscopic work criterion, while the partition approach is interesting to make a direct link bewteen the meso-scale and the macro-scale (thanks to spatial averaging). Definitions of meso-stress, meso-strain and associated second-order mesoscopic work were carefully analyzed in order to be consistent whith related macroscopic quantities. It was shown that only the grain averaged second-order work W_2^m and the Weber second-order work W_2^{Weber} are suitable candidates to compute the second-order mesoscopic work. The partition formulation W_2^m is prefered in order to map the sample domain and detect areas of mechanical instabilities

based on the vanishing of the second-order mesoscopic work. The structural approach W_2^{Weber} is more convinient to analysis meso-structures individually. The comparison between the effective and real meso-porosity highlihts the presence of rattlers.

Meso-structures as grain loops have proven to be useful to better understand the behaviour of granular materials. Grain loops evolution (incremental evolution, surviving rate, lifespan and life expectancy) is a powerful quantitative measurements to understand the propagation of bursts and their occurrences, which can not be seen at the macro-scale. The vanishing of the second-order mesoscopic work is shown to be as a precursor of the occurence of bursts of kinetic energy. Moreover, it has been shown that a burst appears in an area with more contacts close to sliding, and that contains loops of high order with larger loop area (for similar orders) than outside the burst domain. During the burst propagation, meso-structures rearrangement mostly concerns high order loops (in terms of proportions of the loop populations). Small order loops are broken to create rattlers or high order loops as the the kinetic energy increases, then high order loops collapse to reform smaller order loops as the kinetic energy decreases. During a burst, the meso-structures in the burst area reorganize at a rate much higher than in the rest of the sample not affected by the burst. A burst remains localized if the meso-structure can rearrange efficiently and stops the propagation. This can be observed with the variation of the Weber second-order mesoscopic work, that becomes positive after the peak of energy, when the meso-structure stabilizes again.

In the case of the localization of the deformation, bursts of kinetic energy come from the shear band only. If there is a localization of the deformation in the granular material, the mesoscopic mechanical instabilities are also concentrated, in the same area as the deformation. If there is no localization of the deformation, bursts of kinetic energy are more likely to appear everywhere in the sample.

6.1.2 Triggering of gravitational instability

One of the application of the study of bursts of kinetic energy is the triggering of gravitational instabilities. A 2D idealized modelling was used, with two boundary conditions: periodic boundary conditions and rigid boundary conditions. The main difference in the results was the stress state in the sample. With periodic boundary conditions, the whole sample reaches failure for the same slope angle (the stress ratio q/p is homogeneous in the sample). On the contrary, with rigid boundary conditions, the Mohr-Coulomb failure criterion is reached for different slope angles depending on the depth. The upper layer is the first part of the sample to reach the failure surface. Expanding to

larger scales, this observation is consistent with the use of safety barrier on steep slope for snow and rock avalanches. They act as anchors in the ground, responsible for a decrease in the deviatoric stress in the soil. Despite this difference, both boundary conditions exhibit the same behaviour regarding the triggering of the inertial transition. No permanent inertial regime is observed for rigid boundary conditions because of the presence of the top wall which prevents the granular packing from sliding permanently. For both type of boundary conditions, there is an pre-avalanche interval, before the inertial transition, when the granular system exhibits strong micro-structure rearrangements. The pre-destabilization angle (smaller slop angle from which reorganizations appears) seems to be lower than the internal friction angle, according to lifespan and life expectancy of grain loops and bursts analysis. Moreover, the triggering of bursts of kinetic energy relies on similar microstructure features in both cases.

6.1.3 From bursts of kinetic energy to inertial transition

The gravitational instability simulations allowed to observe the transition between small and localized bursts of kinetic energy and the global movement of the sample, with a velocity gradient. The steeper the slope gets, the less localized the reorganisations in the meso-structures are. Bursts are becoming larger and tend to fuel themselves creating zones of instability, such as the free surface, until the inertial transition establishes. Bursts of kinetic energy can be interpreted as short term reorganizations, and the accumulation of bursts can be regarded as long term reorganization.

6.2 Perspectives

6.2.1 Improving the modelling

Accounting for grain rotations

Grain rotation is disregarded from the definition of the meso-strain, meso-stress and second-order mesoscopic work. However grain rotations are proved to play a great role in the behaviour of granular materials (Oda and Kazama, 1998; Da Cruz et al., 2005; Liu et al., 2018).

Grain shape

In this work, grains are simplified as spheres in order to reduce computational cost. Several methods make possible to take into account, in an exact

or simplified way, the shape of the grains: use of the Level-set method (Duriez and Galusinski, 2021), polyhedron forms (Azéma et al., 2009; Quezada et al., 2012), clumps (Mede et al., 2018) and the introduction of a rolling friction (Hosn et al., 2017), to simulate more complex forms for grains in granular material simulations with a discrete element method.

2D to 3D modelling

The notion of grain cycles as a partition of the sample domain is only valid in 2D conditions: it is the starting point for an analysis at this intermediate scale. In 3D, there is still not general agreement for defintion of 3D grain loops (Nguyen et al., 2020). A 3D defining for grain loops is needed, which is the aim of very recent works (Chueire et al., 2021). This is the only lock that prevented mesoscopic analysis of three-dimensional simulations.

6.2.2 Force chains

As force chains definition involves the mean stress within the assembly considered, this requires that the stress within the assembly is nearly homogeneous. In the context of granular packing on a slope, the stress increases with depth. Force chains evolution can be the object of further research provided that the standard definition is adapted. Even at REV scale, the standard definition makes force chains artificially short lived meso-structures since it assumes that force chains are linear structures. Branching is disregarded which makes force chains disappearing and reappearing frequently under small contact forces fluctuations. As an illustration, considering the biaxial test, the relative evolution (Equation 2.33 and 2.32) of force chains for the selected bursts presented in the dense sample S_1 and the loose sample S_2 does not give much information about a contrast between inside or outside the burst area (Figure 6.1). Even if the reorganization is more noisy and intense inside the burst area (Figure 6.1(A1) and 6.1(B1)), it appears that force chains are rearranging with a constant rate either inside or outside the burst area.

Zhu et al. (2016c,b); Tordesillas et al. (2011) have proven that the grain loops surrounding the force chains ensure their stability. It will be then interesting to focus on the behaviour of grain loops surrounding force chains during bursts of kinetic energy and to track their co-evolutions.

6.2.3 Global microstructure reorganization as a sequence of burts of kinetic energy

At critical state, we have shown that bursts of kinetic energy have a finite size and thus inertial transition is limited. There is also a higher rate of reorganizations inside the burst area than where the burst does not propagate. According to the work of Na Deng (Deng et al., 2021b), there is two time scale mechanisms forcing the micro-structure to reorganize : short time reorganization and long time reorganization. It will be interesting to invest, qualitatively, the rate of reorganization during a burst of kinetic energy, in the burst domain, to link the bursts to the short time reorganization mechanisms. Thus, this future work can enable to understand how successive bursts result in global micro-structure reoranization. Similary, successive bursts of kinetic energy seem to lead to the inertial transition in the context of a slope. The analysis of a bursts sequence at different slope angles will be able to confirm if the mechanisms observed in the biaxial test are recovered also in the context of gravitational instability.

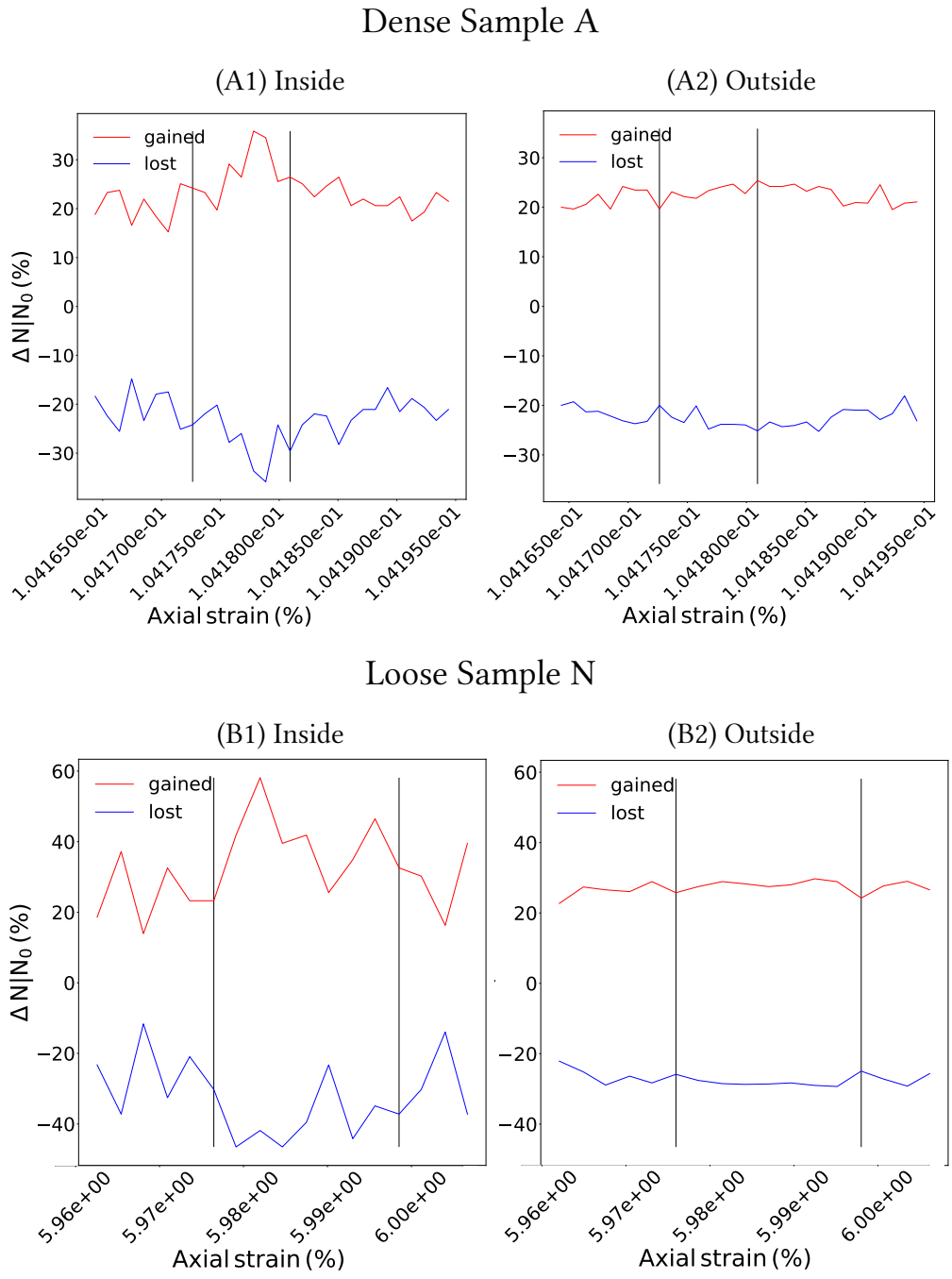

Figure 6.1 – Relative evolution of force chains for the burst presented for the dense sample A (resp. loose sample N) inside (A1) (resp.(B1)) and outside the burst area (A2) (resp. (B2)).

Appendix A

Liste de publications

Le présent manuscrit redonne de la cohérence aux différents résultats obtenus au cours des trois ans de thèse. Certains résultats du Chapitre 3 et 4 plupart des résultats peuvent être retrouvés dans les deux articles de journaux ou actes de conférence suivants :

Articles de journaux :

Adriane Clerc, Antoine Wautier, Stéphane Bonelli, and François Nicot. Mesoscale signatures of inertial transitions in granular materials *Granular Matter*, 23(2), 2021.

Actes de conférence :

Adriane Clerc, Antoine Wautier, Stéphane Bonelli, and François Nicot. Mesoscale inertial transition in granular materials. In *EPJ Web of Conferences*, volume 249, page 10004. EDP Sciences, 2021.

Annexe B

Résumé étendu en français

B.1 Contexte général

Un milieu granulaire est composé de grains en contacts dans une phase fluide (du gaz et/ou de l'eau). Composants d'un pierrier, d'une dune de sable, d'un manteau neigeux, d'une digue maritime ou fluviale, les milieux granulaires sont omniprésents. Derrière leur apparente simplicité à l'échelle d'un grain, ces milieux présentent une grande diversité de comportements selon les sollicitations imposées à l'échelle de plusieurs grains. Leur complexité et leur originalité résident dans le fait que ces milieux peuvent se comporter comme un solide, un liquide et même un gaz. Une avalanche, un mouvement de terrain, la rupture d'un barrage en remblais sont les conséquences de la transition solide - fluide d'un matériau granulaire (Figure B.1). Les régions montagneuses concernées représentent environ un quart du territoire français métropolitain. De plus, la France présente un nombre conséquent de barrages (plusieurs dizaines de milliers de petits barrages, environ mille grands barrages) et plusieurs milliers de kilomètres de digues fluviales et maritimes (Bonelli, 2012). En relation avec les nombreuses applications associées à la gestion du risque, il est nécessaire de mieux comprendre les mécanismes de la transition de l'état solide à l'état fluide, appelée transition inertielle, et plus particulièrement d'identifier les causes de son initiation et les éventuels signaux précurseurs.

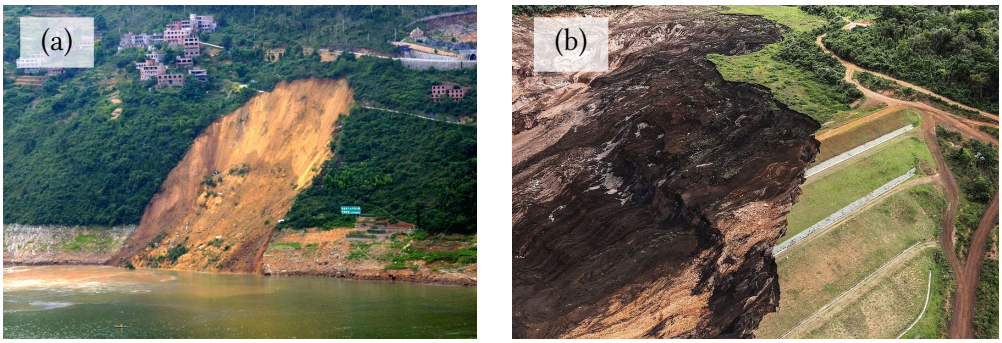

FIGURE B.1 – Exemples de conséquences de la transition solide - fluide dans un milieu granulaire : (a) Mouvement de terrain rotationnel sur les bords de la rivière Daning, Comté de Wushan, Chine (24.06.2015) (b) Barrage de retenue de déchet minier après liquéfaction, Mine exploitée par Vale SA, Brumadinho, Brézil (25.01.2019)

B.2 Objectifs et méthodologie

Afin d'étudier la transition inertielle dans les milieux granulaires, nous avons chercher à identifier et analyser des évènements inertiels, appelés bouffées d'énergie cinétique. Les bouffées d'énergie cinétiques sont considérées comme des évènements précurseurs à une transition inertielle (Darve et al., 2004; Wautier, 2018). L'objectif principal de cette thèse est d'analyser des bouffées d'énergie cinétique sous un angle micromécanique pour identifier leurs précurseurs. Ce travail est réalisé d'un point de vue numérique en prenant en compte la nature discrète des milieux granulaires en choisissant une méthode aux éléments discrets (DEM) pour modéliser les milieux granulaires. Ainsi, un milieu quasi 2D (grains 3D centrés sur un plan), composés de grains sphériques dont les interactions sont régies par des lois élastoplastiques, est simulé via le logiciel en license open source YADE (Šmilauer et al., 2010). Les analyses multi-échelles sont souvent mises en oeuvres pour étudier les milieux granulaires (Liu et al., 2018; Staron and Hinch, 2005; Zhu et al., 2016b) en reliant les deux échelles extrêmes que sont les échelles micro- et macro-scopique. Par exemple, une rupture de digue a des origines microsco-

piques (rupture des contacts entre les grains) et des conséquences à l'échelle macroscopique (glissement du talus). Suivant cette logique, une analyse à l'échelle mésoscopique (à l'échelle d'un petit nombre de grains) est proposée. Dans un milieu quasi 2D, des méso-structures peuvent être définies par partition du réseau de contacts (Zhu et al., 2017; Liu et al., 2018) : les cycles de grains. Les cycles de grains ont déjà prouvé leur capacité à rendre compte des réorganisations au sein du milieu. Dans le contexte de la mécanique des milieux continus, y compris les milieux granulaires, les instabilités dépendent de l'état contrainte/déformation comparé aux conditions de chargement. En reprenant la condition nécessaire de stabilité de Hill Nicot et al. (2017) et Nicot et al. (2009, 2012b) ont formulé un critère nécessaire au développement d'une instabilité. Pour un point matériel et pour de petits incréments, ce critère donne la potentialité du système à développer de l'énergie cinétique sans sollicitation extérieure et depuis un état d'équilibre ($\boldsymbol{\sigma}$,$\boldsymbol{\varepsilon}$) atteint après un historique de chargement donné, si $W_2^{int} = \Delta\boldsymbol{\sigma} : \Delta\boldsymbol{\varepsilon} < 0$. L'annulation du travail du second ordre est une condition nécessaire à la transition inertielle (Nicot et al., 2009; Daouadji et al., 2011). Dans le cadre de la recherche de précurseurs aux bouffées d'énergie cinétique et d'une étude multi-échelle, une expression mésoscopique pour le travail du second ordre est proposée.

B.3 Quantités à l'échelle mésoscopique

Afin de définir une échelle mésoscopique, il existe deux approches complémentaires. D'un coté, l'approche par partition définit le méso-domaine comme étant la partie interne (aire ou volume) d'un cycle de grains (Figure B.2 (a)). Dans ce cas, la quantité macroscopique est retrouvée par moyenne spatiale des quantités mésoscopiques. D'un autre coté, le méso-domaine de l'approche structurelle comprend la partie externe d'un cycle de grains (Figure B.2 (b)) et la quantité macroscopique est calculée à partir de la moyenne statistique des quantités mésoscopiques. Cette approche est nécessaire pour le calcul du travail extérieur du second ordre et elle permet la mise en place d'un bilan énergétique lié au critère du travail du second ordre.

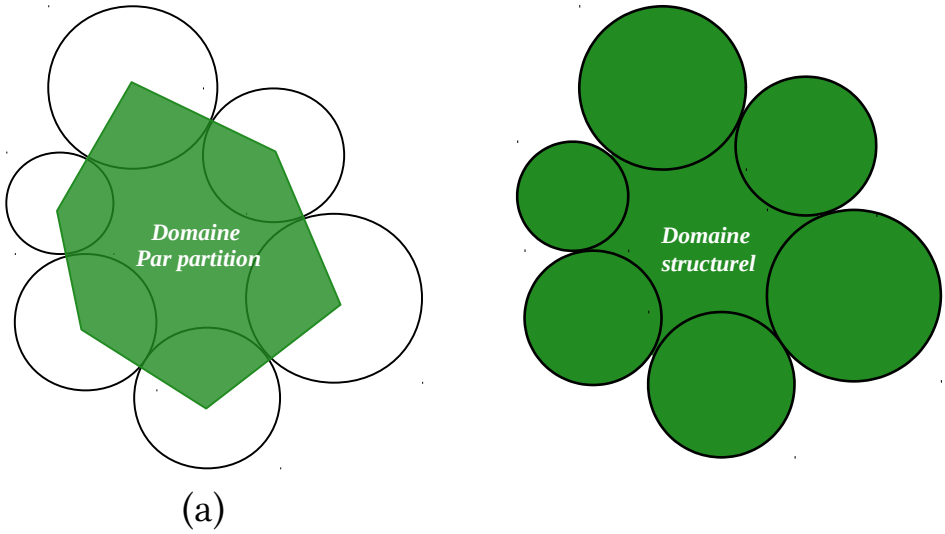

FIGURE B.2 – Les deux approches pour définir un méso-domaine : (a) approche par partition (b) approche structurelle

Selon l'approche choisie, l'énergie cinétique, l'énergie élastique et la porosité peuvent être définies à l'échelle mésoscopique. Les particules libres piégées dans les cycles de grains, peuvent être incluses, ou non, dans les calculs. La comparaison entre des données (de porosité plus particulièrement) avec ou sans particules libres est intéressante pour mieux définir le rôle de ces particules. Un des objectifs de ce travail est de proposer une expression du critère du travail du second ordre à l'échelle mésoscopique. Une contrainte mésoscopique $\boldsymbol{\sigma}$ et une déformation mésoscopique $\boldsymbol{\varepsilon}$ doivent être donc définies. Elles sont définies bien que, à l'échelle mésoscopique, petite par rapport à la taille d'un VER, il n'y a pas d'unicité de leur définition et bien qu'il n'y ait *a priori* aucune raison pour que les méso-domaines remplissent les deux conditions à l'utilisation de l'annulation du travail du second-ordre comme marqueur d'instabilité mécanique qui sont un état initial d'équilibre et un travil extérieur nul. En faisant l'hypothèse que la condition d'homogénéité macroscopique peut s'appliquer sur un méso-domaine Ω, alors le travail du second ordre est exprimé ainsi à l'échelle mésoscopique :

$$\left(W_2^{int}\right)_\Omega = \langle \Delta\boldsymbol{\sigma} \rangle_\Omega : \langle \Delta\boldsymbol{\varepsilon} \rangle_\Omega \tag{B.1}$$

Une déformation (incrémentale) mésoscopique peut être définie comme la déformation (incrémentale) moyenne sur le cycle de grains, via le déplacement (incrémental) des grains de la méso-structure et par interpolation le long

des bords du méso-domaine (Bonelli et al., 2012; Liu et al., 2020). Pour la contrainte, la définition d'une contrainte mésoscopique n'est pas si triviale et dépend de l'approche choisie. Dans le cas d'une approche par partition, la contrainte mésoscopique est la contrainte moyenne sur le méso-domaine Ω_l (Figure B.2(a)). Le calcul fait apparaitre la contrainte moyenne dans la portion du grain inclu dans le méso-domaine $V_p \cap \Omega_l$, V_p étant le volume de la particule p. En faisant l'hypothèse que la contrainte moyenne dans cette portion est égale à la contrainte moyenne dans la particule entière. On écrit alors :

$$\langle \boldsymbol{\sigma} \rangle_{\Omega_l} = \frac{1}{|\Omega_l|} \sum_{p \in \Omega_l} |V_p \cap \Omega_l| \langle \boldsymbol{\sigma} \rangle_{V_p} \tag{B.2}$$

Dans le cas de l'approche structurelle, la contrainte mésoscopique reprend la formulation de Bagi. Il y a un terme, dit de Weber, qui prend en compte la contrainte due aux forces internes au cycle de grains, et un terme dit de correction de Bagi qui prend en compte la contrainte due aux forces extérieures, s'exerçant sur la frontière du méso-domaine (Figure B.2(b)). Ainsi pour la contrainte à l'échelle mésoscopique avec une approche structurelle, il existe deux définitions possibles : celle de Weber (Equation B.3) et celle de Bagi (Equation B.4). Ces deux définitions ainsi que la définition par partition sont toutes cohérentes avec la définition de la contrainte à l'échelle du VER lorsqu'on considère suffisement de mesostructures.

$$\left\langle \boldsymbol{\sigma}^{Weber} \right\rangle_{V^{struct}} = \frac{1}{|V^{struct}|} \sum_{p \in V^{struct}} \boldsymbol{f}_{p+1/p} \otimes (R_p + R_{p+1}) \boldsymbol{n}_{p/p+1} \tag{B.3}$$

$$\begin{aligned} \left\langle \boldsymbol{\sigma}^{Bagi} \right\rangle_{V^{struct}} =& \frac{1}{|V^{struct}|} \sum_{p \in V^{struct}} \boldsymbol{f}_{p+1/p} \otimes (R_p + R_{p+1}) \boldsymbol{n}_{p/p+1} \\ &+ \frac{1}{|V^{struct}|} \sum_{p \in \partial V^{struct}} \boldsymbol{f}_{p_{ext}/p} \otimes R_p \boldsymbol{n}_{p/p_{ext}} \end{aligned} \tag{B.4}$$

avec $\boldsymbol{f}_{a/b}$ la force appliquée par la particule a sur la particule b, $\boldsymbol{n}_{a/b}$ la normale orientée du centre de la particule a vers la particule b, p la particule appartenant au méso-domaine V^{struct} et p_{ext} les autres particules en contact avec le méso-domaine V^{struct}.

Dans le but de choisir la meilleure formulation (vis à vis de la définition d'un travail du second ordre mésoscopique) pour la définition de la contrainte

mésoscopique pour l'approche structurelle, un critère est proposé à partir du bilan d'énergie lié au travail du second ordre (Equation B.5).

$$\Delta t^2 \ddot{E}_c = \Delta t^2 \int_\Omega I dV + \int_{\delta\Omega} W_2^{ext} dS - \int_\Omega W_2^{int} dV \tag{B.5}$$

En exprimant la dérivée seconde de l'énergie cinétique comme la somme de la dérivée première de l'énergie cinétique et la variation de l'énergie cinétique (Equation B.6), nous faisons apparaitre les termes qui vont constituer un *résidu* à minimiser (Equation B.7) :

$$2\left(E_c(t+\Delta t) - E_c(t)\right) - 2\dot{E}_c \Delta t = \Delta t^2 \int_\Omega I dV + \int_{\delta\Omega} W_2^{ext} dS - \int_\Omega W_2^{int} dV \tag{B.6}$$

$$\begin{aligned} \Delta t^2 \int_\Omega I dV + 2\Delta t \dot{E}_c &= 2\Delta E_c - \left(\int_{\delta\Omega} W_2^{ext} dS - \int_\Omega W_2^{int} dV \right) \\ Residu &= 2\Delta E_c - \left(\int_{\delta\Omega} W_2^{ext} dS - \int_\Omega W_2^{int} dV \right) \end{aligned} \tag{B.7}$$

La formulation de la contrainte mésoscopique, par l'approche structurelle, qui minimise le résidu correspond à la formulation permettant de construire le meilleur indicateur de stabilité mécanique à l'échelle mésoscopique.

B.4 Bouffées d'énergie cinétique dans un milieu granulaire 2D soumis à un test biaxial

Une première façon d'étudier le développement de bouffées d'énergie cinétique dans un milieu granulaire soumis à un cisaillement est de réaliser un test biaxial. Plusieurs échantillons quasi 2D de rapport d'aspect différents sont créés. Le test biaxial consiste en une phase de compression isotrope, puis à contrainte latérale constante, un taux de déformation constant est imposé verticalement.

Lors du test biaxial, l'énergie cinétique connait de nombreuses variations de grande amplitude mais d'amplitude plus petite que les variations de dissipation plastique et d'énergie élastique. Ce sont les boufées d'énergie cinétique. Une fois l'état critique atteint, elles sont isolées et définies en fonction de l'énergie cinétique moyenne atteinte dans un domaine dit intérieur (Figure

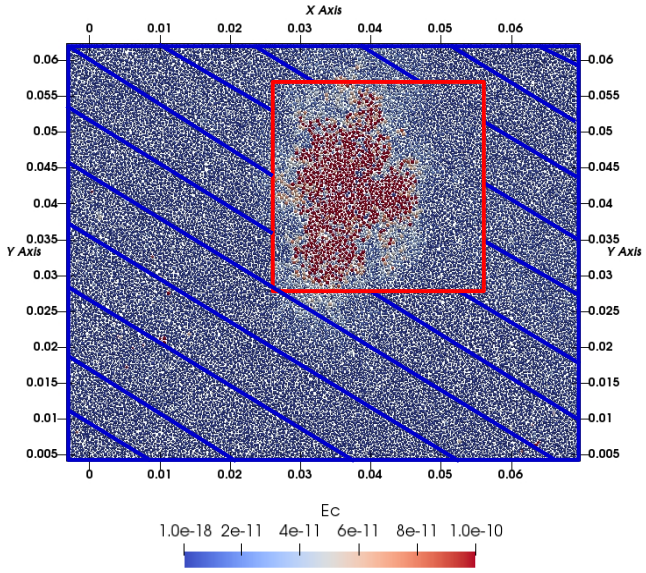

FIGURE B.3 – Exemple d'une bouffée d'énergie cinétique dans un échantillon dense de rapport d'aspect 1. La zone encadrée rouge est la zone où la bouffée apparait et se propage, c'est le domaine interne à la bouffée. La zone hachurée bleue correspond au domaine non concerné par la bouffée d'énergie cinétique, appelé domaine externe.

B.3) comparée à l'énergie cinétique moyenne durant l'état critique du test biaxial. Les résultats obtenus sont similaires pour toutes les bouffées d'énergie cinétique étudiées dans les différents échantillons. Afin de mieux mettre en évidence ce qui peut causer ou ce qui peut résulter d'une bouffée d'énergie, le domaine interne et le domaine externe de la bouffée sont distingués et comparés dans les analyses lors de l'apparition et de la propagation de cette même bouffée d'énergie cinétique (Figure B.3).

Un des objectifs de ce travail est d'identifier des précurseurs à l'apparition des bouffées d'énergie. L'indice de glissement défini à l'échelle d'un contact est un indice qui permet de mesurer la potentialité de rupture d'un contact. Plus l'indice est proche de 1, plus le contact a des chances de disparaitre. En comparant la probabilité de densité de fonction avant et après une bouffée dans les domaines interne et externe, il apparait que le domaine interne contient plus de contacts critiques, c'est à dire plus de contacts proches de la rupture. Parallèlement, si la porosité et la densité des cycles de grains dans chaque domaine sont comparés, il apparait que le domaine interne est plus lâche et comporte moins de cycles de grains. La zone où se développe la bouffée d'énergie cinétique contient davantage de grands cycles de grains.

Le deuxième objectif est de mieux comprendre les réorganisations mecro-structurelles liés à une bouffée d'énergie cinétique. En analysant l'évolution relative des différents catégories de cycles de grain et leur taux de survie durant une bouffée, il est constaté que les réorganisations des méso-structures sont concentrées durant la bouffée et dans le domaine interne. Les cycles les plus grands sont ceux qui sont le plus réorganisés, probablement parce que ce sont ceux qui sont les plus déformables. Les particules libres ont aussi un rôle à jouer, leur appararition et leur disparition étant directement liés aux destructions et créations des cycles de grains. L'évolution relative des cycles de grains atteint un maximum autour du maximum de l'énergie cinétique de la bouffée.

Enfin, les variations des trois définitions du travail du second ordre mésoscopique sont étudiées pour savoir si le critère du travail du second ordre est applicable à l'échelle mésoscopique (Figure B.4). La moyenne pondérée dans le domaine interne de la définition pour l'approche partitionnelle (Figure B.4(a)) et de la définition pour l'approche structurelle de Weber (Figure B.4(c)) s'annulent avant l'apparition de la bouffée d'énergie cinétique. De plus, pour l'approche structurelle, la définition de Weber minimise le résidu comparé à la définition de Bagi. Nous avons donc deux définitions d'un travail du second ordre mésoscopique pour lequel son annulation est un précurseur à l'apparition d'une bouffée d'énergie cinétique.

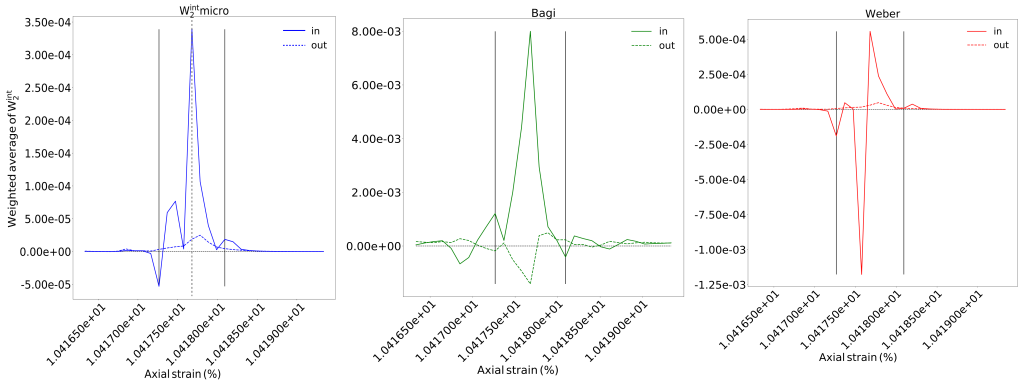

(a) (b) (c)

FIGURE B.4 – Moyenne pondérée des trois définitions du travail du second ordre mésoscopique durant une bouffée d'énergie cinétique : (a) Définition par partition, (b) Définition structurelle de Bagi, (c) Définition structurelle de Weber. Les droites verticales représentent la durée de la bouffée d'énergie cinétique et la droite verticale en pointillée marque le pic de l'énergie cinétique.

Un domaine, plus lâche, avec une forte propabilité de contacts critiques et l'annulation du travail du second ordre mésoscopique sont des précurseurs au développement d'une bouffée d'énergie cinétique dans ce domaine. La bouffée d'énergie cinétique entraine des réorganisations à l'échelle micro- et méso-scopiques localisées dans le domaine interne de la bouffée et durant sa propagation.

B.5 Déclenchement d'instabilités gravitaires

Les conclusions, tirées des tests biaxiaux, sont analysées par la suite dans le contexte d'un cisaillement sur une pente soumise à la gravité. Des échantillons de densité différentes sont créés avec des caractéristiques similaires aux échantillons du test biaxial. La simulation consiste à créer progressivement une pente sur un échantillon avec une surface libre. Pour cela, l'angle entre la verticale et le vecteur gravité est augmenté avec un taux constant. Deux types de conditions limites sont utilisées : conditions limites rigides et conditions limites périodiques.

La transition inertielle est marquée par un nombre inertiel qui devient supérieur à 10^{-3} (Da Cruz, 2004). Les échantillons passent dans le domaine inertiel après 30° (Figure B.5), indépendamment de leur conditions aux limites. Cet angle dépend uniquement de la densité de l'échantillon, les échantillons denses ayant une transition inertielle un peu plus tardive. Par conséquent, les analyses en régime quasi-statiques menées dans ce paragraphe se limitent aux données avant 30°. L'étude de l'évolution des indices de glissement dans tout l'échantillon montre que la transition inertielle est diffuse.

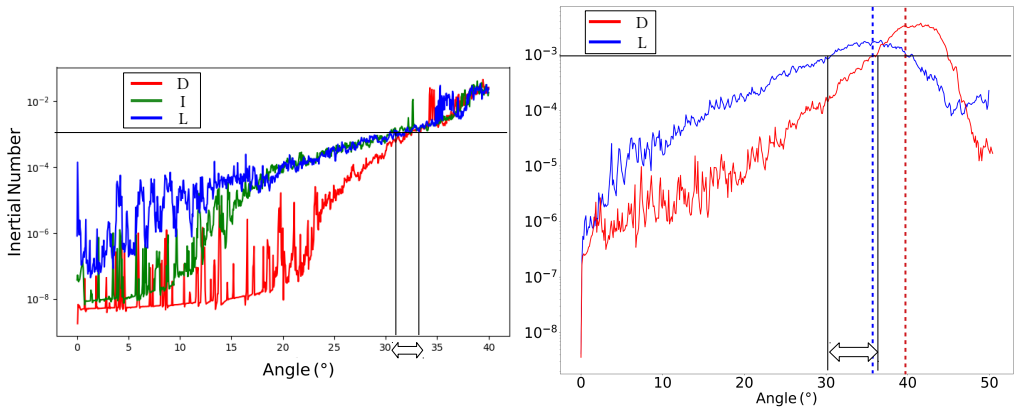

(a) (b)

FIGURE B.5 – Variation du nombre inertiel dans les échantillons avec des conditions périodiques (a) et dans les échantillons avec des conditions aux frontières rigides (b).

L'état de contrainte des échantillons montre qu'une partie (conditions aux frontières rigides) ou que l'intégralité de l'échantillon (conditions périodiques) atteint la limite théorique de rupture de Mohr Coulomb bien avant la transition inertielle. Cet angle dépend de la densité de l'échantillon et de ses conditions aux frontières. Il est inférieur à 20° pour les échantillons denses et supérieur pour les échantillons lâches. Il est étonnant de constater que la rupture statique prédite par Mohr Coulomb est atteinte bien avant que l'échantillon ait perdu la mémoire de son état initial avec la transition inertielle. L'angle de rupture statique et l'angle marquant la fin du régime quasi-statique définissent un intervalle de pré-avalanche (Daerr and Douady, 1999; Staron et al., 2006; Staron, 2008), où les reorganisations sont plus intensives. Cet intervalle est également visible dans l'évolution des cycles de grain. L'analyse des durées de vie et des espérances de vie des cycles de grains mettent en évidence des réorganisations localisées autour de l'angle de rupture statique pour les échantillons denses et des réorganisations immédiates dès la formation d'une pente légère ($> 5°$) pour les échantillons lâches. De même l'évolution du travail du second ordre mésoscopique moyenné sur l'ensemble de l'échantillon s'annule à plusieurs reprises avant que la pente atteigne 15° (Figure B.6). Par conséquent la transtion inertielle n'est pas brusque, mais elle est précédée d'un intervalle où les réorganisations micro-

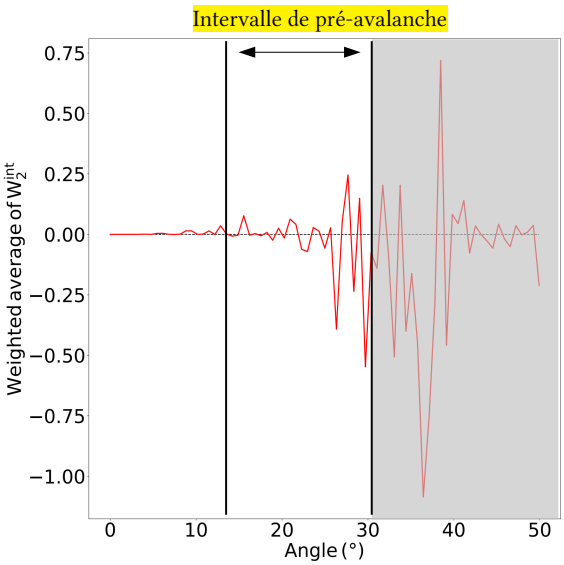

FIGURE B.6 – Moyenne pondérée du travail du second ordre mésoscopique (approche partitionnelle), sur tout l'échantillon lâche avec conditions aux frontières rigides. Le travail du second ordre s'annule avant 15°, et s'annule de plus en plus fréquemment jusqu'à la transition inertielle. La partie grisée correspond au domaine inertiel.

et mésoscopiques sont de plus en plus fortes et où l'échantillon atteint la limite de rupture statique.

Lors de l'étude d'une bouffée d'énergie cinétique dans l'intervalle de pré-avalanche, on retrouve les mêmes précurseurs mis en lumière lors du test biaxial (indice de glissement, porosité et annulation du travail du second ordre mésoscopique), bien que les réorganisations mésoscopiques soient moins concentrées dans le domaine interne à la bouffée. Nous supposons que les bouffées d'énergie cinétique ont les mêmes conséquences (réorganisations limitées à la durée de vie de la bouffée et concentrées dans le domaine interne) que celles répertoriées dans le test biaxial pour de faibles angles de pente. Une fois que l'échantillon atteint le début de l'intervalle de pré-avalanche, les réorganisations sont moins concentrées, aboutissant à des bouffées de plus en plus diffuses, jusqu'à la transition inertielle totale.

Ainsi la transition inertielle apparait ici comme un phénomène moins soudain que l'on pouvait l'imaginer. Il existe un intervalle de pré-avalanche où les réorganisations se font de plus en plus intenses et les bouffées d'énergie cinétique plus diffuses, menant jusqu'à la transition inertielle. Les conditions aux limites influencent quant à elles que l'état de contrainte du milieu et le

chemin de chargement suivi. Les conditions aux limites rigides génèrent une pré-contrainte et modifient l'état de contrainte similairement à des barrières de sécurité sur les flancs rocheux / neigeux à risque.

B.6 Perspectives

La modélisation du milieu granulaire peut être améliorée. Des simulations quasi 2D ont été choisies car il n'existe pour l'instant pas de concensus quant à la définition des cycles de grain en 3D (Nguyen et al., 2020). Des développements récents sont néanmoins prometteurs et permettent d'envisager d'étendre ce travail au cas 3D (Chueire et al., 2021). La forme des particules pourraient aussi être plus réaliste afin de mieux prendre en compte la rotation des grains. L'évolution des bouffées d'énergie cinétique vers la transition inertielle doit être encore mieux cernée. Une des hypothèses à développer est celle d'une réorganisation globale comme une série de bouffées d'énergie cinétique. Les évènements inertiels peuvent être vus comme des réorganisations à court terme et l'accumulation de séquences d'évènements comme une réorganisation à long terme (Deng et al., 2021b). Cette théorie doit être étayée dans le contexte d'un test biaxial - la réorganisation à long terme étant alors l'état critique- et dans le contexte d'une pente soumise à la gravité -la réorganisation à long terme étant la transition inertielle.

Annexe C

Appendices 1

C.1 Results of the sample loose S_2 under a biaxial test

In this section are gathered all the results for a select burst during the drained biaxial test on the loose sample S_2. They are presented in the same order as the results observed in the dense sample S_1 in Chapter 4.

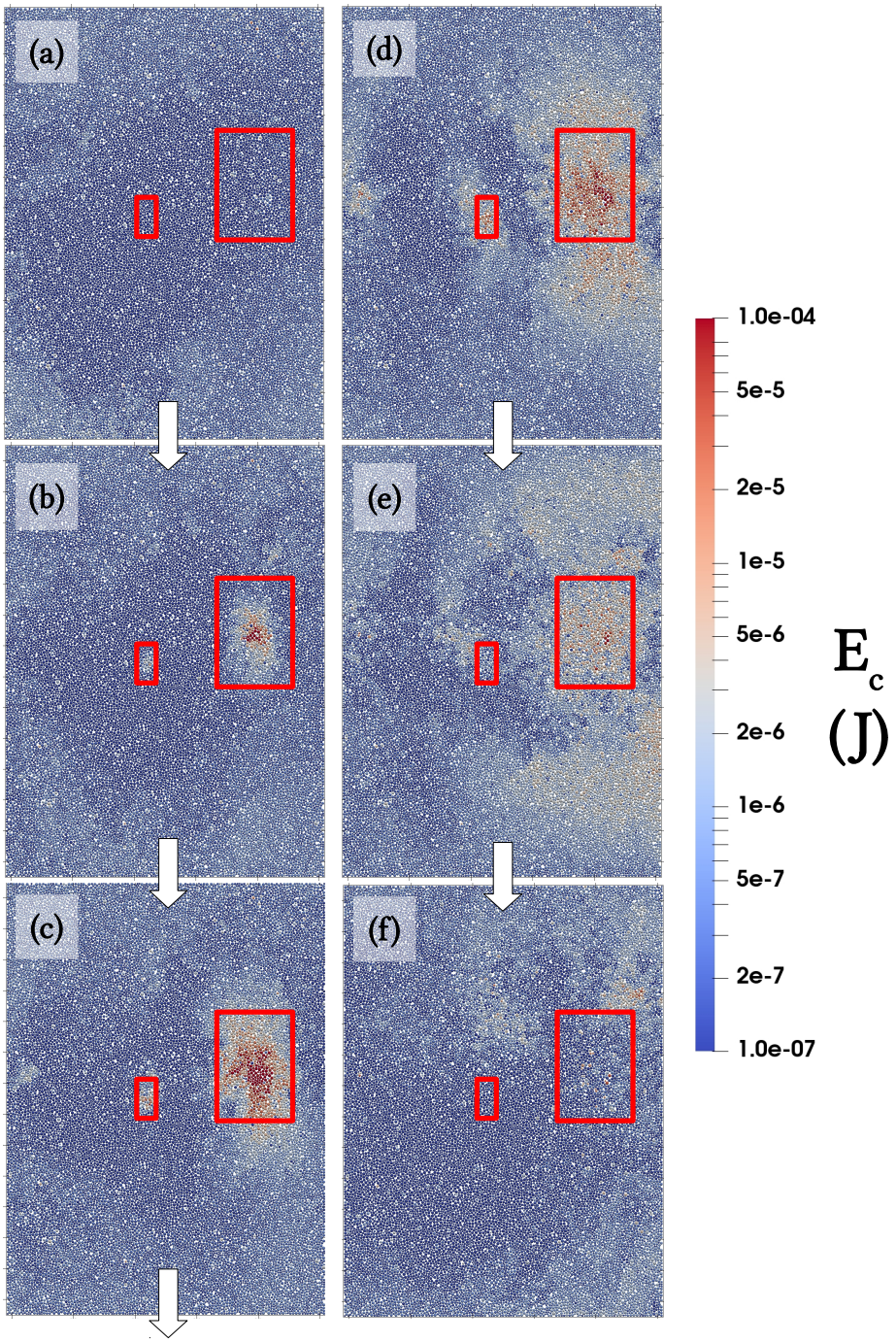

FIGURE C.1 – Reduced time lapse of a burst in the loose sample S_2, during critical state. Particles are coloured according to their kinetic energy expressed in Joule and a log scale is used here to display the kinetic energy. For this timelapse, there are two bursts occuring simultaneously. Thus, two bounding boxes are used to define of the inner burst domain (red boxes).

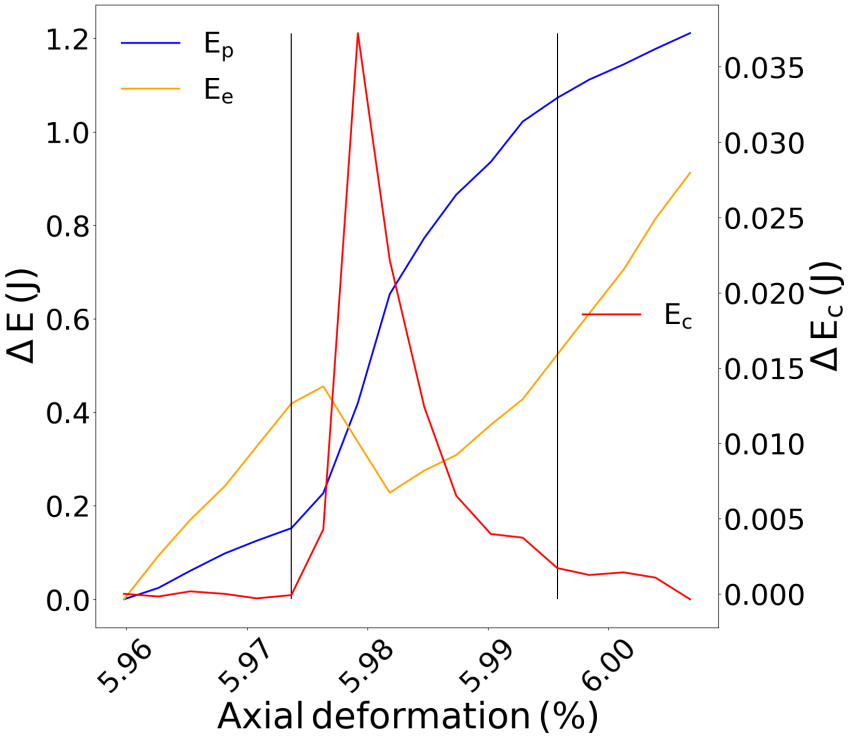

FIGURE C.2 – Evolution of the elastic energy E_e, the plastic dissipation E_p (on the left y-axis), and the kinetic energy E_c during the burst of kinetic energy. Note that the elastic energy decreases latter than in the burst of the dense sample S_1 . This result can be linked to the inner burst domain which is smaller for this burst than the burst presented in the dense sample S_1.

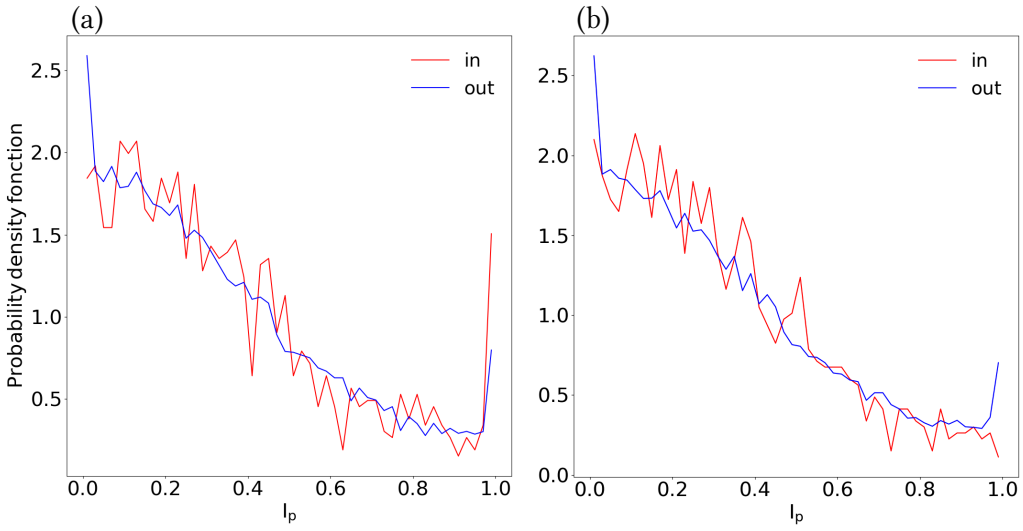

FIGURE C.3 – Sliding Index's propability density before (a) and after (b) the burst of kinetic energy in the inner (red) and outter (blue) burst domains.

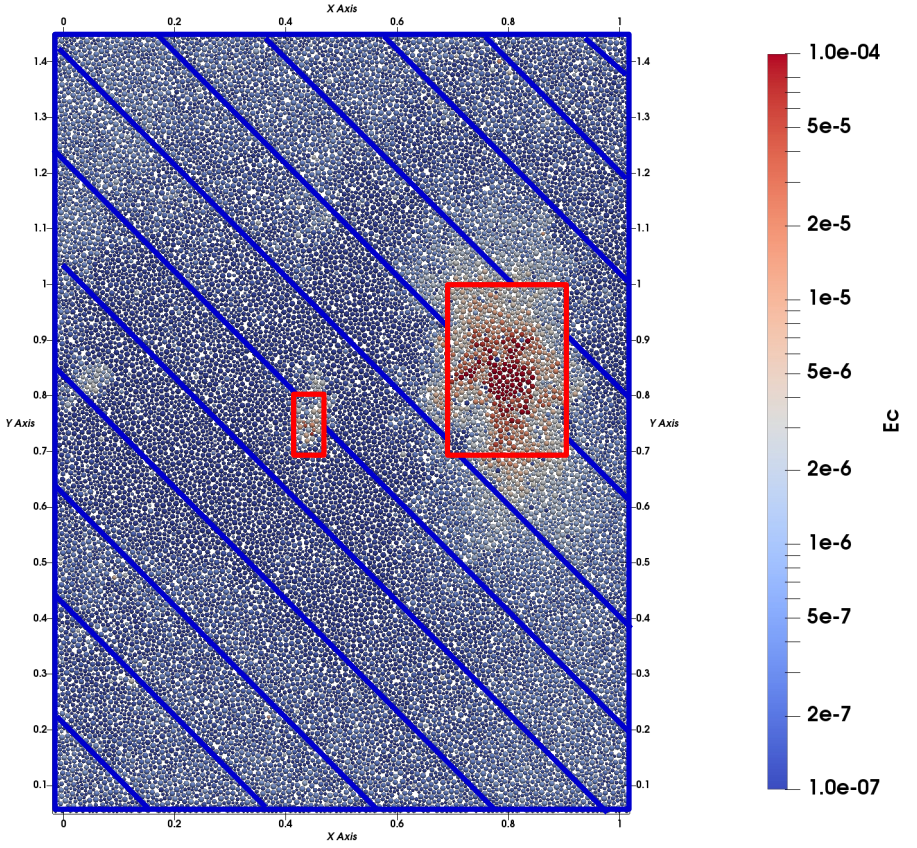

FIGURE C.4 – Inner and outter domains are displayed. The inner burst domain is displayed in red, as in Figure C.1. The outter domain is hatched in blue and concern all the sample but the inner domain.

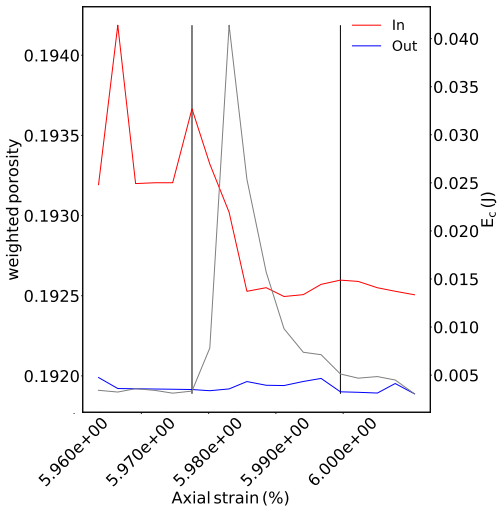

FIGURE C.5 – Porosity in the inner and outter domains. The kinetic energy is recalled (grey curve / right y-axis). The porosity is higher inside the burst domain, which is a similar result to the sample dense S_1 (Figure 4.18). However the decrease in the porosity is not found for the dense sample S_1. A hypothesis is that the rearangements are more efficient in the loose sample (because of contractancy), enabling convergence of the microstructure porosities after the burst.

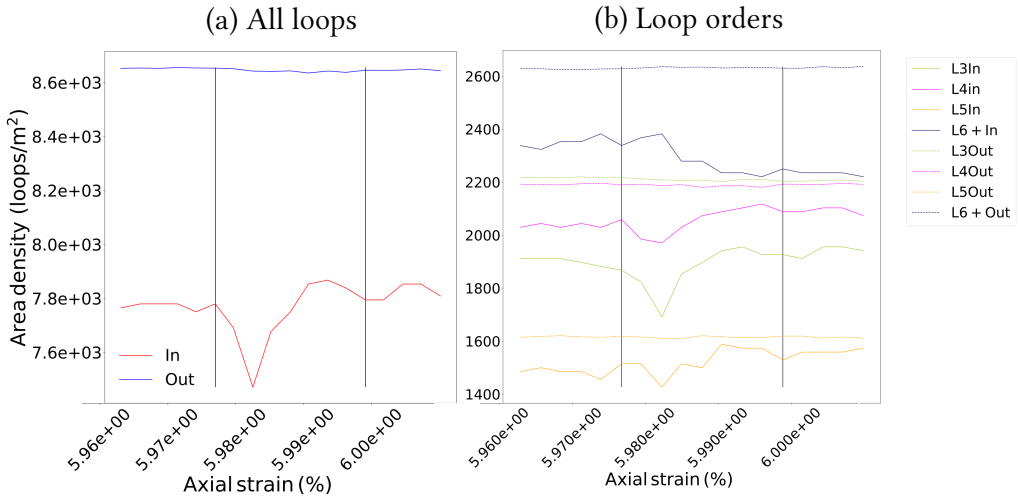

FIGURE C.6 – Loops densities comparison between the inner and outter domains. (a) All order of loops are accounted (b) The different order of loop density are compared. For both graphs, the kinetic energy is displayed to relate the evolution of the porosity to the propagation of the burst.The results are similar to the sample S_1 (FigureC.6). The values of loop density are smaller than in FigureC.6 because the grains are bigger.

(a) Real porosity (with rattlers) (b) Apparent porosity (without rattlers)

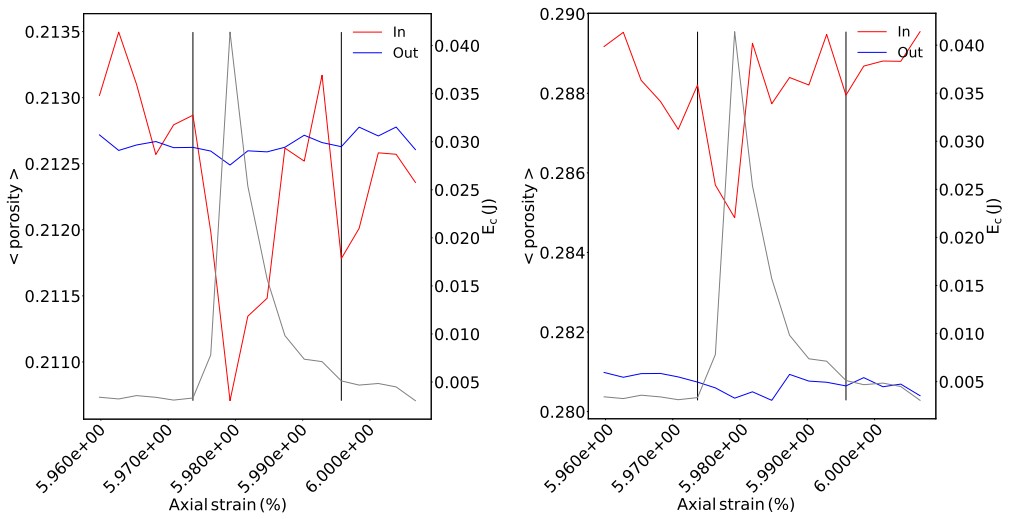

FIGURE C.7 – (a) Mean Real porosity and (b) mean apparent porosity for high order of loops in the inner and outter domains. The kinetic energy is displayed to relate the evolution of the porosity to the propagation of the burst. If real porosity for high order loops inside the burst area is in average similar to the outter domain while its apparent porosity is higher shows that the L6+ loops inside the burst domain contains more rattlers. For this type of sample, the high order loops are bigger and contains more rattlers.

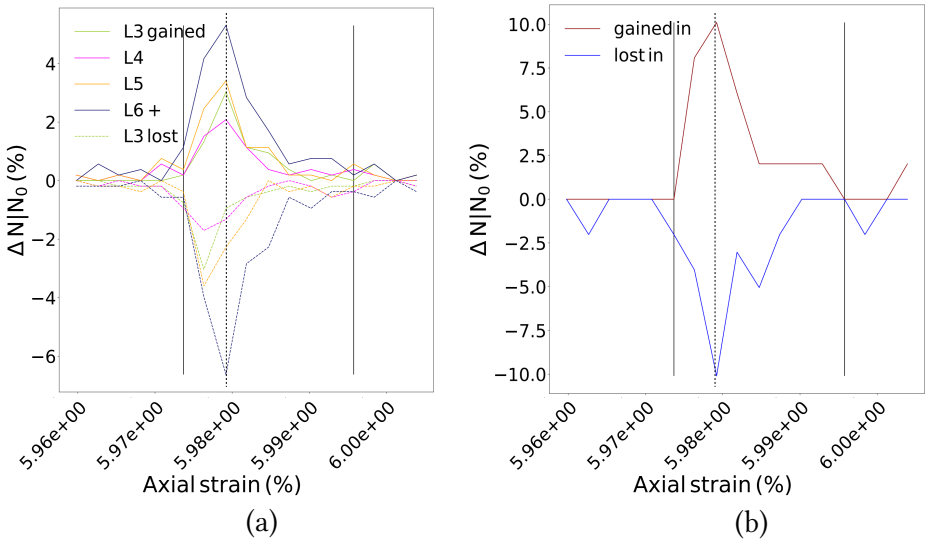

FIGURE C.8 – Relative variation of grain loops (a) and rattlers (b) in the inner burst domain. The vertical dotted lines stands for the maximum of kinetic energy during the burst, as in the previous figures.

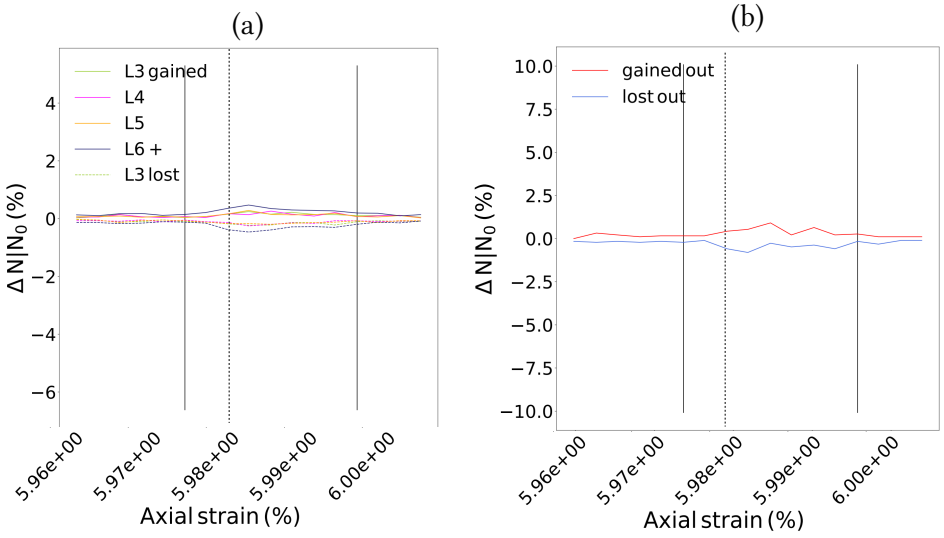

FIGURE C.9 – Relative variation of grain loops (a) and rattlers (b) in the outter burst domain.The vertical dotted lines stands for the maximum of kinetic energy during the burst.

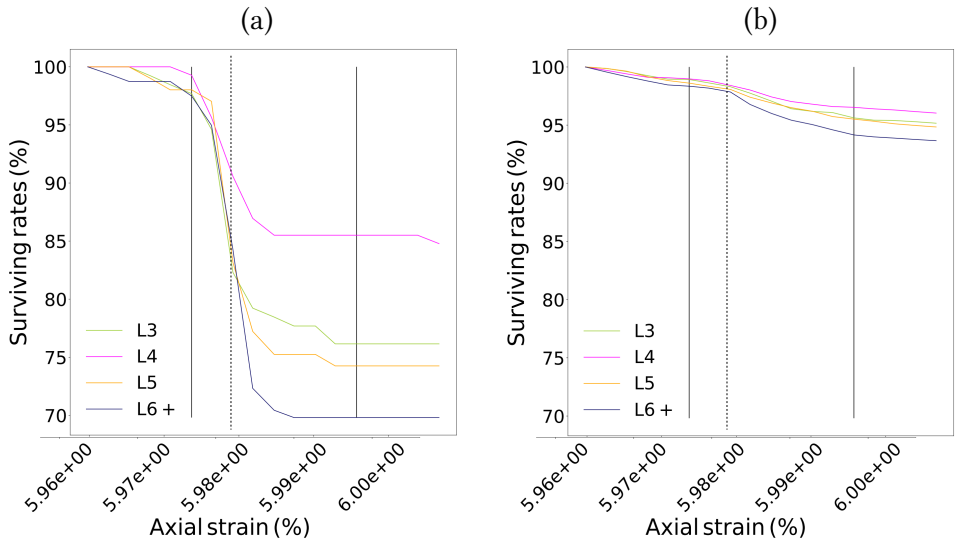

FIGURE C.10 – Surviving rates for the four main grain loops orders in (a) the inner and (b) outter burst domains.The vertical dotted lines stands for the maximum of kinetic energy during the burst. in the outter domain, a single change of slope in the surviving rates is also observed

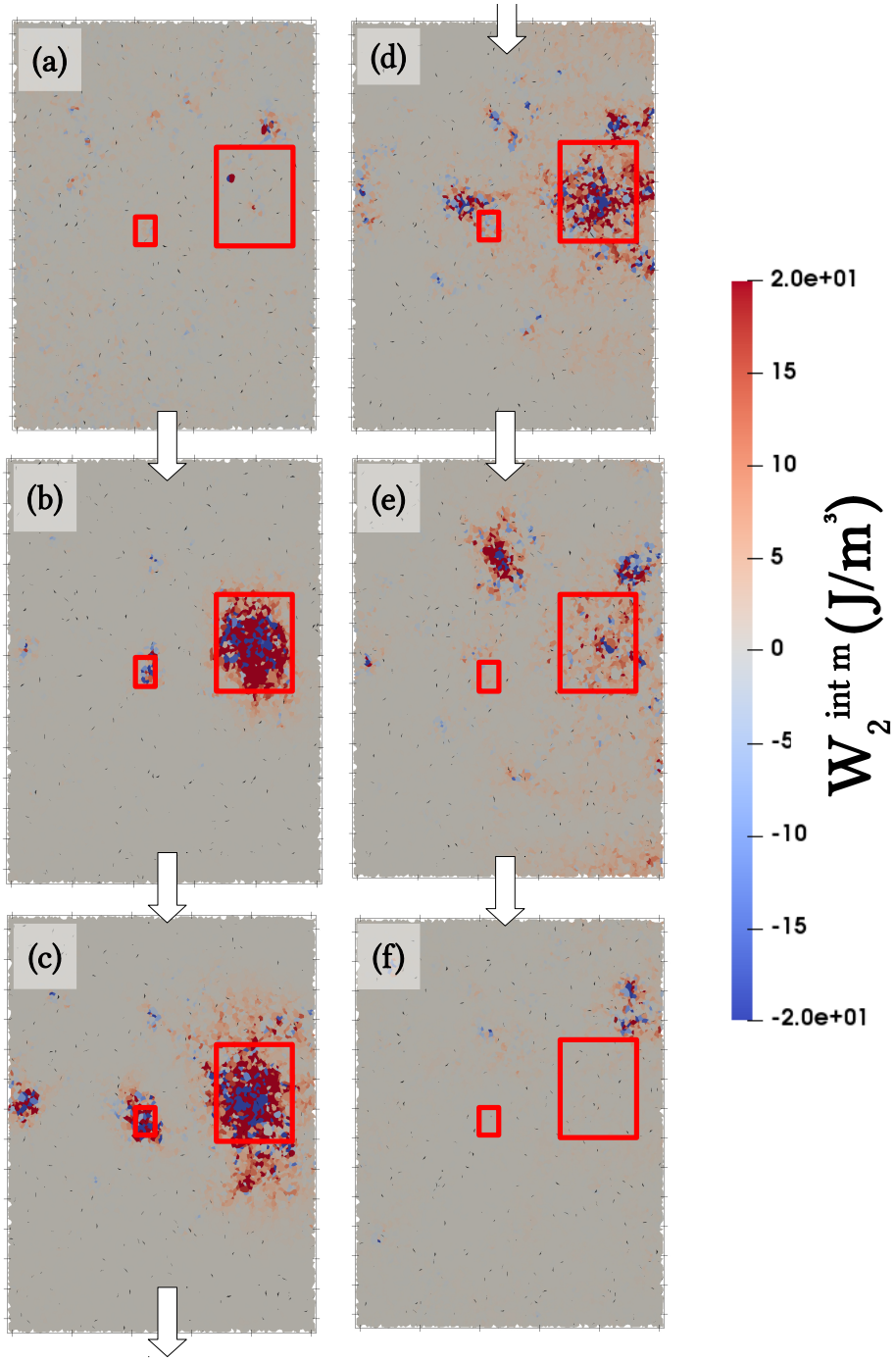

FIGURE C.11 – Reduced time sequence of mesoscopic second-order work W_2^m based on Figure C.1. Contrary to the burst in the sample S_1 (Figure 4.25) no extra panel has been added, no additional information is revealed by the variation of the second-order work W_2^m on the origins of the burst. The propagation of the second-order mesoscopic work variations is wider than the propagation of the burst in Figure C.1, underlining the influence the burst has outside a domain defined only on kinetic energy.

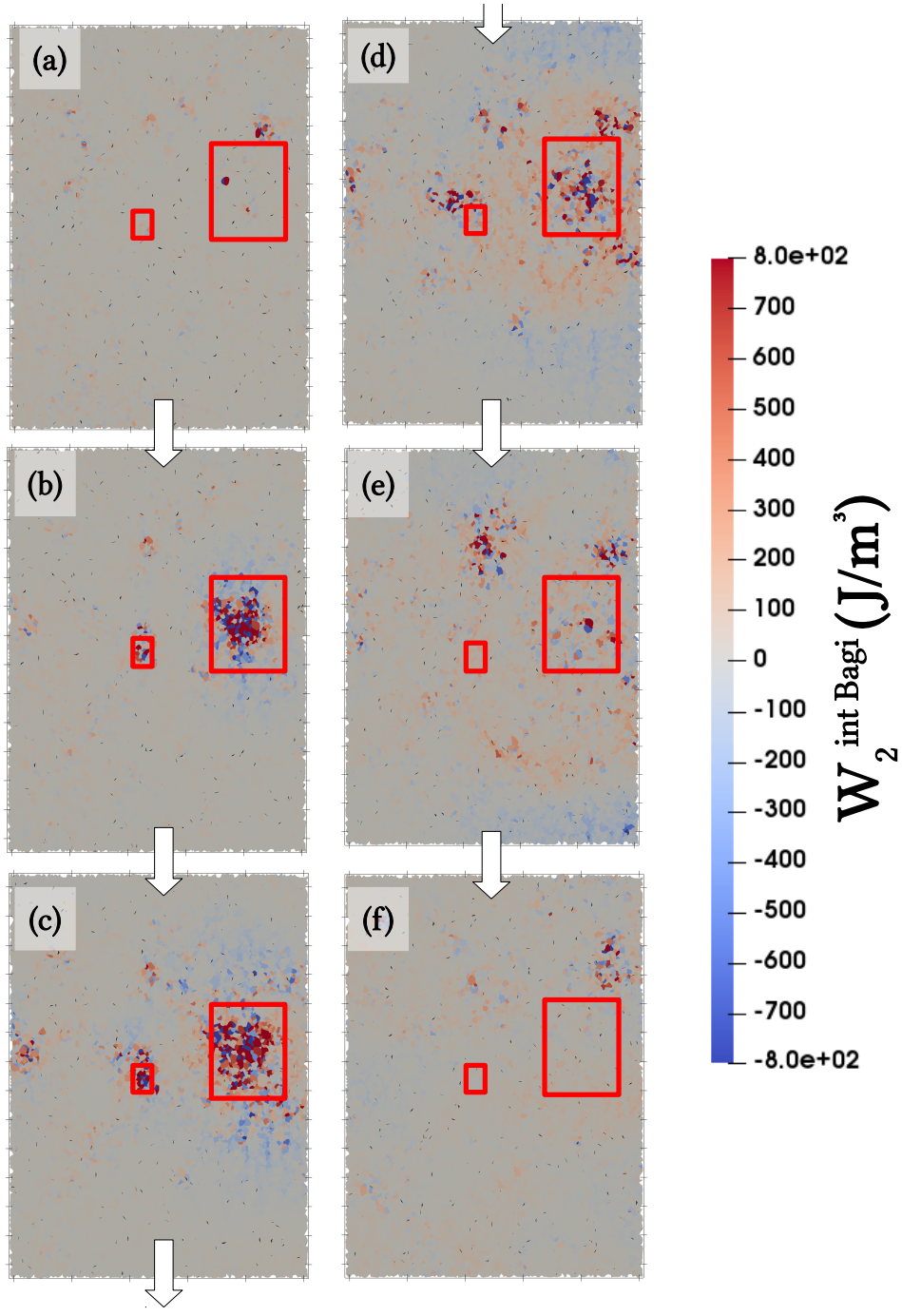

FIGURE C.12 – Reduced time sequence of second-order mesoscopic work W_2^{Bagi} based on Figure C.1.

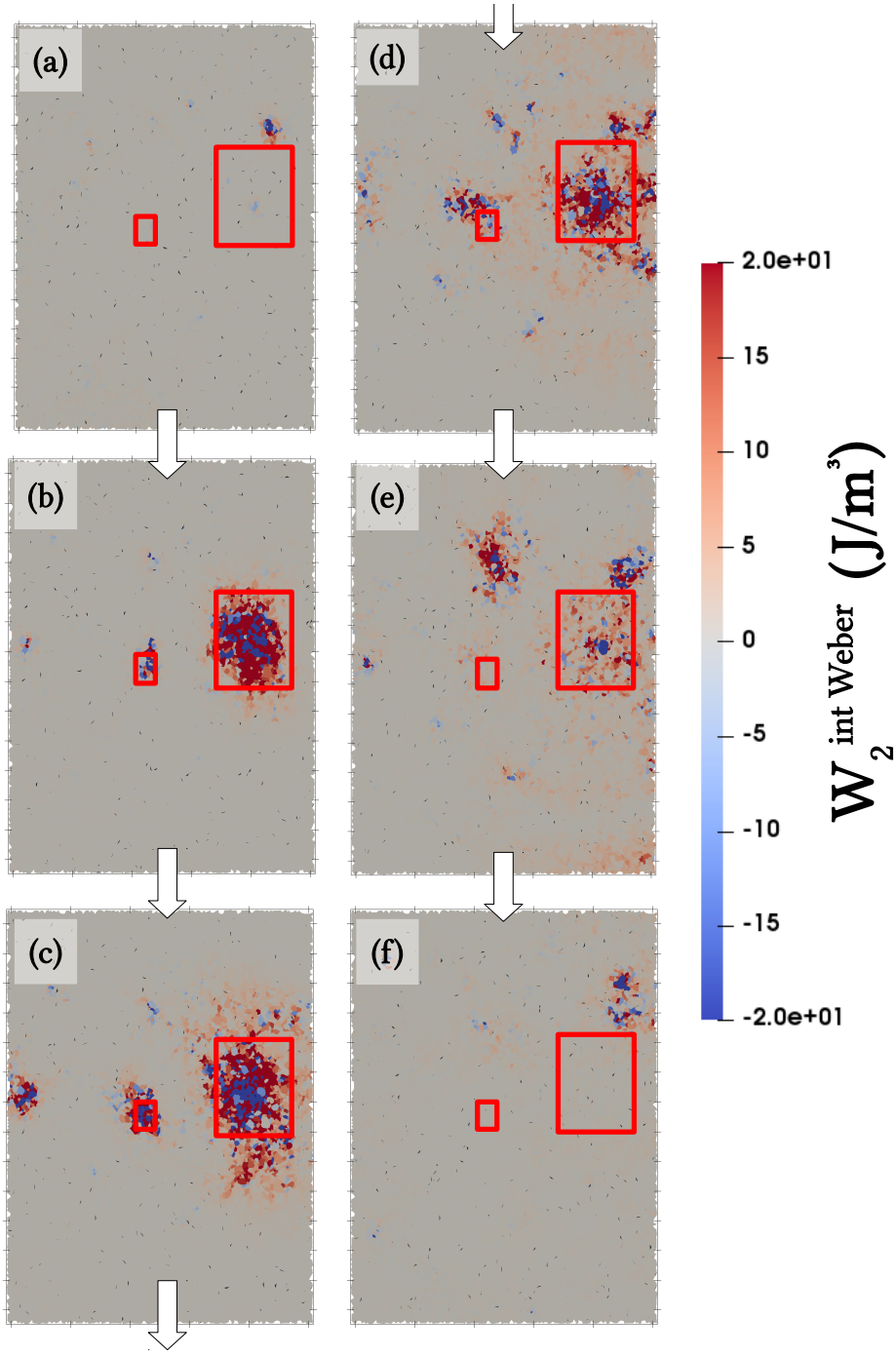

FIGURE C.13 – Reduced time sequence of second-order mesoscopic work W_2^{Weber} based on Figure C.1.

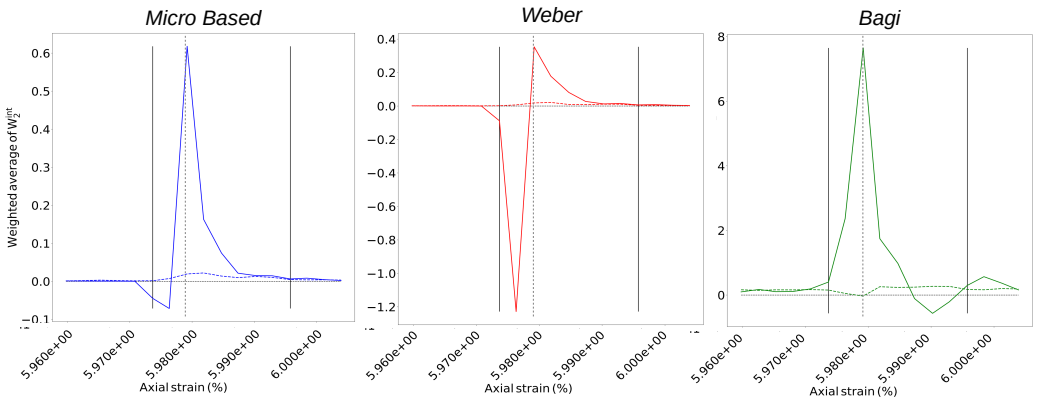

FIGURE C.14 – Volume weighted average of second-order mesoscopic work W_2^m, W_2^{Bagi} and W_2^{Weber} during the burst of energy, in the burst domain. The peak of kinetic energy is represented as the grey dotted vertical line. As a reminder, the meso-volume considered in the avering process are not the same for the three meso-second-order work def : Ω_l (i.e. V^{part}) for W_2^m and V^{struct} for W_2^{Bagi} and W_2^{Weber}.

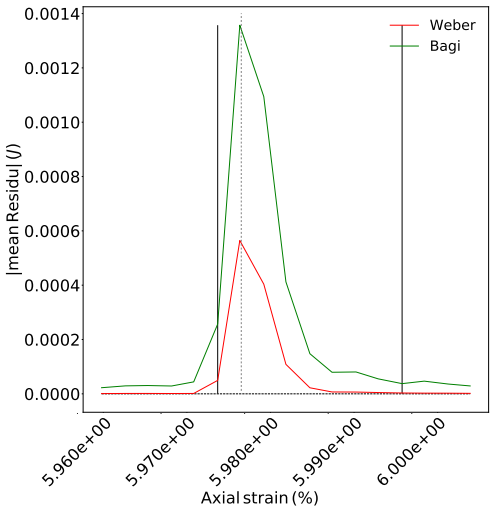

FIGURE C.15 – Mean residue with Bagi and Weber second-order meso-work. The peak of kinetic energy is represented as the grey dotted vertical line.

Bibliography

Aguirre, M., N. Nerone, I. Ippolito, A. Calvo, and D. Bideau
2001. Granular packing: influence of different parameters on its stability. *Granular Matter*, 3(1):75–77. Cited in page 11

Azéma, E., F. Radjai, and G. Saussine
2009. Quasistatic rheology, force transmission and fabric properties of a packing of irregular polyhedral particles. *Mechanics of Materials*, 41(6):729–741. Cited in page 142

Bagi, K.
1996. Stress and strain in granular assemblies. *Mechanics of materials*, 22(3):165–177. Cited in pages 41, 45

Bonelli, S.
2012. *Erosion of geomaterials*. John Wiley & Sons. Cited in pages 2, 147

Bonelli, S., O. Millet, F. Nicot, J. Rahmoun, and G. De Saxcé
2012. On the definition of an average strain tensor for two-dimensional granular material assemblies. *International Journal of Solids and Structures*, 49(7-8):947–958. Cited in pages 41, 151

Cambou, B., M. Jean, and F. Radjaï
2013. *Micromechanics of granular materials*. John Wiley & Sons. Cited in pages 2, 6

Challamel, N., F. Nicot, J. Lerbet, and F. Darve
2010. Stability of non-conservative elastic structures under additional kinematics constraints. *Engineering Structures*, 32(10):3086–3092. Cited in page 8

Chueire, J., A. Wautier, F. Nicot, and A. Daouadji
2021. On the extension of the grain loop concept from 2d to 3d granular assemblies. under review. Cited in pages 30, 142, 159

Clerc, A., A. Wautier, S. Bonelli, and F. Nicot
2021. Meso-scale signatures of inertial transitions in granular materials. *Granular Matter*, 23(2):1–14. Cited in page 4

Cundall, P. A. and O. D. Strack
1979. A discrete numerical model for granular assemblies. *geotechnique*, 29(1):47–65. Cited in pages 13, 15

Da Cruz, F.
2004. *Ecoulement de grains secs: Frottement et blocage*. PhD thesis, Marne-la-vallée, ENPC. Cited in pages 10, 13, 156

Da Cruz, F., S. Emam, M. Prochnow, J.-N. Roux, and F. Chevoir
2005. Rheophysics of dense granular materials: Discrete simulation of plane shear flows. *Physical Review E*, 72(2):021309. Cited in pages 10, 116, 123, 141

Daerr, A. and S. Douady
1999. Two types of avalanche behaviour in granular media. *Nature*, 399(6733):241–243. Cited in pages XIII, 11, 12, 106, 123, 157

Daouadji, A., F. Darve, H. Al Gali, P.-Y. Hicher, F. Laouafa, S. Lignon, F. Nicot, R. Nova, M. Pinheiro, F. Prunier, et al.
2011. Diffuse failure in geomaterials: experiments, theory and modelling. *International Journal for Numerical and Analytical Methods in Geomechanics*, 35(16):1731–1773. Cited in pages 8, 149

Darve, F., E. Flavigny, and M. Meghachou
1995. Constitutive modelling and instabilities of soil behaviour. *Computers and Geotechnics*, 17(2):203–224. Cited in page 6

Darve, F. and F. Laouafa
2000. Instabilities in granular materials and application to landslides. *Mechanics of Cohesive-frictional Materials: An International Journal on Experiments, Modelling and Computation of Materials and Structures*, 5(8):627–652. Cited in page 134

Darve, F., G. Servant, F. Laouafa, and H. Khoa
2004. Failure in geomaterials: continuous and discrete analyses. *Computer methods in applied mechanics and engineering*, 193(27-29):3057–3085. Cited in pages 3, 148

Deng, N., A. Clerc, A. Wautier, Y. Thiery, Z.-Y. Yin, P.-Y. Hicher, S. Bonelli, and F. Nicot
2021a. Landslide modelling: how successive local inertial events can result in a global microstructure reorganization. Presentation at ALERT Workshop 2021. Cited in page 137

Deng, N., A. Wautier, Y. Thiery, Z.-Y. Yin, P.-Y. Hicher, and F. Nicot
2021b. On the attraction power of critical state in granular materials. *Journal of the Mechanics and Physics of Solids*, 149:104300. Cited in pages 26, 51, 137, 143, 159

di Prisco, C. and S. Imposimato
1997. Experimental analysis and theoretical interpretation of triaxial load controlled loose sand specimen collapses. *Mechanics of Cohesive-frictional Materials: An International Journal on Experiments, Modelling and Computation of Materials and Structures*, 2(2):93–120. Cited in page 3

Di Prisco, C. and F. Pisanò
2011. An exercise on slope stability and perfect elastoplasticity. *Géotechnique*, 61(11):923–934. Cited in page 2

Drescher, A. and G. D. J. De Jong
1972. Photoelastic verification of a mechanical model for the flow of a granular material. *Journal of the Mechanics and Physics of Solids*, 20(5):337–340. Cited in page 22

Duriez, J. and C. Galusinski
2021. A level set-discrete element method in yade for numerical, micro-scale, geomechanics with refined grain shapes. *Computers & Geosciences*, 157:104936. Cited in page 142

Forterre, Y. and O. Pouliquen
2008. Flows of dense granular media. *Annu. Rev. Fluid Mech.*, 40:1–24. Cited in pages XIII, 1, 2, 6, 12

Gaume, J., T. Gast, J. Teran, A. Van Herwijnen, and C. Jiang
2018. Dynamic anticrack propagation in snow. *Nature communications*, 9(1):1–10. Cited in page 3

Hadda, N., F. Nicot, F. Bourrier, L. Sibille, F. Radjai, and F. Darve
2013. Micromechanical analysis of second order work in granular media. *Granular matter*, 15(2):221–235. Cited in page 3

Haddad, H., W. Leclerc, M. Guessasma, C. Pélegris, N. Ferguen, and E. Bellenger
2015. Application of dem to predict the elastic behavior of particulate composite materials. *Granular Matter*, 17(4):459–473. Cited in page 13

Hill, R.
1958. A general theory of uniqueness and stability in elastic-plastic solids. *Journal of the Mechanics and Physics of Solids*, 6(3):236–249. Cited in pages 3, 6, 7, 13

Hill, R.
1962. Acceleration waves in solids. *Journal of the Mechanics and Physics of Solids*, 10(1):1–16. Cited in page 8

Hosn, R. A., L. Sibille, N. Benahmed, and B. Chareyre
2017. Discrete numerical modeling of loose soil with spherical particles and interparticle rolling friction. *Granular matter*, 19(1):1–12. Cited in page 142

Jaeger, H. M., S. R. Nagel, and R. P. Behringer
1996. Granular solids, liquids, and gases. *Reviews of modern physics*, 68(4):1259. Cited in page 22

Jain, N., J. M. Ottino, and R. M. Lueptow
2002. An experimental study of the flowing granular layer in a rotating tumbler. *Physics of Fluids*, 14(2):572–582. Cited in pages XIII, 12

Jop, P., Y. Forterre, and O. Pouliquen
2005. Crucial role of sidewalls in granular surface flows: consequences for the rheology. *Journal of Fluid Mechanics*, 541:167–192. Cited in page 11

Jop, P., Y. Forterre, and O. Pouliquen
2007. Initiation of granular surface flows in a narrow channel. *Physics of Fluids*, 19(8):088102. Cited in pages 11, 13, 101

Kruyt, N. P. and L. Rothenburg
1996. Micromechanical Definition of the Strain Tensor for Granular Materials. *Journal of Applied Mechanics*, 63(3):706–711. Cited in page 41

Liu, J.
2018. *Micro- and mesoscopic study on granular materials under complex loading paths*. PhD thesis, Wuhan University. Cited in pages XV, 66, 67

Liu, J., F. Nicot, A. Wautier, and W. Zhou
2019. Role of sliding contacts in shear banding affecting granular materials. In *International Conference on Particle-Based Methods (Particles)-6. International Conference on Particle-Based Methods: fundamentals and applications (Particles 2019)*, Pp. 46–56. International Centre for Numerical Methods in Engineering. Cited in page 8

Liu, J., F. Nicot, and W. Zhou
2018. Sustainability of internal structures during shear band forming in 2d granular materials. *Powder technology*, 338:458–470. Cited in pages XIII, 3, 8, 9, 23, 55, 141, 148, 149

Liu, J., A. Wautier, S. Bonelli, F. Nicot, and F. Darve
2020. Macroscopic softening in granular materials from a mesoscale perspective. *International Journal of Solids and Structures*, 193:222–238. Cited in pages 3, 41, 51, 151

Lois, G., A. Lemaître, and J. M. Carlson
2005. Numerical tests of constitutive laws for dense granular flows. *Physical Review E*, 72(5):051303. Cited in page 10

Lube, G., H. E. Huppert, R. S. J. Sparks, and A. Freundt
2005. Collapses of two-dimensional granular columns. *Physical Review E*, 72(4):041301. Cited in pages XIII, 12

Luding, S.
2004. Micro–macro transition for anisotropic, frictional granular packings. *International Journal of Solids and Structures*, 41(21):5821–5836. Cited in page 13

Lyapunov, A.
1907. Problème général de la stabilité du mouvement. *Annales de la Faculté des sciences de Toulouse*, 9:203–474. Cited in page 6

Majmudar, T. S. and R. P. Behringer
2005. Contact force measurements and stress-induced anisotropy in granular materials. *Nature*, 435(7045):1079–1082. Cited in pages XIII, 22

Mandel, J.
1964. Propagation des surfaces de discontinuité dans un milieu élastoplastique. In *Stress waves in anelastic solids*, Pp. 331–340. Springer. Cited in page 8

Marveggio, P., I. Redaelli, and C. di Prisco
2021. A new constitutive approach for simulating solid-to fluid-like phase transition in dry and saturated granular media. In *International Conference of the International Association for Computer Methods and Advances in Geomechanics*, Pp. 491–497. Springer. Cited in pages 10, 13

Mede, T., G. Chambon, P. Hagenmuller, and F. Nicot
2018. A medial axis based method for irregular grain shape representation in dem simulations. *Granular Matter*, 20(1):1–11. Cited in page 142

MiDi, G.
2004. On dense granular flows. *The European Physical Journal E*, 14:341–365. Cited in page 10

Nguyen, N.-S., H. Magoariec, E. Vincens, and B. Cambou
2020. On the definition of a relevant meso-scale for upscaling the mechanical behavior of 3d granular materials. *Granular Matter*, 22(1):1–5. Cited in pages 30, 142, 159

Nicot, F., A. Daouadji, N. Hadda, M. Jrad, and F. Darve
2013a. Granular media failure along triaxial proportional strain paths. *European journal of environmental and civil engineering*, 17(9):777–790. Cited in page 13

Nicot, F. and F. Darve
2007. A micro-mechanical investigation of bifurcation in granular materials. *International Journal of Solids and Structures*, 44(20):6630–6652. Cited in pages 3, 7

Nicot, F., N. Hadda, F. Bourrier, L. Sibille, R. Wan, and F. Darve
2012a. Inertia effects as a possible missing link between micro and macro second-order work in granular media. *International Journal of Solids and Structures*, 49(10):1252–1258. Cited in page 11

Nicot, F., N. Hadda, M. Guessasma, J. Fortin, and O. Millet
2013b. On the definition of the stress tensor in granular media. *International Journal of Solids and Structures*, 50(14-15):2508–2517. Cited in page 41

Nicot, F., N. P. Kruyt, and O. Millet
2017. On hill's lemma in continuum mechanics. *Acta mechanica*, 228(5):1581–1596. Cited in pages 8, 38, 149

Nicot, F., L. Sibille, and F. Darve
2009. Bifurcation in granular materials: An attempt for a unified framework. *International Journal of Solids and Structures*, 46(22-23):3938–3947. Cited in pages 3, 7, 8, 149

Nicot, F., L. Sibille, and F. Darve
2012b. Failure in rate-independent granular materials as a bifurcation toward a dynamic regime. *International Journal of Plasticity*, 29:136–154. Cited in pages 3, 7, 8, 149

Nicot, F., L. Sibille, F. Donze, and F. Darve
2007. From microscopic to macroscopic second-order work in granular assemblies. *Mechanics of materials*, 39(7):664–684. Cited in page 3

Oda, M. and H. Kazama
1998. Microstructure of shear bands and its relation to the mechanisms of dilatancy and failure of dense granular soils. *Geotechnique*, 48(4):465–481. Cited in pages 8, 141

Oda, M., T. Takemura, and M. Takahashi
2004. Microstructure in shear band observed by microfocus x-ray computed tomography. *Géotechnique*, 54(8):539–542. Cited in page 22

Oger, L., R. Delannay, and Y. Le Gonidec
2021. Robust experimental study of avalanche precursory events based on reproducible cycles of grain packing destabilizations. In *EPJ Web of Conferences*, volume 249, P. 03023. EDP Sciences. Cited in page 11

Pouliquen, O., C. Cassar, Y. Forterre, P. Jop, and M. Nicolas
2005. How do grains flow: towards a simple rheology for dense granular flows. *Powders and Grains*, Pp. 859–865. Cited in pages 13, 101

Quezada, J. C., P. Breul, G. Saussine, and F. Radjai
2012. Stability, deformation, and variability of granular fills composed of polyhedral particles. *Physical review E*, 86(3):031308. Cited in page 142

Radjai, F., M. Jean, J.-J. Moreau, and S. Roux
1996. Force distributions in dense two-dimensional granular systems. *Physical review letters*, 77(2):274. Cited in page 3

Radjai, F., D. E. Wolf, M. Jean, and J.-J. Moreau
1998. Bimodal character of stress transmission in granular packings. *Physical review letters*, 80(1):61. Cited in page 22

Roux, J.-N. and G. Combe
2002. Quasistatic rheology and the origins of strain. *Comptes Rendus Physique*, 3(2):131–140. Cited in page 10

Roux, S. and F. Radjai
1998. Texture-dependent rigid-plastic behavior. In *Physics of dry granular media*, Pp. 229–236. Springer. Cited in page 10

Rudnicki, J. W. and J. Rice
1975. Conditions for the localization of deformation in pressure-sensitive dilatant materials. *Journal of the Mechanics and Physics of Solids*, 23(6):371–394. Cited in page 8

Sadrekarimi, A. and S. M. Olson
2010. Shear band formation observed in ring shear tests on sandy soils. *Journal of geotechnical and geoenvironmental engineering*, 136(2):366–375. Cited in page 8

Šmilauer, V., E. Catalano, B. Chareyre, S. Dorofeenko, J. Duriez, A. Gladky, J. Kozicki, C. Modenese, L. Scholtès, L. Sibille, et al.
2010. Yade reference documentation. *Yade Documentation*, 474(1). Cited in pages 20, 148

Šmilauer, V., B. Chareyre, J. Duriez, A. Eulitz, A. Gladky, N. Guo, C. Jakob, J. Kozicki, F. Kneib, C. Modenese, et al.
2015. Using and programming. *Yade Documentation, 2nd Edn., The Yade Project, https://doi. org/10.5281/zenodo*, 34043. Cited in pages 13, 14, 21

Staron, L.
2008. A numerical study of the onset of granular avalanches. *Journal of the Acoustical Society of America*, 123(5):3291. Cited in pages 11, 106, 123, 157

Staron, L. and E. Hinch
2005. Study of the collapse of granular columns using two-dimensional discrete-grain simulation. *Journal of Fluid Mechanics*, 545:1–27. Cited in pages XIII, 12, 148

Staron, L., F. Radjai, and J.-P. Vilotte
2005. Multi-scale analysis of the stress state in a granular slope in transition to failure. *The European Physical Journal E*, 18(3):311–320. Cited in page 3

Staron, L., F. Radjai, and J.-P. Vilotte
2006. Granular micro-structure and avalanche precursors. *Journal of Statistical Mechanics: Theory and Experiment*, 2006(07):P07014. Cited in pages 11, 106, 123, 157

Tordesillas, A.
2007. Force chain buckling, unjamming transitions and shear banding in dense granular assemblies. *Philosophical Magazine*, 87(32):4987–5016. Cited in page 3

Tordesillas, A., Q. Lin, J. Zhang, R. Behringer, and J. Shi
2011. Structural stability and jamming of self-organized cluster conformations in dense granular materials. *Journal of the Mechanics and Physics of Solids*, 59(2):265–296. Cited in page 142

Tordesillas, A. and M. Muthuswamy
2009. On the modeling of confined buckling of force chains. *Journal of the Mechanics and Physics of Solids*, 57(4):706–727. Cited in page 22

Tordesillas, A., M. Muthuswamy, and S. D. Walsh
2008. Mesoscale measures of nonaffine deformation in dense granular assemblies. *Journal of engineering mechanics*, 134(12):1095–1113. Cited in page 8

Vardoulakis, I., M. Goldscheider, and G. Gudehus
1978. Formation of shear bands in sand bodies as a bifurcation problem. *International Journal for numerical and analytical methods in Geomechanics*, 2(2):99–128. Cited in page 8

Vescovi, D., D. Berzi, and C. di Prisco
2018. Fluid–solid transition in unsteady, homogeneous, granular shear flows. *Granular Matter*, 20(2):1–10. Cited in pages 2, 6, 10

Vescovi, D., I. Redaelli, and C. di Prisco
2020. Modelling phase transition in granular materials: From discontinuum to continuum. *International Journal of Solids and Structures*, 202:495–510. Cited in page 10

Walker, D. M. and A. Tordesillas
2010. Topological evolution in dense granular materials: a complex networks perspective. *International Journal of Solids and Structures*, 47(5):624–639. Cited in page 13

Walker, D. M., A. Tordesillas, and G. Froyland
2014. Mesoscale and macroscale kinetic energy fluxes from granular fabric evolution. *Physical Review E*, 89(3):032205. Cited in page 3

Wan, R., F. Nicot, and F. Darve
2016. *Failure in Geomaterials, a Contemporary Treatise*. ISTE/Elsevier. Cited in page 3

Wan, R., F. Nicot, and F. Darve
2017. *Failure in geomaterials: a contemporary treatise*. Elsevier. Cited in page 3

Wan, R., M. Pinheiro, A. Daouadji, M. Jrad, and F. Darve
2013. Diffuse instabilities with transition to localization in loose granular materials. *International Journal for Numerical and Analytical Methods in Geomechanics*, 37(10):1292–1311. Cited in page 8

Wang, T., A. Wautier, S. Liu, and F. Nicot
2021. How fines content affects granular plasticity of under-filled binary mixtures. *Acta Geotechnica*. Accepted. Cited in page 76

Wautier, A.
2018. *Analyse micro-inertielle des instabilités mécaniques dans les milieux granulaires, application à l'érosion interne*. PhD thesis, Aix-Marseille. Cited in pages 3, 148

Wautier, A., S. Bonelli, and F. Nicot
2018a. Flow impact on granular force chains and induced instability. *Physical Review E*, 98(4):042909. Cited in pages 2, 26

Wautier, A., S. Bonelli, and F. Nicot
2018b. Micro-inertia origin of instabilities in granular materials. *International Journal for Numerical and Analytical Methods in Geomechanics*, 42(9):1037–1056. Cited in pages 8, 25, 73

Wautier, A., S. Bonelli, and F. Nicot
2019. Rattlers' contribution to granular plasticity and mechanical stability. *International Journal of Plasticity*, 112:172–193. Cited in pages 76, 78

Welker, P. and S. McNamara
2011. Precursors of failure and weakening in a biaxial test. *Granular Matter*, 13(1):93–105. Cited in page 3

Wenrui, C.
2021. Analyse multi-échelle du déclenchement d'une instabilité gravitaire par simulations numériques aux éléments discrets. Master's thesis, Ecole Nationale des Ponts et Chaussées. Cited in pages 98, 113, 137

Zhu, H.
2015. *Including a meso-structure in multi-scale modeling of granular soils*. PhD thesis, Université Grenoble Alpes. Cited in pages XIII, 22

Zhu, H., H. N. Nguyen, F. Nicot, and F. Darve
2016a. On a common critical state in localized and diffuse failure modes. *Journal of the Mechanics and Physics of Solids*, 95:112–131. Cited in pages 13, 26

Zhu, H., F. Nicot, and F. Darve
2016b. Meso-structure evolution in a 2d granular material during biaxial loading. *Granular Matter*, 18(1):3. Cited in pages 23, 142, 148

Zhu, H., F. Nicot, and F. Darve
2016c. Meso-structure organization in two-dimensional granular materials along biaxial loading path. *International Journal of Solids and Structures*, 96:25–37. Cited in pages 3, 23, 142

Zhu, H., G. Veylon, F. Nicot, and F. Darve
2017. On the mechanics of meso-scale structures in two-dimensional granular materials. *European Journal of Environmental and Civil Engineering*, 21(7-8):912–935. Cited in pages 3, 23, 149

Titre : Analyse mésoscopique de la transition inertielle dans les milieux granulaires.

Mots clefs : matériaux granulaires, transition inertielle, mésostructures, instabilités, méthode aux éléments discrets.

Résumé : L'un des caractères remarquables du comportement des milieux granulaires est leur capacité à se comporter comme un solide ou un fluide. C'est cette propriété qui est à l'origine des avalanches ou des glissements de terrain par exemple.
La transition inertielle, qui est le passage d'un régime quasi-statique à un régime dynamique, est assimilable à un brusque changement de comportement, de solide à fluide. C'est l'objet d'étude de cette thèse. Les bouffées d'énergie cinétique, premiers signes d'une instabilité, sont analysées à l'échelle mésoscopique en simulant des matériaux granulaires en conditions quasi 2D, soumis à un cisaillement, avec ou sans gravité. Les cycles de grains sont des structures importantes permettant une analyse fine de l'évolution du milieu à une échelle intermédiaire, entre l'échelle des grains et celle du volume élémentaire représentatif. Sur cette base, une échelle mésoscopique est définie, et de nouvelles grandeurs sont définies à cette échelle, notamment un tenseur des contraintes mésoscopique et un travail du second-ordre mésoscopique.
Dans le contexte d'un essai biaxial sans gravité, il est observé que des bouffées d'énergie cinétique apparaissent dans des zones lâches, où les contacts sont plus proches du seuil de glissement que dans le reste de l'échantillon. L'évolution des méso-structures illustre les réorganisations microscopiques localisées dans le temps et dans l'espace créées par une bouffée localisée. Ces observations montrent que le critère du travail du second ordre est aussi applicable à l'échelle mésoscopique et que son annulation est un précurseur à l'apparition d'une bouffée d'énergie cinétique. Des résultats similaires sont retrouvés lors de l'analyse du déclenchement du glissement d'une pente soumise à la gravité. Plus la pente augmente, plus les réorganisations liées aux bouffées d'énergie cinétique sont fréquentes, jusqu'à un glissement généralisé qui marque la fin de la transition inertielle.

Title : Mesoscopic scale analysis of inertial transition in granular materials.

Keywords : granular materials, inertial transition, mesostructures, instabilites, discrete element method.

Abstract : One of the remarkable characters of granular materials behaviour is their capacity to behave like a solid or a fluid. This is this property which leads to snow avalanches or landslides for example.
The inertial transition, which is the transition from a quasi-static regime to a dynamical regime, is consider as a sudden change in the behaviour, from solid to fluid. This is the subject of this PhD thesis. As first clues of inertial instability, bursts of kinetic energy are studied at the mesoscopic scale in different quasi 2D volumes of granular materials, under shearing with or without gravity. Grain loops are important structures allowing a sharp analysis of the media evolution at an intermediate scale, between the grain scale and the scale of a representative elementary volume. On this basis, a mesoscopic scale is defined, and new mesoscopic quantities, in particular a mesoscopic stress tensor and a second-order mesoscopic work.
In the context of a biaxial test without gravity, bursts of kinetic enrgy are shown to appear in a loose areas, where the proportion of critical contacts (close to sliding) is higher than in the rest of the granular specimen. Meso-strucure evolutions underline the time and space dynamics of microscopic reorganizations induced by localized bursts of kinetic energy. These observations show that the second-order work criterion can be applied at the mesoscale and that the vanishing of the second-order mesoscopic work is a precusor of bursts of kinetic energy. Similar results are found for the triggering of slope sliding subjected to gravity. The steeper the slope is, the more frequent the reorganizations linked to bursts of kinetic energy are, until the end of the inertial transition marked by a overall displacement of all grains.